

POLITECNICO DI TORINO

SCUOLA DI DOTTORATO

Research Doctorate Course in
Elettronica e delle Comunicazioni
XXVI ciclo

Final Dissertation

**Advanced Signal Processing
Techniques for Interference
Removal in Satellite Navigation
Systems**



Luciano Musumeci

Tutor
prof. Fabio Dovis

Coordinator of the Research Doctorate Course
prof. Ivo Montrosset

February 2014

To my father

Acknowledgments

My most sincere thanks go to my supervisor, Prof. Fabio Dovis, for his guidance and support that I constantly received during my Ph.D. studies. I am very grateful for his advice and for giving me the opportunity to begin this extremely exciting and funny journey in the research field and to be part of a nice research group.

My mother and my sister for their encouragement which enabled me to carry out this work with more concentration.

My colleagues for the technical support, suggestions and especially for all the funny moments we have shared during these three years.

Finally special thanks to all of my friends especially those with whom I grew up in my hometown and who are still present and determinant in my life.

Table of contents

Acknowledgments	I
I Fundamentals and State of the Art	5
1 Introduction	6
1.1 Motivation of the Work	6
1.2 Basics on Satellite Navigation	7
1.3 Signal Structure	11
1.3.1 Global Position System	13
1.3.2 The Galileo project	15
1.4 The Receiver	20
1.5 GNSS Vulnerabilities	24
2 Interference classification for GNSS	26
2.1 Introduction: Interference Signals in GNSS	26
2.2 Unintentional Interference Sources Classification and Signal Model	29
2.2.1 Out-of-Band Signals	31

2.2.2	In-band signals	38
2.3	The LightSquared case	43
3	Classical Interference Countermeasures in GNSS	45
3.1	Introduction	45
3.2	Interference monitoring and detection strategies	46
3.2.1	AGC monitoring based method for interference detection	47
3.2.2	Goodness of Fit test	49
3.2.3	Multicorrelators based interference detection techniques	52
3.3	Interference mitigation classification	55
3.3.1	Frequency domain techniques	55
3.3.2	Time domain techniques: Pulse blanking	60
3.3.3	Space-time domain techniques	61
II	Interference Impact on GNSS Aviation Receiver and Advanced Countermeasures	68
4	Interference in the ARNS Frequency Band	69
4.1	Introduction	69
4.2	The DME/TACAN Systems	72
4.3	DME/TACAN interference countermeasures	74
4.4	Pulse Blanking Impact on Signal Quality: Theoretical Derivation	77
4.4.1	β computation	77
4.4.2	R_I calculation	80
4.4.3	The case study of central Europe	82
4.5	Experimental Assessment of DME/TACAN Interference	86

4.6	Pulse blanking non-linearities modeling	92
4.7	Conclusions	98
5	Transformed Domain Techniques for Interference Counter-	
	measure in GNSS	100
5.1	Introduction	101
5.2	The Wavelet Transform	105
5.2.1	Discrete Time Wavelet Transform	108
5.3	The Wavelet Based Interference Suppression Algorithm	109
5.4	The Karhunen-Loève Transform	115
5.4.1	KLT interference detection and suppression algorithm	116
5.5	Experimental Results	121
5.5.1	Acquisition performance	121
5.5.2	Tracking performance	123
5.6	WPD based method: parameters tuning	125
5.6.1	The wavelet decomposition depth N	126
5.6.2	Wavelet families comparison	127
5.6.3	Wavelet filter length	129
5.6.4	Computational complexity	129
5.7	Conclusions	130
6	Pulse Blanking Impact on DS/SS Data Demodulation Per-	
	formance	132
6.1	Introduction	133
6.2	Direct Sequence Spread Spectrum Modulation	134
6.2.1	DS/BPSK system	134

6.2.2	DS/SS Demodulation	136
6.2.3	DS/SS and Coding	137
6.3	Pulse blanking impact on un-coded DS/BPSK system performance	139
6.3.1	AWGN pulsed interference	141
6.3.2	DME/TACAN interference	147
6.4	Pulse blanking non linearities impact on real coded DS/BPSK system: the Galileo E5a case	149
6.4.1	Pulse blanking non linearities	150
6.4.2	The F/NAV message on Galileo E5a-I	152
6.5	Conclusions	156

III Design of a High Sensitivity Receiver for GNSS signal acquisition in harsh environment 158

7 Weak GNSS Signal Navigation 159

7.1	Introduction	159
7.2	State of the art of High Sensitivity Receiver	160
7.3	GNSS environment on the Lunar orbit	162
7.4	Acquisition Scheme and Detection Algorithm	163
7.4.1	Acquisition threshold determination	165
7.4.2	Searching Strategies	168
7.5	Theoretical Acquisition Sensitivity Analysis	173
7.5.1	Coherent SNR	173
7.5.2	Non-Coherent signal accumulation	175

7.6	Assisted GNSS: theoretical performance and requirements definition	178
7.6.1	Search space reduction: Doppler domain	179
7.6.2	Assisted GNSS definition requirements: methodology .	180
7.6.3	Case study:Acquisition on the lunar orbit	182
7.7	Conclusions	194
	Bibliography	196

List of tables

1.1	GPS and Galileo bands	12
1.2	Current and Future GPS Signals	16
1.3	Current and Future Galileo Signals	19
2.1	Main in-band interference system sources	42
4.1	L-band Primary Radar main parameters	70
4.2	Secondary Radar main parameters	71
4.3	Setup settings	88
4.4	Front-End settings	94
5.1	Acquisition performance comparison	123
5.2	Acquisition performance	125
6.1	E5a PRN code	153
7.1	Ideal Front-end parameter for GPS L1 C/A code	174
7.2	E1c Galileo signal: scenario parameters	183
7.3	Assisted Global Navigation Satellite System (GNSS): Theoretical results for pure coherent Galileo E1c signal acquisition	186
7.4	Assisted GNSS: Theoretical results for non coherent Galileo E1c signal acquisition	187
7.5	Lunar Low Orbit scenario: Galileo E1bc CBOC	188

7.6	Assisted GNSS: Theoretical results for pure coherent GPS L1 C/A signal acquisition	190
7.7	Assisted GNSS: Theoretical results for non coherent Global Positioning System (GPS) L1 Coarse/Acquisition (C/A) signal acquisition	190
7.8	Lunar Low Orbit scenario: GPS L1 C/A	191
7.9	Assisted GNSS: Theoretical results for pure coherent E5a-Q channel acquisition	192
7.10	Assisted GNSS: Theoretical results for non coherent Galileo E5a-Q channel acquisition	193
7.11	Lunar Low Orbit scenario: Galileo E5a-Q	193

List of figures

1.1	Basic principle of the localization technique	8
1.2	Effect of Receiver Clock Offset on TOA Measurements	9
1.3	Current GPS satellites constellation	14
1.4	Spectra of the current and planned GPS signals	14
1.5	Galileo Frequency Plan	18
1.6	Generic GPS receiver block diagram	20
2.1	Power Spectrum of a C/A Code.	32
2.2	Potential TV Channel Harmonic Interference.	33
2.3	Possible in-band and out-of-band interferences (a). Secondary harmonics interference within the GPS L1 and Galileo E1 bands (b)	34
2.4	Potential VHFCOM Channel Harmonic Interference.	35
2.5	Potential FM Harmonic Interference.	35
2.6	DME/TACAN and JTIDS/MIDS Frequency Plan.	40
2.7	Interference Harmonics in E5a, E5b and E6 bands.	43
3.1	Classical GNSS receiver architecture	47
3.2	Typical AGC gain in presence and in absence of interference	48
3.3	p-value trend of the Chi-square Goodness of Fit (GoF) test in presence and absence of interference	52

3.4	Results of the sign test applied to Very Early - Very Late correlators in a CW interfered scenario	54
3.5	FDAF functioning scheme	56
3.6	Notch filter structure	58
3.7	Typical Pulse blanking implementation	61
3.8	DME/TACAN pulse before and after blanking	62
3.9	GNSS receiver with space-time array processing	63
3.10	STAP weight control algorithm	64
4.1	DME/TACAN system	72
4.2	DME/TACAN pulse pair shape	73
4.3	DME/TACAN single base-band pulse	78
4.4	DME/TACAN pulse before and after blanking	79
4.5	Ratio between the real blanker activation time and the theoretical activation time T defined in (4.3)	79
4.6	Pulse blanker activation time in presence pulse superposition	82
4.7	Prediction of the effective post correlator Carrier-to-Noise density power ratio (C/N_0)	83
4.8	Prediction of the blanker duty cycle β	83
4.9	Number of Distance Measuring Equipment (DME)/Tactical Air Navigation (TACAN) stations in Line-of-Sight (LoS)	84
4.10	Blanker duty cycle β and R_I factor versus the blanking threshold	85
4.11	Hardware setup	86
4.12	TUR performance under DME/TACAN interference in Galileo E5a and GPS L5 frequency bands	89
4.13	TUR performance during aircraft approach simulation	90

4.14 DME/TACAN interference impact on C/N_0 and Geometric Dilution of Precision	91
4.15 Front-End block scheme	94
4.16 DME/TACAN scenario	95
4.17 Blanker duty cycle β variation for different reaction and recovery time values	96
4.18 N-GENE acquisition performance: (a) α_{mean} . (b) α_{max}	97
5.1 Typical TD technique block scheme	102
5.2 Meyer wavelet filters bank responses	107
5.3 Wavelet Packet Decomposition	110
5.4 DME/TACAN scenario	111
5.5 Time-scale representation	111
5.6 Pulse blanking applied on the single scale	112
5.7 Wavelet Packets statistical analysis	113
5.8 Time-scale after interference excision	114
5.9 Signal comparison: Before and after mitigation	115
5.10 KLT decomposition comparison between interference case and interference free case	117
5.11 GNSS signal energy decay vs. KLT coefficients removed	119
5.12 KLT decomposition and signal energy	120
5.13 Power Spectral density comparison: before and after KLT based interference suppression	121
5.14 Acquisition search space: (a)No countermeasures. (b) After pulse blanking. (c) After WPD based method. (d)After KLT based method	122
5.15 Carrier to Noise density ratio comparison	124

5.16	Early-Prompt-Late correlators	124
5.17	Modulation	125
5.18	Acquisition metric versus WPD depth	126
5.19	Modified Gaussian wavelet filter bank response	128
5.20	Acquisition metric: Gaussian vs Meyer wavelet	128
5.21	Acquisition metric: Gaussian wavelet based filter length	129
6.1	Uncoded DS/BPSK system	134
6.2	Coded DS/BPSK system	138
6.3	Case 1: 2 pulses per each symbol ($\alpha = 2$)	142
6.4	Bit Error Rate for un-coded DS/BPSK system in presence of Additive White Gaussian Noise (AWGN) pulsed interference	143
6.5	Theoretical and simulated pulse blanking performance against AWGN based pulsed interference	146
6.6	Pulse blanking impact on BER for un-coded DS/BPSK system in presence of AWGN pulsed interference	147
6.7	Pulsed peak power to signal power ratio profile	148
6.8	Pulse blanking impact on Bit Error Rate for un-coded DS/BPSK system in presence of AWGN pulsed interference	149
6.9	Ideal versus non-ideal pulse blanking	150
6.10	Blanker duty cycle β for different values of reaction γ and recovery δ time	151
6.11	Effective C/N_0 for different values of reaction γ and recovery δ time	152
6.12	E5a and E5b signal modulation	153
6.13	Galileo E5a signals interfered with DME/TACAN pulses	154

6.14	Pulse blanking impact on E5a-I channel data demodulation performance in presence of DME/TACAN system: hard decoding	155
6.15	Pulse blanking impact on E5a-I channel data demodulation performance in presence of DME/TACAN system: hard decoding	156
7.1	Time parallel acquisition scheme: the Cross Ambiguity Function (CAF) is determined by using a circular convolution employing efficient FFTs	164
7.2	Non-coherent accumulations in acquisition scheme	167
7.3	False alarm probability at search space level versus the number of bins in the search space for a fixed false alarm probability at cell level	171
7.4	False alarm probability at search space level versus false alarm probability at cell level for a fixed number of bins in the search space	172
7.5	Coherent SNR	174
7.6	ROC curve - Coherent integration	175
7.7	Non coherent acquisition performance	176
7.8	ROC curve- Non coherent integration	177
7.9	Squaring loss	177
7.10	Galileo E1c non coherent acquisition: Theoretical ROC curves at cell level	184
7.11	Galileo E1c non coherent acquisition: Acquisition metrics P_{FA}^a vs P_{fa} for different aiding scenario	184
7.12	Galileo E1c non coherent acquisition: Theoretical ROC curve at search space level (P_D)	185
7.13	Galileo E1c non-coherent acquisition: Theoretical ROC curve at search space level (P_{MD})	185

7.14 Galileo E1c non coherent acquisition: Theoretical ROC curve at search space level (P_{FA}^p)	186
7.15 Galileo E1c non coherent acquisition: Search Space	189
7.16 Galileo E1c acquisition at 5 dB-Hz: CAF in the code delay 7.16(a) and Doppler 7.16(b) domain	189
7.17 GPS L1 C/A non coherent acquisition: Search Space	192
7.18 Galileo E5a-Q channel non coherent acquisition: Search Space	194

List of acronyms

3GPP	3rd Generation Partnership Project
A-GNSS	Assisted GNSS
AM	Amplitude Modulation
AR	Auto-Regressive
ARNS	Aeronautical Radio Navigation System
ATC	Air Traffic Control
ADC	Analog to Digital Converter
AGC	Automatic Gain Control
AWGN	Additive White Gaussian Noise
BER	Bit Error Rate
BOC	Binary Offset Carrier
BPSK	Binary Phase Shift Keying
C/A	Coarse/Acquisition
C/N_0	Carrier-to-Noise density power ratio
CAF	Cross Ambiguity Function
CBOC	Composite Binary Offset Carrier

CCF	Cross Correlation Function
CDMA	Code Division Multiple Access
CS	Commercial Service
CWI	Continuous Wave Interference
DFT	Discrete Fourier Transform
DME	Distance Measuring Equipment
DLL	Delay Locked Loop
DS/BPSK	DS/BPSK
DS/SS	Direct Sequence Spread Spectrum
DVB	Digital Video Broadcasting
DWT	Discrete Wavelet Transform
E_b/N_0	Energy per bit to Noise density power ratio
E_b/J_0	Energy per bit to Jammer density power ratio
EGNOS	European Geostationary Navigation Overlay Service
EIRP	Equivalent Isotropic Radiated Power
EU	European Union
FCC	Federal Communications Commission
FDAF	Frequency Domain Adaptive Filtering
FFT	Fast Fourier Transform
FIR	Finite Impulse Response
FLL	Frequency Locked Loop

FM	Frequency Modulation
FOC	Full Operational Capability
HS	High Sensitivity
<i>J/C</i>	Jammer to Carrier power ratio
JTIDS	Joint Tactical Information Distribution System
KLT	Karhunen-Loève Transform
GDOP	Geometrical Dilution of Precision
GNSS	Global Navigation Satellite System
GoF	Goodness of Fit
GPS	Global Positioning System
IF	Intermediate Frequency
IFF	Identification friend or foe
IIR	Infinite Impulse Response
ILS	Instrument Landing System
IOC	Initial Operational Capability
IOV	In-Orbit-Validation
LMS	Least Mean Square
LNA	Low Noise Amplifier
LLO	Low Lunar Orbit
LO	Local Oscillator
LoS	Line-of-Sight

LTE	Long Term Evolution
MA	Moving Average
MAT	Mean Acquisition Time
MBOC	Multiplexed Binary Offset Carrier
MEO	Medium Earth Orbit
MIDS	Multifunctional Information Distribution System
MMSE	Minimum Mean Square Error
MSS	Mobile Satellite Service
MTO	Moon Transfer Orbit
MVDR	Minimum Variance Distortion-less Response
NBI	Narrow-band Interference
OCXO	Oven Controlled Crystal Oscillator
OS	Open Service
PAM	Pulse Amplitude Modulation
PDF	Probability Density Function
PED	Personal Electronic Device
PLL	Phase Locked Loop
PPM	Pulse Position Modulation
PRF	Pulse Repetition Frequency
PRN	Pseudo Random Noise
PRS	Public Regulated Service

PSD	Power Spectral Density
PSR	Primary Surveillance Radar
QMF	Quadrature Mirror Filters
QPSK	Quadrature Phase Shift Keying
ROC	Receiver Operating Characteristic
RF	Radio Frequency
RFI	Radio Frequency Interference
SAR	Search and Rescue Support Service
SBAS	Space Based Augmentation System
SiS	Signal in Space
SNR	Signal to Noise Ratio
SS	Sum-of-Squares
SSR	Secondary Surveillance Radar
STAP	Space Time Adaptive Processing
STFT	Short Time Fourier Transform
TACAN	Tactical Air Navigation
TCAS	Traffic Collision Avoidance System
TCXO	Temperature Compensated Crystal Oscillator
TD	Transformed Domain
TF	Time Frequency
TOA	Time Of Arrival

TTF	Time to First Fix
UHF	Ultra-High Frequency
UWB	Ultra Wide Band
VHF	Very-High Frequency
VOR	VHF Omni-directional Range
WAAS	Wide Area Augmentation System
WBI	Wide-band Interference
WPD	Wavelet Packet Decomposition

Introduction

This thesis investigates the use of innovative interference detection and mitigation techniques for GNSS based applications. The main purpose of this thesis is the development of advanced signal processing techniques outperforming current interference mitigation algorithms already implemented in off-the-shelf GNSS receivers.

State-of-the-art interference countermeasures already investigated in literature, which process the signal at the Analog to Digital Converter (ADC) output, provide interference components suppression in the time domain or in the frequency domain, thus leading to a significant signal degradation in harmful interference scenarios where the GNSS signals spectra at the receiver antenna is completely jammed by external intentional or unintentional Radio Frequency Interference (RFI) sources.

The proposed advanced interference countermeasures overcome such a limit, since they are based on particular signal processing techniques which manipulate the received samples at the ADC output, providing a representation in new domains where interference component can be better detected and separated from the rest of the signal, minimizing the useful signal distortion even in presence of multiple interference sources. At the cost of an increased computational complexity, such techniques can be optimized for increasing the sensitivity and the robustness of GNSS receiver merged in harmful environments.

The work of this thesis addresses the design of such techniques by means of theoretical analyses, their performance assessment by means of simulation

and their validation by means of synthetic and real GNSS data. Furthermore performance comparison with more traditional interference countermeasures is also presented considering a variety of harmful interference scenarios.

In addition to the investigation of such new interference countermeasures, part of the thesis deals with the limit of current interference suppression technique, such as the pulse blanking, and its impact on the data demodulation performance. A very general investigation of the pulse blanking impact on the data demodulation performance for un-coded Binary Phase Shift Keying (BPSK) Direct Sequence Spread Spectrum (DS/SS) is provided. Then, the analysis focuses on the assessment of the navigation data demodulation performance for the current Space Based Augmentation System (SBAS), then providing a proposal for system improvements, in terms of robustness and data rate increase, in future SBAS generation.

Among the different interference scenarios considered, the thesis focuses on the potential interference environment expected in aviation context, since the Galileo E5 and GPS L5 bands, where the future GNSS based aviation services will be broadcast, are shared with other Aeronautical Radio Navigation Systems (ARNSs) broadcasting strong pulsed interfering signals, which may seriously threat the on-board GNSS receiver operations. For such scenarios, simulation and analytic models are discussed and used as benchmark cases for assessing the mitigation techniques, in terms of Signal to Noise Ratio (SNR) gain and data demodulation capability.

The presence of interference (mitigated or not) causes a loss in the carrier to noise density ratio C/N_0 value for the received signal. For this reason, in order to reliably deal with such signals, the GNSS receiver must be able to feature high-sensitivity algorithms at the acquisition and tracking stages. For this reason the last part of the thesis investigates High Sensitivity (HS) acquisition schemes for very weak GNSS signal detection. In particular, the purpose of this part of the work is to present a theoretical methodology for the design of an acquisition scheme capable of detecting signal down to 5

dB-Hz. The analysis carried out assuming the presence of assistance information which allows the receiver employing long coherent integration time (order of seconds). The particular scenario of the GNSS space environment is taken into consideration and the analysis is also focused on the definition of the requirements on the accuracy for potential Doppler aiding sources at the receiver level.

The theoretical analysis is also supported by fully software simulation.

Thesis Outline

The thesis is divided in three parts as follows:

1. *Fundamentals and State of the Art.* Background on GNSS systems, GNSS signals, and GNSS receivers architecture is provided in Chapter 1. Chapter 2 provides an overview of the main unintentional interference sources while in Chapter 3 the main detection and mitigation algorithms presented in literature are reported.
2. *Interference Impact on GNSS Aviation Receiver and Advanced Countermeasures.* After providing a detailed description of the main interference sources for the GNSS services in the ARNSs frequency bands, a detailed assessment of the impact of such pulsed interference sources on GNSS receiver is provided in Chapter 4. Such analysis has been performed in the navigation laboratory of the European Space Research and Technology Centre (ESTEC/ESA), in the Netherlands and results have been published in [1]. Furthermore, the most common pulsed interference such as the pulse blanking will be deeply investigating in Chapter 4. Chapter 5 will focus on the investigation on new advance signal processing based interference detection and mitigation algorithms. In particular two advanced interference countermeasure based Wavelet Packet Decomposition (WPD) and on Karhunen-Loève Transform (KLT) will presented

and their performance in suppressing interference will be assessed. The results achieved from this research activity have been published in [2] [3] [4] and [5].

Chapter 6 provides an assessment of the impact of the pulse blanking and its non linearities effect on the data demodulation performance of coded and un-coded DS/SS system.

3. *Design of a High Sensitivity Receiver for GNSS signal acquisition in harsh environment.* Chapter 7 will address the design of a HS acquisition scheme for weak GNSS signals in space environments. Results of this activity can be found in [6].

Part I

Fundamentals

and

State of the Art

Chapter 1

Introduction

1.1 Motivation of the Work

In a short time new demanding applications, as for instance financial and life critical timing and positioning services, will be included in the plethora of uses of new [GNSS](#) applications. They will require the ability to restrict access to some class of protected information by the user position meaning, provided by some [GNSS](#) technology. Access control tokens using trusted [GNSS](#) receivers will provide the information security core for this kind of applications, including banking, enterprise and secure timestamps. The location-based control concept is based on the definition of a secure architecture able to constrain the position user to the access of particular data or services, such as private documents or business transactions. In this context, the position information provided by [GNSS](#) should be improved, mainly in terms of availability (e.g. using [GPS](#) and the Galileo systems), reliability (e.g. Wide Area Augmentation System ([WAAS](#)) or European Geostationary Navigation Overlay Service ([EGNOS](#))) and security. This last aspect can include encryption techniques using cryptography or involve definition of proper methods for signal authentication and navigation solution quality. These are key issues to consider due to the critical environment condition where the receiver is forced to

operate in.

It is well known that the reception of GNSS signals can be affected by RFI that can partially or totally compromise the correct receiver behavior. Unintentional interfering signals such as harmonics generated by Digital Video Broadcasting (DVB) transmitters or intentional one, as intentional high power signals generated by jammers, can dramatically compromise the navigation data access control mechanism. Intentional disturbs can also be used to inhibit the tracking stage in order to force the receiver status in the re-acquisition mode for spoofing purposes. The development of anti-jamming algorithms is then becoming central not only for Safety of Life applications and professional receiver but also to guarantee location-based services. To assure trusted receiver outputs, valuable tools should be designed in order to protect the reliability of the position estimation.

1.2 Basics on Satellite Navigation

GNSS refers to all the systems either operational or under development which provide location information based on transmission of signals by Medium Earth Orbit (MEO) satellites. The signals transmitted by every GPS and Galileo satellites allow the users to estimate instantaneously and in real time its PVT in a Earth centered reference system. Both GPS and Galileo satellite are based on the Time Of Arrival (TOA) concept, and users determine their position evaluating the time interval between the signal transmission and the signal reception. This is possible thanks to very accurate atomic clocks on-board the satellites; all of them synchronized with respect to a common time scale. Receiver clocks are not synchronized to the system time, and full synchronization can be achieved only when the signal is acquired and tracked and the navigation message demodulated. It is assumed that the position of satellites is precisely known [7]. The time instant at which the signal is transmitted is embedded in the ranging signal, so the receiver can

calculate the propagation time of the signal; multiplying this and the speed of light (i.e. the signal velocity) the receiver determines the user-to-satellite range. Assuming that the receiver clock is perfectly synchronized with the satellite transmitter, the distance \underline{v} between the satellite and the user can be calculated measuring the transit time of the signal. In the three-dimensional space, every \underline{v}_n vector defines a spherical surface having center the satellite n , whose coordinates are represented by the \underline{v}_n^s vector. From the intersection of at least three of these spheres, it is possible to compute a very precise point that represents the true user position.

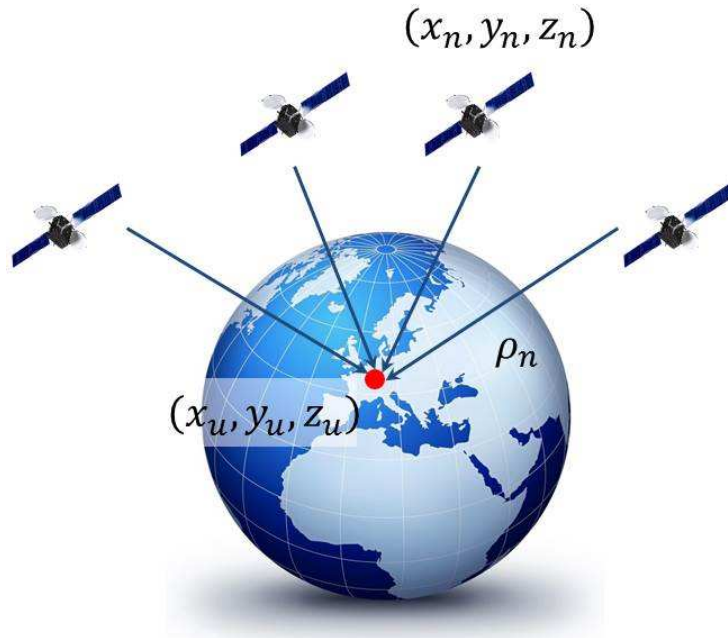


Figure 1.1: Basic principle of the localization technique

Giving the following definition of distance:

$$v_n = \|\underline{v}_n^s - \underline{v}_R\| \quad (1.1)$$

and setting a system of three equations, the solution of \underline{v}_R can be obtained; this vector represents the user coordinates in a cartesian system.

However, in a real situation, the receiver clock is not synchronized with the transmitter. While all the satellite payloads host synchronous clocks, it is not possible to have user clocks aligned with the satellite time scale at low

cost and complexity. Furthermore, GNSS are conceived to be one directional systems (i.e. not requiring the user to interact with the satellite constellation), thus not allowing two-way methods for keeping the satellites and the receivers aligned to the same time-scale. The measure of the distance suffers of a bias as shown in Figure 1.2 by the ε term, that is common to each satellite.

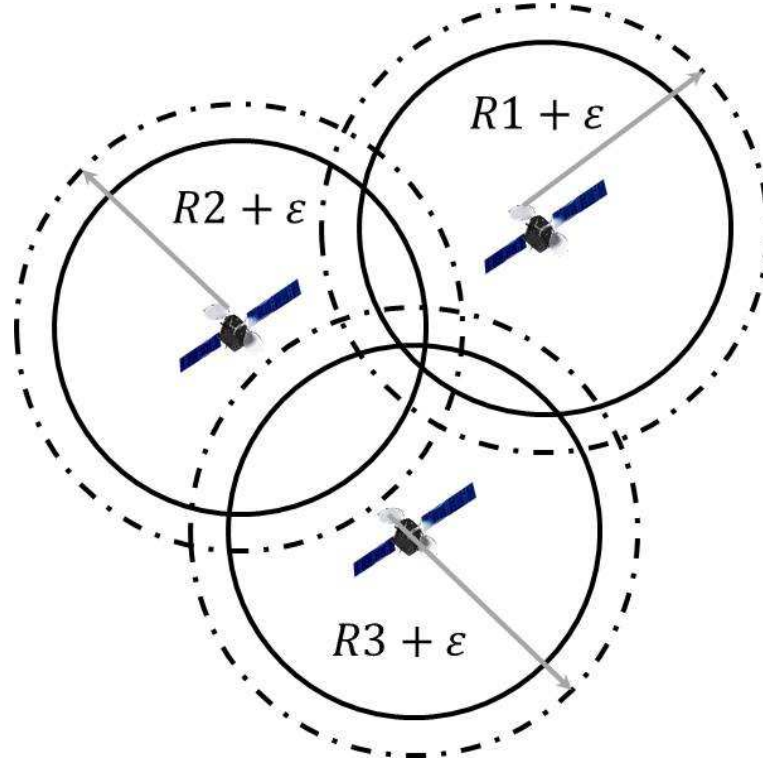


Figure 1.2: Effect of Receiver Clock Offset on TOA Measurements

This bias represents the shift of the receiver time scale with respect to the GNSS time scale. The measurement performed by the receiver is then called *pseudorange* ρ and it is defined as the sum of the true distance R_j and a term due to the time scale misalignment. Analytically the pseudorange can be written as

$$\rho_j = R_j + \varepsilon = R_j + c \cdot \delta t_u \quad (1.2)$$

where c is the speed of the light and δt_u is the user clock bias. This term cannot be recovered using the data contained in the satellite signal, therefore, the intersection of another sphere generated on a further satellite is necessary. The generic j -th pseudorange can be written as

$$\rho_j = \sqrt{(x_j - x_n)^2 + (y_j - y_n)^2 + (z_j - z_n)^2} + b_{ut} \quad (1.3)$$

where x_u, y_u, z_u are the user coordinates, x_{sj}, y_{sj}, z_{sj} are the coordinates of four satellites and $b_{ut} = c \cdot \delta t_u$ is the clock bias term. As δt_u can not be recovered using the data contained in the satellite signal the intersection of another sphere generated on a further satellite is therefore necessary. The intersection of four spheres is then given by [8]:

$$\begin{cases} |\rho_1| = \sqrt{(x_1 - x_n)^2 + (y_1 - y_n)^2 + (z_1 - z_n)^2} + b_{ut} \\ |\rho_2| = \sqrt{(x_2 - x_n)^2 + (y_2 - y_n)^2 + (z_2 - z_n)^2} + b_{ut} \\ |\rho_3| = \sqrt{(x_3 - x_n)^2 + (y_3 - y_n)^2 + (z_3 - z_n)^2} + b_{ut} \\ |\rho_4| = \sqrt{(x_4 - x_n)^2 + (y_4 - y_n)^2 + (z_4 - z_n)^2} + b_{ut} \end{cases} \quad (1.4)$$

The solution of (1.4) gives the user location and the value of δt_u , allowing the user to synchronize its own receiver to the GNSS time scale [7]. It has to be noted that in order for a receiver to estimate its position, the receiver must have at least four satellites in view. These satellites must be in LoS, or the relationship between the propagation time and the geometric distance is lost. If a larger number of satellites is in view, a better estimation is possible. In the past, due to computational constraints, the combination of four satellites giving the best performance was chosen. Modern receivers use up to 12 channels (and even more in the future) in order to perform the position and time estimation. The estimation of a pseudorange is performed by the user receiver, processing an electromagnetic signal transmitted by the satellites

Notice that other errors are present in the range measurement, in addition to the time offset, but in the following they have been neglected to keep the analysis terse. As previously stated, the distance r between the satellite and the user is calculated measuring the TOA of the ranging code

$$R = c(T_u - T_s) = c\Delta t \quad (1.5)$$

where T_u is the system time at which the signal is received by the user, T_s is the system time at which the signal was broadcast by the satellite and c is the speed of light. This expression is generally called *geometric range*, but it is not what the receiver really measures. The receiver and the satellite clocks, in fact, generally have a bias error from the reference time (t_u for the receiver and δt for the satellite clock). So the pseudorange ρ is computed as

$$\rho = c[(T_u + t_u) - (T_s + \delta t)] = c(T_u - T_s) + c(t_u - \delta t) = r + c(t_u - \delta t) \quad (1.6)$$

The satellite ground network uploads to the satellites the correction for the offset δt , which is then broadcast to the user by the navigation message; in this way, δt is no longer considered as unknown. Hence,

$$\rho = R + ct_u \quad (1.7)$$

The unknowns to be determined are the user position in three dimension and the offset of the receiver clock from system time t_u , so at least four pseudorange measurements are required. The equations involved in pseudorange determination are nonlinear, so they should be linearized using, for example, an approximate user position around which linearize.

1.3 Signal Structure

As it will be clearer in the following chapters, the effect and the impact of a specific type of interferer strongly depend on the characteristics of the **GNSS** signal itself. Before describing the possible interference sources, an overview on the the main characteristics of the satellite navigation signals available today and foreseen for the future is necessary. In principle **GNSS** signal are **DS/SS** modulated signals, where a sequence of binary symbols $d(t)$ ($+1, -1$) transmitted at a low bit rate R_b is modulated with a so called Pseudo Random Noise (**PRN**) sequence $c(t)$, composed by binary chips ($+1, -1$) transmitted at higher data rate R_c . As an example, the basic **BPSK** signal is

made by navigation data transmitted at 50 bps multiplied by PRN sequence transmitted at 1.023 Mcps. The effect of such operation is a bandwidth expansion of the useful GNSS signal broadcasting in the channel. For such a reason the PRN sequence is also known as spreading sequence. Each satellite of the constellation transmits its own PRN sequence. All the PRNs sequence broadcast by satellites have extremely good un-correlation properties. Thus at receiver level, the user receiver is able to recognize the signal broadcast by a determined satellite through a correlation process between the received signal and a locally generated PRN replica. Such a system is also known as Code Division Multiple Access (CDMA), since all the satellites transmit simultaneously on the same carrier frequency, but they feature a different code uncorrelated with the codes broadcast by the other satellites. Concept of DS/SS modulation and CDMA will be resumed with more detail in Chapter 6. The following sections will focus in particular on the American GPS and the new European civil satellite based positioning system Galileo. For both systems three frequency bands are allocated: L1, L2, and L5 are for GPS, while, E1, E6, and E5 (E5a and E5b) are for Galileo. Portions of bands are shared between the two systems. Table 1.1 provides a summary of the current GPS and Galileo bands

Table 1.1: GPS and Galileo bands

System	Band	Bandwidth (MHz)	Center Frequency (MHz)
GPS	L5	24 [1164-1188]	1176.45
	L2	20 [1217-1230]	1227.60
	L1	24 [1563-1587]	1575.42
Galileo	E5a	27 [1164-1191.795]	1176.45
	E5b	25 [1191.795-1217]	1207.14
	E6	40 [1260-1300]	1278.75
	E1	32 [15559-1591]	1575.42

1.3.1 Global Position System

Current status of the American GPS system can be found in [9]. Born in 1973, the current GPS constellation consists of 31 satellites, 24 of which are maintained available 95% of the time by the United States. GPS satellites fly in medium earth orbit at an altitude of approximately 20.200 km. Each satellite circles the Earth twice a day.

Within the different phases of the GPS system, different satellite blocks have been developed [7]:

- the initial concept validation satellites were called Block I. Ten prototype satellites have been launched between 1978 and 1985;
- 24 satellites of Block II/IIA have been launched between 1989 and 1995, when the system was declared operational. Block II satellites are the initial production satellites, while Block IIA refers to upgraded production satellites;
- block IIR satellites (R stands for replenishment) entered in service in 1997;
- modified Block IIR versions, denoted as Block IIR-M, started in 2005;
- 4 new block IIF (F stands for follow-on) satellites started being launched since 2010 carrying the new 3rd civil signal on L5 frequency (L5);
- block III satellites are in the production stage and first launches are foreseen in 2015. Their payload will feature all the signals transmitted by the block IIF satellites plus the new 4th civil signal on L1 frequency band (L1C)

The current 31 operational satellite are distributed according the table in Figure 1.3


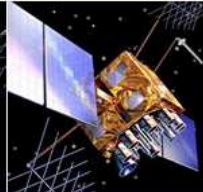
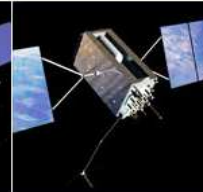
LEGACY SATELLITES		MODERNIZED SATELLITES		
				
BLOCK IIA	BLOCK IIR	BLOCK IIR(M)	BLOCK IIF	GPS III
8 operational	12 operational	7 operational	4 operational	Now in production

Figure 1.3: Current GPS satellites constellation

As far as GPS is concerned, the C/A and P codes are considered as current signals, while all the signals belonging to the modernization phase (L2C, L5, M code) can be classified as part of the evolution phase. In fact, though there are some satellites that are already broadcasting L5, L2C and M code signals, the modernization phase is still under development and its completion is foreseen for the next years.

A qualitative representation of the current and foreseen GPS signals spectra is given by Fig. 1.4. For each signal it is also indicated the satellites block it belongs to, or will belong to.

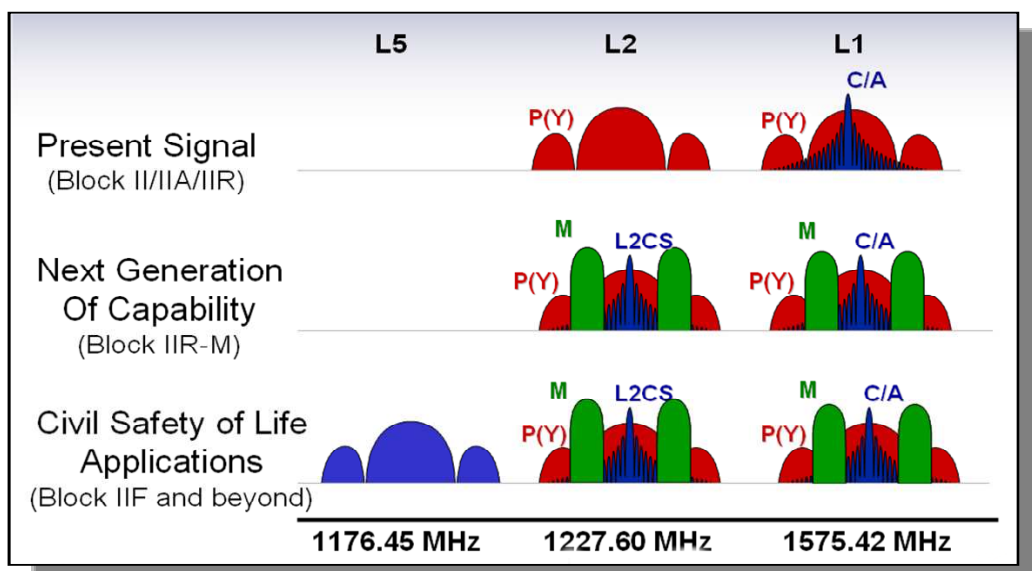


Figure 1.4: Spectra of the current and planned GPS signals

1.3.1.1 GPS Signals baseline

Currently each GPS satellite transmits continuously using two radio frequencies: L1 and L2. Two signals are transmitted on L1, one for civil users, and the other for DoD-authorized users [10]. As far as GPS is concerned, its modernization started in the late 1990s soon after the system became operational and it is still on going, also driven by the potential competition of the growing Galileo. The plans for GPS modernization cover both civil and military fields. Two new civil signals are defined: a signal on L2, called L2C [11], and a signal on L5, called L5 [12]. The M code is the military code, properly designed to have sufficient isolation to prevent mutual interference. In addition the United States is planning to add a modernized civil signal upon the L1 frequency within the Block III time frame, the L1C. L1C is the fourth civilian GPS signal, designed to enable interoperability between GPS and international satellite navigation systems. L1C features a Multiplexed Binary Offset Carrier (MBOC) modulation scheme that enables international cooperation while protecting U.S. national security interests. The design will improve mobile GPS reception in cities and other challenging environments. More detail on technical specification of this new civil signal can be found in [13] As far as the two civil signals L2C and L5, which belong to the Block IIR-M and IIF respectively, they are already operation as shown in Figure 1.3

For the sake of clearness, all the time and spectral characteristics of current and future GPS signals are summarized in Table 1.2.

1.3.2 The Galileo project

The Galileo programme, is an European initiative for the development of a fully autonomous satellite-based positioning, navigation and timing capability , for global high performance services [16]. The Galileo Space Segment will

Table 1.2: Current and Future GPS Signals (from [11] [13][14] [15] [10] [12])

Band/Signal	Modulation Scheme	Code Rate (Mcps)	Data Rate (bps)	Central Frequency	Spectral Occupation ^(*) (MHz)	Min Rx Power (dBW)
L1	BPSK	C/A 1.023	50	1575.42	2.046	-158.5
	BPSK	P 10.23	50	1575.42	10.23	-161.5
L2	BPSK	C/A 0.5115	50	1227.60	1.023	-158.5
	BPSK	P 5.115	50	1227.60	10.23	-161.5
L5	BPSK	10.23	25	1176.45	24	-157.9
L2/L2C	BPSK	CM 511.5E3 CL 511.5E3	50 ^(**) no data	1227.60	2.046	-160
L5	QPSK	I5 10.23E6 Q5 10.23E6	50 no data	1176.45	20.46	-154.5
L1-L2/ M code	BOC(10,5)	c.g. ^(***)	N/A	1575.42 1227.60	30.69	-158
L1/L1C	BOC(1,1) or TMBOC	C _P 1.023E6 C _D 1.023E6 C _O 100	no data 50 or 75 no data	1575.42	4.092	-157

(*) referring to the main lobe/lobes

(**) the data rate includes the FEC

(***) cryptographically generated

include a constellation of a total of 30 MEO satellites. The development of such system has been structured according to the following three phases:

1. Experimental phase (two satellites) Two experimental satellites, GIOVE-A and GIOVE-B, launched respectively December 2005 and April 2008 have characterised and verified the critical technologies needed by Galileo within the medium-Earth orbit (MEO) environment. They have also reserved radio frequencies set aside for Galileo by the International

Telecommunications Union. Both successfully completed their missions and are no longer operational.

2. In-Orbit-Validation (**IOV**) phase (four satellites) The aim of the Galileo **IOV** phase is to validate the system design using a reduced constellation of four satellites, the minimum required to provide exact positioning and timing at the test locations along with a limited number of ground stations. The first two **IOV** satellites were carried into orbit by a Soyuz launcher from Europe's Spaceport in French Guiana on 21 October 2011. The second pair was launched on 12 October 2012. All four **IOV** satellites now are continuously broadcasting their payloads across the three allocated frequency band (see Table 1.1. Some example of **IOV** satellite signal assessment can be found in [17] and [18].
3. Full Operational Capability (**FOC**) phase (four **IOV** satellites plus 26 **FOC** satellites) Launched in parallel to the In Orbit Validation (**IOV**) phase, the **FOC** phase will lead to the deployment of the remaining ground and space infrastructure. It includes an intermediate Initial Operational Capability (**IOC**) milestone with 18 satellites in operation (four **IOV** satellites plus 14 **FOC** satellites). Early services with reduced performance or for demonstration purpose will be provided from mid-2014.

The presence of new Signals in-space stemming from the Galileo satellites, will offer new classes of worldwide services to cover the widest range of user needs, including professional users, scientists, mass-market users and public regulated domains [16]:

- the Open Service (**OS**) is free of charge to the user and provides positioning and synchronisation information intended mainly for high-volume satellite navigation applications; a contribution, by means of Galileo

OS signals and/or in cooperation with other satellite navigation systems, to integrity monitoring services aimed at users of Safety-of-Life applications in compliance with international standards.

- the Commercial Service (CS) for the development of applications for professional or commercial use by means of improved performance and data with greater added value than those obtained through the Open Service. Implementation of the CS is not foreseen in the IOV phase.
- the Public Regulated Service (PRS) restricted to government authorised users, for sensitive applications that require a high level of service continuity, free of charge for European Union (EU) Member States, the Council, the Commission, the European External Action Service and EU agencies. The PRS uses strong, encrypted signals; a contribution to the Search and Rescue Support Service (SAR) of the Cospas-Sarsat system by detecting distress signals transmitted by beacons, locating these beacons and relaying messages to them.

1.3.2.1 Galileo Signals

The Galileo frequency plan is depicted in Fig. 1.5, while the structure of its signals is described by table 1.3.

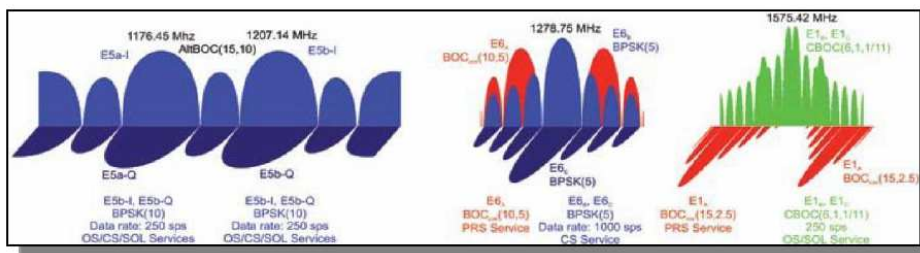


Figure 1.5: Galileo Frequency Plan

Table 1.3: Current and Future Galileo Signals (from [15] [19] [20])

Band/Signal	Service	Modulation Scheme	Code Rate (Mcps)	Data Rate (bps)	Central Frequency	Spectral Occupation ^(*) (MHz)	Min Rx Power (dBW)
E1	OS CS	BOC(1,1)	1.023	125	1575.42	2.046	-157
E6	CS	BPSK	5.115	500	1278.75	40.92	-155
E5a	OS	AltBOC(15,10)	10.23	25	1176.45	51.15	-155
E5b	OS		10.23	125	1207.14		-155
	CS						
E1/OS	OS	CBOC(6,1,1/11)	B 1.023E6 C 1.023E6	125 no data	1575.42	4.092	-160
E1	PRS	BOC _{cos} (15,2.5)	A 2.5575E6	N/A	1575.42	38.805	N/A

(*) referring to the main lobe/lobes

The innovation brought by the Galileo project is the design of new signals, based on an innovative modulation, the Binary Offset Carrier (BOC) modulation also known as split spectrum modulation. Basically it consists in modulating the basic spread BPSK signal (e. g. GPS L1 C/A) with a squared sub-carrier waveform. The effect of such modulation is to split the power spectrum of the Direct Spread Spectrum Sequence (DS/SS) in two main lobes around the considered GNSS carrier frequency, as it is shown in Figure 1.5. The main idea behind BOC modulation is to reduce the interference with BPSK-modulated signals, which have a sinc function shaped spectrum. Therefore, BPSK-modulated signals such as C/A GPS codes have most of their spectral energy concentrated around the carrier frequency, while BOC-modulated signals (used in Galileo system) have low energy around the carrier frequency

and two main spectral lobes further away from the carrier (thus, the name of split-spectrum). More details on such an innovative split spectrum modulation can be found in [19] and [21]. However, the actual OS E1 signal broadcast by the IOV satellites and that will be broadcast by the future Galileo satellites feature an evolution of the BOC modulation, the so called MBOC. Such a modulation is derived by the multiplexing of the standard BOC(1,1) modulation with the BOC(6,1) modulation. Detailed derivation and analysis of the MBOC modulation can be found in [20] and [22].

1.4 The Receiver

This section aims at summarizing the basic architecture and principle operation of a GNSS receiver. The literature in this field is very wide, several are the books devoted to this topic. Among them, detailed explanations on the receiver operation can be found in [10] [7] [23] [8].

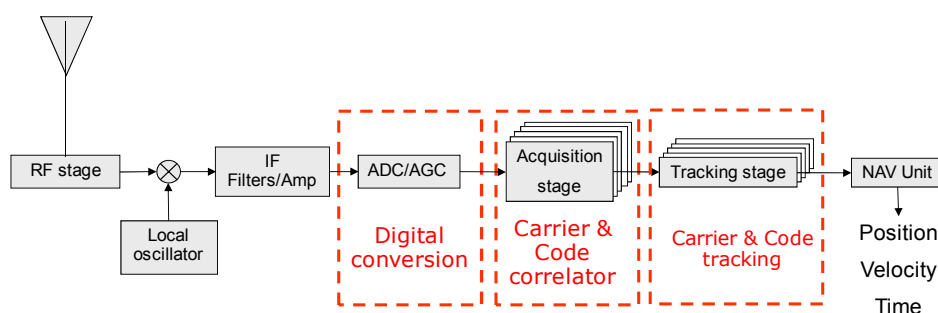


Figure 1.6: Generic GPS receiver block diagram

Figure 1.6 shows a high level block diagram of a generic GPS receiver. Referring to 1.6, the blocks operation can be described as follows [24]:

- after the **antenna** and the **pre-amplifier**, the **front-end** is in charge of the analog signal processing, that involves filtering, amplification, and downconversion. Amplification is straightforward in hard-limiting architectures (1-bit A/D conversion) but multibit receivers must employ

some form of Automatic Gain Control (AGC). Downconversion is performed either in single or multiple stages. Multi-stage architectures allow for adequate image suppression and general bandpass filtering with the final Intermediate Frequency (IF) placed close to baseband (e.g., 4 MHz). Single-stage down conversion is becoming more prevalent, however, and image suppression is achieved by accepting a higher IF (e.g., 30-100 MHz). The final conversion to baseband involves converting the IF signal to the in-phase (I) and quadrature (Q) components of the signal envelope. This is accomplished by mixing the IF signal with two tones generated at the final nominal IF but with one tone lagging the other in phase by $\pi/2$ radians. The output of the two mixers are the baseband components plus the residual Doppler. This conversion to the baseband can be accomplished either before or after the A/D conversion.

- For the **A/D conversion**, both single-bit and multi-bit architectures are currently in use. Most low-cost commercial receivers employ 1-bit sampling in narrow (i.e., 2 MHz) bandwidths. High-end receivers typically use anywhere from 1.5-bit (i.e., three levels) to 3-bit (eight levels) sampling in bandwidth range from 2 to 20 MHz. The degradation of the signal due to finite-bit quantization is dependent upon two factors in addition to the number of quantization levels. First is the IF. Second is the ratio of the maximum A/D threshold to the root mean square noise level.
- **Baseband signal processing** of the digitized signal is typically accomplished using a combination of dedicated hardware and digital signal processors to form the measurements and provide feedback for **acquisition** and **tracking**.

In practice, the signal at the ADC output is split over different channels.

In each of them, the receiver replicates the PRN code that is transmitted by the SV being acquired by the receiver; then the receiver shifts the phase of the replica code until it correlates with the SV PRN code [7] and multiply the incoming signal with a locally generated carrier. The first step in GNSS processing is the *signal acquisition*: the satellites in view are detected and a first rough estimation of the Doppler shift and the code phase is performed. Then the *signal tracking* refines the code synchronization and allows for extracting the information related to the code chip transition, which is fundamental in the pseudorange estimation. These measurements, performed on a set of at least four satellites, are used to compute the user's position through a triangulation procedure.

- **Signal Acquisition** refers to the initial synchronization process [7] [10] performed within each channel of the receiver, in order to obtain a rough alignment between the codes broadcasted by the satellites and the locally generated codes. The signal acquisition can be time consuming, mainly assuming a cold start, since the receiver does not know any a priori information. In this case, the receiver starts seeking satellites chosen randomly [10]. During the acquisition phase the receiver tests all the possible alignments, and if the tested PRN is included in the incoming signal, the correlation peak is detected. The signal acquisition is actually a two-dimensional search in time (code phase) and frequency [7] [8], in fact the correlation peak is detected, only when the Doppler shift on the incoming carrier is estimated. The Doppler shift is not only due to the motion of the satellite, but also on the frequency bias of the receiver clock. Ideally, an improved quality of the receiver would impact the acquisition algorithm in term of a smaller search space. Moreover, modern acquisition strategies are based on the Fast Fourier Transform (FFT), which might speed up the acquisition phase for some receiver architectures. Using the FFT approach when the match between the

local and the incoming codes is found, the whole frequency range of the search space is scanned and the spectrum shows a spike corresponding to frequency of the incoming carrier. The use of modern frequency domain search techniques for rapid acquisition is described in [25].

- **Signal Tracking.** After the acquisition stage has accomplished a rough alignment between the incoming and the local codes, a Delay Locked Loop (DLL) refines such an initial estimate of the code phase and tracks changes into the future [10]. The signal tracking is at the basis of the overall receiver's processing and allows for estimating the pseudorange (and thus the user's position) and decoding the navigation message [7] [10] [8]. The tracking stage can be considered a two-dimensional (code and carrier) signal replication process, since also a carrier tracking is required. The signal at the output of the IF section is generally processed by a coupled loop composed by a Phase Locked Loop (PLL), or a Frequency Locked Loop (FLL), and a DLL. The FLL like the PLL is a carrier tracking loop, but it does not provide the estimate of the carrier phase [10] [7]. This digital code/carrier tracking architecture is well known within the GNSS receiver design community [7] and [10]. In this section only its basic principles are outlined. Roughly speaking, the PLL is used to perform the carrier wipeoff and allows the DLL to synchronize the local and the incoming PRN codes. Assuming the digital local carrier is phase locked with respect to the incoming carrier, the signal at the front-end output is down-converted to baseband and is contained on the in-phase channel. As mentioned above, the DLL is responsible for synchronizing the local and the incoming PRN codes. The baseband signal is correlated with a Prompt, Early and Late version of a locally generated code [10] [8], through a multiplication and integration over a defined period. A feedback control signal is then calculated through a discrimination function and directly applied to the NCO. Such a NCO slows down or speeds up the rate of the local code replica in order to

keep the synchronization.

- The **navigation solution** involves the simultaneous solutions of four unknowns: three dimensional position of the user's receiver and the receiver clock bias. For details on the system solution refer to [10].

1.5 GNSS Vulnerabilities

The performance in terms of position estimation accuracy, reliability and service continuity depend on the ability of the receiver to acquire the GNSS Signal in Space (SiS) and to keep it tracked. Though the system is based on the DS/SS which brings an intrinsic robustness, the received signal power (approximately 20 dB below the noise floor) makes the system vulnerable to different disturbs, as interference or multipath. Many other effects can compromise the localization estimation accuracy: propagation anomalies that can occur in the ionosphere and in the troposphere, failures at the satellite (evil waveform) or the transmission of information that are not suitable for the navigation. In these particular fields, it is fundamental the knowledge of both the user position within predefined error margins and the level of the signal accuracy. In this way it will be possible to warn the user, within a certain time interval, in the case the SIS is corrupted or not reliable. The interruption of the navigation signal or its degradation can have disastrous consequences in security applications, where the accuracy in the position estimation is fundamental for the success of the rescue operation, especially if the user is not alerted in a short time. The most significant GPS interference and faults can be grouped as:

- **Multipath.** It represents the well known signal distortion due to the reflection of multiple paths.
- **Wide Band Interference.** E.g. white Gaussian noise, is a signal with a constant energy spectrum over all frequencies.

- **Narrow band Interference.** This type of fault has a limited bandwidth, usually less than few MHz.
- **Spoofing.** The receiver operations are forced to consider a fake signal as the correct one providing malicious positioning.
- **Evil Waveforms.** They are anomalies related to the malfunctioning of the [SiS](#) generator on-board.

Chapter 2

Interference classification for GNSS

In this Chapter a detailed classification of the main [RFI](#) sources for [GNSS](#) applications is reported.

2.1 Introduction: Interference Signals in GNSS

It is well known that a [GNSS](#) receiver is in principle vulnerable to several types of interference, which can lead to a complete signal disruption. This intrinsic weakness affects the performance of any type of receiver, due to the fact that it has to extract pseudorange information from the [SiS](#), that is received at a very low signal power (typically -160 dBW for [GPS](#) and -155 dBW are expected for Galileo). All the systems transmitting at carrier frequencies close to the band of interest are potential sources of interference for a [GNSS](#) receiver, and even small leakages out of their allocated bandwidth can be threatening for the [GNSS](#) signals. Even if events of unintentional [RFI](#) are generally unpredictable, their presence has been experienced in the past [26] and the increasing number of wireless communication infrastructures is increasing the probability that some out of band energy from signal frequency

located near the GNSS bands could affect the performance of GNSS receivers in a certain region. The presence of interfering power can be due to several reasons, but the main effects can be recognized to be caused by harmonics or intermodulation products. The first ones are integer multiples of the carrier frequency caused by some non-linearity as saturation of an amplifier while the second occur when two or more signals at different frequencies are mixed by passing through some non-linearities. The importance of assuring robust receiver with respect to interference is crucial for all types of applications where the concept of security is needed. Hence, it becomes of main interest to evaluate the possible impact of potential interference in bands of interest as, for example, in the Galileo frequencies bands where frequencies will be reserved for particular services addressing transport applications. Applications based on GNSS that have to be trustable by the users, include maritime, aviation and railway transport scenarios but also emergency applications oriented to the tracking and tracing of sensitive material (as medical or dangerous goods) or financial/assurance aspects.

The classification of the main disturbances for GNSS receiver takes into account heterogeneous aspects. The emission types can be defined in intentional (jamming) or unintentional. The first are common for military scenarios while the latest are usual for a large number of systems present in our daily life emitting RF energy that could interfere with the GNSS L-band. The Continuous Wave Interference (CWI) involves a wide class of Narrow-band Interference (NBI) caused by out of band emissions of electronic systems. This kind of RF interference might saturate the first stage of receiver chain, such as the Low Noise Amplifier (LNA) or the Automatic Gain Control (AGC) for the ADC or might lead to erroneous position estimations. Due to its spectral characteristics [7] [27] this kind of interference is considered one of the most critical for the GPS C/A code. Some of the main out of band signals are reported in Chapter 2 where a detailed interference classification is provided. Even if non-intentional RFI is not a-priori predictable, several cases have been

experienced in the past and reported in literature [26]:

- In 1994, in Germany, Digital Repeater transmissions at 1200 MHz degraded the C/N_0 in L2 band denying a correct acquisition of GPS signal [28];
- In 1995, both in Nice (France) and Vicenza (Italy), disturbs related to secondary harmonics emitted by TV transmissions and microwave interference have been detected in GNSS bands [26];
- In 1995 at the Edinburgh Airport (Germany), an interference due to a DME transmitter caused a C/N_0 degradation [28];
- In 1993, in the metropolitan Boston area, a disturb generated by TV emitters (Channel 10 and Channel 66) affected the quality of GNSS signal forcing low C/N_0 with consequently tracking loss [28];
- In April 2006, DVB spurious emission of TV transmitters located in Torino (Italy) degraded the performance in the acquisition stage of a GNSS receiver operating in the area, with consequently loss of the GPS signal tracking [29]. The disturb was the same that European Space Agency researchers detected using the GETR with the GIOVE-A E1 signals at INRIM (Torino) [30];
- In July 2006, Ultra-High Frequency (UHF) harmonics have been detected in Sidney around TV antennas. The undesired signal in the L1 band corrupted the correct performance of the receiver chain observing significant variations in the AGC/ADC block and in the final user positioning [31].

The intentional interference signals, mainly treated in the military context, are assuming more and more attention also in the civil application. In fact, cheap jammer can be easily bought on the web becoming a serious threat for each kind of user based application. Generally, the jammer output signals

can be considered high power white noise able to obscure the correct signal reception of each GPS channel.

2.2 Unintentional Interference Sources Classification and Signal Model

The received interfered GNSS signal at the receiver antenna can be written as:

$$r(t) = \sum_{l=0}^{L-1} s_{RF,l}(t) + i(t) + \eta(t) \quad (2.1)$$

where L is the total number of GNSS useful signals, $s_{RF,l}(t)$ is the useful GNSS signal received by the l^{th} satellite in line of sight, $i(t)$ is the additive interfering signal transmitted over a carrier frequency f_{int} and characterized by a two-sided bandwidth B_{int} , and $\eta(t)$ is the additive white Gaussian noise. Before being fed to the acquisition and tracking block, the signal is first down-converted to an intermediate frequency, sampled and quantized in the receiver front-end. Thus the composite received signal at the ADC output becomes according to [32] can be written as:

$$r_{IF}[n] = r_{IF}[nT_s] = Q_k^u \left[\sum_{l=0}^{L-1} s_{IF,l}[nT_s] + i[nT_s] + \eta[nT_s] \right] \quad (2.2)$$

where the function Q_k^u denotes the quantization over k bits, and T_s is the sampling frequency. Expanding the term $s_{IF,l}$, the expression for the single digitized GNSS signal affected by noise and interference components becomes (neglecting for the sake of simplicity the subscript l):

$$r_{IF}[n] = Q_k^u \left[\sqrt{2C}d(n - n_0) c(n - n_0) \times \cos(2\pi F_{D,0}n + \phi_0) + i[n] + \eta[n] \right] \quad (2.3)$$

where C is the received GNSS signal power from one satellite in view, d and c are respectively the navigation data message content and the pseudo random noise sequence, $F_{D,0} = (f_{IF} + f_0)T_s$ is the Doppler affected frequency,

$n_0 = \tau_0/T_s$ is the digital code delay and ϕ_0 is the instantaneous carrier phase. $i[n]$ and $\eta[n]$ are the digitized interference and the digital Gaussian noise component respectively. Given B_{IF} the front end bandwidth, it can be shown that sampling the signal at the Nyquist frequency $f_s = 2B_{IF}$, the noise variance becomes:

$$\sigma_{IF}^2 = E \{ \eta^2[n] \} = \frac{N_0 f_s}{2} = N_0 B_{IF} \quad (2.4)$$

where $\frac{N_0}{2}$ is the Power Spectral Density (PSD) of the noise.

A general classification of the interfering signals is based on their spectral characteristics such as its carrier frequency f_{int} or its bandwidth B_{int} :

- **Out of band** interference refers to interfering signals whose carrier frequency is located near to the targeted GNSS frequency band ($f_{int} < f_{IF} - \frac{B_{IF}}{2}$ or $f_{int} > f_{IF} + \frac{B_{IF}}{2}$);
- **In band** interference refers to interfering signals with carrier frequency within the GNSS frequency band ($f_{IF} - \frac{B_{IF}}{2} < f_{int} < f_{IF} + \frac{B_{IF}}{2}$);

Moreover, interference can be further classified according to its characteristics in the frequency domain as:

- **NBI** when the spectral occupation is smaller with respect to the GNSS signal bandwidth ($B_{int} \ll B_{IF}$);
- **Wide-band Interference (WBI)** when the spectral occupation is comparable with respect to the GNSS signal bandwidth ($B_{int} \approx B_{IF}$);
- **CWI** which represents the ultimate limit in NBI and appears as a single tone in the frequency domain ($B_{int} \rightarrow 0$);

Furthermore, in general interference might have time-frequency varying characteristics, as for examples, pulsed interference or chirp signals. The former is mainly characterized by on-off status of short duration (order of μs), which alternate in the time domain, whilst the latter is characterized by a linearly

variation in time of the instantaneous frequency thus resulting in a [WBI](#). More details on interference classification can be found in [\[33\]](#).

All communication systems with frequencies near [GPS](#) band could be a potential source of interference for a [GNSS](#) receiver. It is inevitable that some out of band energy from signal frequency located near the [GNSS](#) bands could interfere with [GNSS](#) receivers, even if it does not belong of the same environment. The potential interference sources could have different band, including [GPS](#)/Galileo frequencies (in band [RFI](#)) or far from the receiver bands (out of band [RFI](#)). For the existing [GPS](#)/Galileo frequencies, the interference threat is well known and extensively studied.

2.2.1 Out-of-Band Signals

The [CWI](#) involve a wide class of [NBI](#) caused by out of band emissions of electronic systems. Even if the [GNSS](#) frequency bands are protected by international and Federal Communications Commission ([FCC](#)) some out of band harmonics could interfere with the Galileo and [GPS](#) signals. In particular the [CWI](#) could strongly impact on a [GNSS](#) receiver on the acquisition and DLL blocks because the interference power is dispersed on the whole search space by the code despreading, compromising the acquisition accuracy and impacting to the other consequent functional blocks. The narrowband interference represent the weightier negative effect on the [GPS](#) receiver performance. This is due to [C/A](#) code characteristics. In fact, the spectrum of a [C/A](#) code presents line components spaced at 1 kHz with different height due to fluctuations in the autocorrelation function code. These components are more sensitive to interference and could generate false lock in the correlator in case of matching between the [C/A](#) reference signal line components and the [CWI](#) interferer [\[34\]](#) [\[7\]](#) [\[23\]](#).

A typical representation of a presence of a interference is illustrated in the [Fig. 2.1](#) below where an emission from an interference source falls in the

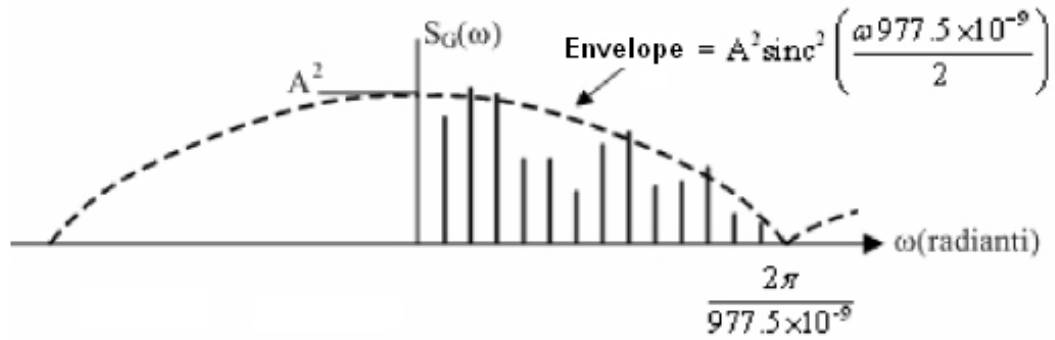


Figure 2.1: Power Spectrum of a C/A Code.

GPS L1 band. The maximum interference power level profiles admitted at the antenna of a GPS receiver are illustrated in [34]. These are specified by some institutions as ARINC 743A, RTCA and EUROCAE. In the following sections, some of the main out of band interference sources will be further analyzed.

2.2.1.1 TV Channels

The TV emissions are veritable sources of interference for a GNSS receiver. They can be as both NBI or WBI: the video carriers are considered as medium/wide band signals whereas the sound carriers are considered as CWI. In the broadcast TV signal, Very-High Frequency (VHF) and UHF bands are used. So both bands, in their sub channel, could represent interference sources for a GNSS receiver. In [26] a case of interference from TV signal is reported. In this case, the interference signal affects the active antenna LNA causing harmonic distortion in the same LNA that result in average 5 dB decreases in C/N_0 . In general, the harmonics of TV ground station can generate potentially dangerous interference for GNSS receivers. In [34] 6 TV channels, French and American equivalents, with their harmonics are analyzed in frequency and power terms. The Fig. 2.2, reports the out of band TV potential interference.

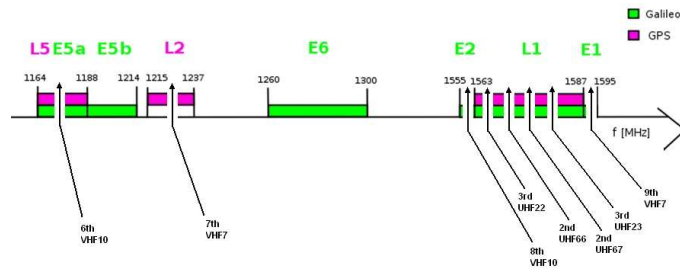


Figure 2.2: Potential TV Channel Harmonic Interference.

2.2.1.2 DVB-T Signals

The Standard DVB has been constituted in 1993 by the European project DVB. The main goal of this project, that today comprehends more than 300 European and extra-European members, is to harmonize the strategies to introduce the digital television and new multimedia interactive services on transmission networks and to define the relative technique specifications. Some results are obtained defining the system specifications for the standard DVB-S, developed for the direct diffusion of TV multi-program from satellite and for standard DVB-C for the distribution of television signals through core networks. The DVB family comprehends also the DVB-T, standard providing the digital terrestrial television. Its definition was achieved in the November 2005 with standard approved in February 1997 by ETSI. The specification is based on the standard MPEG-2 for the audio/video signal source codification while a multi-carriers modulation COFDM has been adopted. The main characteristics of this technique is to distribute the total data stream among a large number of carriers frequency equally spaced while the OFDM process is achieved by a Inverse Fast Fourier Transform (IFFT). The system COFDM is robust to frequency selecting fading. The echo countermeasure adopted is a time delay guard that divides near OFDM symbols. The main modulations used are QPSK or m-QAM, with m typically equal to 16 or 64. In [35] a more complete description of the system is reported and the main transmission frequencies are indicated in [VHF III](#) (174-223 MHz), [UHF IV](#) and [UHF V](#) (470-854 MHz). It is clear that these frequency values do not represent a

directly threat for the GNSS receiver bands but they can cause some problems if the potential harmonics are considered. In [29] a set of on-field experiments aiming at assessing the effect terrestrial DVB and VHF/UHF signals on GNSS receiver are described. Figure 2.3 shows the possible the potential secondary harmonics originated by the DVB-T system and which can fall within the GPS L1.

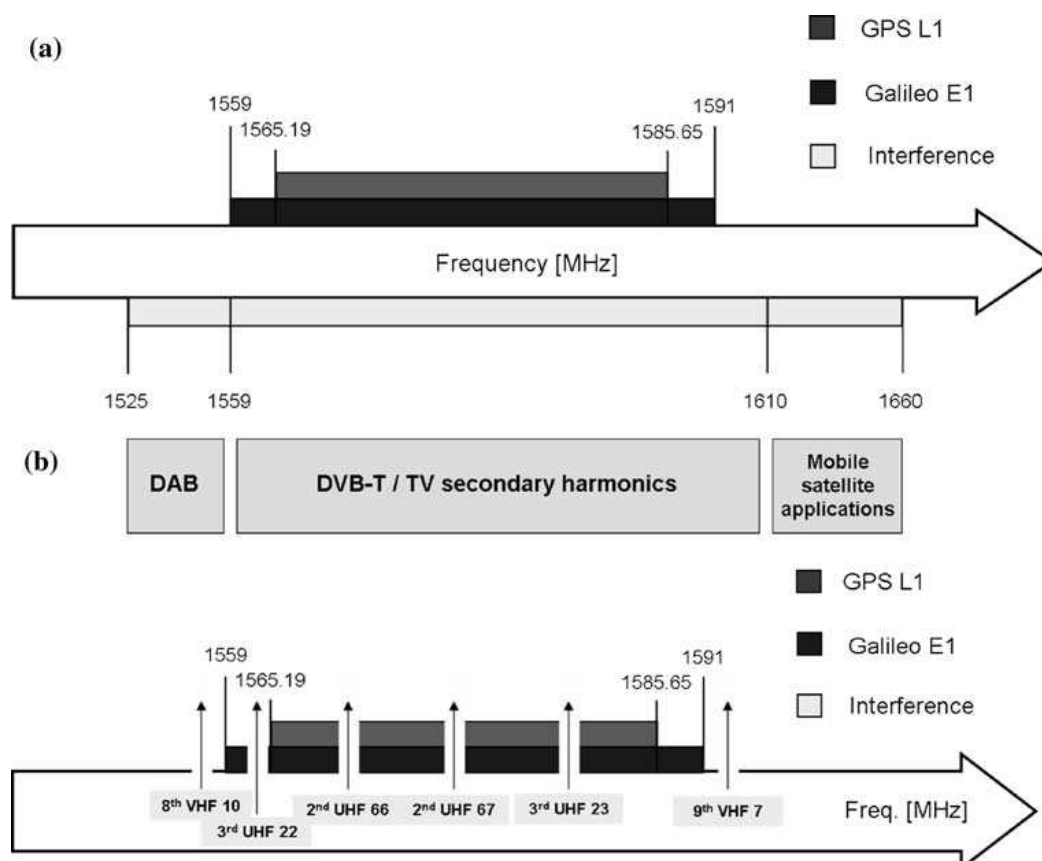


Figure 2.3: Possible in-band and out-of-band interferences (a). Secondary harmonics interference within the GPS L1 and Galileo E1 bands (b)

2.2.1.3 VHF/COM

With VHF TV, other interference sources in VHF band could be considered dangerous for a GNSS receiver. These are the VHF Communication interference [34] [36]. This band (118-137 MHz) containing 760 channel spaced by 25 kHz, is commonly used by the Air Traffic Control (ATC) communications.

The harmonics are considered as **CWI** with bandwidth of about 25 kHz. The **VHF** channels centered at 121.150, 121.175 and 121.200 MHz, have the 13th harmonic within the **GPS** bandwidth while the channel centered at 131.200, 131.250 and 131.300 MHz have the 12th. In Fig. 2.4 the VHF_{COM} potential harmonics are reported.

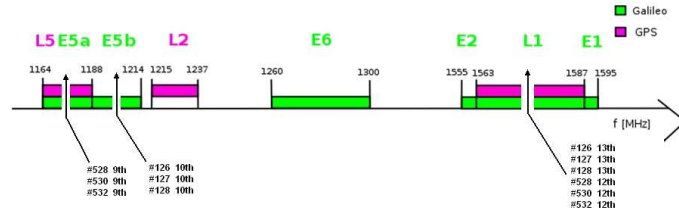


Figure 2.4: Potential VHF_{COM} Channel Harmonic Interference.

2.2.1.4 FM Harmonics

Also small frequency bands inside the Frequency Modulation (**FM**) band (87.5-108 MHz) are harmonics sources that fall in the **GNSS** bands. The channels 104.9 and 105.1 MHz have their 15th harmonics near the Narrow Correlator **GPS** band. The channels are spaced at 150 kHz while the maximum transmitted power is 50 dBW. The harmonics generated by **FM** sources are considered as width band interferer in the sense of the **C/A GPS** signal [34].

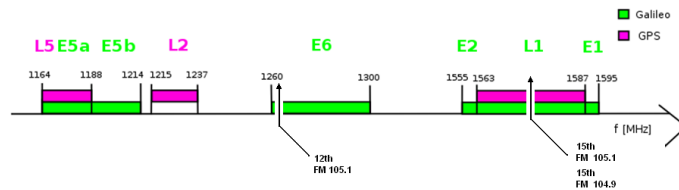


Figure 2.5: Potential FM Harmonic Interference.

2.2.1.5 Personal Electronics Devices

The Personal Electronic Devices (**PEDs**) in proximity of a **GNSS** receiver can cause the disruption of **GNSS** signal reception. They are divided into intentional and non-intentional transmitters (or radiators). The first ones transmit

a signal in order to accomplish their function. They can be summarized in the following non-exhaustive list:

- cell phones
- pagers
- two-way radios
- remote control toys

Probably, next PEDs generations will include Ultra Wide Band (UWB) signal for allowing the development of high bit rate personal devices. These can represent new interference sources for Galileo receivers and should be monitored. The non-intentional transmitters do not need to transmit any signal in order to accomplish their function, but notwithstanding they emit some level of radiation. They can be summarized in the following non-exhaustive list:

- compact-disc players
- tape recorder
- portable consoles
- laptop computers and palm pilots
- laser pointer

2.2.1.6 SATCOM

The SATCOM communications operate in the frequency bands 1626-1660.5 MHz with channel spaced at 0.75 MHz and bandwidth of 20 KHz. Multiple carriers transmission in a SATCOM service produce IMPs which can fall in the GPS band. A possible example is reported on [34]: the channels MHz and MHz generate the 5th order IMP MHz inside the L1 band.

2.2.1.7 VOR and ILS Harmonics

The VHF Omni-directional Range (**VOR**) is a type of radio navigation systems for aircraft that provides information about radial position referred to ground station. The Instrument Landing System (Instrument Landing System (**ILS**)) consists of two radio transmitters providing lateral and vertical guidance to aircraft for approaching landing. **VOR/ILS** emitters are usually positioned at the beginning and at the end and the sides of the airport road. These approaching landing systems operate in 108-117.95 MHz band including 200 channels frequency spaced at 50 KHz. In detail the **VOR** using 12 channels in the 112.24-112.816 MHz band while the **ILS** only two on 4 channels in the 108-111.95 MHz band. Their harmonics, the 14th from **VOR** and 2nd from **ILS** corresponding to 111.9 and 111.95 MHz, enter on the L1 **GPS** band. They are considered **CWI/Amplitude Modulation (AM)** interferers [34].

2.2.1.8 Mobile Satellite Service

The Mobile Satellite Service (**MSS**) System can generate two distinct interference threats to a **GNSS** receiver [26]: the **MSS** Mobile Earth Stations use the 1610-1660.5 MHz band, potentially introducing wideband power in the Galileo band, raising the noise level. Spurious harmonic emission from geostationary satellites transmitting in the 1525-1559 MHz band (nowadays unregulated by ITU).

2.2.1.9 Mobile Phone Interference

In general, no direct consequences from mobile phones on a **GNSS** receiver have been founded in literature. Some information are available for aircraft navigation equipment, such as [37], where a **GPS** receiver is commonly used. In [37], an investigation of spurious emission from six wireless phone technologies is described, analyzing the effects on aircraft systems, among which

a global positioning system. The tests are carried out from semi-anechoic and reverberation chambers using the wireless phone technologies, with different transmission frequencies reported in, and different receiving antennas. The study is conducted evaluating the total radiated power from each cellular versus the frequencies of the system considered. In the analysis, the receiver sensitivity for the GPS receiver is -120 dBm but a more realistic level is considered around -82 dBm. This value is obtained considering a minimum path loss, the amount of signal lost from inside the vehicle to the antennas located outside, of 38 dB. This gap is evaluated in [14], calculating the path loss after having generated signals inside the plane. The results show that all the considered values exceed the receiver system sensitivity level but at the same time are under the more realistic value obtained from the path loss. So, the conclusions of the paper are that the radio frequency emission from the phones tested not interfere with the avionics system examined, among which the GPS.

2.2.2 In-band signals

Since some interference sources have base band directly allocated in the observation bands, they can be considered in band interference signals. They are intersystem and intrasystem interference, military and civil Aeronautical Communication Systems and UWB. A short description of each one is described in the next Sections.

2.2.2.1 Intersystem and Intrasystem Interference

The intersystem and intrasystem interference can be considered in band disturbs. The Galileo system is developed to assure compatibility with the GPS [10]. The two systems should operate independently of each other or with a minimum level of interference on each other. The term intersystem is referred to disturb which GPS transmitter produces on Galileo signal and vice versa.

Instead, the term intrasystem refers to impairments affecting the same system they are produced by. This effect is commonly caused by incomplete carrier suppression that could produce undesired narrowband component with power concentrate around the carrier frequency.

2.2.2.2 Military/Civil Aeronautical Communication Systems

The Military Communications Systems can be considered in-band interferers due to signals band used by systems. The Galileo E5a and E5b bands, located within 1164-1214 MHz, occupy frequencies already used for ARNSs such as TACAN, DME and Secondary Surveillance Radar (SSR), as well as by the DoD Joint Tactical Information Distribution System (JTIDS) and Multifunctional Information Distribution System (MIDS). Other aeronautical systems operate in these frequencies such as Traffic Collision Avoidance System (TCAS), Identification friend or foe (IFF) and planned ADS-B.

The DME/TACAN systems consist of an airborne interrogator and a ground-based transponder that emits high-power pulsed signals that constitute a real threat for the Galileo/GPS receivers. DME and TACAN provide measurements of aircraft range from a ground reference point. The TACAN is a military system which provides range and azimuth measurements. The DME/TACAN system operates in the 960 MHz to 1215 MHz ARNSs frequency band [38] in four different modes: X, Y, W and Z, even if only X mode occupies the 1151 MHz to 1215 MHz frequency band that interferes with the E5a/L5 and E5b GNSS signal (see Fig. 2.6).

Cases of real DME/TACAN interference on GNSS receiver have been presented in [39], Chapter 4 will be entirely focused on the DME/TACAN interference impact on GNSS receiver.

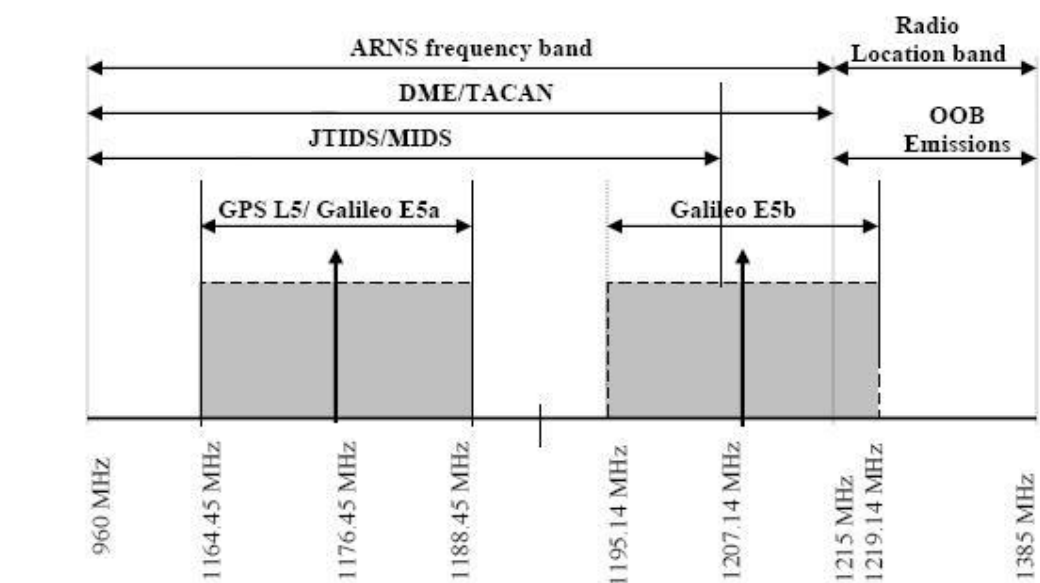


Figure 2.6: DME/TACAN and JTIDS/MIDS Frequency Plan.

2.2.2.3 Ultra Wide Band signals

In 2002, the **UWB** was defined by **FCC** which allocated the largest spectrum for unlicensed use. The definition of **UWB** include any signal that occupies more than 500 MHz between 3.1 and 10.6 GHz and meets the spectrum mask which defines the indoor limits for **UWB** communication systems. The **UWB** signals are emerged as potential solution for low-complexity, low-cost, low-power consumption and high-data-rate wireless connectivity. The technologies based on **UWB** offer simultaneously high data rate communication, with the possibility to offer data transmission rates of 100-500 Mbps at distance of 2-10 meters using average radiated power of a few hundred microwatts, and high accuracy positioning capabilities being utilized in imaging radar technique due to their wall penetration capability. In fact, for this aspect, they have been studied for indoor location and navigation purposes because of their performance in multipath environment [40]. The main advantages of **UWB** are:

- minimization of reflection from clutter

- the ability to penetrate structures with high data rates and high resolution
- minimization of multipath to operate in cities, obstructed areas and indoors
- support of high-precision ranging and radar
- wide bandwidth

which enables low probability of interception by undesired receivers. The data modulation schemes often utilized in **UWB** systems are Pulse Position Modulation (**PPM**) and Pulse Amplitude Modulation (**PAM**). The **UWB** signal generated by using sub-nanosecond pulses that spread the signal energy on wide frequency band. These systems utilize low transmitted signal power level but with extremely wide bandwidth. This is the open problem of **UWB** signals that could affect the existing spectral users, such as Galileo and **GPS** users whose signal power is far below the noise floor. Several studies [41], [42], [43] conclude that **UWB** signals can degrade **GPS** receiver performance. Hence, they result potentially dangerous for a Galileo receiver. Other studies are presented in [44] and in [45] where it is demonstrated, respectively in a simulation and in a WPAN studies, that **UWB** interference effect can be reduced opportunely choosing modulation parameters. A great number of works about the coexistence between the **GPS** and **UWB** have been made but specific works about the impact on Galileo receivers have not been found. Thus, further studies are necessary to determine this kind of interference impact.

2.2.2.4 Potential Harmonics in Galileo Bands

The new services foreseen by the Galileo system require high accuracy and reliability. For this reason a study of possible interference sources which could affect Galileo receivers is here reported to understand which are the potential

threats that should be detected and mitigated. The Galileo frequency bands analysed are the following:

- E5a: (1164 -1188) MHz;
- E5b: (1188 - 1214) MHz;
- E6: (1260 - 1300) MHz;
- L1: (1563 -1587) MHz;

In Table 2.1 the main interference due to interference source band as described in [34] are reported. It has been analyzed if the interference harmonics Galileo/GNSS out of band could be found in the usual/narrow Galileo/GPS band. The Fig. 2.7 shows graphically the harmonics positions.

Table 2.1: Main in-band interference system sources

Usage	Bandwidth (MHz)	Order L1	Order E5a	Order E5b	Order E6
UHF TV	785.71 - 788.71	2 nd			
UHF TV	523.807 - 526.473	3 rd			
Mobile/Station	392.855 - 395.855	4 th	3 rd		
Mobile/Station	314.284 - 315.884	5 th			4 th
Mobile/Station	261.903 - 263.237	6 th			
Broadcasting	224.488 - 225.631	7 th			
VHF TV	196.427 - 197.428	8 th	6 th		
VHF TV	174.602 - 175.491	9 th			7 th
VHF Maritime	157.142 - 157.942	10 th			8 th
VHF Military	142.856 - 143.584	11 th			9 th
VHFCOM	130.952 - 131.618	12 th	9 th		
VHFCOM	120.878 - 121.494	13 th		10 th	
VOR/ILS	112.244 - 112.816	14 th			
FM	104.761 - 105.295	15 th			12 th
FM	98.214 - 98.714	16 th	12 th		13 th

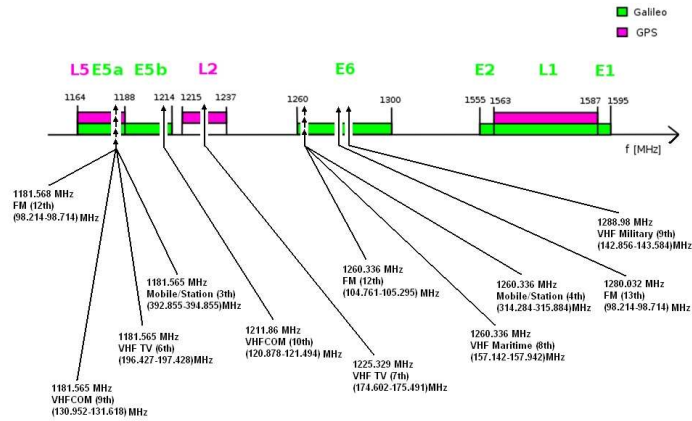


Figure 2.7: Interference Harmonics in E5a, E5b and E6 bands.

2.3 The LightSquared case

One of the most relevant and recent cases of inter-systems interference to the GNSS and which has caused a long controversy in the US communication community has been represented by the LightSquared case. LightSquared Subsidiary LLC is a company seeking FCC approval to provide a wholesale, nationwide, wireless broadband network integrated with satellite coverage. LightSquared intends to combine its existing satellite communications services with a ground-based 4G-Long Term Evolution (LTE) network that transmits on the same radio band as its satellites. The band is right next to the primary GPS frequency L1 [46].

The proposed LTE signals would be transmitted at higher power levels with respect the received GNSS signal levels at the Earth's surface. In January 2011 the FCC issue an order granting a conditional waiver to LightSquared to deploy their ground network. Following this FCC decision, an intense period of study and on-field testing has been performed culminating in the publication of the Technical Working Group TWG report [47]. This report indicated significant degradation of receiver performance across a wide range of receiver types. A second round of test was conducted and again significant interference effect on GPS receiver have been detected. Thus, in response of this test campaign which has revealed that LightSquared signals significantly

threats the [GPS](#) receiver operation, [FCC](#) revoked LightSquared's authorities to deploy their proposed network.

In [\[48\]](#) a compatibility analysis between LightSquared signals and L1/E1 [GNSS](#) reception is presented.

Chapter 3

Classical Interference

Countermeasures in GNSS

The scope of this Chapter is to provide an overview of the state of the art of detection strategies and mitigation techniques already proposed in the [GNSS](#) field.

3.1 Introduction

A general classification of the various state-of-the-art of detection and mitigation strategies already presented in literature, can be done according to the point in which they are applied along the processing chain of a [GNSS](#) receiver, as mentioned in [\[49\]](#). Considering the receiver block scheme depicted in [Figure 3.1](#), detection and mitigation of the interference can be performed at:

- *antenna level*: such techniques can be applied typically in static or slow-changing environment and require a particular hardware configuration, such as antenna arrays;

- *AGC/ADC level*: **AGC** gain observation can provide evidence of interference presence and optimal **AGC/ADC** parameters tuning can be employed for partial interference removal;
- *raw observable level*: such techniques are based on the monitoring of the signal processed at the **ADC** output. In this context, the algorithms are applied on the **IF** samples at the **ADC** output, providing interference detection or excision directly in the time domain as the well known **pulse blanking**, or in the frequency domain observing the spectrum of the incoming signal, based on the use of **FFT** combined with **notch filters**, or finally looking at the stochastic characteristic of the signal, as proposed in the **Goodness of Fit** test.
- *post-correlation level*: such techniques are based on the analysis of the estimated shape of the correlation function exploiting in most of the cases a multi-correlator receiver

All these techniques will be described in the following of this Sections.

3.2 Interference monitoring and detection strategies

The presence of a reliable system capable of the detecting the presence of interfering signals captured by the **GNSS** antenna receiver is fundamental in the design of **GNSS** receiver featuring an interference countermeasure scheme. The possibility to monitor the incoming interfered signal and to adopt a fast interference detection algorithm allows the correct activation of the interference countermeasure system avoiding as much as possible any degradation of the **GNSS** signal distortion and thus keeping operational the **GNSS** receiver even in harsh interference environment.

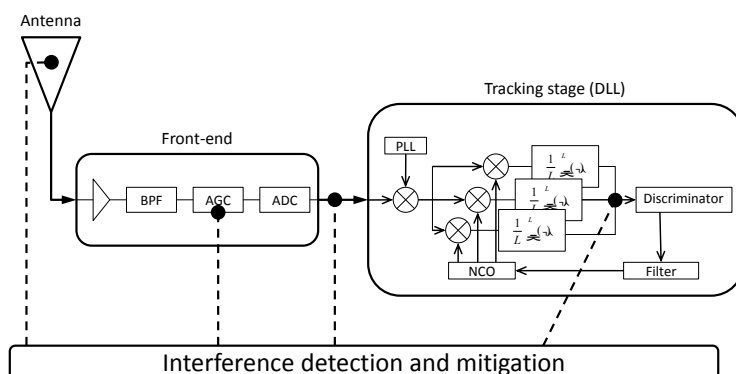


Figure 3.1: Classical GNSS receiver architecture

3.2.1 AGC monitoring based method for interference detection

A method for detecting the presence of interfering signals affecting the GNSS received signal based on the monitoring of the AGC gain within the received front-end has been first presented in [50]. The AGC is a fundamental component present in the GNSS receiver right before the ADC and it is employed in order to minimize quantization losses which can be caused by the presence of a multi-bit quantization operation. In particular, the AGC is in charge of amplifying to match the input dynamics range of the ADC, thus avoiding as much as possible quantization losses and the ADC saturation. The most common AGC-ADC block implementation in the modern GNSS receiver is based on the use of the ADC output samples in order to form metrics steering the AGC gain. As mentioned in [50], in absence of interference since the GNSS signal is completely buried in the noise floor, the AGC is driven by the

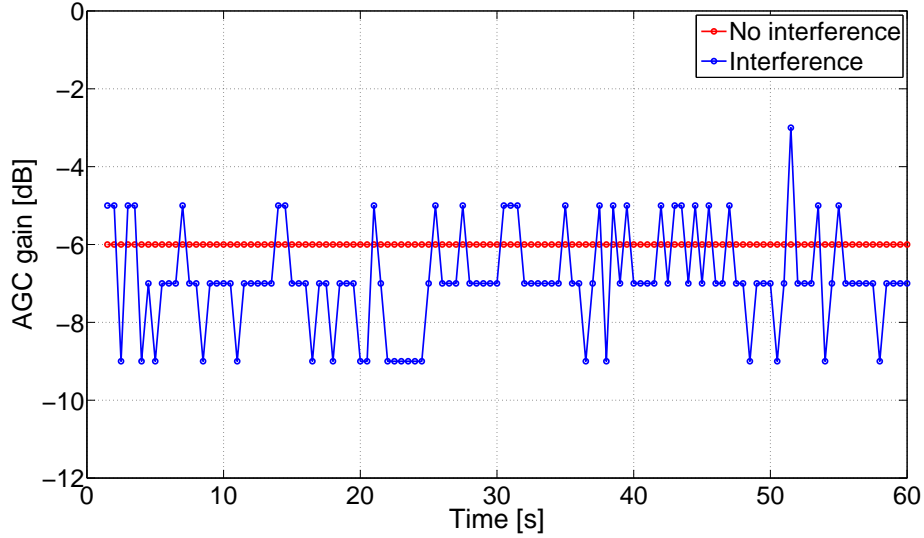


Figure 3.2: Typical AGC gain in presence and in absence of interference

environmental thermal noise rather than the signal power. For such a reason, the observation of the AGC gain trend can be considered a valuable method for assessing the presence of interfering signal. Defining L as the maximum quantization threshold and σ as the noise standard deviation at the ADC input, the SNR degradation post correlator, depends on quantization losses according to the ratio $k = \frac{L}{\sigma}$. In [50] it is shown that for different quantization law and different number of quantization bits an optimal k providing the minimum post correlator SNR degradation, can be found. Then the gain provided by AGC ensures such optimal ratio k is kept in order to reduce the quantization losses and thus the degradation on the post correlation SNR. Therefore, in absence of interference, the gain produced by the AGC is constant, while in presence of a high power interfering signals, its gain starts decreasing in order to compress the signal, adapting it to the ADC input dynamic range. An example of AGC behaviour trend in presence and in absence of interfering signal is provided in Figure 3.2

However, since the AGC gain varies in a limited range, when strong interference is present, ADC saturation may not be avoided. In order to cope with this issue, use of ADC supporting signal quantization on a high number of bits

(8 bits in general) is preferred. As reported in [50], use of AGC combined with a 8 bit ADC usually may be preferred for the design of those GNSS receiver which will cope with the strong pulsed interference in aviation environment originated by the DME systems which will be introduced later and deeply discussed in Chapter 4. The most common interference countermeasure in such a scenario is the so called pulsed blanking, first proposed in [51]. Such simple digital circuitry, implemented after the ADC, provides blanking of the digitized samples at the ADC output whenever a level threshold power is crossed. More details on this countermeasure will be introduced in the following of this Chapter and it will be further discussed in Chapter 4. In this context, the received GNSS signal is quantized exploiting only the lower bits of the ADC. In presence of strong pulsed interference, saturating the AGC, the majority of the pulsed interference, which is not then compressed, is mapped on the higher bits of the ADC in order to be easily detected by the pulse blanking circuitry and suppressed. However, in presence of a pulse blanking, careful design of the AGC-ADC block has to be performed, since the blanked samples should not be used for the AGC gain steering. Another work proving how the AGC can be considered a fundamental tool for interference detection are provided in [52]. Here the authors provide a set of experimental test in the lab focused on assessing the AGC gain behaviour in presence of strong narrowband interference, and on the investigation on the best AGC-ADC parameters tuning for interference mitigation.

3.2.2 Goodness of Fit test

Differently from the AGC gain observation, in [53] an interference detection method based on the observation of the stochastic characteristics of the signal at the ADC output by means of a GoF, is proposed. The signal at the baseband processing block of a GNSS receiver is

$$y[n] = s_{IF}[n] + w[n] \quad (3.1)$$

where $s_{IF}[n]$ is a sequence of samples of the SiS and $w[n]$ is a realization of a zero-mean white discrete-time Gaussian noise. In the presence of interference or in general of signal nuisances, the digitized signal becomes

$$x[n] = y[n] + \nu \cdot q[n] \quad (3.2)$$

where $q[n]$ is the interference signal at IF and ν is a generic amplitude factor. Interference detection consist in the evaluation of the presence of $q[n]$, based on the measurement of N samples of $x[n]$. The signal $x[n]$ is a realization of the random process $X[n]$ defined as

$$X[n] = Y[n] + V \cdot Q[n] \quad (3.3)$$

where V is equal to zero in absence of interference, or a stochastic process (random variable with a given Probability Density Function (PDF)) when interference is present. The Chi-square test on GoF is based on a binary hypothesis testing problem as

$$\begin{cases} H_0 & \text{RFI absent : } V = 0 : p_X(x) = p_Y(x) \\ H_1 & \text{RFI present : } V = 1 : p_X(x) \neq p_Y(x) \end{cases} \quad (3.4)$$

where $p_X(x)$ and $p_Y(x)$ are first order PDF of a stationary random process. It is noted that the knowledge of the process distribution when there are no interfering signals (H_0) is the only requirement posed by Chi-square GoF; no other pieces of information on the interference characteristics are required. More specifically, the decision on H_0 is taken comparing the p -value against the significance level. The p -value is defined in [54] as the *probability, computed assuming H_0 is true, that the test statistic would take a value as extreme or more extreme than that actually observed*. The smaller the p -value is, the stronger the evidence against H_0 provided by the data.

The method works according to the following steps:

1. The discrete version of the PDF of $X[n]$ is evaluated when the H_0 hypothesis is verified and the reference discrete histogram ($E = \{E_1, E_2, \dots, E_k\}$) representing $p_X(x)$ is obtained.

2. A set of measurements of the signal are taken, and the observed histogram ($O = \{O_1, O_2, \dots, O_k\}$) representing $p_Y(x)$ is built accordingly.
3. The test statistic is evaluated according to

$$T_X(x_m) = \sum_{i=1}^k \frac{(O_i - E_i)^2}{E_i} \quad (3.5)$$

When the two histograms coincide, no nuisances are present and $T_X(x_m) = 0$; the higher is the value of $T_X(x_m)$, the larger is the difference between the two histograms.

4. Since $T_X(x_m)$ can be seen as an instance of the Chi-square distributed random variable $T_X(x)$, a p-value can be evaluated as

$$p_m = Pr \{T_X(x) > T_X(x_m)\} \quad (3.6)$$

It is observed that $p_m \simeq 1$ means that the histograms are almost identical and that no interference is presence; vice versa with $p_m \simeq 0$ the two distributions are different.

5. The decision is taken by fixing a threshold p_α , known as level of significance, as it follows

$$\begin{cases} p_m > p_\alpha : H_0 \text{ is accepted} \\ p_m < p_\alpha : H_0 \text{ is rejected} \end{cases} \quad (3.7)$$

Figure 3.3 shows an example of result of the Chi-square GoF test on real GNSS signals. In particular, IF samples are taken at the output of a RF front-end sampling GPS L1 signals.

It can be proved that strong interference degrades the signal processing and induces errors in the estimated position. Chi-square GoF test is able to reveal the presence of interference: while in the first part of the test when no interference is present, the p-value remains constant and close to 1, satisfying H_0 (red line), when CWI is injected the p-value tends to 0.

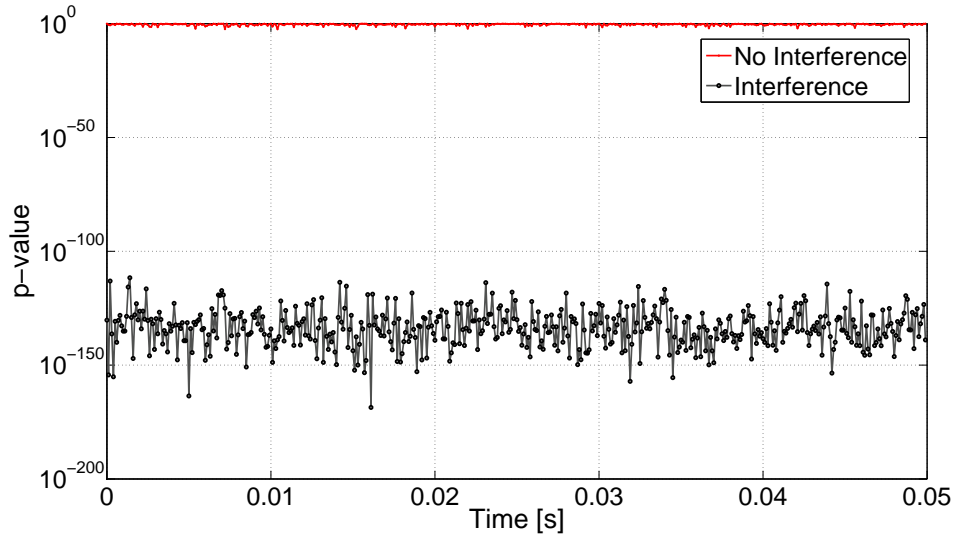


Figure 3.3: p-value trend of the Chi-square [GoF](#) test in presence and absence of interference

3.2.3 Multicorrelators based interference detection techniques

Use of interference detection techniques at tracking stages exploiting the observation of the correlation function have been already widely investigated in literature. First examples of such studies can be found in [55] and [56], where use of multicorrelators for [CWI](#) detection in [GNSS](#) receiver is shown. The idea behind this techniques is to monitor the shape of the correlation function at tracking stage possibly exploiting multicorrelators scheme and to extract the harmonic components in the correlation itself. [CWI](#) can be easily observed at correlators output due to the presence of a visible sinusoidal shape which is generated by the cross correlation between the [CWI](#) whose carrier frequency perfectly matches with the strongest line of a certain [PRN](#) code.

It has to be remarked that post-correlation techniques are usually employed to detect any kind of impairment affecting the signal (multipath, and waveform).

However interference detection at post-correlation level can be also performed

not only by means of visual inspection on the correlation shape, but also in a statistical domain, as mentioned [57]. Here two statistical methods applied at post-correlation level are described as methods for revealing the presence of interference: the former is the **Chi-Square GoF** test already described in Section 3.2.2 as interference detection method working at raw observable level, the latter is named **Sign Test**. Both methods rely on the assumption that at tracking level, both the Early and Late correlations in absence of interference are discrete-time Gaussian random process, whilst in presence of interference their distributions have different statistics. Concerning the application of the Sign Test, the assumption is that in nominal conditions, a pair of E-L multi-correlators equally spaced from the Prompt can be modelled as normally distributed random variables with the same mean

$$\mu_E = \mu_L = \mu \quad (3.8)$$

Furthermore, if the Early Late spacing is larger than one chip, it is possible to show that E and L correlators are independent and $D = E - L$ results to be a normally distributed random variable with zero mean, $\mu_D = 0$. The sign test is then used to test the null hypothesis

$$H_0 : \mu_D = 0 : \text{ the correlation function is not distorted.} \quad (3.9)$$

On the contrary, if an impairment able to affect the correlation function (due to interference, spoofing, or multipath) is mixed with the SiS, the condition H_0 is not verified any more and H_0 has to be rejected.

The procedure of the **Sign Test** is the following:

1. Let $D = [d_1, d_2, \dots, d_M]$ be the stream of sample data. In order to perform the **Sign Test**, the sample data are divided in two groups which are denoted by a positive sign, S^+ , and by a negative sign S^- , respectively.
2. for $n > 30$, the test statistic is $x = \frac{S^+ - S^- + 1}{\sqrt{n}}$;

3. the p -value is found as $p - value = P(X < x)$, where X is a normal distribution with zero mean and unitary variance ($\mathcal{N}(0,1)$);
4. if $p - value < \alpha$, where α is the significance level, then the hypothesis H_0 is rejected, otherwise H_0 is accepted

As an example, a GPS L1 signal has been simulated with a CWI present only in certain time intervals. Figure 3.4 shows the result of the sign test applied to Very Early - Very Late correlators: the test decision assumes positive values only in correspondence of the second and fourth segments, demonstrating again the effectiveness of the algorithm.

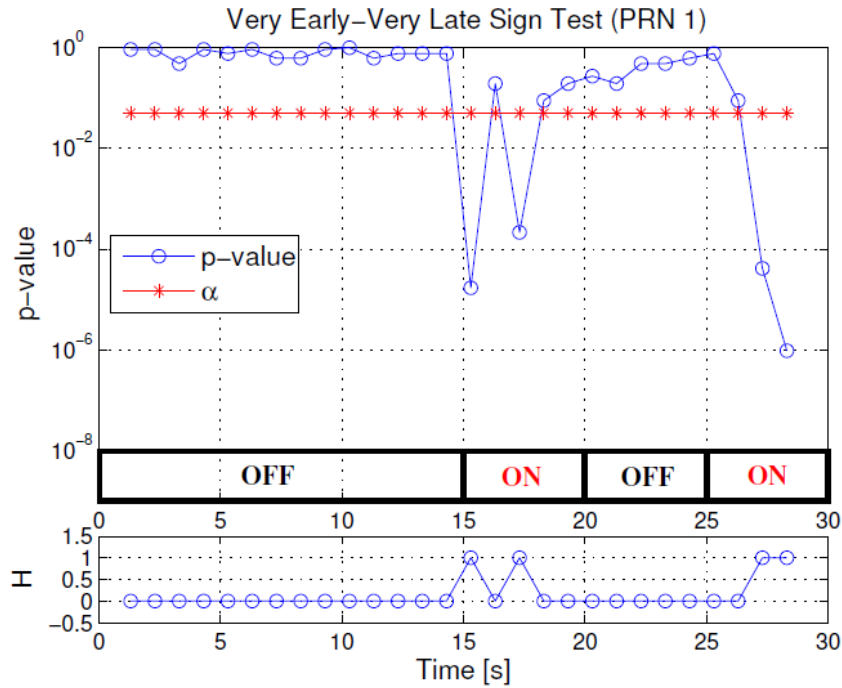


Figure 3.4: Results of the sign test applied to Very Early - Very Late correlators in a CW interfered scenario

The fact that not all the p -value points within the ON sections exceed the threshold is because the impact of the CWI on the CAF shape also depends on the relative phase between the CWI and the SiS. In fact, it can be shown that the same CWI would not affect at all another PRN; this well underlines

the importance of applying the monitoring test at the post-correlation stage, where the actual impact of the impairments can be measured.

3.3 Interference mitigation classification

As mentioned in Section 3.1, interference suppression techniques can be classified also according to the domain in which the interference excision process takes part. Thus, such techniques can be grouped as:

- **Frequency domain techniques** where interference suppression is performed in the frequency domain looking at the interfered received GNSS signal spectrum characteristic;
- **Time domain techniques** operated at both AGC and raw observable level: in the first case interference excision is performed finding the best AGC-ADC parameters tuning which can decrease the interference impact, whilst in the latter case, signal at the ADC output is processed;
- **Time-Space domain** techniques which are based on processing the signal at the ADC output but requires extremely complex hardware configuration mostly exploiting antenna arrays;

3.3.1 Frequency domain techniques

Among all the techniques which operate interference excision in the frequency domain, the most important are the Frequency Domain Adaptive Filtering (FDAF) and the Notch filtering. A basic review of both algorithms is proposed hereafter.

3.3.1.1 Frequency Domain Adaptive Filtering

The FDAF is an interference detection and mitigation algorithm based on spectral estimation of the incoming signal at the ADC output, obtained by

applying signal processing techniques such as the Discrete Fourier Transform (DFT) on a predefined number of samples.

In Figure 3.5 the FDAF functioning scheme is shown. The amplitude of

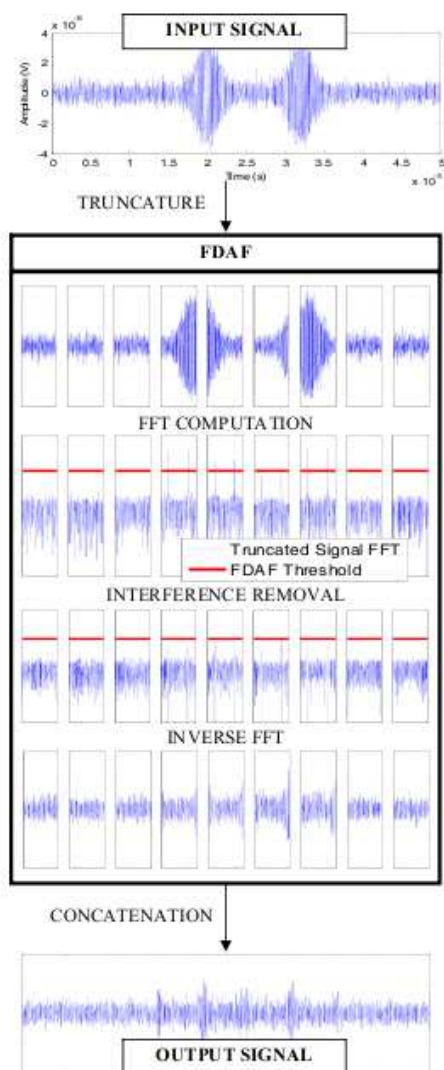


Figure 3.5: FDAF functioning scheme

each point of the signal’s Fourier representation is compared to a theoretical threshold usually determined according to a statistical model representing the received signal in an interference-free environment. Since all the incoming signal is below the thermal noise floor, the FFT representation should be ideally flat. If certain points of the incoming signal’s Fourier transform exceed this threshold, they are considered corrupted by an interference and

set to zero. Finally the inverse FFT of the manipulated incoming signal is performed so as to obtain the signal back in the time domain.

The Fourier analysis requires the incoming signal to be split into pieces composed of a determined number of samples. A large number of samples will increase the frequency resolution of the Fourier transform but, it will also induce an increase of the computation load. A trade-off between performance and computation load has then to be found. A detailed description of such a FFT based algorithm and its application against pulsed interference is presented in [58].

3.3.1.2 Adaptive notch filtering

Notch filtering has been proved to be an efficient mitigation algorithm for a family of interfering signals called CWI, pure sinusoid, which appears as a spike in the spectral domain. As it has been discussed in Chapter 2, this kind of interfering signals, usually generated by UHF and VHF TV transmitters, VOR and ILS stations, are spurious signals caused by power amplifiers working in non-linearity region or by oscillators present in many electronics devices. Notch filters are usually characterized by a frequency response which is null in correspondence of the CWI carrier frequency, thus providing attenuation of the interfering signal and preserving as much as possible the useful GNSS signal spectral components. The most common class of notch filters, which has been already proposed for CWI countermeasure in the past [59], is represented by Infinite Impulse Response (IIR) filters with constrained poles and zeroes. For these notch filters the zeros are constrained on the unit circle and the poles lie on the same radial line of the zeros. In [60], the design of a two-pole notch filter integrated with an adaptive unit for CWI carrier frequency detection algorithm is presented. The detection algorithm for the determination of the CWI frequency component perturbing the received GNSS signal is based on the removal of the constraint on the location of the filter zeros whose amplitude is adjusted by an adaptive unit. Through

this algorithm, the notch filter is able to detect the presence of the interfering signal and to decide whether to use its filtered output or input signal. In presence of multiple sinusoids, a multi-pole notch filter, based on the use of several two-pole notch filters in cascade, can be used. In this scenario the first two-pole notch filter in the chain mitigates the most powerful disturbing signal, whereas the others remove the residual sinusoids with progressively decreasing power. The transfer function of the two-pole notch filter is given by

$$H(z) = \frac{1 - 2\Re\{z_0\}z^{-1} + |z_0|^2z^{-2}}{1 - 2k_\alpha\Re\{z_0\}z^{-1} + k_\alpha^2|z_0|^2z^{-2}} \quad (3.10)$$

The numerator of the filter transfer function represents the Moving Average (MA) part of the two-pole notch filter, the structure of which is depicted in Figure 3.6.

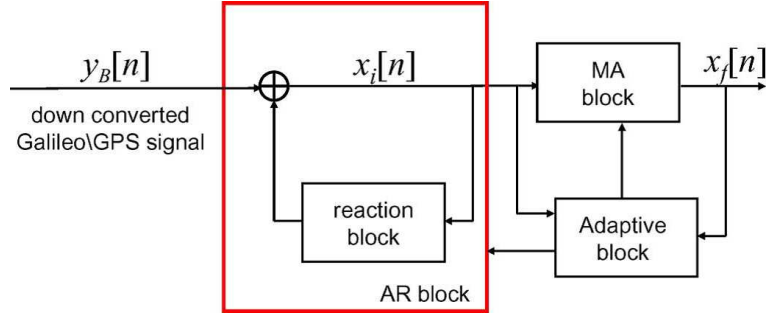


Figure 3.6: **Notch filter structure**

Here z_0 represents the zero placed in correspondence of the interfering frequency

$$z_0 = \beta \exp \{j2\pi f_i\} \quad (3.11)$$

Since the interfering signal is unknown, an adaptive block is used for providing the zero estimation which is then fed to the MA and Auto-Regressive (AR) blocks. In order to compensate for the effect introduced by the MA part, an AR is added, the transfer function of which is represented by the denominator

in (3.10), where the parameter $0 < k_\alpha < 1$, known as pole contraction factor, determines the width of the notch filter. The more k_α is close to the unity the more the notch is narrow, which in turns means a reduction of the distortion on the useful GNSS signal. However k_α cannot be chosen arbitrarily close to unity for stability reasons and thus a compromise has to be adopted. The core of notch filter structure is represented by the presence of the adaptive block, which is in charge of estimating the interference frequency and tracking its variation over the time. The presence of the adaptive block makes the entire notch filter suitable also for suppressing the harmful interference produce by jammers. Such devices, available on the web for few dollars, transmit strong chirp signals sweeping several MHz in few μs , thus appearing in the spectrum as WBI. More details on the use of such two-pole notch filter for jamming suppression can be found in [61]. The adaptive algorithm, proposed in [60] is based on an iterative normalized Least Mean Square (LMS) which minimizes the following cost function

$$f_C[n] = \mathbb{E} \{ |x_f[n]|^2 \} \quad (3.12)$$

where $x_f[n]$ is the output of the filter. The minimization is performed with respect to the complex parameter z_0 , using the iterative rule

$$z_0[n + 1] = z_0[n] - \mu[n] \cdot g(f_C[n]) \quad (3.13)$$

where $g(f_C[n])$ is the stochastic gradient of the cost function $f_C[n]$ and $\mu[n]$ is the algorithm step, which is set to $\mu[n] = \frac{\delta}{\mathbb{E}_{x_i[n]}}$,

with $\mathbb{E}_{x_i[n]}$ being an estimate of $\mathbb{E} \{ |x_i[n]|^2 \}$, which is in turn the power of the AR block output $x_i[n]$. δ is the un-normalized LMS algorithm step that controls the convergence properties of the algorithm. In [62], it is shown how the position of the z_0 with respect the unit circle is impacting on the distortion of the signal at the notch filter output. Here a different adaptive algorithm, consisting in forcing the zero of the filter to move on the unit

circle, is proposed. Furthermore, in order to improve the convergence speed of the adaptive algorithm, a run-time change of the pole contraction factor and of the LMS step is performed. In the absence of interferences the notch width is wide and the LMS step is large. When the interference appears, the notch becomes narrower, the convergence step smaller and the zeros is forced to move on the unit circle, according to

$$z_0^F = \frac{z_0}{|z_0|} \quad (3.14)$$

where z_0 is the zero produced by the adaptive block and z_0^F is the zero employed in the filter transfer function. Although the notch filter represents an effective countermeasure when dealing with CWI, it does not represent the best solution for coping with multiple interfering signals jamming all the GNSS received signal bandwidth. In this context, implementation of notch filters for suppressing multiple narrow-band interference spread all over the GNSS useful signal spectrum would become extremely complicated, as mentioned in [63].

3.3.2 Time domain techniques: Pulse blanking

An example of interference environment where the use of notch filtering or FFT based techniques would not be sufficient can be found in aviation scenarios. Here, many ARNSs based on strong pulsed signal transmission from the ground beacons, such as the DME or TACAN, which will be discussed in the next Chapter, transmit on several carrier frequency within the same frequency range of GPS L5 and Galileo E5 signals. Additional details on such interference environment can be found in [64]. In such a scenario, the interference affecting the on-board GNSS receiver is represented by the composite strong pulsed signals transmitted from all the DME/TACAN ground stations in LoS. The most common pulse interference countermeasure, already implemented in modern GNSS receivers is represented by the pulse blanking circuitry. Such a simple technique was first proposed using analog technology

as explained in [51], but then fully digital implementation has been proposed first in [65]. A block scheme of the digital pulse blanking implementation within the digital GNSS receiver front-end is shown in 3.7.

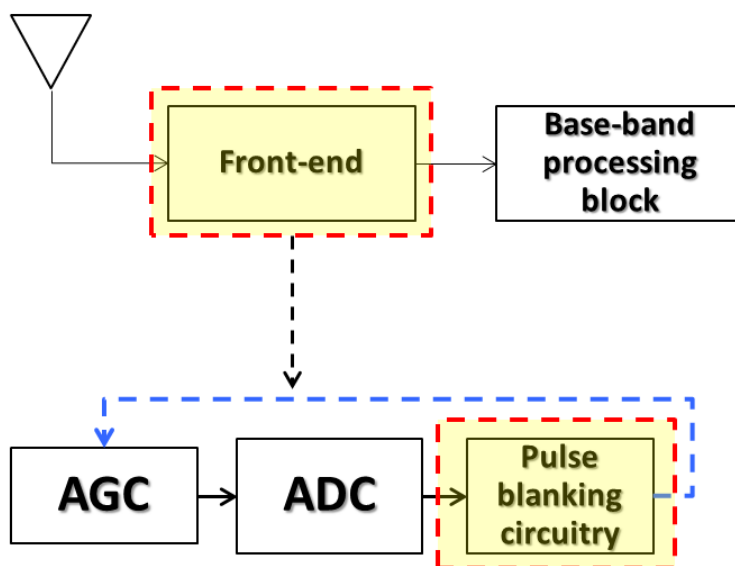


Figure 3.7: Typical Pulse blanking implementation

Such a digital circuitry provides pulsed interference excision by means of a thresholding operation on the samples at the ADC output. Basically each sample is compared to a digital threshold level, which is set according to an estimation of the thermal noise power only, and it is blanked whenever the threshold is exceeded. Figure 3.8 provides an example of pulse blanking operation performed on a typical DME/TACAN modulated pulse.

Such a simple technique will be fully discussed in then next Chapter which will provide a detailed analysis of the pulsed interference environment in aviation context.

3.3.3 Space-time domain techniques

As mentioned in the introduction, interference suppression algorithm in the space-time domain are based on the processing of the signal at the ADC

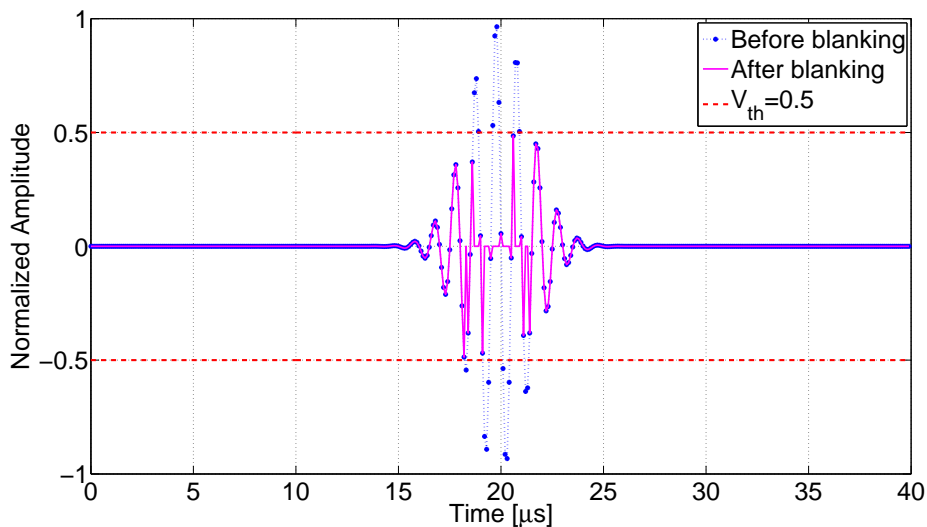


Figure 3.8: DME/TACAN pulse before and after blanking

output but at the same time, they require high complex hardware configuration exploiting antenna array capable of rejecting interference coming from determined direction. Two class of techniques are presented next:

- Space Time Adaptive Processing ([STAP](#)) techniques;
- Spatial filtering through sub-space decomposition;

3.3.3.1 Space-time adaptive processing techniques

Reference [66] describes two [STAP](#) techniques which provides simultaneous pulsed and [CWI](#) suppression in the spatial domain exploiting a [GNSS](#) antenna array receiver. Figure 3.9 shows typical configuration of [GNSS](#) receiver implementing a [STAP](#) algorithm.

The antenna array is composed by M elements followed by a Radio Frequency ([RF](#)) front-end which provides amplification and down-conversion to an intermediate frequency. The digital signal at the output of each front-end is fed to an adaptive (Finite Impulse Response ([FIR](#))) with K time taps. The signal at the output of each filters are then summed up to produce a digital [STAP](#) output which can be written as

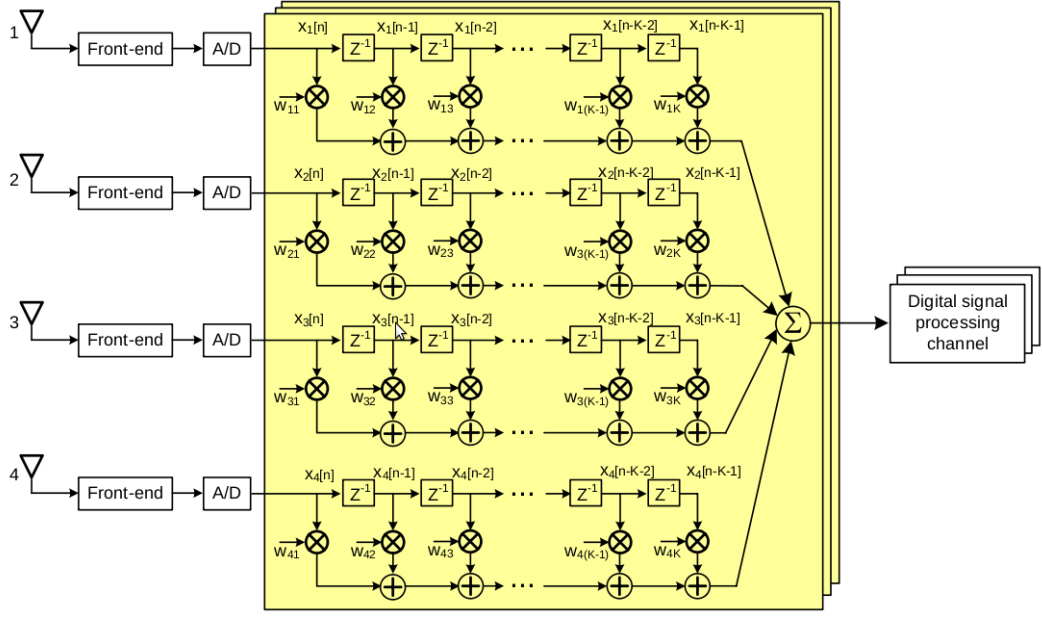


Figure 3.9: GNSS receiver with space-time array processing

$$y[n] = \sum_{m=1}^M \sum_{k=1}^K w_{mk} x_m[n - k + 1] = W^T X \quad (3.15)$$

where w_{mk} is the STAP weight at the k^{th} tap of the FIR filter after the m^{th} array element, $x_m[n]$ is the n^{th} sample of the m^{th} array element output, and the STAP input and weight ($MK \times 1$) vectors, X and W correspondingly, are defined as

$$X = [x_1[n], \dots, x_1[n - K + 1], \dots, x_M[n], \dots, x_M[n - K + 1]]^T \quad (3.16)$$

$$W = [w_{11}, \dots, w_{1K}, \dots, w_{M1}, \dots, w_{MK}]^T \quad (3.17)$$

The interference rejection is operated by the control algorithm depicted in Figure 3.10 which is in charge of updating the weights of each FIR filters in the STAP scheme.

Two weight control algorithm are proposed in [66]:

- Minimum Mean Square Error (MMSE) algorithm which updates the STAP weight in order to minimize the mean square difference between

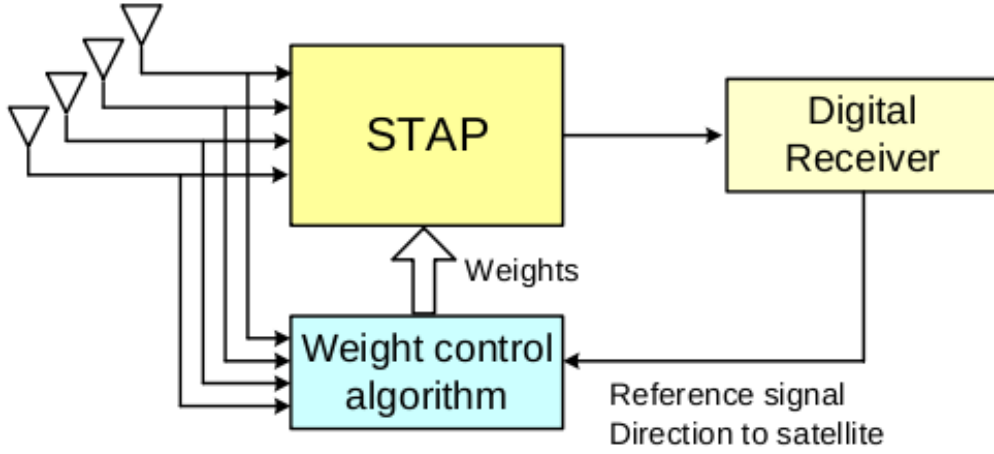


Figure 3.10: STAP weight control algorithm

the desired reference signal s_{ref} and the **STAP** output. In this case the following optimisation problem has to be solved

$$W_{opt} = \arg \min_W \mathbb{E} \{ |s_{ref} - W^T X|^2 \} = R^{-1} G_s \quad (3.18)$$

where $R = \mathbb{E} \{ X X^H \}$ is the **STAP** covariance matrix while $G_s = \mathbb{E} \{ X \cdot s_{ref} \}$ is the cross correlation vector between the **STAP** input and the reference signal.

- Minimum Variance Distortion-less Response (**MVDR**) technique that minimizes the **STAP** output power while preserving a predefined gain at the desired direction. In this case, the optimization problem is formulated as follows

$$W_{opt} = \arg \min_W W^H R W \quad (3.19)$$

subject to $W_i^T A = 1$ and $W_j^T|_{j \neq i} = 0$

Thus, the optimization problem can be rewritten

$$W_{opt} = R^{-1} C (C^H R^{-1} C)^{-1} F \quad (3.20)$$

where C and F are respectively a $(MK \times K)$ matrix and $(1 \times K)$ array defined as

$$C = \begin{bmatrix} A & \mathbf{0} & \dots & \mathbf{0} \\ \mathbf{0} & A & \dots & \mathbf{0} \\ \mathbf{0} & \mathbf{0} & \ddots & \mathbf{0} \\ \mathbf{0} & \mathbf{0} & \dots & \mathbf{0} \end{bmatrix} \quad (3.21)$$

$$F = \begin{bmatrix} f_1 & f_2 & \dots & f_k \end{bmatrix}, f_i = 1, f_{j \neq i} = 0 \quad (3.22)$$

The vector $W_i = [w_{1,i}, w_{2,i}, w_{m,i}, w_{M,i}]^T$ is the weight vector at the i^{th} tap that is the central tap in the [STAP FIR](#) filter; A is a $(M \times 1)$ array steering vector in the desired direction and $\mathbf{0}$ is a $(M \times 1)$ vector with all nulls. Concerning the estimation of the covariance matrix R and the cross-correlation matrix G_s , an adaptive block based on a iterative least squares is proposed in [\[66\]](#), and it is defined as follows

$$\hat{R}[l+1] = \gamma \hat{R}[l] + X[l]X^H[l] \quad (3.23)$$

$$\hat{G}_s[l+1] = \gamma \hat{G}_s[l] + X[l]S_{ref}[l] \quad (3.24)$$

where γ is a memory factor that defines to which extent the older estimations are accounted for obtaining a new one; $X[l]$ is a $(MK \times N)$ matrix that collects N [STAP](#) inputs over some adaptation time interval; $S_{ref}[l]$ is a $(N \times 1)$ vector containing N samples of the reference signal in the adaptation interval.

3.3.3.2 Sub-space method for spatial filtering

In [\[67\]](#) the use of antenna array together with a digital embedded spatial filtering technique which acts as a digital beam-forming operation, is described.

Given an antenna array with M sensors elements it is possible to define the digital signal at the input of the interference mitigation block at epoch k in a matrix form

$$X[k] = S[k] + Z[k] + N[k] \quad (3.25)$$

where $X[k]$, as well as $S[k]$, $Z[k]$, and $N[k]$ are $(M \times N)$ complex matrices containing respectively the composite received signal, the useful GNSS received signal component, the interference component and the noise component coming from the M different front-end connected to each of the sensors present in the antenna array. The spatial covariance matrix of the received signal considering the k^{th} period can be given by

$$R_{XX}[k] = \mathbb{E} [x [(k-1)N + n] x^H [(k-1)N + n]] \quad (3.26)$$

and due to the uncorrelation between useful GNSS signal, interference and noise components, the spatial covariance matrix becomes

$$R_{XX}[k] = R_{SS}[k] + R_{zz}[k] + R_{nn}[k] \quad (3.27)$$

Since the power of the GNSS signal is completely buried in the noise floor, and it is extremely smaller compared to the interference power, the spatial covariance matrix can be approximated as

$$R_{XX}[k] \approx R_{zz}[k] + R_{nn}[k] \quad (3.28)$$

Thus, the eigen-decomposition of the spatial covariance matrix becomes

$$R_{XX}[k] \approx \begin{bmatrix} U_I & U_N \end{bmatrix} \begin{bmatrix} \Lambda_I & 0 \\ 0 & 0 \end{bmatrix} \begin{bmatrix} U_I^H \\ U_N^H \end{bmatrix} \quad (3.29)$$

where the columns of the unitary matrix $U_I \in \mathbb{C}^{M \times I}$ span the interference subspace, the columns of the unitary matrix $U_N \in \mathbb{C}^{M \times (M-I)}$ span the noise subspace, and Λ_I denotes a diagonal matrix which contains the non-zero

eigenvalues $\lambda_1, \dots, \lambda_i, \dots, \lambda_I$ with respect to the interference subspace in the noise free case. For all the eigenvalues $\lambda_i \gg \sigma_n^2$ a pre-whitening matrix to suppress interference in $X[k]$ can be derived according to

$$R_{XX}^{-\frac{1}{2}} \approx \frac{1}{\sqrt{\sigma_n^2}} U_N U_N^H = \frac{1}{\sqrt{\sigma_n^2}} P_I^\perp[k] \quad (3.30)$$

where $P_I^\perp[k]$ is the projector onto the interference free sub-space for the k^{th} period. Thus, interference suppression can be achieved applying the projector matrix to the received digital signal as follows:

$$\tilde{X}[k] = P_I^\perp[k] X[k] \quad (3.31)$$

The projector matrix $P_I^\perp[k]$ can be derived from an eigen-decomposition of an estimate of the pre-correlation spatial covariance matrix of the k^{th} period.

Part II

Interference Impact on GNSS Aviation Receiver and Advanced Countermeasures

Chapter 4

Interference in the ARNS Frequency Band

This chapter is devoted to the analysis of the interference environment for the [GNSS](#) based services in the aeronautics frequency band. A description of the potential [ARNSs](#) affecting the on board [GNSS](#) receiver operations will be provided. Their actual impact on the [GNSS](#) signal quality degradation has been assessed through an intense test campaign activity performed at the European Space Research and Technology Centre (ESTEC) in the radio-navigation signal laboratory. [GNSS](#) receiver performance in presence of pulsed interfering signal generated by nav-aids, such as the [DME](#) or [TACAN](#), has been assessed and results of the campaign have been published in [1].

4.1 Introduction

As it has been already anticipated in Chapter 2, the Galileo E5a and [GPS](#) L5 frequency bands, which will be devoted to the future [GNSS](#) based aviation services, are shared with other [ATC](#) systems and [ARNSs](#) providing surveillance and relative positioning information to the civil and military aircraft. In [64] a general description of the several [ARNSs](#) and [ATC](#) systems potentially

affecting the GNSS aeronautics receivers, is provided and it is summarized in the following:

- **Primary Surveillance Radar (PSR)** that measures the range and bearing of the targeted aircraft from a ground station by detecting reflected radio signals, operates in the L-band (1250-1350 MHz) and may represent a pulse in-band and out-of-band interference for the Galileo E5 and GPS L5 frequency bands. The L-band PSR main features are listed in Table 4.1.

Table 4.1: L-band Primary Radar main parameters

Signal Modulation	Coded Pulses with non linear frequency modulation
Pulse Width	32 – 150 μs
PRF	300 Hz
Frequency Band	1250 – 1350 MHz
Transmission Power	24 kW
Mean Power (worst case)	1.08 kW
Coverage	200 NM
Height	10 m
Antenna Gain	36 dB
Aperture in Azimuth	1.2°
Azimuth Pattern	Gaussian
Elevation Pattern	Square Cosecant
Rotation Speed	6 rpm
Polarization	Linear Vertical or Circular
Additional Losses	1.2 dB

- **Secondary Surveillance Radar (SSR)** is a cooperative system which relies on a piece of equipment aboard the aircraft known as a transponder. The secondary radar ground station emits pulses centred up to 1130 MHz whose power may impact the Galileo E5a frequency band. The aboard transponder is a radio receiver and transmitter which replies

to signals from an interrogator (usually, but not necessarily, a ground station co-located with a primary radar) by transmitting a coded reply signal containing the requested information on the 1090 MHz frequency. Unlike the [PSR](#), the [SSR](#) also provide additional information from the aircraft itself such as its identity and altitude. Main feature of the [SSR](#) system (either Monopulse and Mode-S Radar) are summarized in [Table 4.2](#).

Table 4.2: Secondary Radar main parameters

Signal Modulation	Monopulse / Mode-S
Pulse Width	27.78 μs / 1375 μs
PRF	360 Hz / 240 Hz
Frequency Band	1090 – 1130 MHz
Transmission Power	2 kW
Mean Power (worst case)	20 W / 660 W
Coverage	250 NM
Height	10 m
Antenna Gain	27 dB
Aperture in Azimuth	2.35°
Rotation Speed	12 rpm or 15 rpm
Polarization	Linear Vertical
Additional Losses	7 dB

- **Distance Measuring Equipment ([DME](#)) and Tactical Air Navigation ([TACAN](#))** are two [ARNSs](#) providing slant range information between the aircraft and a ground reference stations, and they represent the main pulsed interference sources for the [GNSS](#) based aviation services in the Galileo E5a and [GPS](#) L5 frequency bands and for this reason they are extensively described in [Section 4.2](#).

4.2 The DME/TACAN Systems

The **DME** and **TACAN** systems provide continuous and accurate indication in the cockpit of the slant range distance between an equipped aircraft and an equipped ground reference station. Both systems are based on the communication between two components, one installed on board of the aircraft (interrogator) and another one placed on the ground (transponder).

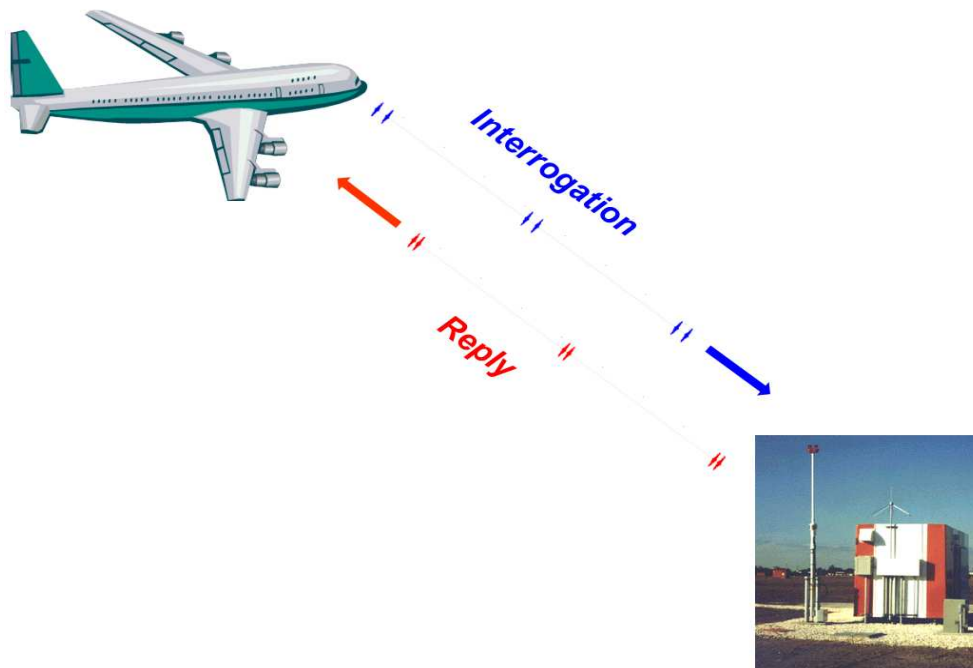


Figure 4.1: DME/TACAN system

As it is shown in Figure 4.1, the interrogator sends request to the **DME/TACAN** ground stations broadcasting towards the ground a pulse pair sequence; the ground beacons reply to the received pulse pair sequence with the same pulse pair sequence delayed of $50 \mu\text{s}$ towards the sky, thus allowing the on board **DME/TACAN** transponder to compute the slant range measurement based on a round trip time measurement. **DME/TACAN** system may operate in four different modes (X, Y, W and Z) each of which identifies a different method of coding the pulse pair transmissions by time spacing pulses within a pulse pair. However, only the X-mode replies that are transmitted in the

frequency range 1151-1213 MHz, represent a real threat for the on board GNSS receivers. These replies are made of pulse pair sequences where each pulse duration is equal to $3.5 \mu\text{s}$ and the spacing between each pulse pair is $12 \mu\text{s}$. These trains of pulse pairs are transmitted from the ground station with a maximum Pulse Repetition Frequency (PRF) equal to 2700 pulse pair per second (ppps) for the DME and 3600 ppps for the TACAN, when a maximum of 100 aircraft have to be served.

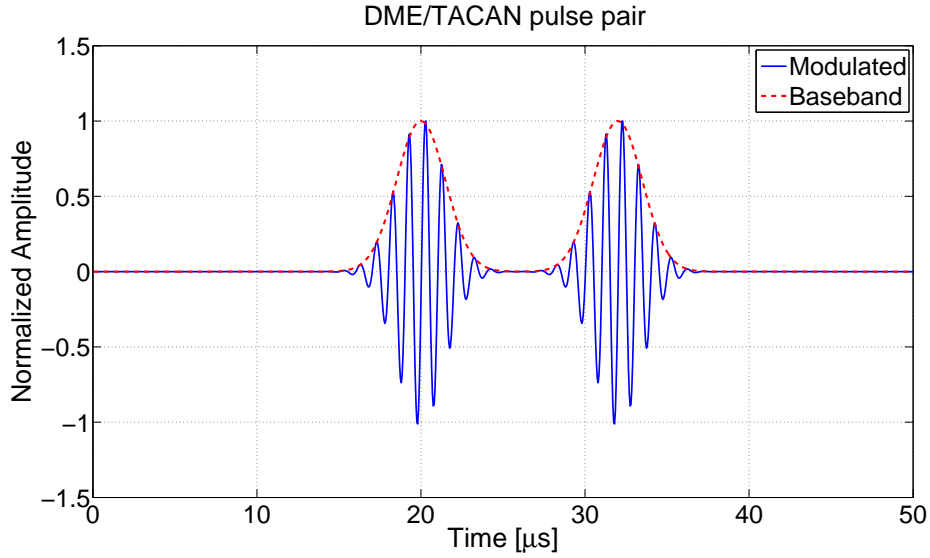


Figure 4.2: DME/TACAN pulse pair shape

A realistic example of DME/TACAN pulse pair shaping is provided in Figure 4.2 where both modulated version (blue line) and baseband version (red line) are shown. An analytical expression for the down-converted and filtered DME/TACAN double pulses signal is provided in [38], as

$$j(t) = \sqrt{J \cdot |H(f_j)|^2} \sum_k [w(t - t_k) + w(t - t_k - \Delta t)] \cos(2\pi f_j t + \theta_j) \quad (4.1)$$

where:

- $w(t) = e^{-\left(\frac{\alpha}{2}\right)t^2}$ is the single DME/TACAN baseband Gaussian pulse;
- J is the jammer peak power at the antenna port;
- f_j is the received jammer carrier frequency

- $\{t_k\}$ is the ensemble of pulse pairs arrival times
- Δt is the time spacing between the two pulses
- θ_j is the jammer carrier phase

As defined in [68], the pulse duration is the time interval the 50% amplitude point on the leading and trailing edges of the pulse envelope. Concerning the pulse power, the maximum Equivalent Isotropic Radiated Power (EIRP) transmitted by the DME/TACAN ground beacons is 40 dBW. Thus, the DME/TACAN pulse power reaching an on board antenna at high altitude but still within the maximum coverage range of a ground station (about 519 Km), is quite higher than the GNSS signal power level. More detailed specifications on both systems can be found in [68].

The DME/TACAN interference environment in the GPS L5 and Galileo E5 frequency bands has been already widely investigated by receiver manufacturers and research centres. In [69] a set of on-field test carried out in order to perform data collection of realistic DME/TACAN pulsed signal in the vicinity of the Brussels International airport is described. The logged baseband samples revealed that, these pulses sometime saturated the front-end amplifier of the employed GPS L5 receiver. In [39], a measurement of the DME/TACAN interference experienced by aboard GNSS receiver, has been performed by means of several Flight Trials at different altitude. The several data collections in the Galileo E5 frequency band performed at different Flight Level revealed that, at approximately 40000 ft, the GNSS aboard receiver antenna receive strong DME/TACAN pulses from about 48 ground stations in LoS.

4.3 DME/TACAN interference countermeasures

Several interference countermeasures against this type of pulsed interference produced by such ARNSs have been proposed in literature. Several techniques

among the one described in Chapter 3 can be tuned to cope with the typical aeronautical interference:

- **Pulse Blanking**, already introduced in Chapter 3 may represent an high performing pulsed interference suppression mechanism when the pulsed interference at the receiver antenna is not so dense in time. On the contrary, when in presence of high dense in time pulsed interference, as the **DME/TACAN** scenario that will be analysed in the following of this Chapter, great signal degradation may be observed, since large portions of useful signal components are blanked together with the interference. Furthermore, due to the Gaussian shape (see Figure 4.2), pulse tails are not correctly suppressed. In the following Sections it will be shown how the **GNSS** receiver tracking operation can not survive in presence of multiple pulsed interference sources even when a digital pulse blanking circuitry is employed.
- unlike the pulse blanking, **Notch Filtering** performs pulsed interference suppression in the frequency domain where **DME/TACAN** signals appear as narrow-band frequency tones. Here, only the frequency components of the received composite signal crossing the noise level spectral density are suppressed. Through this method, even the pulses' tails are suppressed. However, such a frequency based interference suppression removes also useful signal frequency components in correspondence of the **DME/TACAN** frequencies. Furthermore, in presence of multiple **DME/TACAN** sources, which broadcast strong pulses on adjacent carrier frequencies, a more complex notch filter design is needed.
- **Hybrid Blanking** combines advantages of both pulse blanking and notch filtering. When a pulsed interference is detected in the time-domain, the notch filtering of a slice of $12 \mu s$ of signal centred around

the estimated pulse position is triggered. In this case, the filter design is simple, since the notch is activated only in presence of pulsed interference.

The [FDAF](#), already introduced in Chapter 3, can be adopted for pulsed interference suppression. For the [DME/TACAN](#) interference scenario, both sampling frequency and the number of points N over which the [FFT](#) is computed, are crucial for the achieved interference mitigation performance. Increasing N , the [FFT](#) resolution increases as well as the number of operations for its computation. Thus a trade-off design between optimal representation of the pulse interference in the frequency domain and complexity is needed.

Finally in [66] two [STAP](#) methods, already described in Chapter 3 are adopted for coping with the [DME/TACAN](#) interference. Here, multiple pulsed interference suppression is achieved in the time-space domain, since the composite received signal, processed by the [RF](#) front-end of each antenna, is further processed by a mitigation unit which control, through a recursive signal processing algorithm, the beam of the antenna arrays. However, such a technique presents a high complexity regarding its hardware implementation thus resulting in a non-optimal solution for pulsed interference suppression.

So far, the most traditional interference countermeasures in [GNSS](#) have been discussed in terms of their capabilities in suppressing pulsed interference. Such techniques will be resumed in the following Chapter of this dissertation. Next Section will provide a theoretical derivation of the [GNSS](#) signal quality degradation for an airborne receiver when merged in a harsh [DME/TACAN](#) interference environment and when a traditional pulse blanking circuitry is employed.

4.4 Pulse Blanking Impact on Signal Quality: Theoretical Derivation

In literature the effect of a pulse blanking circuit on GNSS receiver performance has been widely investigated. A theoretical model for computing a prediction of the pre correlator C/N_0 in presence of strong and dense in time DME/TACAN interference is first proposed in [70] and then presented in [71],

$$(C/N_{0,eff}) = \frac{C}{N_0} \cdot \frac{(1 - \beta)}{1 + \frac{I_{0,WB}}{N_0} + R_I} \quad (4.2)$$

where β , representing the blanker duty cycle, is the total mean activation time of the blanker and R_I is the aggregate post-correlator ratio between the residual DME/TACAN power, after the blanker, and the receiver thermal noise. The residual DME/TACAN power is generated by all the pulses' samples below the blanking threshold, that contribute to increase the noise floor. As mentioned in Section 4.2, due to the Gaussian shape of the DME/TACAN pulse, both strong pulses, whose peak power crosses the blanking threshold, as well as weak pulses contribute to the increase of the noise floor. Hereafter, a theoretical derivation of the blanker duty cycle β and the component R_I is provided.

4.4.1 β computation

The total mean activation time β of the blanker is determined by all the pulses whose peak power is above the blanking threshold. A revision of the blanker duty cycle β derivation, first proposed in [38], is presented in this Section. The mean activation time T for the blanking circuitry in presence of one single DME pulse and in absence of pulses collisions is derived assuming (4.1) as the analytical expression for the DME signal. Considering only the Gaussian envelope of the pulse, as depicted in Figure 4.3,

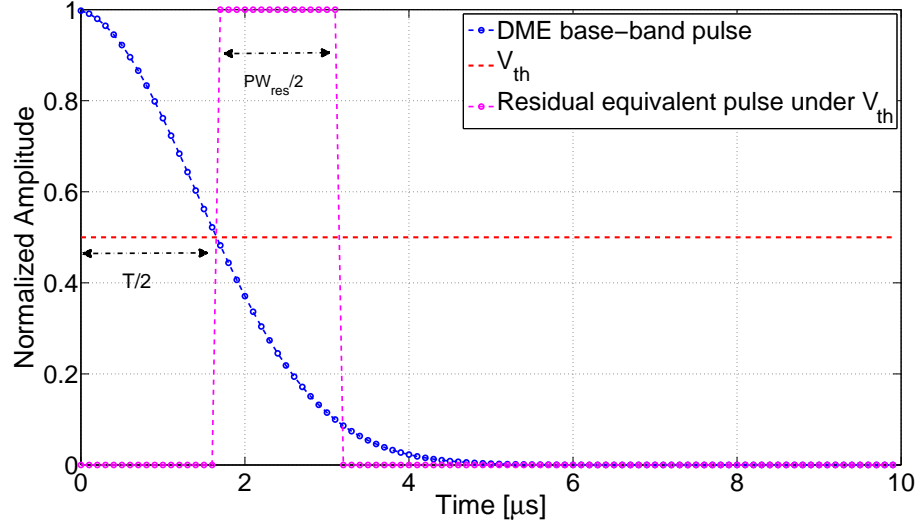


Figure 4.3: DME/TACAN single base-band pulse

it can be easily shown that

$$T = 2 \cdot \sqrt{2 \cdot \frac{\ln(P_{strong}/V_{th})}{\alpha}} \quad (4.3)$$

where V_{th} is the blanking threshold level power and P_{strong} is the pulse peak power. As stated in [38], any additional strong pulses superposing to the initial pulse would decrease the mean activation time of the blanker. Thus the total activation time, in presence of pulse collision has to be computed averaging T over all the possible pulse collisions scenarios. Furthermore, due to the modulation, not all the samples belonging to the pulse are blanked, as it is shown in Figure 4.4.

Thus assuming the arrival times of all the pulses transmitted by the ground beacons to the on-board GNSS receiver distributed according to a Poisson process, the mean activation time becomes

$$T_m = \gamma \left(\frac{P_{strong}}{th} \right) \cdot \left(T e^{-\lambda T} + \frac{T (\lambda T)}{2 \cdot 1!} e^{-\lambda T} + \frac{T (\lambda T)^2}{3 \cdot 2!} e^{-\lambda T} + \dots \right) \quad (4.4)$$

where:

- γ is a reduction factor dependent on the ratio between the pulse peak power P_{strong} and the blanking threshold V_{th} , which takes into account

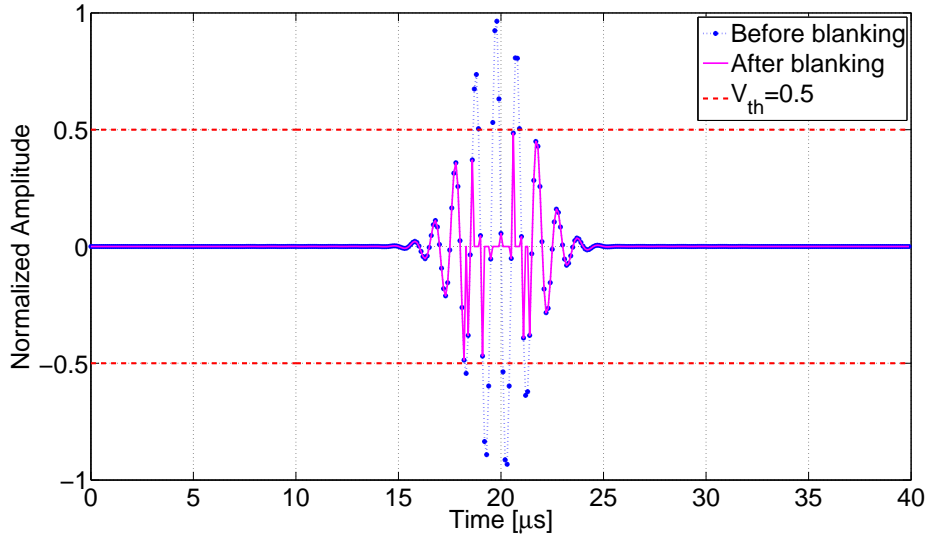


Figure 4.4: DME/TACAN pulse before and after blanking

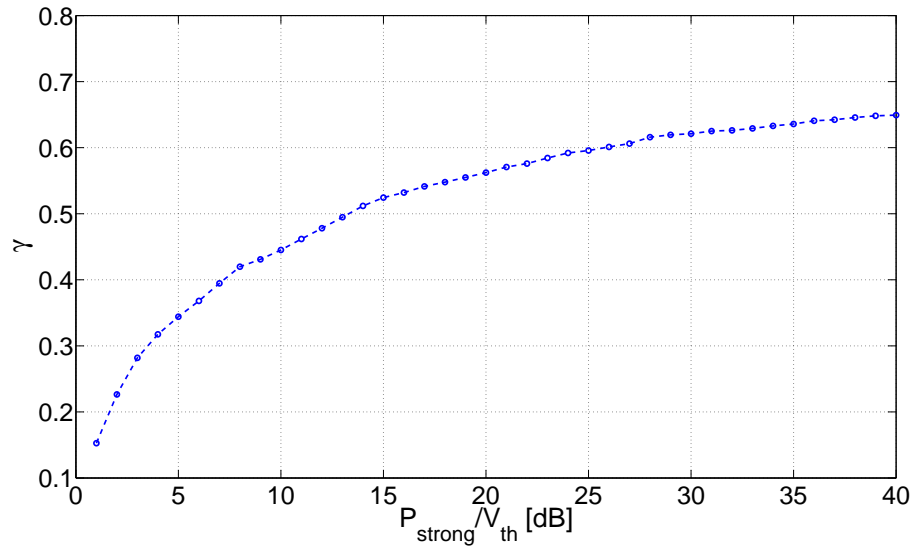


Figure 4.5: Ratio between the real blanker activation time and the theoretical activation time T defined in (4.3)

the carrier variation over the pulse duration. Figure 4.5 provides the trend of such a parameter with respect the P_{strong}/V_{th} ratio, obtained by means of simulations.

- λ is the composite arrival rate of the pulses coming from all the ground beacons at the receiver antenna port. Knowing that the maximum PRF for the DME and TACAN ground stations are respectively 2700

and 3600 ppps, if there are N_{DME} stations and N_{TACAN} stations, λ can be computed as:

$$\lambda = 2700 \cdot N_{DME} + 3600 \cdot N_{TACAN} \quad (4.5)$$

Thus, the real mean activation time of a blanker in presence of strong multiple **DME/TACAN** interference becomes

$$T_{blanker} = 2 \cdot \left(2700 \cdot \sum_{i=1}^{N_{DME}} T_{m,DME}(i) + 3600 \cdot \sum_{i=1}^{N_{TACAN}} T_{m,TACAN}(i) \right) \quad (4.6)$$

This duration can be considered as the blanker duty cycle β , since it is computed over 1s. The factor 2 is introduced due to the presence of a pulse pair.

4.4.2 R_I calculation

Reference [71] has been taken into account, for the theoretical derivation of the component R_I , which is defined as

$$R_I = \frac{1}{N_0 \cdot B_{fe}} \cdot \sum_{i=1}^N P_i \cdot dc_i \quad (4.7)$$

where $N = N_{DME} + N_{TACAN}$ is the total number of **DME/TACAN** sources; P_i is the received peak power of the i^{th} **RFI** pulsed signal source; B_{fe} is the pre correlator **IF** bandwidth and dc_i is the duty cycle of the i -th signal source without any pulse collision. R_I is defined splitting the contribution of strong and weak **DME/TACAN** signals. Weak pulsed signal (with peak power below the blanking threshold) will contribute with their total power to the interfering power. Equation (4.7) can then be elaborated as

$$\begin{aligned} R_I &= \frac{1}{N_0 \cdot B_{fe}} \cdot \sum_{i=1}^N P_i \cdot dc_i \\ &= \frac{1}{N_0 \cdot B_{fe}} \cdot \left(\sum_{j=1}^{N_{DME}} P_{strong,j} \cdot dc_{res,j} \right) + \\ &+ \frac{1}{N_0 \cdot B_{fe}} \cdot \left(\sum_{k=1}^{N_{TACAN}} P_{weak,k} \cdot dc_{weak,k} \cdot k_{ls} \right) \end{aligned} \quad (4.8)$$

where the spectral separation coefficient k_{ls} is introduced as weighting factor for those DME/TACAN signal whose peak power is below the blanking threshold, and it is defined according to [72] and [73], as

$$k_{ls} = \int_{-B_{fe}/2}^{B_{fe}/2} G_l(f)G_s(f)df \quad (4.9)$$

with $G_l(f)$ and $G_s(f)$ are respectively the normalized PSD of the narrow-band interference and of the useful received GNSS signal. In [38] and [70], rectangular equivalent pulse width of 2.64 μs is used for modelling the contribution to the noise floor caused by weak DME/TACAN pulses, the peak power of which is below the blanking threshold V_{th} . Thus, the duty cycle for weak DME/TACAN signals can be written as

$$dc_{weak,k} = 2 \cdot 2.64(\mu s) \cdot PRF_{weak,k} \quad (4.10)$$

where $PRF_{weak,k}$ is the pulse repetition frequency of the k^{th} weak DME/TACAN signal.

Concerning the contribution due to the strong DME/TACAN pulses (with peak power over the blanking threshold), in [70] and [71] the residual portion of pulse below the blanking threshold is assumed to equate the duration of an equivalent rectangular pulse duration, as shown in Figure 4.3. Thus, taken into account (4.3), it follows that

$$PW_{res} = 2 \cdot \int_{T/2}^{+\infty} e^{-\frac{\alpha}{2}t^2} dt = \sqrt{\frac{2\pi}{\alpha}} \cdot \text{erfc} \left[\sqrt{\ln \left(\frac{P_{strong}}{V_{th}} \right)} \right] \quad (4.11)$$

Then, the duty cycle for the residual portion of strong DME/TACAN signals which contributes to the noise floor becomes

$$dc_{res,j} = PW_{res,j} \cdot PRF_{strong,j} \quad (4.12)$$

A more realistic example of pulse blanking operation on a DME/TACAN pulses train in presence of pulse superposition is shown in Figure 4.6.

The presence of multiple pulses non perfectly overlapped lead to a greater pulse blanking activation time.

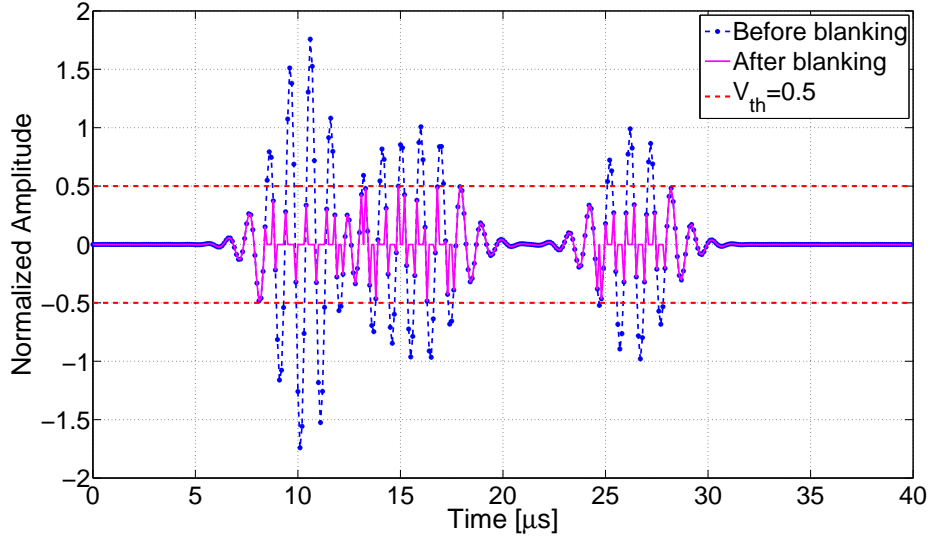


Figure 4.6: Pulse blanker activation time in presence pulse superposition

4.4.3 The case study of central Europe

Using the theoretical model so far described, a prediction of the C/N_0 degradation due to the DME/TACAN signals has been performed, by means of simulations, for a grid of locations at 40000 feet over Europe. A complete data base of all DME/TACAN ground beacons spread around the Europe, containing reliable information about locations, carrier frequencies for the pulsed signals transmission and EIRP, has been taken into account. In particular, for the GNSS signal degradation in the ARNS frequency band, only those ground stations transmitting within the GPS L5 and Galileo E5a bands, have been considered and for each of them maximum PRF has been assumed. Moreover both DME/TACAN beacons pattern antenna defined in [70] and GNSS typical aircraft antenna pattern have been simulated in order to perform an accurate calculation of the received pulsed interference level power at the GNSS on board antenna. A reference blanking threshold level power V_{th} of about -116 dBW, about 9 dB over the noise floor has been assumed for the simulation. It is worth to outline that no aircraft body attenuation has been taken into account.

Figure 4.7 shows the profile of the predicted post-correlator C/N_0 degradation caused by the composite pulsed signals coming from all the DME/TACAN ground stations represented by the black dots.

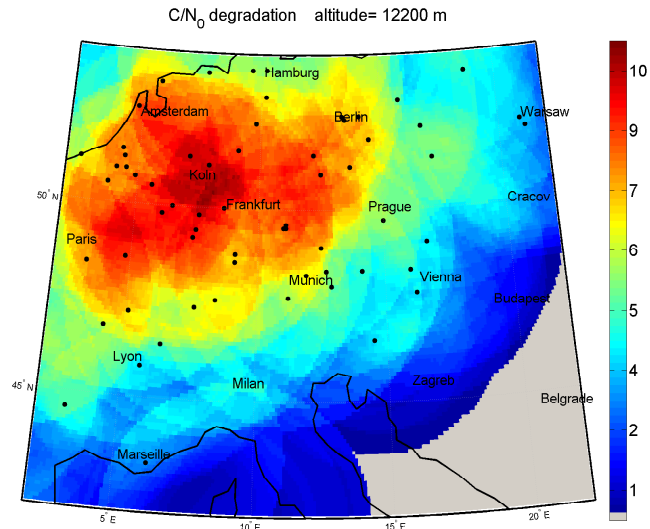


Figure 4.7: Prediction of the effective post correlator C/N_0

Figure 4.8 and 4.9 provides respectively the profile of the expected blanker duty cycle β and the number of DME/TACAN stations in LoS.

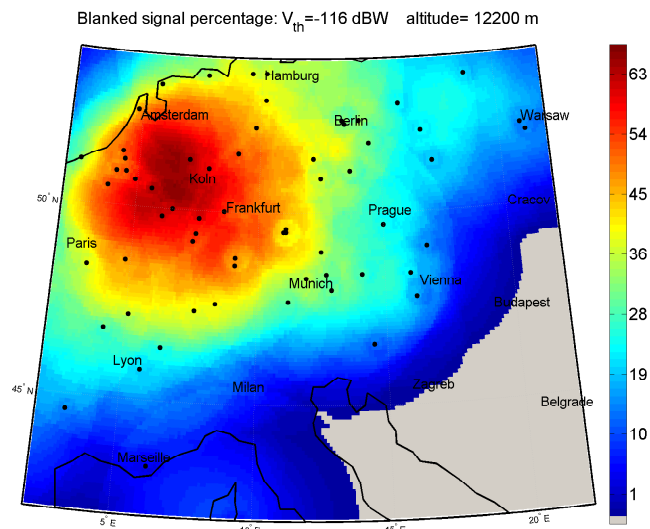


Figure 4.8: Prediction of the blanker duty cycle β

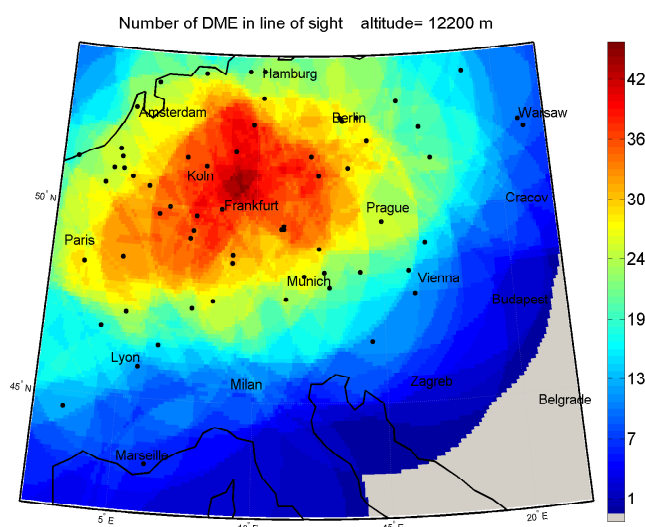
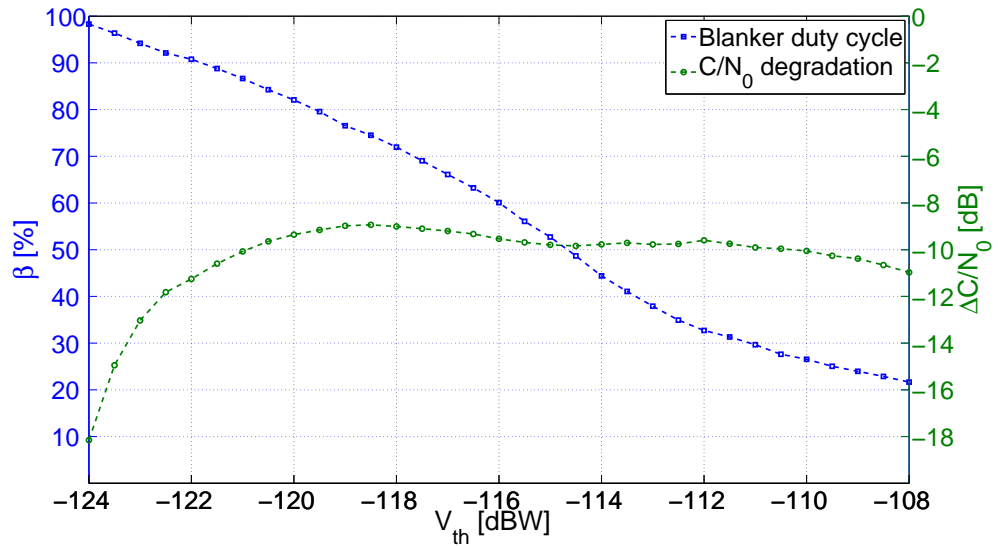


Figure 4.9: Number of DME/TACAN stations in LoS

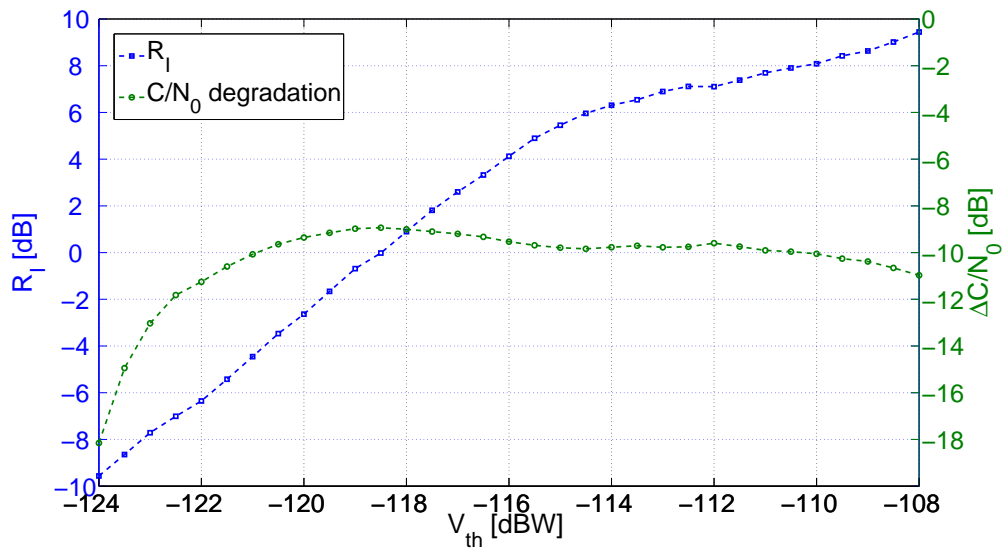
The worst location in terms of C/N_0 degradation is identified for a latitude of $50,4^\circ$ and for a longitude of $8,1^\circ$ at the altitude of 40000 feet. At this location, roughly corresponding to the area over the Frankfurt airport, GNSS receiver operation might be corrupted by the composite pulsed signal coming from up to 40 DME/TACAN stations broadcasting within the GPS L5 and Galileo E5a frequency bands. Under this simulated interference environment, the blanking circuit cuts off about 60% of the total GNSS received signal, thus producing a degradation on the $C/N_{0,eff}$ of about 9.5 dB.

Figure 4.10 shows the trend of the C/N_0 degradation, of the blanker duty cycle β and of the factor R_I with respect to the value of the blanking threshold, simulated at the DME/TACAN hotspot location previously identified. As expected, Figure 4.10(a) shows that, the blanker duty cycle β is decreasing with the increasing of the blanking threshold, while the degradation on the C/N_0 has an optimum point. This is due to the fact that a low blanking threshold would increase the percentage of the signal been blanked while an higher blanking threshold would cut off a minor percentage of received signal, allowing the majority of the pulsed interference to go through the correlator, increasing the noise floor due to an increased R_I contribution, as can be

observed in Figure 4.10(b) where the factor R_I is plotted versus the blanking threshold. Thus, a careful design of the blanking circuit has to be performed in order to achieve the best trade off between percentage of signal blanked and C/N_0 degradation.



(a)



(b)

Figure 4.10: Blanker duty cycle β and R_I factor versus the blanking threshold

The analysis performed in this case study, shows that the blanking threshold should be optimized, in order to avoid unacceptable drops in the C/N_0 due

to the presence of multiple interfering pulses. Moreover, a priori optimization of the threshold value by simulation requires a large amount of details of the **DME** and **TACAN** ground stations, thus making this task not easy to accomplish.

4.5 Experimental Assessment of DME/TACAN Interference

In order to validate the results based on the theoretical model, a test campaign has been performed at the ESTEC navigation laboratory using the powerful Interference Test Facility (ITF). The ITF is a hardware software platform capable of generating a wide range of realistic interference scenarios and it is mostly devoted to the testing of **GNSS** hardware receiver performance under interference. More details on the different capabilities and configurations of this tool can be found in [74].

The ITF configuration is shown in Figure 4.11.

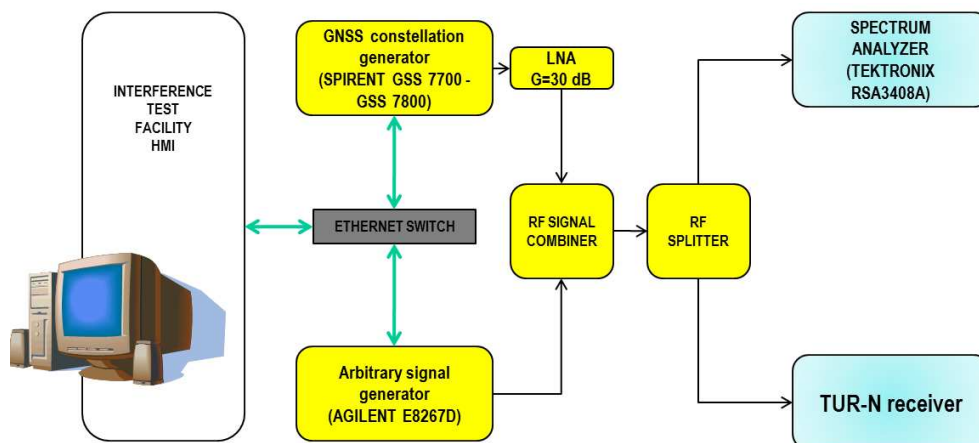


Figure 4.11: Hardware setup

A Spirent **GNSS** constellation simulator and signals generator as well as an Agilent signals generator have been used. They are connected to an ethernet network together with a desktop PC hosting the software managing the ITF.

Through this network connection, both Spirent and Agilent generators have been driven remotely from the ITF Human Machine Interface (HMI). Latest release of the ITF software provides the possibility to generate a wide range of realistic [DME/TACAN](#) interference environments by a proper settings of the following parameters:

- the number of ground beacons to simulate;
- carrier frequency and pulse repetition frequency for each simulated beacon;
- pulse width, inter pulses spacing and pulse peak power for each [DME/TACAN](#) ground stations;
- [DME/TACAN](#) pulse arrival time to the on board [GNSS](#) antenna.

Once these parameters have been defined, a file of IQ stream samples with a user-defined length have been generated and loaded automatically to the Agilent signals generator which is in charge of replaying it in a loop. Then, the composite [DME/TACAN](#) interference is combined with the [GNSS](#) signal generated by the Spirent at Radio-Frequency. Eventually, the composite [GNSS](#) signal interfered by [DME/TACAN](#) signals has been fed to an RF splitter, the outputs of which have been connected with a Tektronix Spectrum Analyzer and a hardware Test User Receiver (TUR) respectively. It has to be outlined that the [GNSS](#) signal is amplified by using a 30 dB Low Noise Amplifier ([LNA](#)) before being fed to the RF combiner, while for the [DME/TACAN](#) composite interference the amplification is simulated adjusting the power levels from the ITF HMI. This choice has been adopted to avoid a further increase of the noise that would happen if the signal coming from the Agilent is fed to the [LNA](#) as well. Since the overall losses introduced by both RF combiner and splitter is about 10 dB, a power adjustment of 40 dB from the ITF HMI has been provided in order to simulate the [LNA](#) gain and recover from the losses in the setup. [GPS](#) L5 and Galileo E5a signals have been generated

Table 4.3: Setup settings

Parameter setup	Value
LNA gain	30 dB
GNSS aviation antenna gain	4 dB
Setup losses	10 dB
E5a input power at receiver	−103 dBm
Nominal C/N_0	44 dB-Hz
Power adjustment from ITF	40 dB

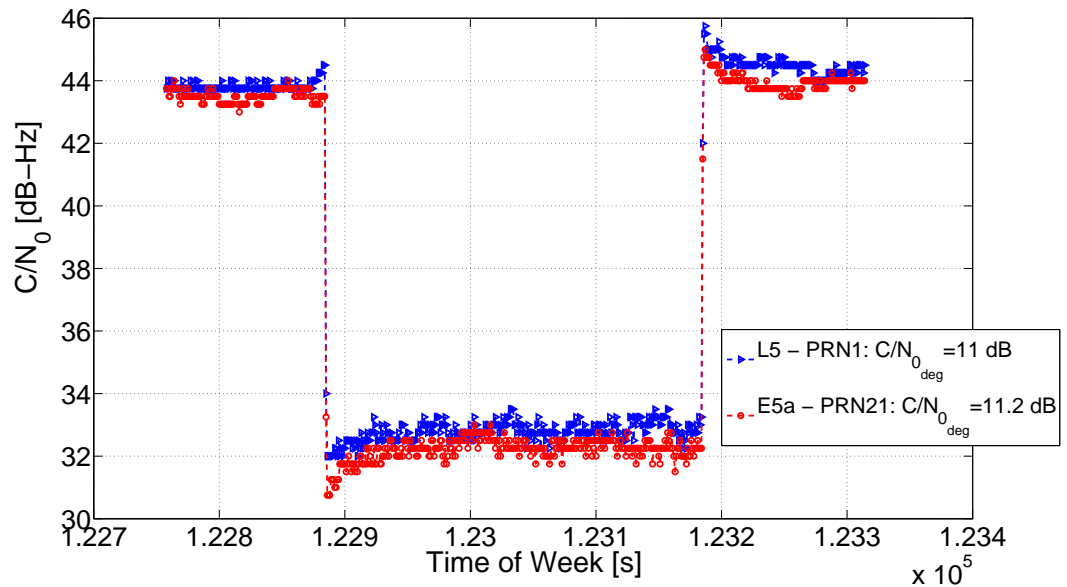
with a power level such that the pre-correlator carrier to noise density ratio estimated by the TUR receiver is equal to 44 dB-Hz for both signals in an interference-free environment.

Table 4.3 summarizes all the setup parameters.

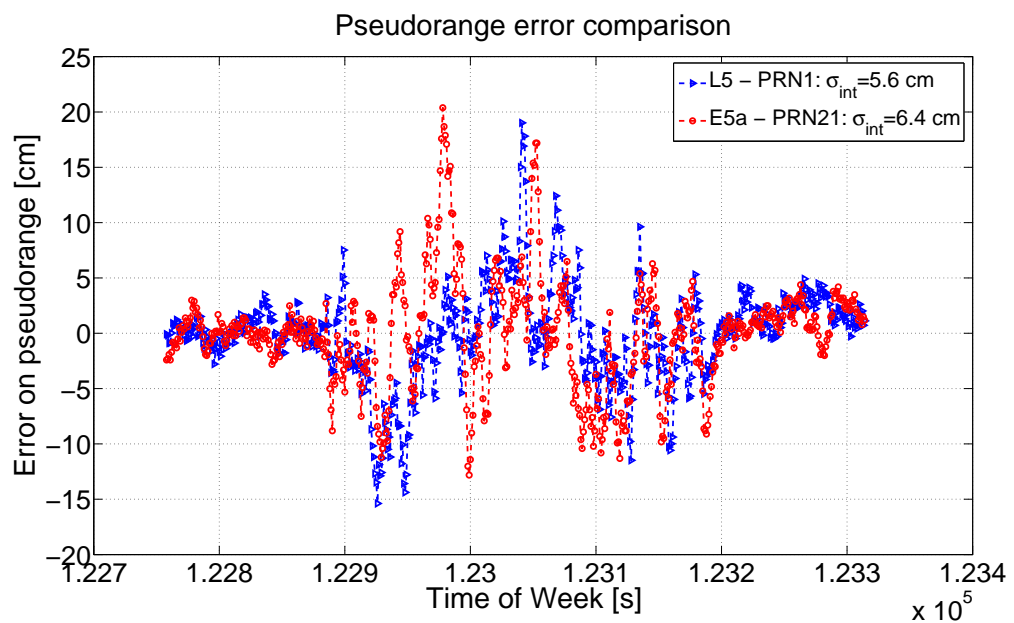
Each performed test had a duration of about 10 minutes; after an initial period of about 2 minutes when the receiver is tracking the GNSS signal in a steady state, 5 minutes of DME/TACAN composite signal are injected in the setup. Tests have been performed on both GPS L5 and Galileo E5a frequency bands.

Figure 4.12 shows the TUR receiver performance in tracking the Galileo E5a and GPS L5 signals (PRN 21 and 1 respectively), under the DME/TACAN interference environment considered.

In particular Figure 4.12(a) provides a comparison between the C/N_0 estimated by the TUR receiver in both Galileo E5a (red line) and GPS L5 (blue line) frequency band, during all the test duration. As soon as the DME/TACAN signal is injected in the setup, a drop on the C/N_0 of about 11 dB is observed in both figures, and the blanker duty cycle value during all the interference period is around 56%. Such value of degradation is approximately 1 dB far from the theoretical value estimated by using the model and that can be observed in Figure 4.10(a). Furthermore, according to Figure 4.10(a), in correspondence of a blanker duty cycle β of 56%, a blanking threshold level



(a)



(b)

Figure 4.12: TUR performance under DME/TACAN interference in Galileo E5a and GPS L5 frequency bands

power of -115.5 dBW can be observed and assumed as a potential equivalent blanking threshold for the TUR blanker circuitry. Despite a large portion of signal is cut off by the blanking circuit, the TUR receiver is still able to keep the tracking of both GNSS signals, computing pseudorange measurements affected by an increased error, as shown in Figure 4.12(b).

Figure 4.13 shows the C/N_0 degradation in the Galileo E5a and GPS L5 frequency bands (top plot) and the blanker duty cycle (bottom plot) for multiple DME/TACAN interference scenario, simulating the path of an aircraft landing on Frankfurt airport.

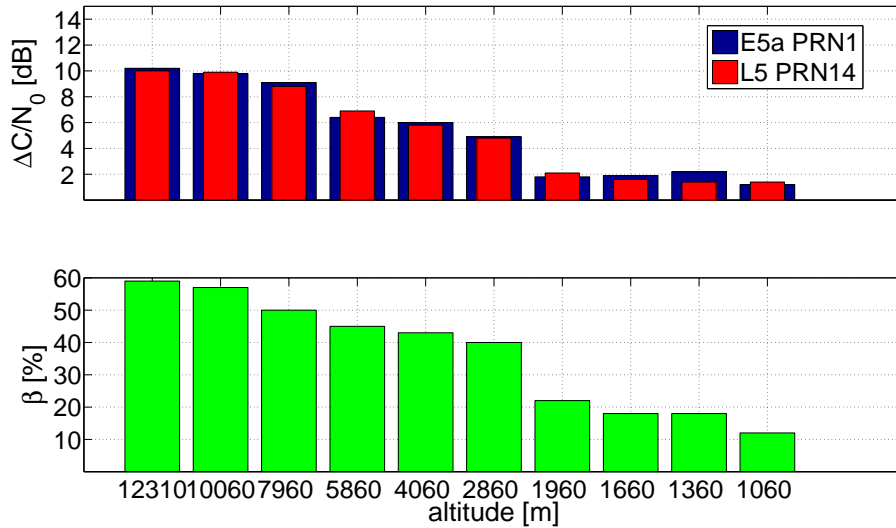


Figure 4.13: TUR performance during aircraft approach simulation

These results are obtained computing for each location along the descending path the number of DME/TACAN stations in LoS and the DME/TACAN peak power reaching the GNSS on-board antenna. The experimental results for each interference scenario are achieved following the same test procedure described for the previous experimental tests. As expected, the C/N_0 degradation as well as the blanker duty cycle decrease with the decreasing altitude, since the number of DME/TACAN stations in LoS for the GNSS on-board antenna is decreasing as well. This results confirm that the DME/TACAN interference is a real threat for aviation GNSS receivers operation only at

high altitude. Although at low altitude, the received pulse peak power at the GNSS antenna port is extremely high, only a small percentage of received signal is suppressed since the composite DME/TACAN signal is the combination of a smaller number of replies from the ground beacons. Finally, a set of experimental tests in the laboratory have been devoted to the analysis of the DME/TACAN impact on the Geometrical Dilution of Precision (GDOP) available for a realistic on board receiver enabling a determined GNSS antenna pattern from the SimGen option panel controlling the Spirent simulator. Results are shown in Figure 4.14.

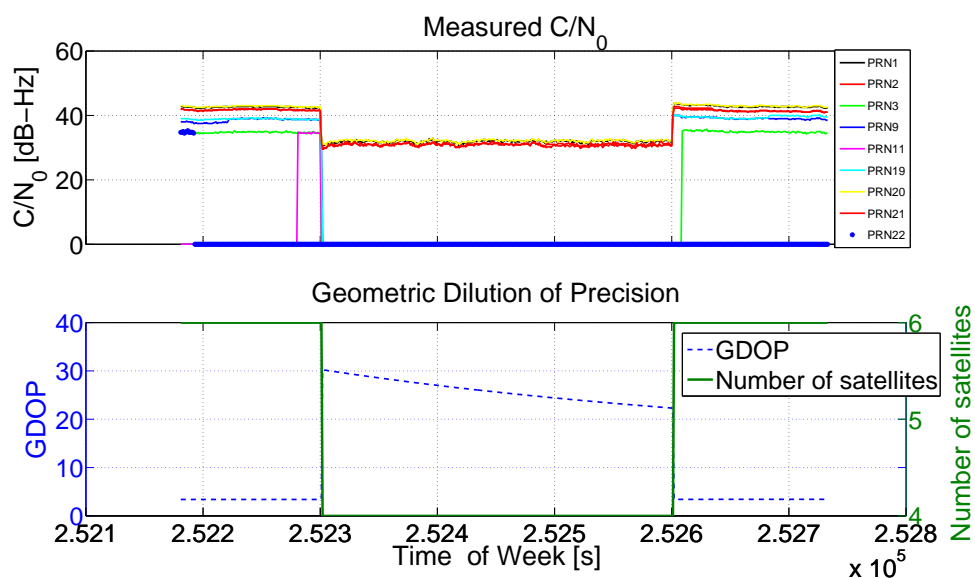


Figure 4.14: DME/TACAN interference impact on C/N_0 and Geometric Dilution of Precision

The upper plot shows the C/N_0 estimated by the TUR receiver for each E5a PRN tracked during the all test duration, while the plot on the bottom shows the trends of the GDOP (blue line) and the number of satellites used by the TUR in the GDOP computation (green line). Since a GNSS aviation pattern antenna is simulated, GNSS signal coming from satellites at low elevation are tracked with a lower initial C/N_0 . Once the DME/TACAN interference is injected into the setup, the TUR receiver immediately loses the track of weakest GNSS signals, thus impacting on the GDOP as shown in the bottom plot. During the interference-free period, a good GDOP value was computed

on the basis of 6 satellites, while during the interference period only 4 satellites were used for the fix. A great increase on the GDOP value is observed when the TUR receiver is under DME/TACAN interference, thus impacting on the final position computation.

This test campaign revealed that DME/TACAN interference in some cases might represent a disruptive interference even if the GNSS receiver is equipped with a blanker circuitry. Great losses on the C/N_0 , caused by the suppression of large portions of useful GNSS signals (high values of β), might lead the receiver losing the tracking of feeble GNSS received signals, thus impacting on the final user position accuracy, worsening both the quality of the pseudorange and the GDOP factor.

4.6 Pulse blanking non-linearities modeling

The experimental results presented so far showed how the traditional pulse blanking countermeasure may not be sufficient in presence of multiple strong pulsed interference sources. In such a scenario the pulse blanking circuitry is triggered by the composite strong pulsed signals reaching the on board GNSS receiver antenna, causing the suppression of large portions of useful GNSS signal power together with interference power, thus increasing the probability to fail the acquisition and tracking of the signal itself as demonstrated in Figure 4.14. Moreover, the pulse blanking circuit performance can be negatively influenced by the impact of pulsed signals on the active components within the receiver front-end. Very strong pulses or very strong received power due to the combination of multiple pulses can cause the saturation of the active components in the GNSS receivers (e.g. amplifiers), which may require a recovery time to go back to a normal state when the interference ends. In [51] it is mentioned that for a particular commercial receiver, an interference pulse signal with peak power 15 dB above the thermal noises is sufficient to saturate

the last amplification stage within the receiver front-end. Under this interference environment condition, pulse blanking may perform signal suppression even during the off state of the pulse for a time period equal to the recovery time needed by the amplifiers to resume normal operation. For a commercial receiver, typical recover times for amplification stages is about 40 ns/dB of input level beyond the saturation point [51]. In general pulsed interference signals impact on receiver front-end component might be different depending especially on the pulse peak power level and on the pulse duration. Furthermore, the AGC, needed when multibit quantization is implemented in the digital part of the receiver front-end, has to be carefully designed. The AGC is in charge to properly set the amplitude dynamic of the ADC input signal. A slow AGC set the ADC input levels averaging the input signal power over a large time during which, if too many pulses oscillations are present, the input dynamics of the ADC is not properly set [51]. It has also to be taken under consideration the fact that the blanked samples should not be used for the AGC tuning in order to avoid ADC overloading. Due to these several reasons blanking operation might not be efficient, since high percentage of the received signal may be blanked [65]. In order to assess the impact of such non-linear behaviours, a software simulation of the pulse blanking operations has been performed considering different values of reaction time and recovery time. IF samples of a set of data collected in the GPS L5 and Galileo E5a frequency bands were used. Such data collections have been performed at the ESTEC navigation laboratory, using a discrete components Front-End, the block scheme of which is reported in Figure 4.15.

The considered Front-End has been used in the same hardware setup configuration described in Section 4.5, connecting one of the outputs of the RF splitter at its input. Table 4.4 summarizes the settings of the Front-End chosen for the specific data collection. Such a Front-end is characterized by two amplification stages followed by a down-conversion to an intermediate frequency of 225 MHz. Additional amplification stages followed by a

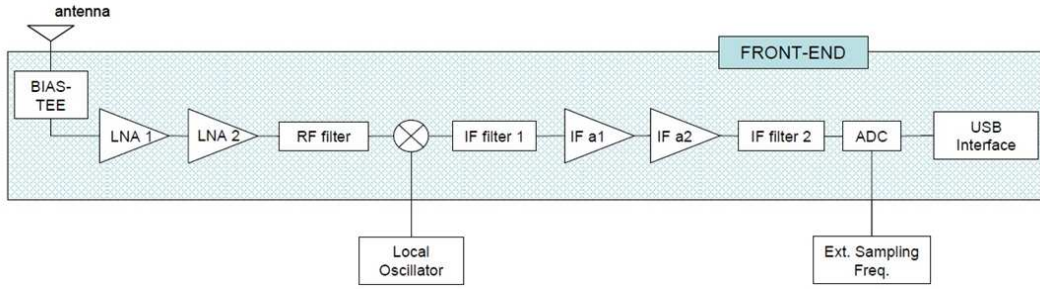


Figure 4.15: Front-End block scheme

Table 4.4: Front-End settings

Component	Value
RF filter	$f_0 = 1175.45 \text{ MHz} / BW = 40 \text{ MHz}$
IF filter 1	$f_0 = 225 \text{ MHz} / BW = 20 \text{ MHz}$
IF filter 2	$f_0 = 225 \text{ MHz} / BW = 18 \text{ MHz}$
Ext. Sampling frequency	$f_s = 36 \text{ MHz}$
ADC	8 bits

final filtering stage with an 18 MHz IF filter bandwidth produced the output signal for the ADC where the signal is sampled at 36 MHz and quantized over 8 bits. An USB interface integrated in the Front-End is in charge of transferring the quantized samples from the ADC to a user terminal where a data grabber software is installed. It has to be remarked that, no AGC is implemented in the considered device and the amplification stages within it have been designed such that the ADC saturation is avoided in presence of DME/TACAN interference. Moreover, all the amplification stages are realized with amplifiers which allow an input power level up to 10 dBm, thus avoiding any saturation effects within the receiver Front-End. More details on the components used for the Front-End design can be found in [75] and [76]. An example of collected data in presence of DME/TACAN interference at the hotspot location, is shown in Figure 4.16. Spectral characteristics of the single DME/TACAN pulsed signal are shown in the plot on top.

DME/TACAN pulses train reaching the GNSS antenna appear as a series of narrowband interferences, each with approximately 300 kHz bandwidth.

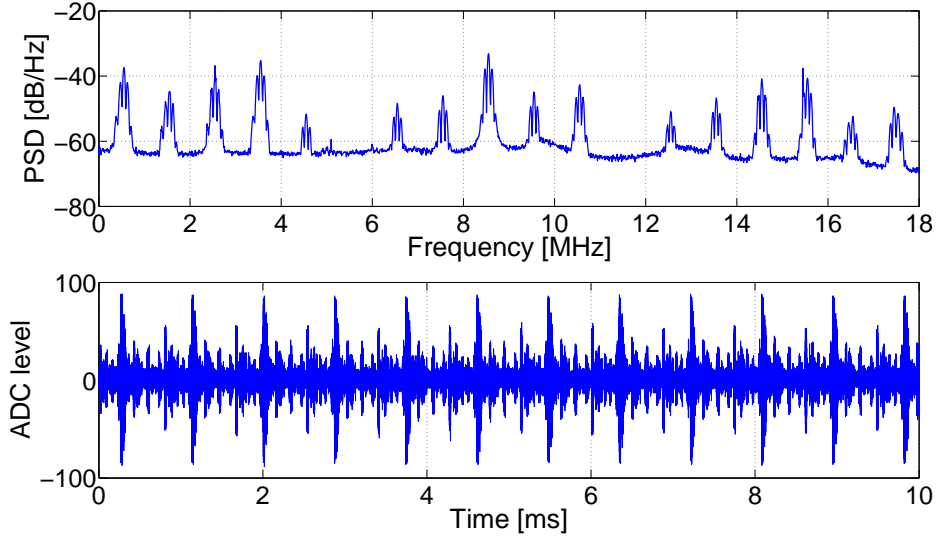


Figure 4.16: DME/TACAN scenario

The entire spectrum is jammed due to the fact that several ground beacons have been simulated broadcasting pulses on different carrier frequency within the Galileo E5a and GPS L5 frequency bands. The impact of different pulse blanking non-linear behaviours on GNSS receiver performance have been assessed exploiting a fully software receiver, N-Genie, capable of processing Galileo and GPS signals over all the GNSS frequency bands [77]. The employed software receiver is realized with a fast FFT based acquisition scheme parallel in the time domain and tracking loops based on 2^{nd} order loop filters.

Figure 4.17 shows the trend of the blanking duty cycle β with respect the blanking recovery time and for 3 different pulse detection time values which can be identified as ideal behaviour, slow pulse blanking (reaction time equal to $0.5\mu s$) and very slow pulse blanking (reaction time equal to $1\mu s$).

As expected, increasing the pulse blanking recovery time, larger percentage of incoming signal are suppressed. On the contrary, the introduction of a pulse detection delay would decrease the amount of signal to be suppressed.

Figure 4.18(a) and Figure 4.18(b) shows the acquisition metrics denoted as α_{mean} and α_{max} in presence of pulse blanking non-linear behaviours modelled

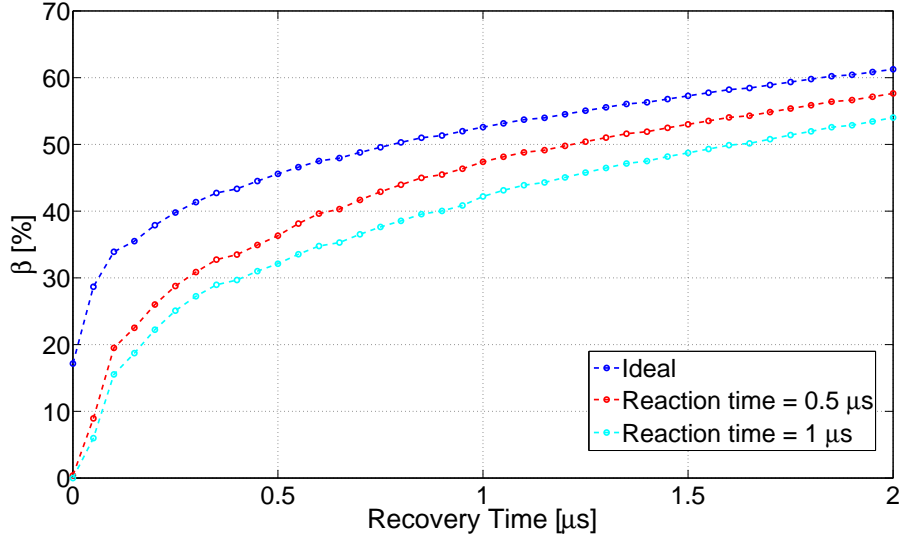


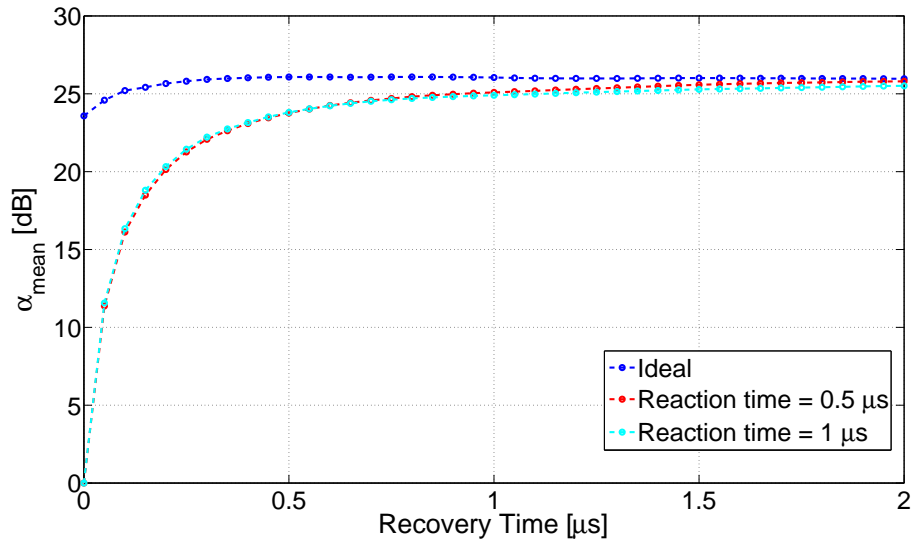
Figure 4.17: Blanker duty cycle β variation for different reaction and recovery time values

according different values of recovery and reaction time. Both acquisition metrics are defined respectively as follows:

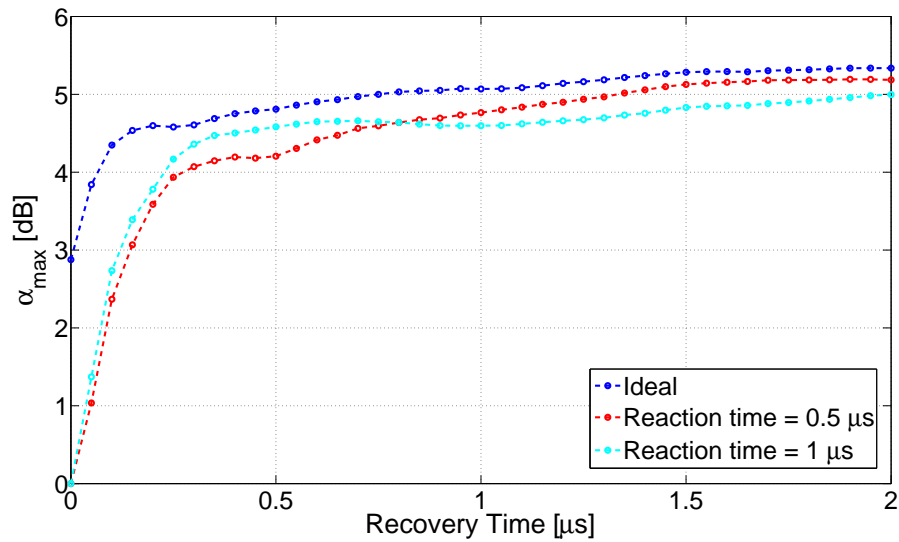
- $\alpha_{mean} = \frac{R_p}{M_c}$ is the ratio between the highest correlation peak and the correlation noise floor;
- $\alpha_{max} = \frac{R_p}{R_{2p}}$ is the ratio between the highest correlation peak and the second highest correlation peak;

Such values of α_{mean} and α_{max} have been obtained as outputs of the software receiver acquisition process of the Galileo E5a pilot channel (PRN 20) after manipulating the data set with a pulse blanking operation.

In both Figure 4.18(a) and Figure 4.18(b) it is possible to notice that the introduction of a non-zero delay in the pulse detection would seriously threaten the correct GNSS signal acquisition process. A pulse blanking reaction time equal to 0.5 or 1 μs would let the majority of the received pulsed interference going through the correlators thus increasing the noise in the acquisition search space, as confirmed from the trend of both acquisition metrics (red line and cyan line), thus masking the true correlation peak. However, when



(a)



(b)

Figure 4.18: N-GENE acquisition performance: (a) α_{mean} . (b) α_{max}

dealing with this type of pulsed interference, the presence of an increasing recovery time would surprisingly improve the receiver acquisition performance. In fact both α_{mean} and α_{max} increase with the increasing recovery time. This is due to the fact that, a delay in detecting the end of the pulse would allow the blanker to suppress also those interference samples in the pulse tail, thus achieving higher interference suppression. This result cannot be assumed

valid when dealing with non-modulated rectangular pulse made interference. In fact in this case, the presence of a recovery time would lead the blanker suppressing more GNSS useful signal samples, which in turns would lead to a higher degradation in the correlation peak of the search space.

In Chapter 6 the problem of the pulse blanking will be faced more in details, investigating the effects of its non-linear behaviour on the navigation data demodulation performance.

4.7 Conclusions

In this Chapter, the interference environment for the future GNSS based aviation services has been investigated. By means of several test campaign performed at the ESTEC navigation laboratory, it has been shown how this strong pulsed interference generated by the DME/TACAN ground stations may seriously threat the on-board GNSS receiver even if equipped with the traditional pulse blanking interference countermeasure. Pulse blanking can represent a simple as well as effective method for coping with not so dense in time pulse interference. However, in presence of harsh pulsed interference environment, as the DME/TACAN interference environment at the hotspot location, the pulse blanking is forced to suppress great portion of received signal thus leading to an enormous degradation and distortion of the GNSS useful signal. Furthermore, such a traditional countermeasure presents several drawbacks when dealing with DME/TACAN pulse interference; in fact, due to the interference Gaussian pulse shape and to the presence of the modulation, pulse blanking is not able to suppress all the samples belonging to the pulse, as demonstrated in Figure 4.4. Furthermore, pulse blanking design has to be carefully performed together with the front-end design. In fact, its performance may have a strong dependence with the reaction of some active components like amplifiers, within the receiver front-end, when merged

in a strong interference environment. For such a reason, new advanced signal processing techniques, which can be designed at receiver level, capable of extracting the interference components within the composite received signal, without distorting the useful GNSS signal, have to be investigated. In Chapter 5 two innovative interference detection and mitigation algorithms based respectively on the use of the WPD and of the use of the KLT will be presented.

Chapter 5

Transformed Domain Techniques for Interference Countermeasure in GNSS

This Chapter will introduce two innovative interference detection, characterization and suppression algorithms based on two advanced signal processing techniques: the [WPD](#) and the [KLT](#). For both methods, decomposition stages, detection algorithms and interference removal processes will be presented. The algorithms have theoretically designed and tested by simulation. Eventually, a set of experimental results will be presented in order to provide a validation of such innovative algorithms in suppressing interference components. Results will be focused on [GNSS](#) receiver performance at acquisition and tracking stage, after applying both methods to several interference scenarios. For this purpose, a fully software [GNSS](#) receiver will be employed. Furthermore, a comparison between such innovative techniques and the more traditional interference countermeasures in terms of interference suppression performance and computational complexity will be presented.

5.1 Introduction

The test campaign performed at the ESTEC radio-navigation laboratory, which has been presented in Chapter 4, has shown that in presence of a harsh pulsed interference environment, the pulse blanking circuitry may not be enough. GNSS receiver operation can be seriously threatened since extremely large portions of GNSS signal are suppressed together with the interference. In such a context the receiver itself loses the tracking of the weakest GNSS signals which in turns causes a worsening of the available satellites geometry thus increasing the error on the final user position.

For such a reason, innovative receiver based interference countermeasures, capable of identifying, isolating and suppressing interference components without distorting the GNSS received signal properties, need to be investigated. In the last years, researchers in the GNSS field have started investigating a new family of interference detection and suppression techniques based on the use of advanced signal processing techniques which allow the representation of the signal at the ADC output in a different domain, where information related to the interference can be better identified, isolated, processed or remove. Such a new family of algorithm is defined as Transformed Domain (TD) techniques, the block scheme of which is reported in Figure 5.1. First step of such algorithms is to provide a representation of the digitized signal in another domain; such a representation is achieved by processing the IF samples at the ADC output by means of a mathematical transformation. Once the signal is projected on the new domain, an interference detection algorithm is in charge of identifying the interference coefficients. The majority of the transformed domain techniques which have been investigated in literature rely on a detection algorithm based on a thresholding operation; basically each coefficients in the transformed domain is compared to a mask which represents the expected GNSS signal representation in absence of interference. However a different detection strategy based on the signal energy estimation will be

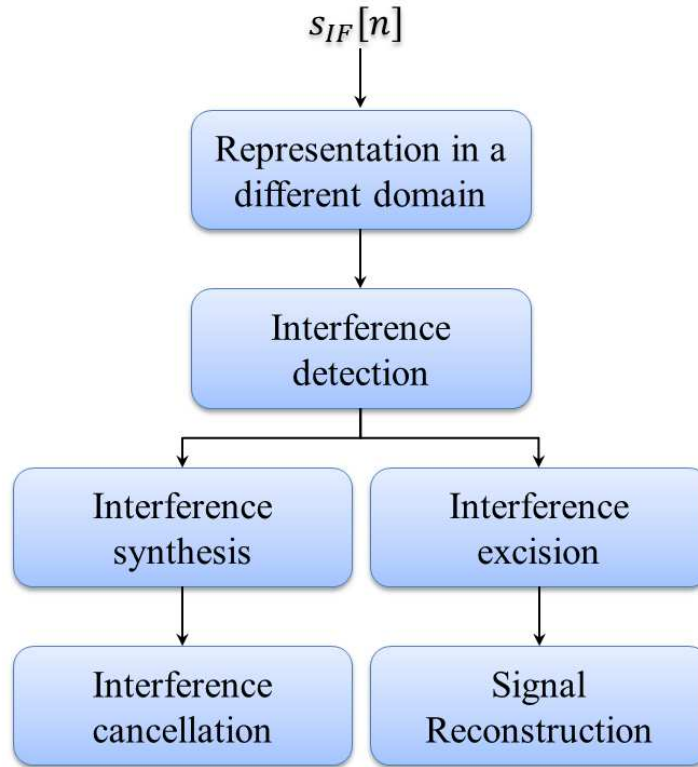


Figure 5.1: Typical TD technique block scheme

presented later on this Chapter. Finally, two interference suppression algorithms are foreseen: the former is based on a synthetic reconstruction of the interfering signal, by means of an anti-transformation process operated on the identified interference coefficients, which can be then subtracted from the composite received signal, whilst the latter is based on a direct suppression process of the interference coefficients in the transformed domain followed by an anti-transformation operation for the signal reconstruction.

First research activities investigating the capability of the TD based algorithms for interference suppression, were based on the observation of the received interfered signal in the Time Frequency (TF) domain. As an example, in [78] the authors propose two advanced signal processing techniques for achieving a high resolution TF representation of the received signal. The former is based on a simple discrete-time spectrogram, introduced first in [79],

obtained by means of a Short Time Fourier Transform (STFT) according to

$$S_p(n, f) = |STFT(n, f)|^2 \quad (5.1)$$

being the STFT defined as

$$STFT(n, f) = \sum_{i=n}^{n+L-1} s_a[i]h[i-n] \exp \{-j2\pi if\} \quad (5.2)$$

where $s_a[n] = s_{IF}[2n]$ is the down-sampled digitized signal, and $h[n]$ is the analysis window of length L . As mentioned in [78], the spectrogram has poor TF localization properties and its characteristics strictly depend on the analysis window. However, it requires a low computational load and it is suitable for real time application.

The latter TF representation is based on the use of the Wigner-Ville distribution which according to [80] is defined as

$$W_{x,x} = \sum_i s_a[i]s_a^*[n-i] \exp \{-j4\pi if\} \quad (5.3)$$

and differently from the spectrogram representation, it does not suffer from the time versus frequency resolution trade-off problem. However, higher computational load is required for its implementation with respect the spectrogram implementation. Concerning the interference frequency components detection in the TF plane, a statistical based method relying on the signal representation distribution on each point of the TF plane in absence of interference, is employed. Such a representation acts as a interference detection threshold, and it is defined according to a required false alarm probability, defined as

$$p_{fa}(\beta_d, n, f) = P(|TFR(n, f)| > \beta_d | H_0) \quad (5.4)$$

where β_d is the interference detection threshold, and $TFR(n, f)$ is the chosen Time-Frequency representation and H_0 is the null hypothesis (interference absent). Thus, knowing the TF representation distribution and inverting (5.4), it is possible to derive the interference detection threshold β_d . Another

activity concerning the interference detection and excision based on TF representation achieved by means of Spectrogram is presented in [81].

A recent work proposing chirp signal, linearly frequency modulated signal, detection and suppression by means of TF representation is presented in [82]. Here the authors propose a TF representation of the signal at the ADC output based on the use of the so called orthogonal-like Gabor expansion [83]. The detection process is based on a comparison of the achieved TF representation with the ideal TF representation of the GNSS signal in absence of interference. Once the interference coefficients in the TF plane is achieved, a synthetic reconstruction of the interfering signal is obtained and then subtracted to the composite received signal. More details of this TF based interference excision method can be found in [82] and [49]. In this Chapter, two innovative interference detection and suppression strategies based respectively on the use of the WPD and on the use of the KLT will be presented.

First attempts of developing an innovative interference mitigation algorithm based on the use of the wavelet transformation have been presented in [84] and [85], for pulsed interference mitigation. Here wavelet transform is employed to obtain the time-scale representation of the incoming interfered signal. In the GNSS framework, the wavelet transform has been already investigated for different purposes. As an example, in [86] a new trend extraction technique for multipath mitigation in carrier phase measurements domain using wavelet multi resolution analysis, is presented. A more detailed descriptions of this algorithm can be found in [87] [88] [89] and [90]. Multipath mitigation is not the only context where wavelet transform has been employed. For instance, in [91], a singularity detection technique for GPS cycle slips based on the wavelet decomposition is described. In [92] an empirical mode decomposition exploiting the wavelets' properties is described as a method to reduce the carrier phase measurements error. Finally in [93], methodology based on wavelet transform to evaluate the terrain and extract features along the vehicle path is presented. Of particular interest are those features which can be hazardous

to a following vehicles path.

Concerning the [KLT](#), its use for space application has been proposed first in [\[94\]](#). Here, [KLT](#) is employed as an instrument to detect very weak signals hidden in noise, in the framework of the Search for Extra Terrestrial Intelligence program. However, in [\[95\]](#) a first attempt of [CWI](#) detection based on the use of [KLT](#) is also presented.

In the following Sections of this Chapter interference mitigation algorithms based respectively on the [WPD](#) and [KLT](#) which are more advanced with respect those already presented in literature, will be discussed.

5.2 The Wavelet Transform

The set of orthogonal basis functions which are employed for the [STFT](#) decomposition have equal frequency bandwidths and represent a set of windows in time with equal duration. The use of the set of functions in [\(5.2\)](#) leads to a different resolution in the characterization of the frequency components of the signal. Many cycle of a high frequency signal can be captured within the duration $h(n)$, while this is not the case for a low frequency signal. For such a reason, the resolution of the [STFT](#) is poor at low frequency while it improves as the frequency increases [\[96\]](#).

In fact, the [STFT](#) can be seen as a band pass uniform filter bank where each filter frequency response has same bandwidth and different central frequency. Such a frequency resolution issue is solved by the wavelet transform. The wavelet transform of a signal provides a representation of the signal components in a different domain, similarly to a [STFT](#). In the wavelet transform, a set of functions which adjust their frequency-time behaviour according to the frequency components of the signal to characterize is employed. From such basis functions, a filters bank where the low-pass filters response have narrower bandwidths (so wider in the time domain) than the high-pass filters response, can be derived. The basis functions employed in the wavelet

transform belong to the set

$$h_k(t) = a^{-k/2}h(a^{-k}t), \quad (5.5)$$

which represent the filter responses. Equivalently in the frequency domain the transfer functions can be written as

$$H_k(j\Omega) = a^{k/2}H(ja^k\Omega) \quad (5.6)$$

where $a > 1$ and $k \in \mathbb{Z}$.

As seen in (5.5) and (5.6), all the responses are obtained by frequency-scaling operation of a prototype response $H(j\Omega)$, thus resulting in a non uniform filters bank. The scale factor $a^{-k/2}$ is introduced as a normalization factor in order to ensure constant energy independent from k , as well as the ratio between the bandwidth and the center-frequency Ω_k . Given an arbitrary input $x(t)$, the output of the filter $h_k(t)$ can be computed as

$$\int_{-\infty}^{\infty} x(t)h_k(\tau - t)dt = a^{-k/2} \int_{-\infty}^{\infty} x(t)h(a^{-k}(\tau - t))dt \quad (5.7)$$

Furthermore, since the filter bandwidth $H_k(j\Omega)$ is smaller for larger k , its output can be sampled at lower rate. Equivalently in the time domain, the width of $h_k(t)$ is larger, thus it is possible to move the window by a larger step size [96]. The continuous variable τ can be sampled at na^kT , where n is an integer, to obtain a Discrete Wavelet Transform (DWT). In this way, the step size for the windows movement is a^kT , and it increases as the center-frequency of the filter Ω_k decreases. Thus, the set of coefficients obtained according to

$$X_{DWT}(k,n) = a^{-k/2} \int_{-\infty}^{\infty} x(t)h(nT - a^{-k}t)dt = \int_{-\infty}^{\infty} x(t)h_k(na^kT - t)dt \quad (5.8)$$

represents the convolution between $x(t)$ and $h_k(t)$ evaluated at a discrete set of points na^kT , that is the convolution output is sampled at a^kT . Figure 5.2 shows the transfer functions of each branch of the non-uniform filters bank obtained by a dyadic scaling operation ($a = 2$) of the Meyer wavelet function

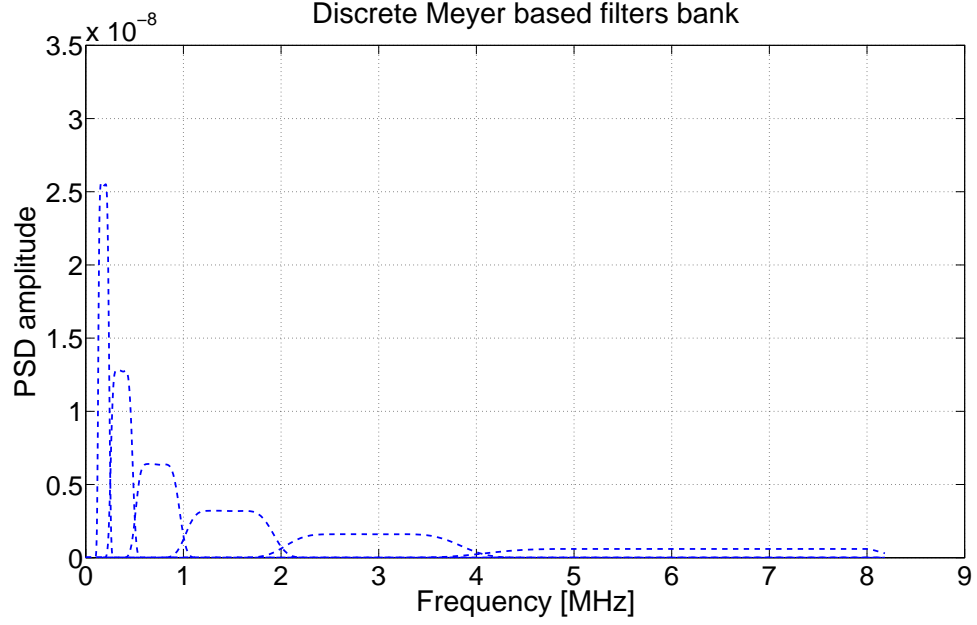


Figure 5.2: Meyer wavelet filters bank responses

[97]. The family of filters denoted as $h_k(t)$ represents the set of the analysis filter.

Perfect reconstruction of the signal $x(t)$ can be achieved choosing a proper synthesis filters bank. Given a set of wavelet coefficients $X_{DWT}(k,n)$, the inverse **DWT** can be achieved according to

$$x(t) = \sum_k \sum_n X_{DWT}(k,n) \psi_{kn}(t) \quad (5.9)$$

where $\psi_{kn}(t)$ is a set of basis functions obtained by dilation ($t \rightarrow a^{-k}t$) and shifting ($t \rightarrow t - na^kT$) of a prototype function $\psi(t)$, that is

$$\psi_{kn}(t) = a^{-k/2} \psi [a^{-k} (t - na^kT)] \quad (5.10)$$

In [96] it is shown that if $\{\psi_{kn}(t)\}$ is a set of orthonormal functions, that is

$$\int_{-\infty}^{+\infty} \psi_{kn}^*(t) \psi_{lm}(t) dt = \delta(k-l) \delta(n-m) \quad (5.11)$$

from (5.9) follows that

$$X_{DWT}(k,n) = \int_{-\infty}^{+\infty} x(t) \psi_{kn}^*(t) dt \quad (5.12)$$

thus leading to the following relationship between the analysis and synthesis filters

$$\psi_{kn}(t) = h_k^*(-t) \quad (5.13)$$

Thus the signal analysis/synthesis can be achieved by perfect reconstruction paraunitary Quadrature Mirror Filters (QMF) banks in which each filter has a response of the kind (5.13).

5.2.1 Discrete Time Wavelet Transform

The relation defined in 5.8 is the DWT since k and n are integer number, but it is not the discrete-time since t is continuous. In [96] it is shown that an orthonormal basis functions can be generated by discrete-time QMF bank under certain condition. As an example, let consider the case $a = 2$ known as dyadic wavelet decomposition, and further assume $T = 1$. Given a paraunitary pair frequency responses $H(z)$ and $G(z)$, the wavelet function $\psi(t)$ will satisfy the equation

$$\psi(t) = 2^{1/2} \sum_{n \in \mathbb{Z}} h[n] \phi(2t - n) \quad (5.14)$$

where $\phi(t)$ is the so call scaling function, which satisfy the scaling equation

$$\phi(t) = 2^{1/2} \sum_{n \in \mathbb{Z}} g[n] \phi(2t - n) \quad (5.15)$$

being $h[n]$ and $g[n]$, the wavelet vector and the scaling vector respectively, derived as the inverse Zeta-transform of $H(z)$ and $G(z)$. The scaling function $\phi(t)$ and the wavelet function $\psi(t)$, satisfying (5.14) and (5.15), under the assumption that $H(z)$ and $G(z)$ forms a paraunitary filters pair, are shift-orthogonal and span orthogonal subspaces V_i and W_i , where V_i is spanned by

$$\{2^{i/2} \phi(2^i t - n) \forall n \in \mathbb{Z}\} \quad (5.16)$$

while W_i is spanned by

$$\{2^{i/2} \psi(2^i t - n) \forall n \in \mathbb{Z}\} \quad (5.17)$$

From the orthogonality properties of the subspaces spanned by the wavelet and scaling function, the wavelet and scaling vectors must be individually shift-orthogonal and orthogonal to each other

$$\begin{aligned} \sum_{n \in \mathbb{Z}} h[2m+n]h[2l+n] &= \delta_{m,l} \\ \sum_{n \in \mathbb{Z}} g[2m+n]g[2l+n] &= \delta_{m,l} \\ \sum_{n \in \mathbb{Z}} h[2m+n]g[2l+n] &= 0 \quad \forall m,l \end{aligned} \quad (5.18)$$

$H(z)$ and $G(z)$ represent the pair QMF which will be employed for the discrete-time WPD. The equivalent expression for (5.6) in the digital domain is

$$H_k(e^{j\omega}) = H(e^{j2^k\omega}) \rightarrow H_k(z) = H(z^{2^k}) \quad (5.19)$$

where k is a non negative integer. In [96] it is shown that $H_k(z)$ is a multi-band (rather than pass-band) filter, thus in order to obtain pass-band filters, a low pass filter $G(z)$ is employed. Thus, according to a dyadic scaling operation, the non-uniform filters bank responses are obtained as follow

$$H(z), G(z)H(z^2), G(z)G(z^2)H(z^4) \dots \quad (5.20)$$

5.3 The Wavelet Based Interference Suppression Algorithm

The proposed wavelet based mitigation algorithm is completely based on the WPD, where the discrete-time signal is passed through a uniform wavelet based filter bank, as shown in Figure 5.3.

In the WPD, the scaling and shifting process is also iterated at higher frequencies, thus resulting in an uniform filter bank, the output of which is providing a set of coefficients (scales) representing a determined frequency portion of the incoming decomposed signal. Each stage of the uniform filters bank is composed by a filtering process through $H(z)$ and $G(z)$, respectively the wavelet

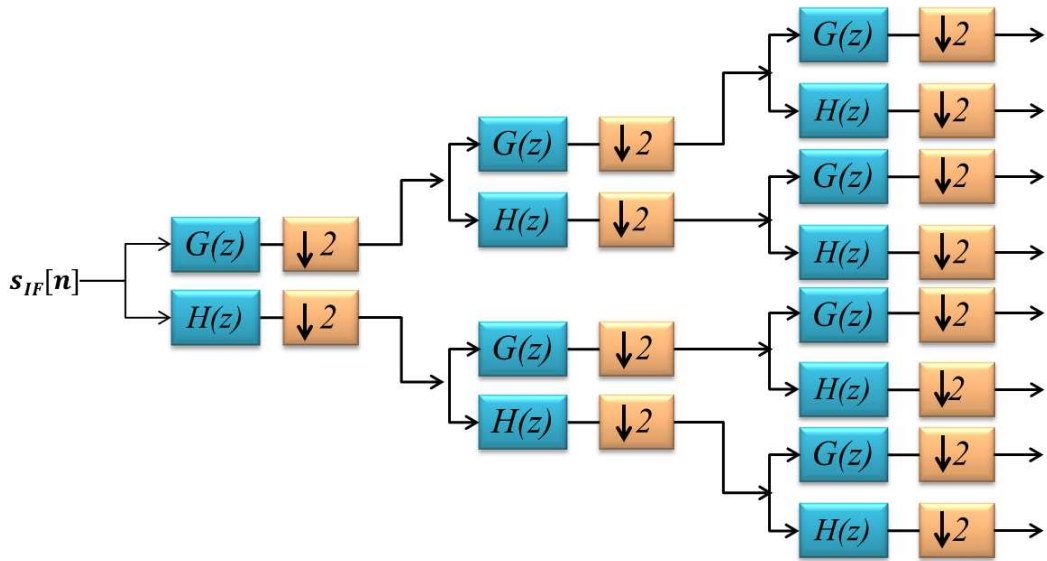


Figure 5.3: Wavelet Packet Decomposition

vector and the scaling vector individually shift orthogonal and orthogonal to each other, which produce a decomposition of the signal in high frequency component and low frequency component, followed by a down-sampling operation. The algorithm for interference detection and suppression is mainly based on three steps:

- the **Decomposition** phase where the incoming GNSS interfered signal is passed through the uniform filter bank thus achieving the so call time-scale representation. The number of wavelet stages to apply for the signal decomposition is a free parameter. In the following of this work, the optimal number of wavelet decomposition stages will be assessed with respect the interference spectral characteristics and with respect the GNSS receiver performance at both acquisition and tracking level.

An examples of time-scale representation of the signal at the ADC output is shown in Figure 5.5, where 5 stages of WPD have been employed on the IF samples of the pulsed interfered data-set shown in Figure 5.4.

Meyer [97] wavelets have been considered in order to derive all the filter frequency responses employed in the uniform filter bank. After 5 stages

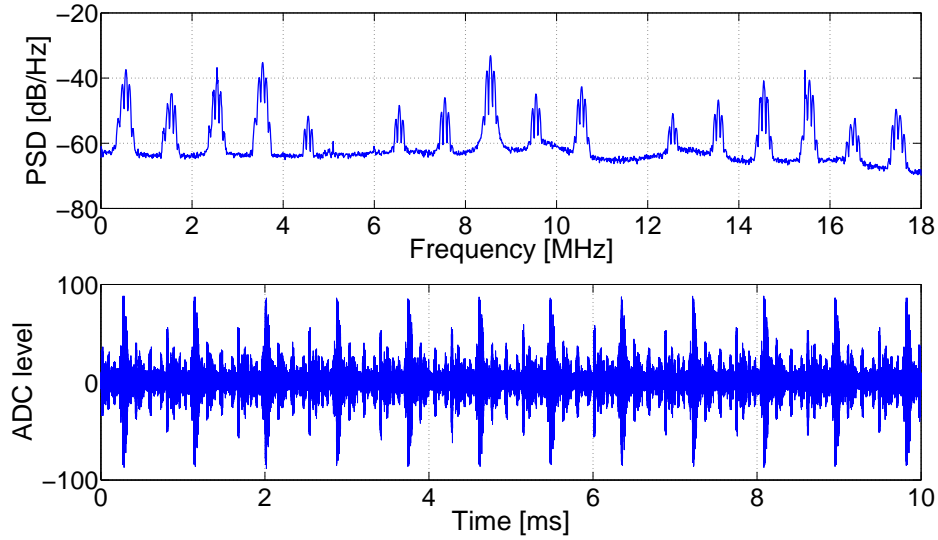


Figure 5.4: DME/TACAN scenario

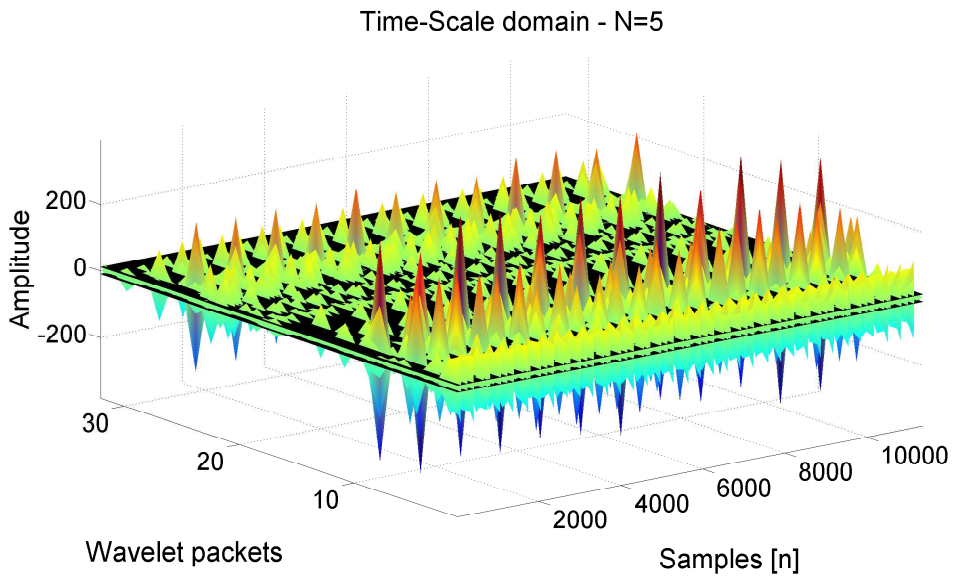


Figure 5.5: Time-scale representation

of WPD, 32 scales are obtained, each of which represents a determined frequencies region of the interfered received Galileo E5a signal. As it is shown in Figure 5.5, the total DME/TACAN signal reaching the user antenna has components spread all over the time-scale domain.

- the **Detection-Mitigation** phase is performed in each scales obtained at the output of the filters bank. The interference excision is performed

applying a blanking operation on the time-series of the coefficients. Such a process is based on the suppression of those coefficients in each scale crossing a determined blanking threshold level. An example of this operation is reported in Figure 5.6 where the set of coefficients obtained at the output of a generic branch of the WPD filters bank, are shown before (blue line) and after (red line) the blanking suppression.

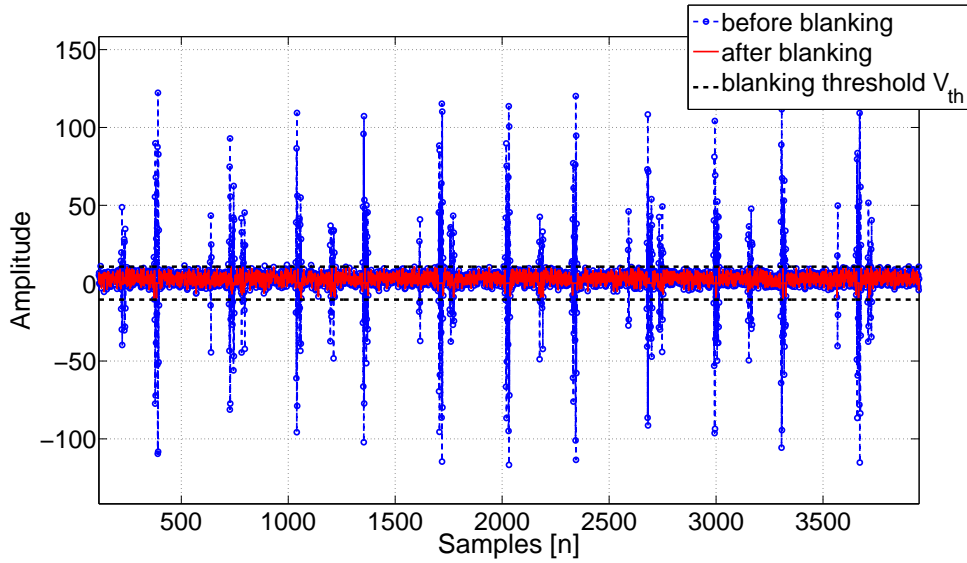


Figure 5.6: Pulse blanking applied on the single scale

For such a reason, a criteria for the blanking threshold determination is needed. The adopted criteria is mainly based on a statistical characterization of the GNSS received signal at the ADC output. It is well known that, GNSS signal is completely buried in the noise at the user antenna level. In Nyquist condition, the filtered digitized noise can be considered still uncorrelated thus it is allowed to assume that at the ADC output, the samples in an interference-free environment are still Gaussian distributed with zero mean and variance σ^2 . The digitized signal is then processed by the WPD filters bank, made by filters response which are orthonormal to each other. Thus, the samples at the output of each branch of the filter banks in absence of interference can be assumed still Gaussian distributed with zero mean and variance σ^2 . This conclusion

is confirmed by Figure 5.7 where the mean and the standard deviation of the wavelet packets obtained at the filters bank output. In this case, the 5 stages WPD are applied on a simulated Galileo E5a-Q signal in absence of interference and in presence of a flat ideal front-end. The

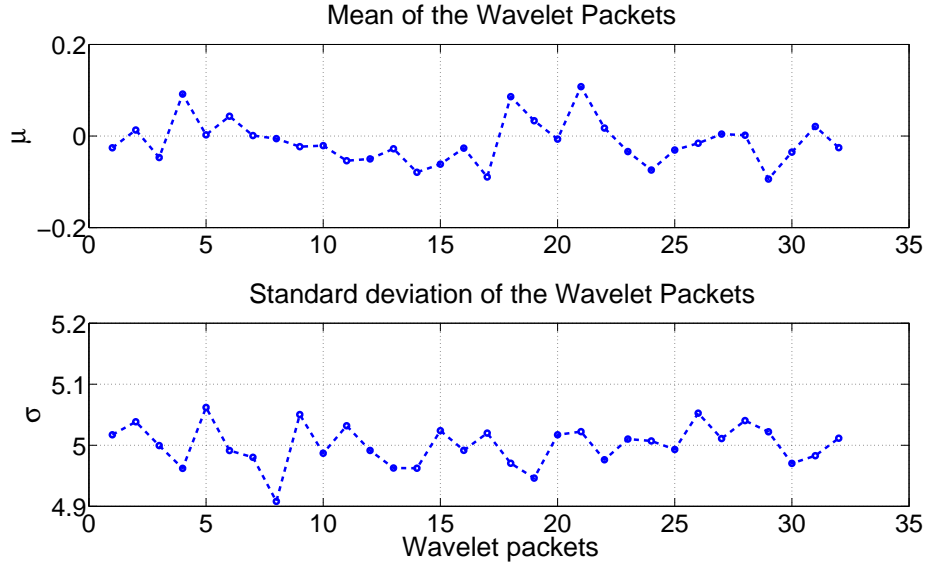


Figure 5.7: Wavelet Packets statistical analysis

statistics for the 32 scales are quite similar with a variation among the scales of less than 10%. The introduction of a realistic front-end filtering operation would change the statistics only of those wavelet packets representing the frequency regions outside the filter cut-off frequencies. Thus a front-end bandwidth with a quasi-flat frequency response at the GNSS frequency band is preferred in order to assume a single blanking threshold to be applied to the overall time-scale plane.

Denoting the false alarm probability p_{fa} as the probability of the event that in absence of interference, a generic sample at the ADC output crosses the blanking threshold V_{th} , it follows that

$$p_{fa} = 2 \cdot \int_{V_{th}}^{\infty} \frac{1}{\sigma\sqrt{2\pi}} e^{-\frac{x^2}{2\sigma^2}} \quad (5.21)$$

Thus for a required false alarm probability p_{fa} , inverting (5.21) it follows

$$V_{th} = \sigma\sqrt{2} \cdot \text{erfc}^{-1}(p_{fa}) \quad (5.22)$$

The black floor in Figure 5.5 represents the blanking threshold applied for the interference component detection within each wavelet scale, and computed according to a false alarm probability p_{fa} of 10^{-3} . Each coefficients in the time-scale floor exceeding the blanking threshold are suppressed, as it is shown in Figure 5.8. Such modified scales will be

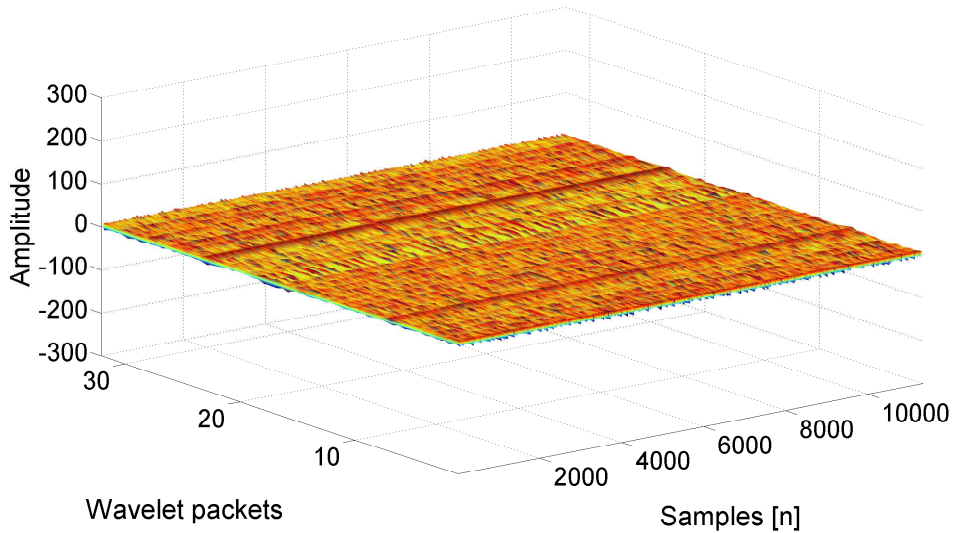


Figure 5.8: Time-scale after interference excision

fed to a wavelet based anti-transformation block which is in charge of the signal reconstruction.

- the **Reconstruction** phase is achieved through an inverse wavelet transform starting from those scales modified after the interference coefficients suppression. Figure 5.9 provides a comparison between the time-spectral characteristics of the signal before and after the interference suppression through the WPD algorithm. Practically the signal reconstruction is achieved through a uniform filter bank matched with the uniform filter bank employed for the signal decomposition depicted in Figure 5.3, as mentioned in [96]. Benefits of this algorithm can be observed looking at the spectrum achieved after the mitigation (see Figure 5.9). DME/TACAN signals coming from the different ground stations

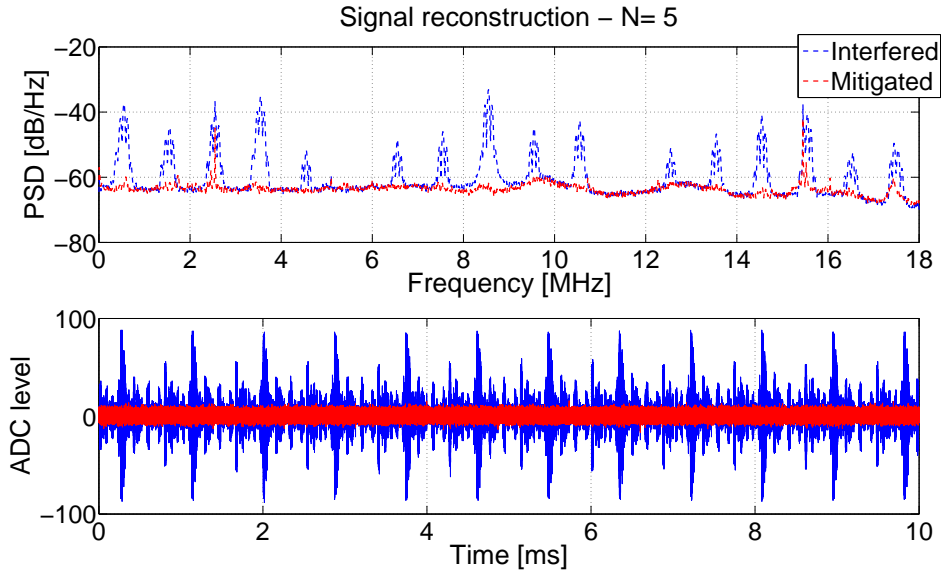


Figure 5.9: Signal comparison: Before and after mitigation

are highly suppressed. Furthermore, unlike a common interference mitigation technique performed in the time domain, as the pulse blanking, where useful signal components are suppressed together with interference, the majority of the useful GNSS signal power is saved, as confirmed by the absence of drops in the spectrum. The main advantages of this algorithm with respect the Gabor expansion based algorithm is that, no signal storage for the signal decomposition as well as no synchronization operation at signal reconstruction are needed.

5.4 The Karhunen-Loève Transform

The KLT provides a decomposition of the signal in a vectorial space using orthonormal functions which can have in principle any shape, differently from the other transforms, as for instance in the Fourier transform where the basis functions are sinusoidal functions. The KLT decomposition of a general time dependent function is given by

$$x(t) = \sum_{n=1}^{\infty} Z_n \phi_n(t) \quad (5.23)$$

where Z_n are scalar random variables that are statistically independent and $\phi_n(t)$ are the basis functions, derived from the covariance matrix of the stochastic process $x(t)$. The **KLT** offers the better separation between the deterministic components within the received signal and the stochastic ones. What will be shown in the next sections is that in several interfered scenarios the useful **GNSS** signal is hidden in the noise while the interference is identified by the **KLT** as the only deterministic component in the received signal. Differently from the basis functions which represent the behaviour in time of the signal to be decomposed, the random variables Z_n are obtained projecting the given stochastic process $x(t)$ over the corresponding eigenvector $\phi_n(t)$, that is

$$Z_n = \int_{-\infty}^{+\infty} x(t)\phi_n(t)dt \quad (5.24)$$

In [95] it is stated that the KL expansion is the only possible statistical expansion in which all the expansion terms are uncorrelated from each other. The nature of the **KLT** is independent of the specific kind of interfering signal, thus making the **KLT** capable to successfully detect not only **CWI**, but also **NBI**, **WBI** and chirp interference.

5.4.1 **KLT interference detection and suppression algorithm**

The **KLT** decomposition has been implemented according to the following steps:

- computation of the Toeplitz matrix of the autocorrelation of the interfered signal;
- Eigenvalues and eigenfunctions determination of the Toeplitz Matrix;
- Z_n coefficients determination according to (5.24)

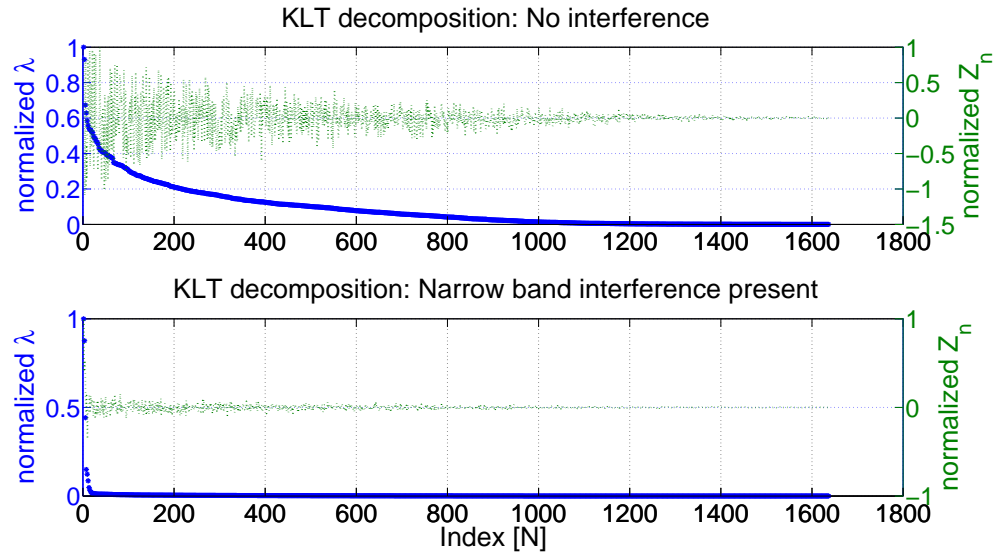


Figure 5.10: KLT decomposition comparison between interference case and interference free case

Figure 5.10 shows the capability of the **KLT** of separating the deterministic components within the signal to decompose, from the stochastic one. Here the **KLT** decomposition has been achieved solving the eigenvalues problem for the Toeplitz matrix of the autocorrelation function of $100 \mu\text{s}$ of **GPS C/A** code signal in two cases:

- interference-free environment
- interfered with a **NBI** signal (10 kHz) centered on the intermediate frequency with a power equal to -120 dBW

The **GPS C/A** code signal has been simulated by means of a fully software **GNSS** signal generator N-Fuels [98]. Figure 5.10 reports the trend of the normalized eigenvalues λ and the Z_n coefficients obtained from the **KLT** decomposition.

It is possible to notice that, the distribution of the eigenvalues suggests a method for detecting interference. In fact, when the interference is present there is a small number of eigenvalues which have a great magnitude with respect the others (bottom plot), differently from the case of interference-free

environment (top plot). The proposed interference detection and excision based on the eigenvalues magnitude observation and preliminary results have been discussed in [3]. Basically, the highest magnitude eigenvalues, which represent the interference components, are detected and an inverse **KLT** is applied considering only the eigenfunctions representative of the noise in which the **GNSS** component is embedded. In order to define a threshold value based on analytical justifications the statistical distribution of the Z_n coefficients for a signal in a interference-free environment should be studied. In [94] it is stated that the distribution of the **KLT** coefficients for a unitary stationary white noise is Gaussian. However, this is not our case, because even if the **GNSS** signal is completely buried in the noise, some deterministic components due to the **GNSS** code are contained in it. Furthermore it would be desirable to have a method that is independent of the interference features. Thus, an energy based detection algorithm has been developed, analysed and proposed in [5].

In case of interfered signal, after the **KLT** decomposition, eigenfunctions are excluded such that the energy of the reconstructed signal is comparable with the energy that the **GNSS** received signal would have in an interference-free environment. This thresholding rule can be better understood looking at Figure 5.11.

The blue dots in the figure represent the energy of the interfered signal with respect to the index n when the largest magnitude **KLT** coefficients Z_i for $0 \leq i \leq n$ are removed in the reconstruction stage. The threshold on the number of functions to be excluded is obtained as the intersection of the blue curve with the red line which represents the expected energy for a signal in an interference-free environment.

However, such a detection method may suffers in presence of an **AGC** followed by a quantization stage over few bits, since the incoming interfered signal would be compressed by the **AGC** gain thus leading to energy of the interfered signal being not extremely far from the energy of the signal in an

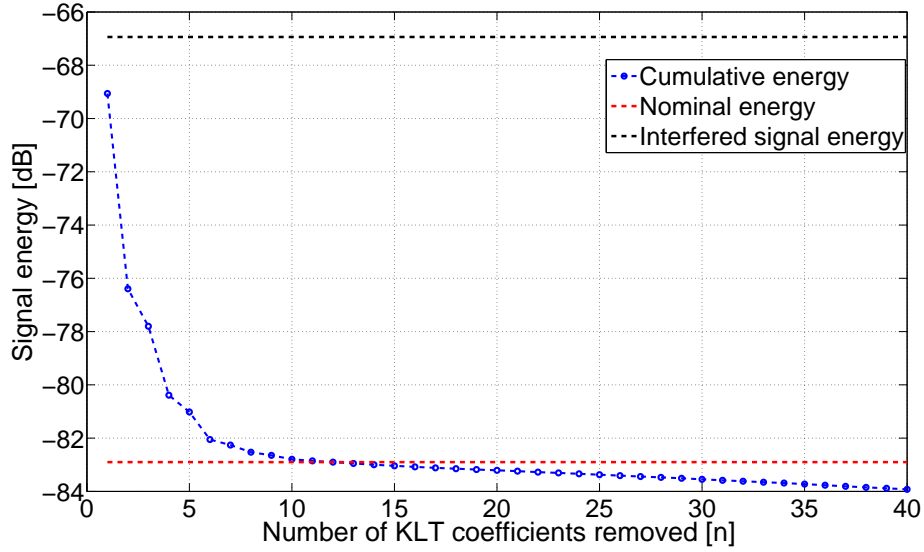


Figure 5.11: GNSS signal energy decay vs. KLT coefficients removed

interference-free environment. For such a reason, this technique, as well as the WPD based technique, are more suited for those receiver architecture featuring quantization over a large number of bits, where the received GNSS signal in absence of interference is mapped exploiting a limited number of bits, leaving the highest bits free for interference detection.

The KLT based method offers good performance in extracting the interference information from the received signal, but the computational burden of its implementation is quite heavy since an eigenvalues problem has to be solved. KLT based decomposition and signal reconstruction have been implemented on the pulsed interfered data shown in Figure 5.4. Since the software implementation of these steps requires great computational capabilities, the KLT decomposition has been performed on small slices, the duration of which is about $16 \mu\text{s}$. Figure 5.12 shows the KLT coefficients trend (blue curve) and the total energy of the reconstructed signal when the highest magnitude KLT coefficients up to N are not considered for the reconstruction (green curve). As it has been mentioned, the criterion used for the determination of the number of Z_n coefficients to exclude is based on the signal energy analysis. The intersection point between the green curve, which represents the energy of the

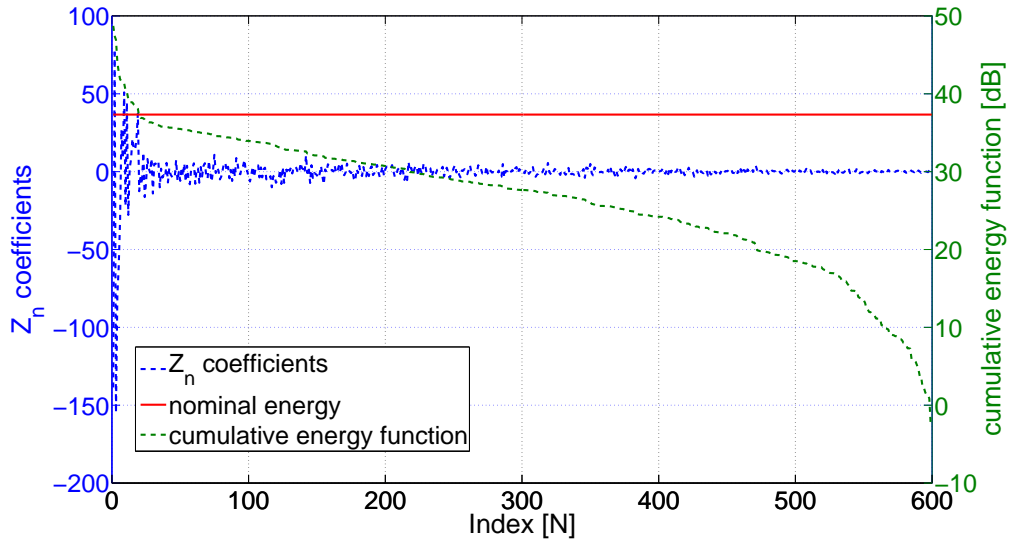


Figure 5.12: KLT decomposition and signal energy

reconstructed signal when excluding the first N highest Z_n coefficients, and the ideal GNSS signal energy threshold in an interference-free environment (red line) provides the number of highest Z_n coefficients to be suppressed. Following this criterion, the number of KLT coefficients excluded is such that the reconstructed signal energy is about the ideal energy of the signal in an interference-free environment. Operating according to this criterion, the first 20 eigenvalues are excluded from the signal reconstruction. Figure 5.13 shows a comparison of the PSD of the received signal before (blue line) and after (red line) the KLT based pulsed interference excision. From this result it can be observed that also the KLT based method, as the WPD based algorithm, offers high performing capabilities in detecting, isolating and suppressing the dominant deterministic components, which are usually related to the interfering signal, contained in the received signal, without causing large distortion of the useful GNSS signal.

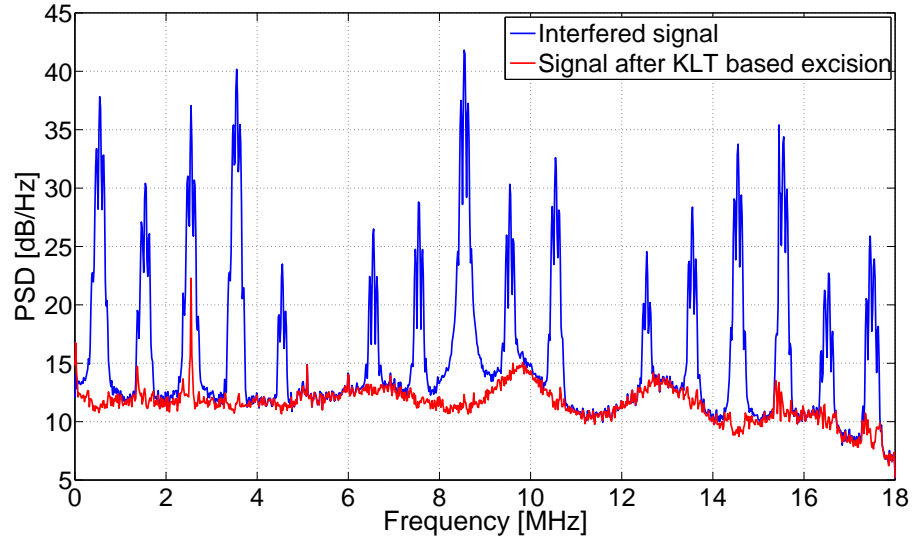


Figure 5.13: Power Spectral density comparison: before and after KLT based interference suppression

5.5 Experimental Results

WPD and **KLT** based algorithm steps for interference suppression have been presented. The meaning of the representation of the signal in a new domain has been discussed, as well as their interference detection criteria and interference components suppression techniques. In order to assess the interference suppression capabilities of both advanced methods and their advantages with respect the use of a traditional pulse blanking operation, a fully software receiver, N-Genie has been exploited and its performance at both acquisition and tracking level have been observed.

5.5.1 Acquisition performance

Figure 5.14 shows the acquisition search spaces of the Galileo E5a pilot channel (PRN 20) obtained in different scenarios. In particular, Figure 5.14(a) the acquisition performance of the N-gene software receiver when no interference countermeasure is adopted, is shown. In this scenario, correct acquisition of

Doppler frequency and code delay can be achieved when using 1 ms of coherent integration time combined with 80 non-coherent accumulations. Acquisition performance improves when a simple pulse blanking operation is adopted as pulsed interference countermeasure. In this case, the best combination of reaction and recovery time, identified in the sensitivity analysis performed in Section 4.6 of Chapter 4, has been considered for the pulse blanking software implementation, and correct acquisition of the true correlation peak is achieved after 10 non-coherent accumulations, as shown in Figure 5.14(b). However, when using the WPD or the KLT based algorithm for pulsed interference suppression, N-gene acquisition performance improves considerably, as can be observed respectively in Figure 5.14(c) and 5.14(d). In both cases, the correlation peak clearly emerges from the noise floor and crosses the acquisition threshold after 10 non-coherent accumulations. N-gene acquisition

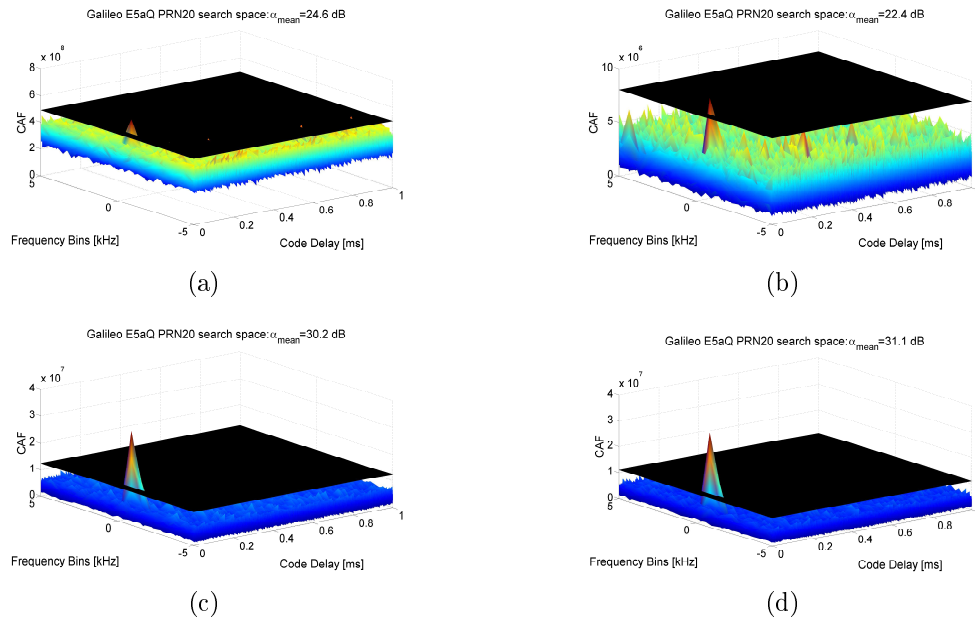


Figure 5.14: Acquisition search space: (a) No countermeasures. (b) After pulse blanking. (c) After WPD based method. (d) After KLT based method

performance is summarized in Table 5.1 which is reporting the acquisition metrics α_{mean} , already defined in Section 4.6, in all the four cases depicted in Figure 5.14. It can be clearly observed how such advanced signal processing

Table 5.1: Acquisition performance comparison

Scenario	Non coherent accumulations K	α_{mean} [dB]
Interference free	10	32
DME/TACAN Interfered	80	24.6
After Pulse blanking mitigation	10	22.4
After WPD based mitigation	10	30.2
After KLT based mitigation	10	31.1

algorithms provides higher pulsed interference suppression resulting in acquisition spaces where the separation between the correlation peak and the noise floor is higher with respect the case related to the use of a simple blanking operation.

5.5.2 Tracking performance

Concerning the tracking stage, estimated C/N_0 , early-prompt-late correlations and noise on the data demodulation are analysed for 10 seconds of Galileo E5a pilot channel (PRN 20) tracking and reported respectively in Figure 5.15, Figure 5.16 and Figure 5.17, for the four scenarios considered for the acquisition performance analysis.

Concerning the estimated C/N_0 , it is possible to observe that, such advanced signal processing techniques provide almost a complete interference components suppression with negligible distortion of the useful GNSS signal components. In fact, when adopting the pulse blanking as interference countermeasure, the C/N_0 estimated by the software receiver is around 36.1 dB-Hz while, when adopting both transformed domain techniques, about 4 dB of gain can be observed. Same conclusion can be drawn also looking at Figure 5.16 and Figure 5.17 where Early-Prompt-Late correlators are respectively in absence of interference countermeasure, after the application of a simple pulse

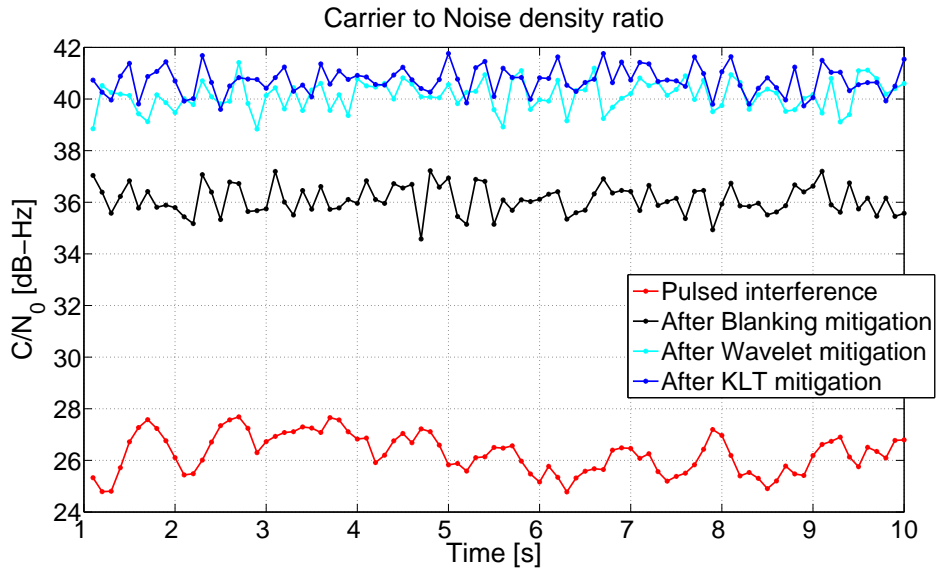


Figure 5.15: Carrier to Noise density ratio comparison

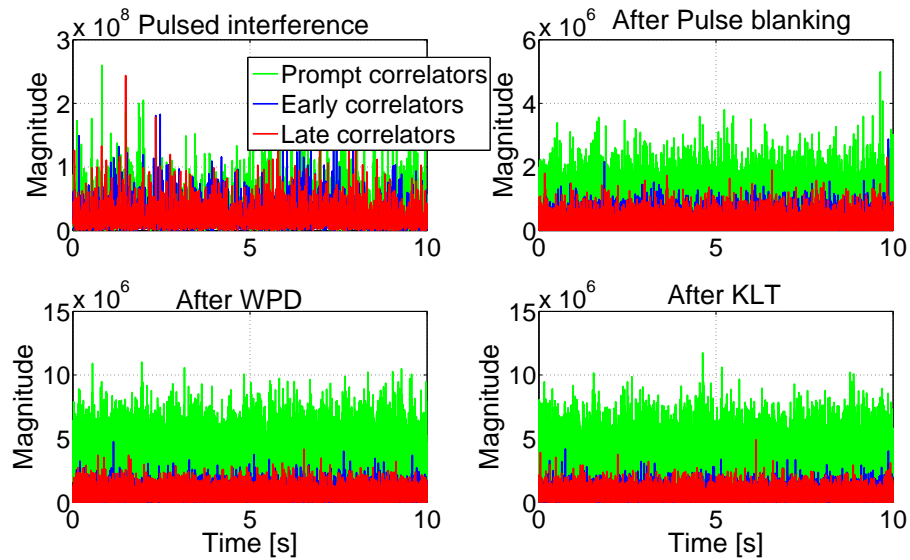


Figure 5.16: Early-Prompt-Late correlators

blanking operation, after the [WPD](#) interference mitigation algorithm and after the [KLT](#) based interference mitigation algorithm. In particular Prompt correlations amplitude distance from the early and late correlations is higher in case of [WPD](#) and [KLT](#) implementation than the pulse blanking case implementation, as it can be seen in [Figure 5.16](#). Furthermore, in [Figure 5.17](#) the I-Q floor is noisier in the case of pulse blanking implementation rather than the case of [WPD](#) and [KLT](#) based method for interference suppression. These

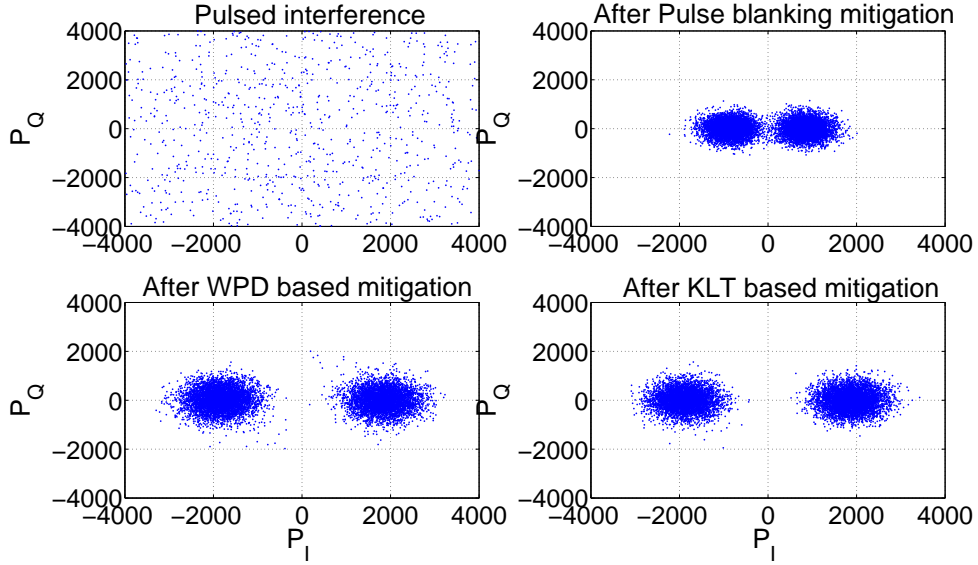


Figure 5.17: Modulation

Table 5.2: Acquisition performance

Scenario	C/N_0 [dB-Hz]	σ_{DLL} [cm]
DME/TACAN Interfered	26.6	-
After pulse blanking mitigation	36.1	76.5
After WPD based mitigation	40.1	72.6
After KLT based mitigation	40.6	73

results have been obtained setting a predetection integration time T equal to 1 ms and choosing loops bandwidth equal to 2 and 15 Hz respectively for the [DLL](#) and [PLL](#).

A summary of the software receiver tracking performance is provided in [Table 5.2](#), where average estimated C/N_0 and [DLL](#) jitter during the tracking operations are shown.

5.6 WPD based method: parameters tuning

This Section is devoted to the performance analysis of the [WPD](#) based algorithm in mitigating [NBI](#). The analysis addresses the problem of finding

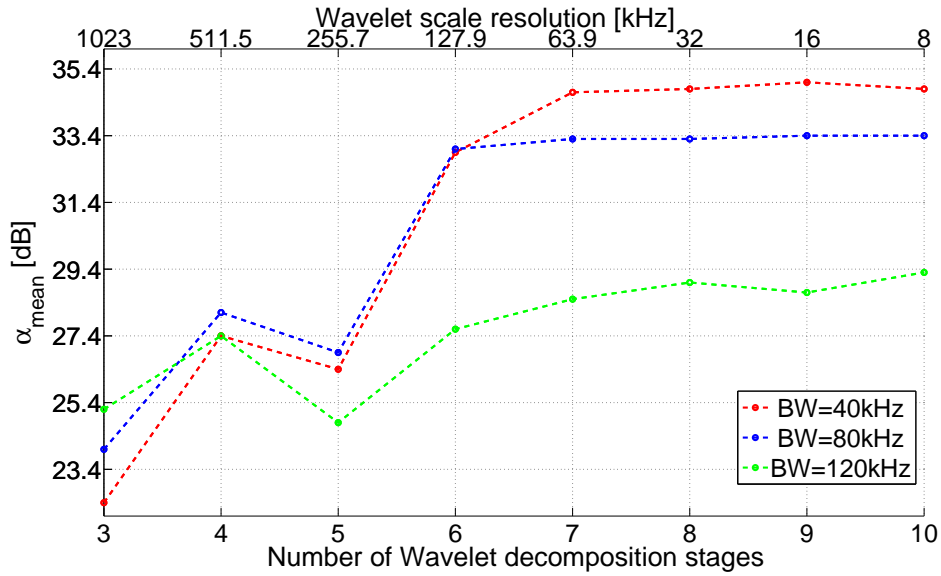


Figure 5.18: Acquisition metric versus WPD depth

the best trade-off between the choice of the wavelet based mitigation technique parameters such as number of wavelet decomposition stages N and its computational burden. Such trade-off analysis will be correlated with the **NBI** spectral characteristics showing how wavelet can be used as interference detection method.

Several **NBI** scenarios have been considered, and a parametric study with respect to the interference bandwidth B_{int} , interference carrier frequency f_{int} , and number of wavelet decomposition stages N has been performed.

5.6.1 The wavelet decomposition depth N

This first analysis has been devoted to the study of the impact of the number of wavelet decomposition stages with respect to the **NBI** suppression performance. Three different interference scenario have been considered, combining **GPS** L1 **C/A** code signals with **NBI** 200 kHz far from the intermediate frequency, and results are shown in Figure 5.18. Here the trend of the acquisition metric α_{mean} achieved versus the number of wavelet decomposition stages, is

shown. Acquisition performance are achieved using 1 ms of coherent integration time, and 20 non-coherent accumulations. The three lines are referred to three different interference scenarios characterized by the presence of **NBI** with respectively 40, 80 and 120 kHz of bandwidth. Increasing the number of **WPD** stages, increases the wavelet scale resolution and thus its frequency selectivity. In all the three interference scenarios, increasing N provides better performance in capturing and isolating the **NBI** components which in turn means better interference suppression without removing useful signal components, as shown from the increasing trend of α_{mean} . However, a saturation effect can be observed for higher value of N (greater than 7). In such a region, acquisition performance are not any-more improving since wavelet scale resolution is already comparable or narrower with respect the interference bandwidth. Moreover, as expected, performance of such a technique are limited by interference bandwidth. At higher interference bandwidth, lower acquisition metric values are achieved.

5.6.2 Wavelet families comparison

So far, the time-scale representation of the signal at the **ADC** output has been achieved through an iterative filtering process exploiting filter response derived by the Meyer wavelet family. Several other wavelet function exist, and most of them are discussed in [99]. Further analysis have been focused on the use of a different wavelet function in order to generate the filters response exploited for the **WPD**. In particular, a different wavelet function, derived from an orthogonalization process of a Gaussian function, has been adopted: the so called modified Gaussian function, which is fully described in [99] [100].

Figure 5.19 shows the wavelet filters bank obtained from the Gaussian wavelet function. It can be observed that, such gaussian wavelet filters are characterized by a more frequency selective response and higher orthogonality between the filters bank shown in Figure 5.2.

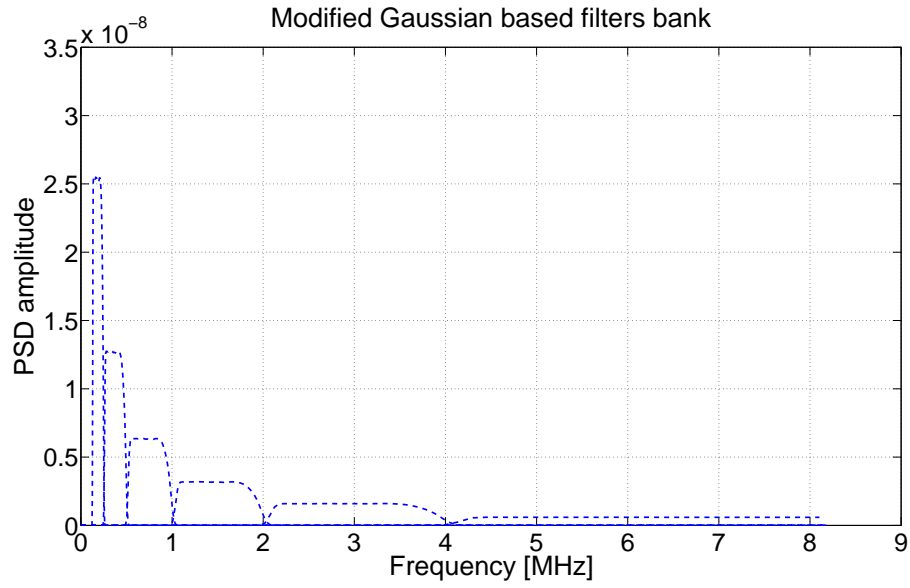


Figure 5.19: Modified Gaussian wavelet filter bank response

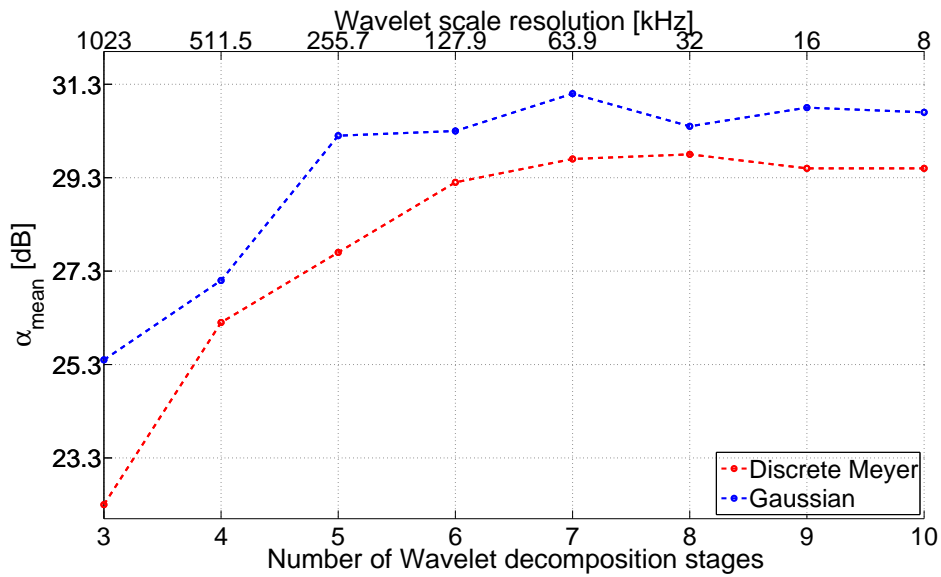


Figure 5.20: Acquisition metric: Gaussian vs Meyer wavelet

Figure 5.20 shows the acquisition metrics α_{mean} with respect the number of wavelet decomposition stages when mitigating a **NBI** on a carrier frequency 200 kHz far from the intermediate frequency and with a bandwidth of 120 kHz. The blue lines are related to the time-scale decomposition achieved exploiting modified Gaussian wavelet function, while the red one refers to the **WPD** exploiting Meyer wavelet function. It can be clearly observed that a

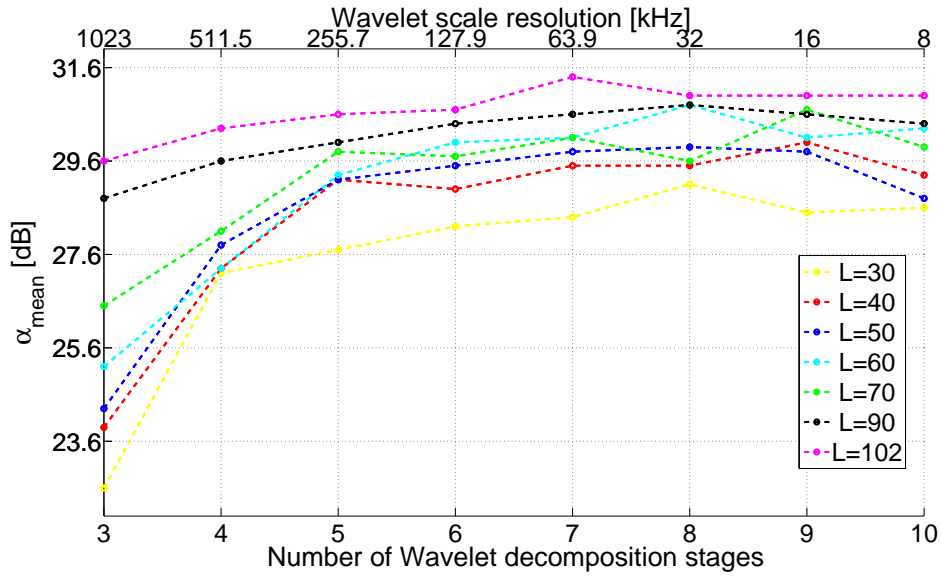


Figure 5.21: Acquisition metric: Gaussian wavelet based filter length

gain of 1.5 dB is achieved when using the modified Gaussian wavelet function.

5.6.3 Wavelet filter length

Final investigation has been performed in order to analyse the impact of the filter length on the interference suppression. Same NBI scenario has been considered, the modified Gaussian wavelet functions have been adopted for the WPD, and results are shown in Figure 5.21. It can be observed that, increasing the number of filter coefficients, acquisition performance improves. This is due to the fact that increasing the wavelet filter length, wavelet function side-lobe are lowered thus resulting in a higher orthogonality between the filters response in the frequency domain.

5.6.4 Computational complexity

Although Wavelet based mitigation algorithm provides high capability in interference components suppression, its implementation is characterized by a not negligible complexity. Computational burden is mainly determined by

the number of wavelet decomposition stages N which determines the number of filtering operation according to the exponential law 2^N . Furthermore, the same number of filtering operation is employed for signal reconstruction purposes. All filtering operation are realized with FIR filters with length L . Each output sample is obtained with L products and 1 single sum, thus the total number of performed operations for decomposition and reconstruction of n samples of incoming signal is

$$O(n,N,L) = 2 \cdot 2^N \times (nL + n) \quad (5.25)$$

However the filter bank implementation allows for the processing sample by sample of the incoming signal, at the price of the delay of the decomposition stage and by the reconstruction filter bank operating on the thresholded samples. Furthermore this, the wavelet based algorithm can represent an efficient post processing technique for interference detection and characterization.

5.7 Conclusions

Based on different principles, the WPD and the KLT based algorithm showed to be two extremely high performance algorithm for interference detection and suppression. In both cases, representation of the incoming interfered received GNSS signal in a different domain where interference components can be extracted and separated with a negligible distortion on the GNSS useful signal, as demonstrated looking at the achieved receiver performance at both acquisition and tracking stage. However, the total computational burden required for their implementation is obviously higher than the complexity foreseen for a simple pulse blanking implementation or notch filtering design. As it has been already mentioned, concerning the WPD, complexity is mainly determined by the number of wavelet decomposition stages N which determines the number of filtering operation according to the exponential law 2^N . Anyway, the presence of smarter algorithms in literature which provide WPD

with a complexity which is logarithmic with the number of wavelet decomposition stages N may represent a solution for the complexity required for its real-time implementation in GNSS receiver. Differently, real-time KLT implementation seems to be a quite hazardous operation due to the fact that such a decomposition foresees an eigenvalues problem solving.

Chapter 6

Pulse Blanking Impact on DS/SS Data Demodulation Performance

Pulse blanking interference mitigation algorithm has been introduced in Chapter 3 and its performance in mitigating realistic pulsed interfering signals, such as those generated by DME and TACAN beacons nearby the airport in the ARNS frequency bands, has been discussed in Chapter 4. A specific aspect to address is the impact of the losses generated by the blanker on the data demodulation stages of the GNSS receiver. Few works in the literature deal with this aspect, taking into account not only the C/N_0 drop but the impact of the coding strategy and the structure of the navigation message.

In several works the structure of the navigation message is provided as a fact. In this Chapter it is analysed how some of the parameters (e.g. data rate) could be optimized in order to improve the robustness to the interference in future evolutions of GNSS systems.

After a brief general review of the DS/SS, this Chapter will provide a description of the impact of the pulse blanking mitigation algorithm on the data demodulation performance for both uncoded and coded DS/BPSK systems. In particular, theoretical derivation of the expected Bit Error Rate (BER)

will be provide. Theoretical derivation is supported by a set of fully software simulations, thanks to the use of a fully and flexible DS/BPSK system simulator developed during the Ph.D research activity.

6.1 Introduction

Galileo E5 and GPS L5 frequency bands will be allocated to the GNSS based services for the civil transportation, where accurate precise and reliable positioning information are needed, as an example, during the landing operation of the civilian aircraft. Nevertheless, as presented in Chapter 4, in both frequency bands a very harsh interference environment is expected due to the presence of other ARNS systems as the DME and the military TACAN which broadcast strong pulsed ranging signal. Furthermore, in such band, GNSS based positioning aids are provided by the SBAS, as for example the EGNOS [14]. While today SBAS-messages are being transmitted in L1 only, future transmission may use L1 and L5, where additional quadrature phase channels with data rate to be defined may be introduced. The use of higher data-rate transmission for the future GNSS standard may then be taken under consideration especially in those scenarios where, in principle, the GNSS signal quality is expected to be extremely high (as in aviation) and reduced coherent integration time may be employed. In such a condition, higher navigation message data-rates would lead to faster navigation message demodulation and thus to an higher positioning rate or a reduced Time to First Fix (TTFF). In this context, the paper investigates the limit concerning the use of higher data-rate in presence of multiple pulsed interference for a GNSS receiver equipped with a traditional pulse blanking. In such an interfered scenario, the presence of a pulse blanking circuitry may represent a limit for the possibility of increasing the navigation data-rate. This problem will be addressed in the following Sections, investigating the current SBAS standard system

performance in terms of data demodulation when exploiting higher data-rate and in presence of non-linear pulse blanking behaviours.

6.2 Direct Sequence Spread Spectrum Modulation

In this Section a quick review of the basic DS/SS modulation will be presented based on [101].

6.2.1 DS/BPSK system

Figure 6.1 shows a general block scheme of an uncoded DS/BPSK system.

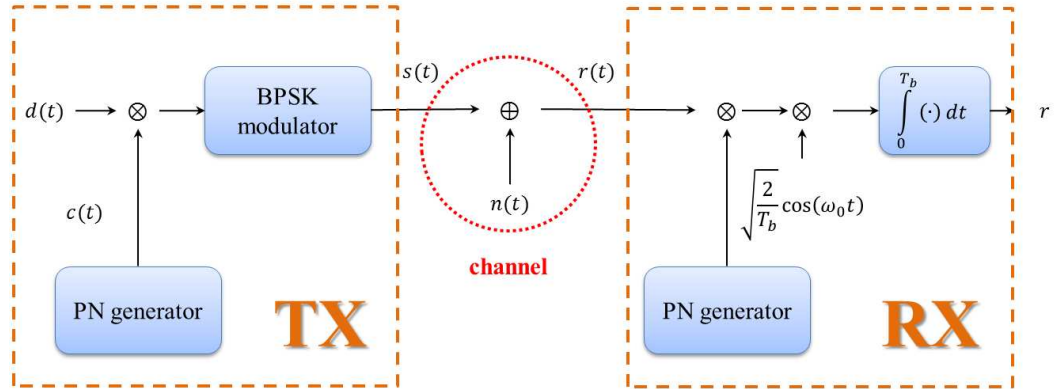


Figure 6.1: Uncoded DS/BPSK system

Let denote a sequence of binary data-symbols as

$$d_n \in \{+1, -1\} \quad (6.1)$$

We denote their symbol rate by R_b and their symbol time by $T_b = 1/R_b$. The base-band data signal to be transmitted is

$$d(t) = \sum_n d_n p_b(t - nT_b), \quad (6.2)$$

where $p_b(t)$ is the shaping filter. In the following, we will consider a rectangular shaping filter, i.e., $p_b(t)$ is a rectangular window of unitary amplitude

from 0 to T_b .

DS/SS is obtained by using a PRN sequence of binary symbols called chips

$$c_k \in \{+1, -1\} \quad (6.3)$$

which is G time faster than the data sequence. These chips are characterized by a chip rate $R_c = GR_b$ and a chip time $T_c = 1/R_c = T_b/G$. The number G represents the number of PRN chips corresponding to one data symbol. It plays a key role for DS/SS systems, and is called processing gain. GNSS signals feature periodic PRN sequence of duration of L chips. As an example, GPS L1 signals are characterized by periodic Gold codes of 1 ms duration modulating a stream of data-bits of 20 ms duration, whilst in the Galileo E1 OS signal, the bit duration is tiered to the length of the primary code period 4 ms.

By using a rectangular shaping filter $p_c(t)$ with unitary amplitude between 0 and T_c , the PRN signal can be written as

$$c(t) = \sum_k c_k p_c(t - kT_c) \quad (6.4)$$

The data signal and the PRN signal are directly multiplied, to obtain the spread signal

$$x(t) = c(t)d(t) \quad (6.5)$$

Since each data symbol is multiplied by G chips of the PRN sequence, the sequence $x(t)$ is characterized by the same chip rate R_c of $c(t)$ and its amplitude depends on both d_n and c_k . By using a BPSK modulation, the DS/SS signal is given by

$$s(t) = \sqrt{2S}x(t) \cos(2\pi f_0 t) = \sqrt{2S}c(t)d(t) \cos(2\pi f_0 t) \quad (6.6)$$

where S is the transmitted power. The PSD of this signal is centred around f_0 and has a $(\sin f/f)^2$ envelope, with a main lobe width equal to $2R_c$ and secondary lobes width equal to R_c . The useful bandwidth of the DS/SS signal will be denoted by W_{SS} and depends on the useful band of the original BPSK

signal before the spreading process W by

$$W_{ss} = GW \quad (6.7)$$

Bandwidth expansion of the useful signal provides a better protection against band-limited interference. Furthermore, at receiver level, the despreading operation will provide a gain to the effective SNR, since the interference power outside the the BPSK signal useful bandwidth W will be mitigated.

6.2.2 DS/SS Demodulation

Considering an AWGN channel with ideal frequency response and white Gaussian noise with constant power spectral density of value $N_0/2$, the received signal is

$$r(t) = s(t) + n(t) \quad (6.8)$$

The data symbols recovery is a despreading operation where the received signal $r(t)$ is multiplied by a locally generated and synchronized PRN sequence $c(t)$. The ideal despreading operation leads to

$$\begin{aligned} r'(t) &= \sqrt{2S}c(t)d(t) \cos 2\pi f_0 t \cdot c(t) + n(t) \cdot c(t) = \\ &= \sqrt{2S}c^2(t)d(t) \cos(2\pi f_0 t) + n(t) \cdot c(t) = \\ &= \sqrt{2S}d(t) \cos(2\pi f_0 t) + n(t) \cdot c(t) \end{aligned} \quad (6.9)$$

since $c^2(t) = 1$ for all t (if perfect synchronization with the received PRN sequence is achieved). Thus the data symbols d_n can be recovered by projecting the despread signal over the function

$$f_n(t) = \mu p_b(t - nT_b) \cos(2\pi f_0 t) \quad (6.10)$$

where μ is a constant such that

$$\int_{nT_b}^{(n+1)T_b} f_n^2(t) dt = 1; \quad (6.11)$$

Considering rectangular shaping filter, it follows that

$$f_n(t) = \sqrt{\frac{2}{T_b}} p_b(t - nT_b) \cos(2\pi f_0 t) \quad (6.12)$$

By projecting the despread signal over $f_n(t)$, the recovered data can be expressed as

$$r = \int r'(t) \cdot f_n(t) = A + n \quad (6.13)$$

where

- $A = \sqrt{ST_b}d_n = \sqrt{E_b}d_n$ where $E_b = \sqrt{ST_b}$ is the energy per data symbol
- n is a sample of a Gaussian random variable with zero mean and variance $N_0/2$ obtained from

$$n = \int n(t)c(t) \cdot f_n(t)dt \quad (6.14)$$

Typical BPSK decision rule is

$$\hat{d}_n = \begin{cases} 1, & \text{if } r > 0 \\ -1, & \text{if } r \leq 0 \end{cases} \quad (6.15)$$

For an un-coded DS/BPSK system, the expression of the BER is given by [101]

$$P_b = \frac{1}{2} \operatorname{erfc} \left(\sqrt{\frac{E_b}{N_0}} \right) \quad (6.16)$$

6.2.3 DS/SS and Coding

Channel coding introduces redundancy in the binary data sequence, which allows to reduce the impact of the impairments at the receiver side. A convolutional code is a binary code $C(n,k)$ where the code-block have infinite length. The convolutional encoder has memory, since the n coding bits depend not only on the corresponding k information bits but also on the previous information bits. In this way, the bit rate increases from R_b to

$$R_e = R_b \cdot \frac{n}{k} = \frac{R_b}{R} \quad (6.17)$$

where $R = \frac{k}{n} < 1$ is the coding rate. A practical example is represented by the signal in space broadcast by SBAS satellites, where a convolutional

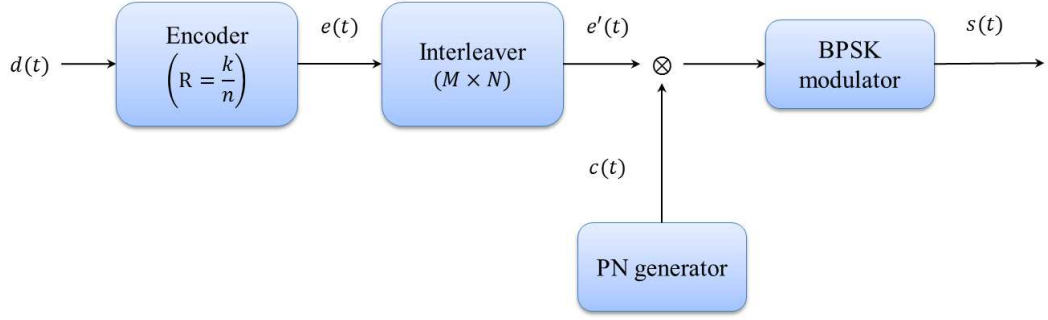


Figure 6.2: Coded DS/BPSK system

encoding of R equal to $1/2$ is employed. Figure 6.2 shows the block scheme of a coded DS/BPSK system transmitter. The coded signal becomes

$$e(t) = \sum_j e_j p_e(t - nT_e) \quad (6.18)$$

where $p_e(t)$ is the rectangular pulse of unitary amplitude for $0 < t < T_e$. The corresponding BPSK signal before the spreading operation is

$$m(t) = \sqrt{2P}e(t) \cos(2\pi f_0 t). \quad (6.19)$$

The PSD of this signal has a $(\sin f/f)^2$ behaviour, with a null-to-null bandwidth $W_e = 2R_e$ centred around f_0 and secondary lobes with bandwidth R_e . Then, the bandwidth W_e of the coded BPSK is the scaled in frequency of a n/k factor with respect to the un-coded BPSK PSD.

After the coding, according to the DS/SS modulation, the coded sequence is multiplied with the PRN sequence as

$$x(t) = e(t)c(t) \quad (6.20)$$

where each coded symbol is multiplied by $G' = G \frac{k}{n}$ chips. As expected, the presence of a coding techniques reduces the processing gain introduced by the spreading modulation. Finally, the resulting BPSK signal after the spreading is

$$s(t) = \sqrt{2P}x(t) \cos(2\pi f_0 t) = \sqrt{2P}e(t)c(t) \cos(2\pi f_0 t) \quad (6.21)$$

For the BPSK DS/SS coded system, the BER related to the bit transmitted over the AWGN channel is higher with respect the case of the un-coded BPSK DS/SS system, and it is given by

$$P_e = \frac{1}{2} \operatorname{erfc} \left(\sqrt{R \cdot \frac{E_b}{N_0}} \right) \quad (6.22)$$

This is due to the bandwidth expansion which in turns leads to an increase of the noise floor at the code bit demodulator. However, due to the corrective capability of the code, the BER on the information bits is expected being smaller than the BER for the un-coded system expressed in (6.16). Modern coding scheme are characterized by the presence of an interleaver (Figure 6.2). This device commutes the coded data bits, before the transmission on the channel. Basically each code-block is written in each row of a $M \times N$ matrix. Once all the rows of the matrix are filled, the bits from the matrix are read column by columns. Such an interleaving operation increases the corrective capability of a coding scheme when in presence of burst errors.

6.3 Pulse blanking impact on un-coded DS/BPSK system performance

The received signal in presence of an AWGN channel and pulsed interference can be written as follows

$$r(t) = s(t) + n(t) + j(t) \quad (6.23)$$

where $j(t)$ refers to the additive pulsed interference component whilst $s(t)$ is the DS/SS signal expressed in (6.6). At receiver side, data-symbol recovery is achieved by projecting the received signal $r(t)c(t)$ over the function $f_n(t)$ in (6.12). Thus, the demodulated data is given by

$$R = \int_{nT_b}^{(n+1)T_b} r(t)c(t)f_n(t)dt = A + n + I \quad (6.24)$$

where I is the result of the projection of the jamming signal $j(t)c(t)$ on the function $f_n(t)$

$$I = \int_{nT_b}^{(n+1)T_b} j(t)f_n(t)dt = \sqrt{\frac{2}{T_b}} \int_{nT_b}^{(n+1)T_b} j(t)c(t) \cos(2\pi f_0 t)dt \quad (6.25)$$

Since we are assuming $j(t)$ as Gaussian white noise, I is a Gaussian random variable with zero mean. Its variance depends on the pulse characteristics. Pulsed interference impact on data demodulation depends on the relation between the pulse duty cycle ρ and the data bit duration T_b . In fact three cases can be identified:

- $D \leq T_b, T \leq T_b$ (possible scenario: very low symbol rate)
- $D \leq T_b, T \geq T_b$ (possible scenario: very low symbol rate, rarely acting short but strong jamming pulses)
- $D \geq T_b, T \geq T_b$ (possible scenario: medium/high symbol rate)

In this Section, the analysis of the pulse blanking effect on the DS/SS systems data demodulation performance will be carried out considering two kind of pulsed interfering signal:

- [AWGN](#) based pulsed interference
- [DME/TACAN](#) pulsed interference

As it has been described in Chapter 4, the pulsed interference scenario originated by all the ground [DME/TACAN](#) stations is seen by the on-board receiver as an equivalent pulsed interference source extremely dense in time made by short pulsed duration. For such a reason, the investigation of the impact of pulse blanking on the data demodulation performance will be limited to the case 1 in both the considered interfered scenarios.

6.3.1 AWGN pulsed interference

With the name [AWGN](#) based pulsed jamming, we refer to a pulsed interfering signals with the following characteristics:

- White Gaussian noise;
- Bandwidth equal to useful DS-SS signal band W_{ss} ;
- Discontinuous, with pulse active time D and period T : the pulse is active for a fraction of time (also called duty cycle) $0 < \rho = \frac{D}{T} \leq 1$
- Power J_P during the active time D (and zero for the remaining time $T - D$).

During the active time, the jamming signal has a power spectral density which is constant over the W_{ss} band, with value $J_{0P}/2$ where $J_{0P} = \frac{J_P}{W_{ss}}$.

For proper comparison, it is useful to introduce an equivalent (with the same energy) Gaussian continuous jamming signal. Since the same energy is transmitted over T instead of D , it has a power $J = \rho J_P$. This equivalent jamming signal has a power spectral density constant over W_{SS} , with value $J_0/2$, where $J_0 = J/W_{SS} = \rho J_{0P}$.

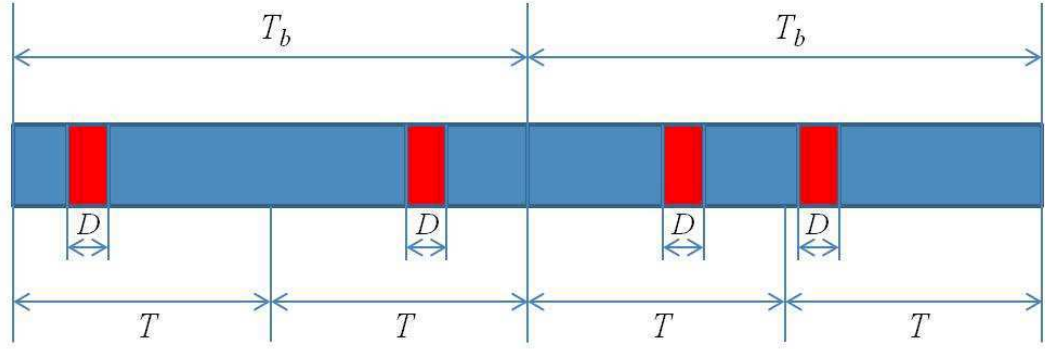
When both D and T are below the data bit duration T_b , the jamming increases the noise level for each transmitted symbol. Let us denote by

$$\alpha = \frac{T_b}{T} \quad (6.26)$$

the integer number of jamming period (thus the number of pulses) in each data symbol. An example with $\alpha = 2$ is provided in [Figure 6.3](#).

The jamming component is given by

$$I = \int_{nT_b}^{(n+1)T_b} j(t)f_n(t)dt = \sum_{i=1}^{\alpha} \int_{t_i}^{t_i+D} j(t)f_n(t)dt \quad (6.27)$$


 Figure 6.3: Case 1: 2 pulses per each symbol ($\alpha = 2$)

where t_i is the starting time of the i^{th} pulse within the symbol. Since the jamming signal is Gaussian noise with constant spectral density $J_{0P}/2$, I is a Gaussian random variable with zero mean and variance

$$\sigma^2(I) = \frac{J_{0P}}{2} \sum_{i=1}^{\alpha} \int_{t_i}^{t_i+D} f_n^2(t) dt \quad (6.28)$$

Considering rectangular shaping filter, the energy contained into an interval is proportional to its time amplitude

$$\int_{t_i}^{t_i+D} f_n^2(t) dt = \frac{2}{T_b} \int_{t_i}^{t_i+D} c^2(t) \cos^2(2\pi f_0 t) dt = \frac{D}{T_b} \quad (6.29)$$

Then

$$\sigma^2(I) = \frac{J_{0P}}{2} \alpha \frac{D}{T_b} = \frac{J_0}{2} \frac{T}{D} \frac{T_b}{T} \frac{D}{T_b} = \frac{J_0}{2} \quad (6.30)$$

The jamming impact is the same for each symbol and does not depend on the value of ρ . Thus, the impact is equivalent to that of a continuous jamming signal with the same energy. To summarize, in this case for each symbol the variance of the noise samples increases from $\frac{N_0}{2}$ to $\frac{N_T}{2} = \frac{N_0}{2} + \frac{J_0}{2}$, thus leading to the following [BER](#) formulation

$$P_b = \frac{1}{2} \operatorname{erfc} \left(\frac{E_b}{N_0 + J_0} \right) \quad (6.31)$$

In order to confirm the validity of such a model, a set of simulations of $2 \cdot 10^5$ bits transmitted at a data-rate R_b of 4 kbps according to an un-coded [DS/BPSK](#) scheme has been performed. A spreading [PRN](#) sequence at rate $R_c = 1.023$ Mcps has been adopted for obtaining the [DS/SS](#) signal. Several

AWGN based pulsed interference scenarios have been simulated considering different $\frac{E_b}{J_0}$ values ranging from 0 to 20 dB. For each $\frac{E_b}{J_0}$ value, the generated pulsed interfering signal is made of pulse train of $3 \mu\text{s}$ duration with a duty cycle ρ of 50% and results are shown in Figure 6.4. The validity of the model is

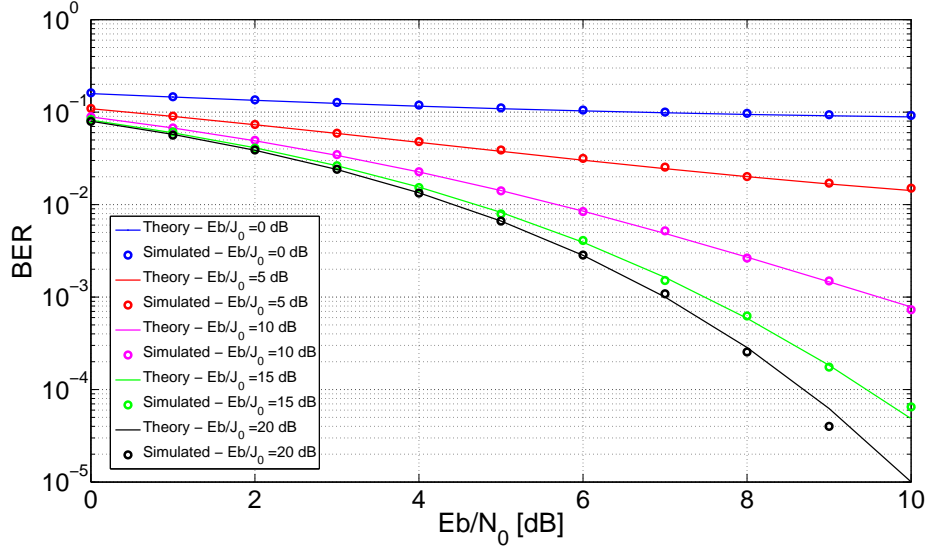


Figure 6.4: Bit Error Rate for un-coded DS/BPSK system in presence of AWGN pulsed interference

confirmed by the results shown in Figure 6.4, where the BER values achieved by simulations perfectly fit the trend of the theoretical expected BER defined in (6.31). In order to analyse the effect of the pulse blanking on the BER for un-coded DS/BPSK transmission, formulation of the degradation on post correlator C/N_0 (e.g. the Energy per bit to Noise density power ratio (E_b/N_0) at the demodulator) is needed. In presence of an ideal pulse blanking, the degradation on the E_b/N_0 is defined as

$$(E_b/N_{0,eff}) = \frac{E_b(1 - \beta)}{N_0 + J_{0,res}} \quad (6.32)$$

where, β is the well know blanker duty cycle, and $J_{0,res}$ is the residual portion of residual pulsed interference power spectral density. Recalling the model (4.2), the component $J_{0,res}$ is related to the component R_I by

$$J_{0,res} = N_0 \cdot R_I \quad (6.33)$$

Hereafter, a theoretical derivation for both β and $J_{0,res}$ components will be presented.

6.3.1.1 β computation

In order to compute the blanker duty cycle β , blanking detection performance have to be defined. In particular, it is possible to defined the following probabilities:

- detection probability p_d : the probability that a generic sample of the incoming received signal during the pulse activation time D is crossing the blanking threshold V_{th} ;
- missed-detection probability p_{md} : the the probability that a generic sample of the incoming received signal during the pulse activation time D is not crossing the blanking threshold V_{th} ;

Derivation of both probabilities can be performed making a statistical assumption of the received signals during the pulse activation time D at the [ADC](#) output. Since [AWGN](#) based pulsed interference is considered, it can be shown that, the samples at the [ADC](#) output during D are Gaussian distributed with zero mean and variance σ^2 equal to

$$\sigma^2 = (N_0 + J_{0P}) \cdot B_{fe} \quad (6.34)$$

where B_{fe} is the front-end bandwidth. Thus, the pulse blanking detection probability becomes

$$p_d = 2 \int_{V_{th}}^{+\infty} \frac{1}{\sigma\sqrt{2\pi}} e^{-\frac{x^2}{2\sigma^2}} dx = \operatorname{erfc}\left(\frac{V_{th}}{\sigma\sqrt{2}}\right) \quad (6.35)$$

As a consequence, the pulse blanking missed-detection probability is

$$p_{md} = \operatorname{erf}\left(\frac{V_{th}}{\sigma\sqrt{2}}\right) \quad (6.36)$$

Then the theoretical blanker duty cycle β can be computed as:

$$\beta = p_d \cdot \rho \quad (6.37)$$

6.3.1.2 $J_{0,res}$ computation

For the $J_{0,res}$ component derivation, an approximated upper-bound model is employed. If β is the percentage of the blanked samples computed over the total received signal, it is possible to assume that the signal after the blanker is still corrupted by an equivalent residual pulsed interference characterized by a duty cycle ρ_{res} , defined as

$$\rho_{res} = \frac{D_{res}}{T} = \frac{\left(1 - \frac{\beta}{\rho}\right) \cdot D}{T} = \rho - \beta \quad (6.38)$$

During the equivalent residual pulse activation time D_{res} , samples at the ADC output are Gaussian distributed with zero mean and variance σ_{res}^2 given by

$$\sigma_{res}^2 = (N_0 + J_{0P,res}) \cdot B_{fe} \quad (6.39)$$

where $N_0 B_{fe} \leq \sigma_{res}^2 \leq V_{th}^2$. The approximated model for the $J_{0,res}$ computation is based on the assumption that the average power of the signal at the blanker output during the residual pulse activation time is

$$\sigma_{res}^2 \approx \frac{V_{th}^2 + N_0 B_{fe}}{2} \quad (6.40)$$

which leads to the final $J_{0,res}$ computation

$$J_{0,res} \approx J_{0P,res} \cdot \rho_{res} = \frac{1}{2} \frac{(V_{th}^2 - N_0 B_{fe})}{B_{fe}} \cdot \rho_{res} \quad (6.41)$$

The validity of the model has been tested through a set of simulations. Transmission of $2 \cdot 10^5$ bits at $R_b = 4$ kbps according to a DS/BPSK system multiplied by a PRN sequence transmitted at rate R_c equal to 1.023 Mcps has been performed for the spreading operation, and results are shown in Figure 6.5. The spread spectrum signal is then transmitted over a AWGN channel, after being BPSK modulated. A strong AWGN pulsed interference providing an $\frac{E_b}{J_0}$ ratio equal to -15 dB has been also simulated over the channel. At receiver level, the ideal pulse blanking simulator suppressing only the samples crossing the blanking threshold V_{th} has been enabled. First results are

shown in Figure 6.5(a) and Figure 6.5(b) where blanker duty cycle β and residual interference power spectral density $J_{0,res}$ are respectively reported. Here it can be observed that the presented theoretical derivation for β and $J_{0,res}$ represents a valid model, as confirmed by the measured data (dashed red lines).

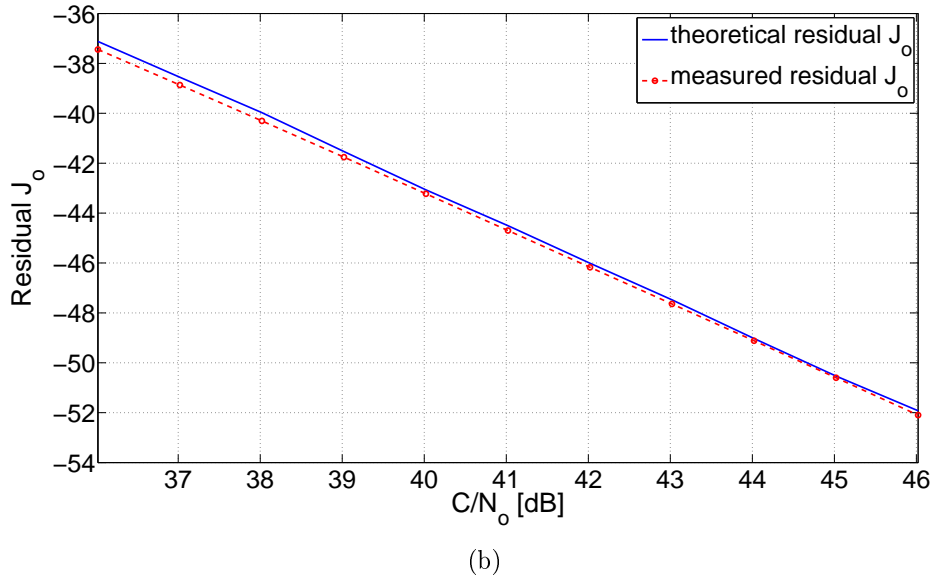
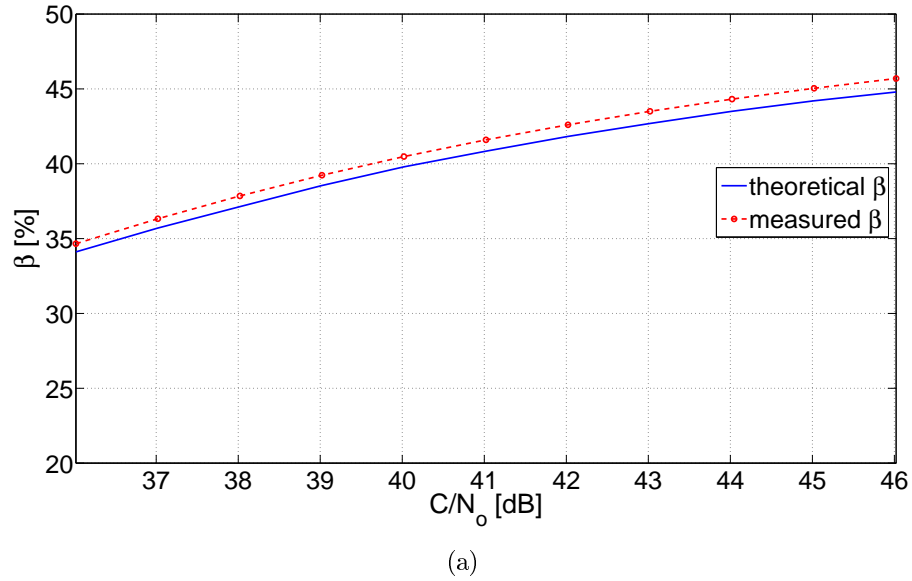


Figure 6.5: Theoretical and simulated pulse blanking performance against [AWGN](#) based pulsed interference

Figure 6.6 shows the effective pulse blanking impact on the data demodulation

for the un-coded DS/BPSK system affected by AWGN pulsed interference and confirms the validity of the model presented in (6.32).

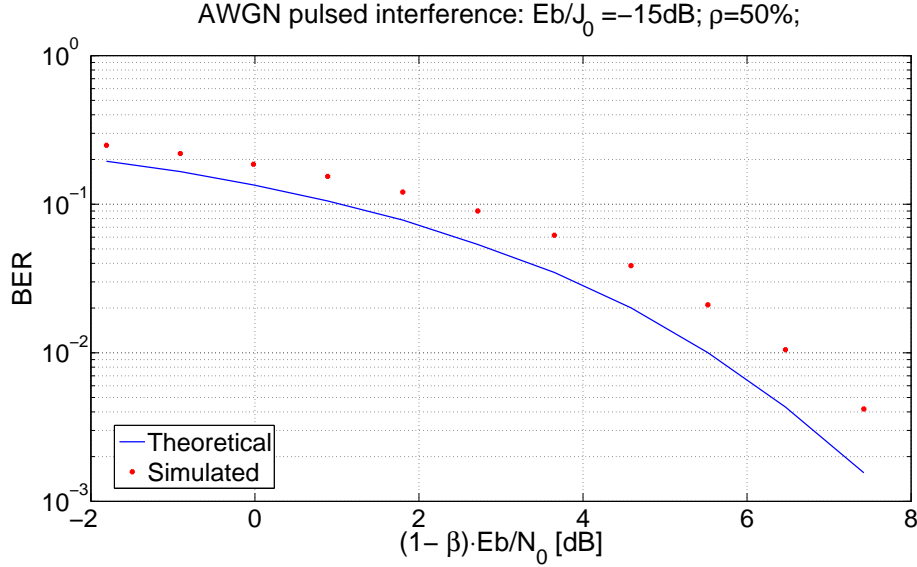


Figure 6.6: Pulse blanking impact on BER for un-coded DS/BPSK system in presence of AWGN pulsed interference

6.3.2 DME/TACAN interference

On the basis of the model in (4.2) defined in Chapter 4, in presence of an ideal pulse blanking, it is possible to define

$$(Eb/N_{0,eff}) = \frac{E_b}{N_0} \cdot \frac{(1 - \beta)}{1 + R_I} \quad (6.42)$$

where β and R_I have been already defined and derived in Sections 4.4.1 and 4.4.2. In order to validate (6.42), a set of simulations of an un-coded DS/BPSK system in presence of DME/TACAN interference has been performed. In particular, the simulated DME/TACAN interference is represented by the composite pulsed signals generated by 21 ground stations and achieving the on-board GNSS receiver antenna. A PRN sequence of 1023 chips transmitted at 1.023 Mcps has been employed for spreading purposes,

and 4 MHz front-end filter bandwidth has been considered for the signal simulation at the blanker input. Figure 6.7 shows the profile of the pulsed peak power to the signal power ratio Jammer to Carrier power ratio (J/C) for the considered scenario. Performance of the un-coded DS/BPSK system have been assessed at different values of E_b/N_0 , given a constant signal power C and a bit rate R_b equal to 4 kbps.

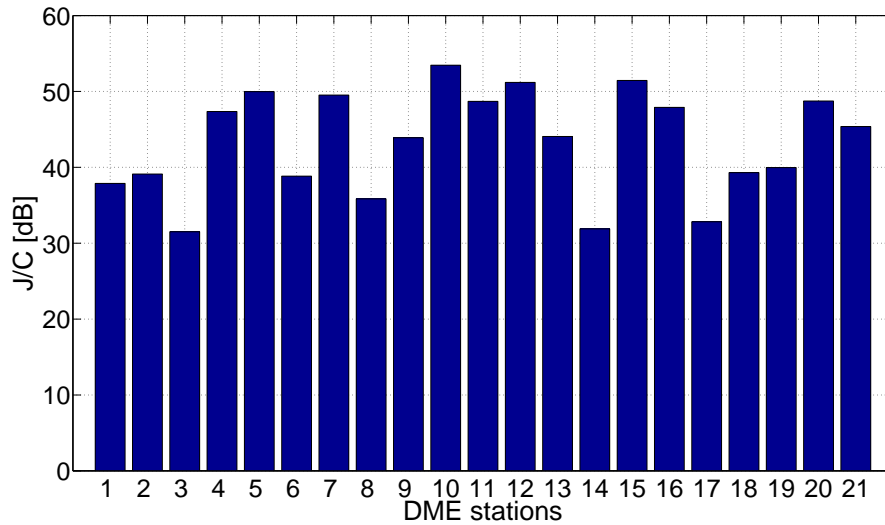


Figure 6.7: Pulsed peak power to signal power ratio profile

From Figure 6.7 it is possible to notice that the considered interference environment is extremely harsh due to the higher values of the J/C ranging between 30 and 53 dB, thus leading to an Energy per bit to Jammer density power ratio (E_b/J_0) approximately equal to -9 dB before the application of the pulse blanking.

Figure 6.8 shows the DS/BPSK system performance in terms of BER when the pulse blanking circuitry is adopted.

It can be clearly observed that, the model in (6.42) perfectly matches the achieved results. Furthermore, worst data demodulation performance are achieved even at higher E_b/N_0 . This is due to the fact that, the ideal pulse blanking operation not completely removes the DME/TACAN pulses thus leading to a high post blanking E_b/J_0 .

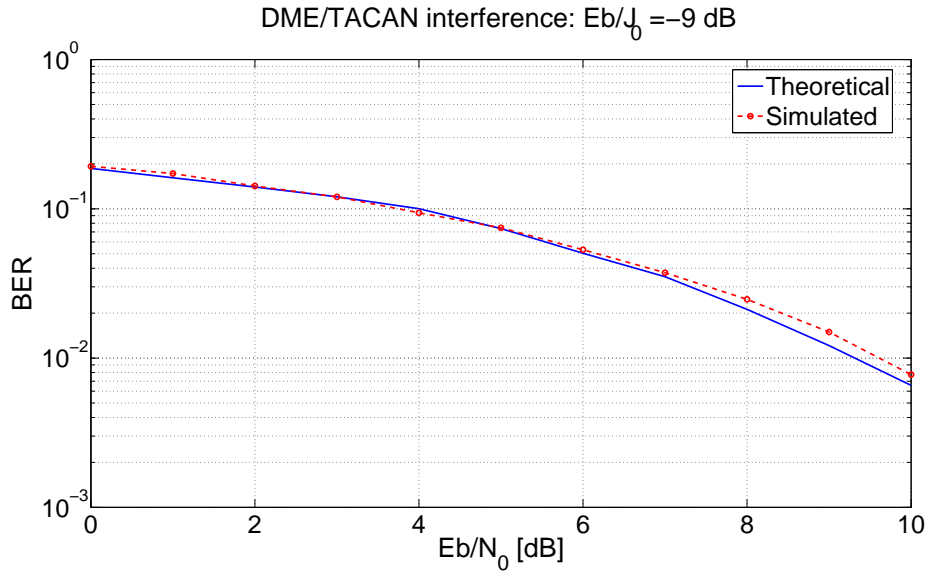


Figure 6.8: Pulse blanking impact on Bit Error Rate for un-coded DS/BPSK system in presence of AWGN pulsed interference

6.4 Pulse blanking non linearities impact on real coded DS/BPSK system: the Galileo E5a case

This Section will investigate the impact of the pulse blanking on real coded DS/BPSK system. In particular, the transmission of the F/NAV message on the Galileo E5a-I channel will be considered, and demodulation performance at receiver level will be assessed taking into account all those non-linear behaviours characterizing realistic pulse blanking circuitry. Furthermore, the system will be assessed considering higher data-rates transmission in the range 2–4 kbps with respect the standard data rate transmission on the E5a-I channel equal to 50 bps. The scope of this analysis is to investigate if the pulse blanking non linearities, which are not taken into account in the several theoretical derivations present in literature, have a not negligible impact on the expected signal degradation at the demodulator input. Moreover, investigation of the possibility to increase the data-rates for future SBAS transmission on GPS L5 and Galileo E5a frequency bands is also presented.

6.4.1 Pulse blanking non linearities

The concept of pulse blanking non-linear behaviour has been already introduced in Chapter 4. Such behaviours may be caused by the reception of strong pulsed interfering signals which cause the saturation of the active components in the receiver front-end thus impacting also on the pulse detection performance of the blanking circuitry. Figure 6.9 provides a comparison between the effect of an ideal pulse blanking and the effect of a non-ideal blanking performed on the DME/TACAN double pulses. The a non perfect blanking

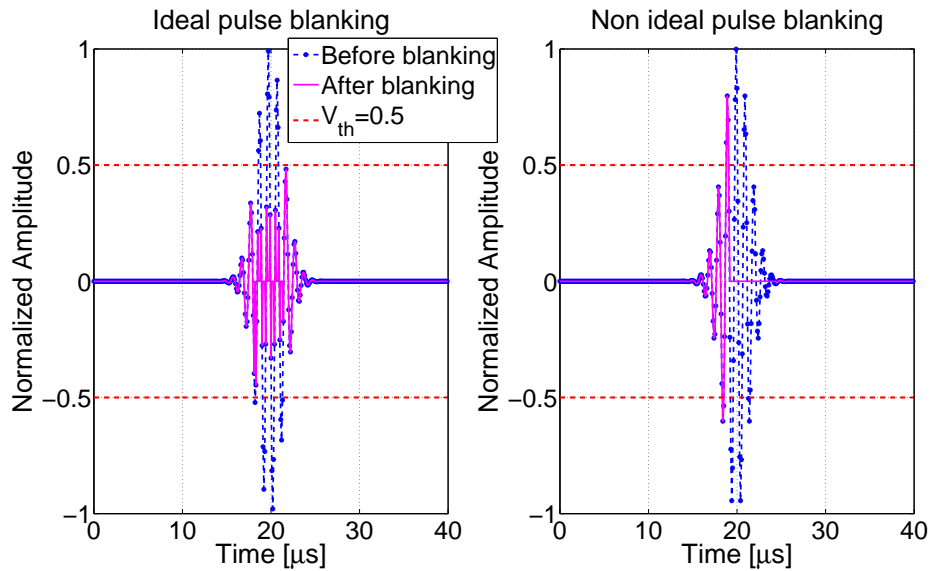


Figure 6.9: Ideal versus non-ideal pulse blanking

leads not only to a delay on the detection of the initial part of the pulses, but also to a delay of a pulse blanking deactivation time, thus leading to a non-perfect suppression of the interference and to a greater degradation of the useful GNSS signal. Thus summarizing, two parameters can be identified in order to characterize the pulse blanking non linear behaviours:

- *reaction time* γ which represents the delay in the detecting the initial part of pulse.
- *recovery time* δ which represents the delay of the blanker in detecting the end of the pulse.

A parametric analysis considering values of γ and δ in the range $0 - 3 \mu s$ has been performed and results are presented in Figure 6.10 and Figure 6.11 where the blanker duty cycle β and the effective post correlation C/N_0 are shown respectively. As expected the blanker duty cycle increases with the increasing recovery time δ , while it decreases with the increasing reaction time γ . In fact, a slow pulse blanking detection time allows great portions of DME/TACAN pulsed interference going through the correlators thus leading to a high degradation in the C/N_0 . It can be also observed that for a fixed value of γ , an increasing value of δ within a determined range (e.g. $0.1 \mu s \leq \delta \leq 1 \mu s$ for $\gamma = 0 \mu s$) lead to a gain in the post correlator C/N_0 . This is due to the fact that, slightly increasing δ , even those samples belonging to the DME/TACAN pulse's tails are suppressed. However, for high values of recovery time, a large portion of the received signal is suppressed ($\beta \geq 70\%$) leading to a high degradation in the effective post correlation C/N_0 .

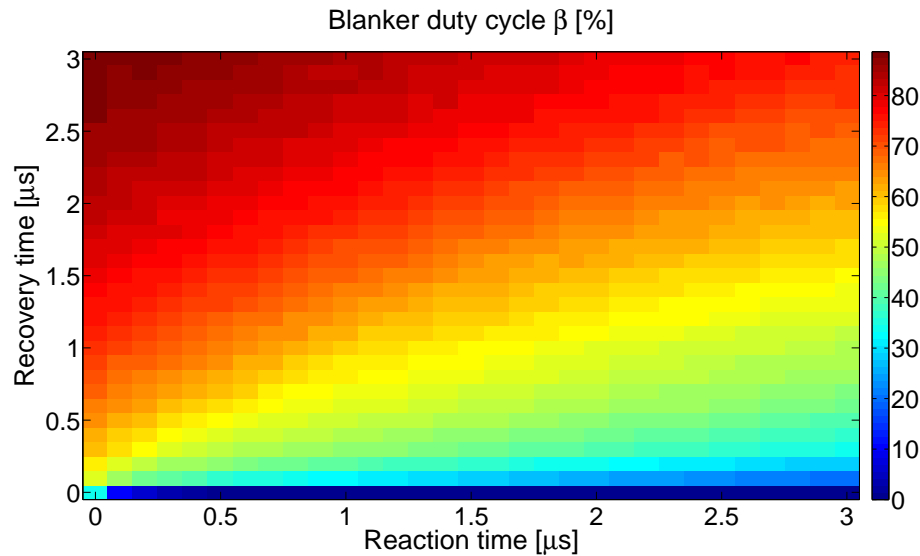


Figure 6.10: Blanker duty cycle β for different values of reaction γ and recovery δ time

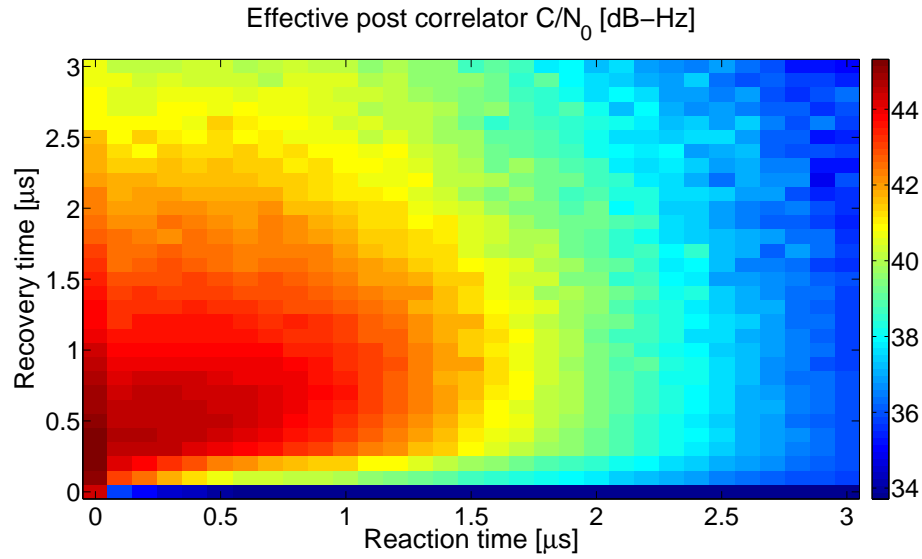


Figure 6.11: Effective C/N_0 for different values of reaction γ and recovery δ time

6.4.2 The F/NAV message on Galileo E5a-I

The Galileo **SiS** transmitted in Galileo E5a frequency band, where the strong **DME/TACAN** interference environment is expected, is composed by two quadrature phase channels, E5a-I, carrying the navigation data bits, and E5a-Q representing a pure pilot channel. The same Quadrature Phase Shift Keying (**QPSK**) like signal modulation is also transmitted in the Galileo E5b band, as shown from Figure 6.12, where the scatter plots, obtained processing real collected data coming from the second Galileo acIOV satellite, the Flight Model 2, in both E5 side-bands are shown.

From the scatter plots it can be observed that each channel is a **BPSK** like signals. In particular, concerning the E5a-I data channel, the navigation data transmitted at 50 bps are modulated with a **PRN** code sequence made of a primary code and a longer secondary code, thus resulting in a tiered code length of 20 ms. Table 6.1 summarizes the primary and secondary code properties featured in both E5a-I and E5a-Q channels.

Many other details, on primary and secondary code generation can be found in [15].

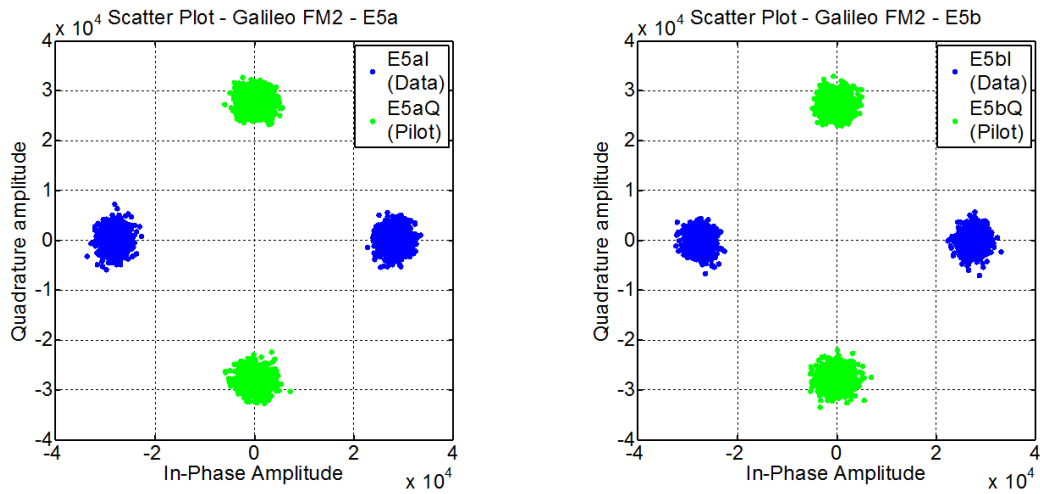


Figure 6.12: E5a and E5b signal modulation

Table 6.1: E5a PRN code

Signal	Tiered Code Period	Primary Code Length [chips]	Primary Code Rate [Mcps]	Secondary Code Length [chips]
E5a-I	20	10230	10.23	20
E5a-Q	100	10230	10.23	100

Concerning the data message format, the F/NAV message is transmitted over the Galileo E5a-I channel. The single F/NAV word of 244 bits length, is encoded through a convolutional encoder of 1/2 code rate, and processed by a 61×8 interleaving matrix before being modulated by the tiered code and transmitted over the channel. Additional details on the convolutional encoder properties and F/NAV message structure can be found in [15].

Performance of F/NAV message demodulation has been assessed in presence of the strong DME/TACAN interference scenario described in Section 4.5 of Chapter 4. Such an interfered scenario is representative of the expected environment in the so called DME/TACAN hotspot location, described in [1]. In Figure 6.13, the spectrum of 10 ms of Galileo E5a signal combined with DME/TACAN interference is shown.

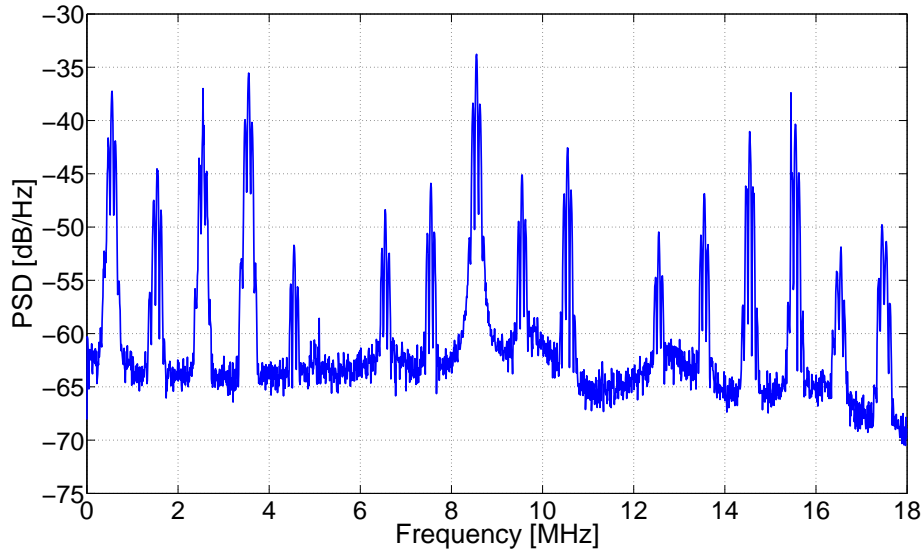


Figure 6.13: Galileo E5a signals interfered with DME/TACAN pulses

The entire spectrum is completely jammed by several narrow-band interference each representing the [DME/TACAN](#) double pulse pair train received from a determined ground beacon. However, the number of narrow-band interference in the spectrum are not representing the total number of [DME/TACAN](#) stations in [LoS](#) to the receiver on-board (about 40) since some of them is transmitting the pulsed signal on the same carrier frequency.

The pulse blanking was enabled during the whole test duration, consisting in the transmission of $2 \cdot 10^5$ bits. The performance of the system have been assessed in terms of [BER](#) and for different values of blanking recovery time δ and reaction time γ in the range $0 - 3 \mu\text{s}$. Furthermore, the pulse blanking threshold has been set according to a $p_{fa} = 10^{-3}$ and the [AWGN](#) channel has been simulated according to a $C/N_0 = 49.9 \text{ dB-Hz}$.

Since the aim of the test was to investigate the possibility of exploiting higher data rate (order of kbps), the coded DS-BPSK system, representative of the data bit transmission over the E5a-I channel, has been tested for different data rate in the range $2 - 4 \text{ kbps}$. [Figure 6.14](#) and [Figure 6.15](#) shows the F/NAV navigation data demodulation performance in case of hard decoding and soft decoding respectively considering four different behaviour of the

pulse blanking:

- *Ideal blanking*: $\gamma = 0\mu s$ and $\delta = 0\mu s$;
- $\gamma = 1\mu s$ and $\delta = 2\mu s$;
- $\gamma = 2\mu s$ and $\delta = 1\mu s$
- $\gamma = 3\mu s$ and $\delta = 3\mu s$

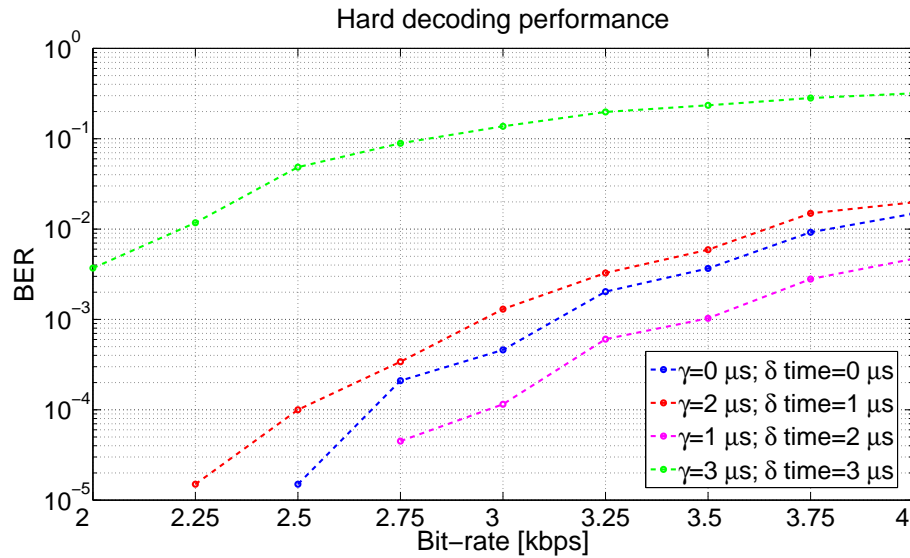


Figure 6.14: Pulse blanking impact on E5a-I channel data demodulation performance in presence of DME/TACAN system: hard decoding

The achieved results are in line with those reported in Figure 6.11. Best F/NAV demodulation performance are achieved when exploiting an ideal pulse blanking (blue line), since the effective C/N_0 post correlation and thus the E_b/N_0 at the demodulator is higher with respect the E_b/N_0 achieved in presence of non-ideal blanking (see Figure 6.11). Furthermore results confirm that soft decoding should be preferred with respect the hard decoding scheme as expected. The simulated pulse blanking non linearities have a not negligible impact on the data demodulation performance of the simulated system. Worst performance are achieved simulating a blanking characterized by slow detection and recovery time (green line). In this scenario, due to the

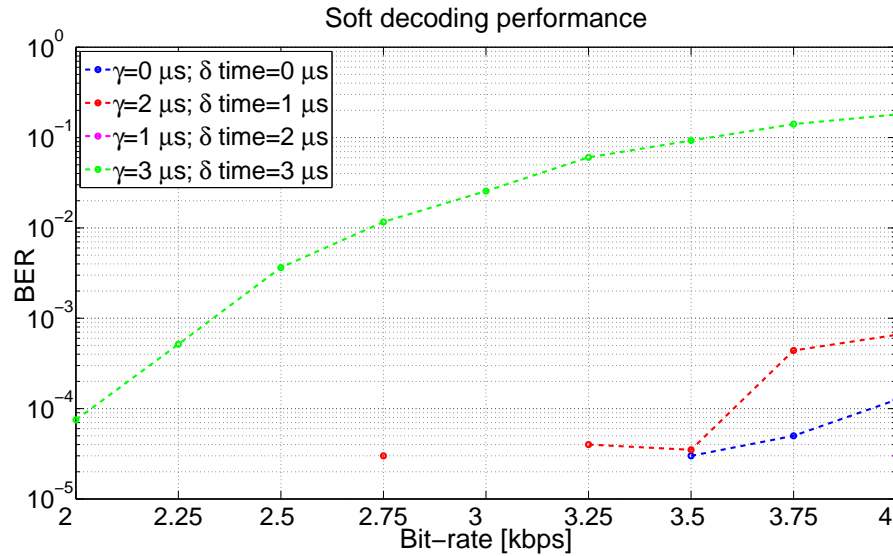


Figure 6.15: Pulse blanking impact on E5a-I channel data demodulation performance in presence of DME/TACAN system: hard decoding

composite and dense in time pulsed interference at the receiver input, a slow detection time combined with a slow recovery time causes the suppression of large portions of useful GNSS signal, comparable to the duration of several adjacent bits.

Furthermore, Figure 6.15 shows that in such a scenario, higher data rates (up to 2.5 kbps) with respect those employed in the standard F/NAV navigation data transmission can be accepted but careful front-end receiver and pulse blanking design are required.

6.5 Conclusions

The analysis addressed in this Chapter revealed that, un-coded DS/BPSK systems operating in strong pulsed interference may be threatened seriously even in presence of a pulse blanking countermeasure. The investigation of un-coded DS/BPSK systems performance, carried out in presence AWGN pulsed interference and the more realistic DME/TACAN interference, revealed that the use of higher data bit rate (4 kbps) with respect those exploited in the

standard GNSS (50 or 250 bps) lead to a non acceptable data demodulation performance, since the presence of a blanking mechanism can potentially suppress long portions of signal comparable to the data bit duration. For such a reason, looking also at the future SBAS standard evolution on the GPS L5 and Galileo E5a, data protection scheme provided by the use of data encoding and interleaving should be implemented, as shown from the analysis addressed in Section 6.4. Here it has been shown that, using the same coding and interleaving scheme employed for the F/NAV message transmission on the Galileo E5a-I data channel, good data demodulation performance can be achieved even at higher data rate (order of kbps) in presence of a strong DME/TACAN interference and pulse blanking as a countermeasure. However a careful design of a pulse blanking circuitry capable of detecting the pulsed interference and suppressing also those DME/TACAN components below the blanking threshold as much as possible, is needed.

Part III

Design of a High Sensitivity

Receiver for GNSS signal

acquisition in harsh environment

Chapter 7

Weak GNSS Signal Navigation

This Chapter is devoted to the study and design of a **HS** receiver capable of detecting and processing feeble **GNSS** signals. Investigation on the aiding requirements needed for correct acquisition and tracking of very weak signals is carried out first theoretically and then by means of software simulation.

7.1 Introduction

So far, the thesis has provided a description of the most common interference mitigation algorithms for **GNSS** applications and, advanced signal processing techniques for interference suppression, which increase considerably the **GNSS** receiver robustness in harmful interfered scenarios, have also been presented. However, in many other environments, where the number of **GNSS** based applications is constantly growing, such as in indoor, urban canyon, or space scenarios, receivers performance are seriously threatened since they have to deal with several factors like multipath, low satellites visibility and weak signal reception. For such a reason, in the last years **GNSS** community has focused its attention on the investigation and development of high sensitivity solutions and signal processing techniques which can be integrated in **GNSS** receivers in order to improve their robustness and their sensitivity.

After providing a general overview of the state of the art for **HS** receivers, methodology and design of a **HS** acquisition scheme for weak **GNSS** signal detection are provided in the next Sections.

7.2 State of the art of High Sensitivity Receiver

The conventional acquisition stages are designed to work in open-sky conditions, where a nominal received signal strength is expected to be captured by the receiver antenna. In harsh environments, **HS** acquisition strategies are required to deal with the reduced received power. In principle, as a nature of **DS/SS**, the longer the coherent integration time T_{int} between the local and the received signals is, the better the de-spreading gain (i.e. signal-to-noise ratio improvement) that can be obtained after the correlation process. However, the presence of unknown data bit transitions limits the value of $T_{int} \leq T_b$, being T_b the data bit duration (e.g. $T_{int} \leq 20$ ms as for **GPS** L1 **C/A** signal) to avoid the correlation loss. A major issue for indoor **GNSS** signals is the extremely low **SNR** (e.g. $C/N_0 = 5\text{dB-Hz} - 30\text{ dB-Hz}$), because the typical sensitivity of a common **GNSS** receiver (about $35\text{ dBHz} - 40\text{dBHz}$) is not sufficient to guarantee proper indoor detection performance. In particular the acquisition stage may fail in identifying correct correlation peaks corresponding to the best estimation of the code delay and Doppler shift. There are several analogies between the typical indoor environment and the space environment in terms of expected C/N_0 , thus making feasible the adaptation of indoor techniques.

Acquisition sensitivity can be increased by extending the coherent integration time, but the maximum achievable performance is bounded primarily by the presence of data bits which introduce sign reversals within the integration window and may result in a partial or even total cancellation of correct correlation peak. This limitation is only neglected if there is an external-aiding source, which provides the data transition information. Furthermore

the sensitivity improvement obtained by increasing T_{int} is traded-off with an increased computational complexity. The Doppler step width (Δf) reduces as T_{int} becomes larger and this fact increases the search-space size. Furthermore, the instability of the receiver clock causes difficulties for the acquisition stage, especially if T_{int} is large, because of the carrier and code Doppler effects. Therefore, one should consider the trade-off between the sensitivity improvement and the complexity increase when changing the value of T_{int} . It is well known that in order to overcome the issue of data bit transitions, non-coherent accumulation can be performed [102]. Non coherent accumulation makes also the acquisition stage robust to Doppler variations that may not be negligible when dealing with long integration periods. Common GNSS receivers typically adopt non-coherent accumulation of subsequent coherent correlations. This technique is insensitive to bit transitions but suffers the squaring loss issue. This means that the theoretical gain obtained by increasing the number of accumulated blocks is lower than for a pure coherent integration of equivalent length.

The sensitivity assistance technique, also adopted in 3rd Generation Partnership Project (3GPP) specifications in the framework of mobile applications, enables HS acquisition, since it provides approximate code-phase/Doppler frequency estimates along with fragments of the navigation message. This allow for wiping off data-bit transitions and for extending the coherent integration time. Furthermore, the knowledge of a rough estimate of the delay and Doppler shift allows for a reduction of the size of the acquisition search space, thus improving the probability of detection at search space level. Long signal snapshots are typically required by HS correlation algorithms. Hence, sensitivity losses can still be experienced due to:

- the residual Doppler error (including the finite search resolution in frequency and the contribution of the user dynamics);
- the uncertainty on the Local Oscillator (LO) frequency. These effects

impact the observed carrier frequency and can be relevant with long coherent integrations;

Finally, a trade-off between sensitivity and complexity is necessary. Reduced sampling rates are mandatory to minimize the computational load of the baseband processing as well as the optimization of the assistance information exchange is fundamental in order to minimize the communication load. Thus, as remarked in [102], the problem of achieving HS acquisition can be summarized in the design of a proper combination of coherent integration (achieving the best gain in terms of noise averaging) and non coherent accumulations (insensitive to data transition and residual Doppler effects).

This Chapter will investigate the design of an HS acquisition scheme for weak GNSS signals detection beyond the GNSS satellites orbit, as an example in the harsh lunar scenario. The analysis will cover the determination of optimal coherent integration time T_{int} and non-coherent accumulations K which allow the receiver to acquire very low GNSS signals (down to 5 dB-Hz) with good detection probability. As we will see, extension of T_{int} in the order of seconds is needed. Thus the assumption that the on-board GNSS receiver employs self assistance techniques for secondary code synchronization or data wipe-off is taken into account.

7.3 GNSS environment on the Lunar orbit

The design of the GNSS receiver acquisition scheme for weak signal processing as well as the investigation on the required Doppler aiding accuracy is analysed taking into account the study of the Lunar GNSS environment presented in [6]. The main challenges for a GNSS receiver operating in lunar exploration mission can be identified as:

- Extremely weak GNSS signal power available at the on-board receiver;

- Poor satellites availability and satellites geometry (high **GDOP** values) i.e. low **LoS** visibility;
- Large power differences between stronger (main satellite antenna lobes) and weak signals (secondary satellite antenna lobes). Reception of strong **GNSS** signal (27-30 dB-Hz), may threat the correct acquisition of weaker signals (5-10 dB-Hz) especially if both strong and weak signals are characterized by similar dynamics. This problem is known as the near far effect;
- High dynamic environment (Doppler in the range +20 dB-Hz –20 dB-Hz);

7.4 Acquisition Scheme and Detection Algorithm

As it has been described in Section 7.3, the **GNSS** environment along the Moon Transfer Orbit (**MTO**) trajectory is extremely harsh. Low C/N_0 up to 5 dB-Hz, together with expected high Doppler and not negligible Doppler rate values, force the use of aiding information. An Assisted GNSS (**A-GNSS**) system is needed for providing information such as an a-priori knowledge of the navigation data sequence, allowing a data wipe-off operation in case of large coherent integration time and a prediction of the expected Doppler frequency. Moreover, a fast acquisition scheme would be needed for reducing the Mean Acquisition Time (**MAT**). In such scenario, an **FFT** based acquisition scheme parallel in the time domain has been considered.

Figure 7.1 shows the **FFT** based acquisition scheme, parallel in the time domain. The digital signal at the receiver front-end output received by one single satellite can be written as

$$y_{IF} = \sqrt{2C} c(nT_s - \tau) d(nT_s - \tau) \cos(2\pi(f_{IF} + f_D)n + \phi) \quad (7.1)$$

where

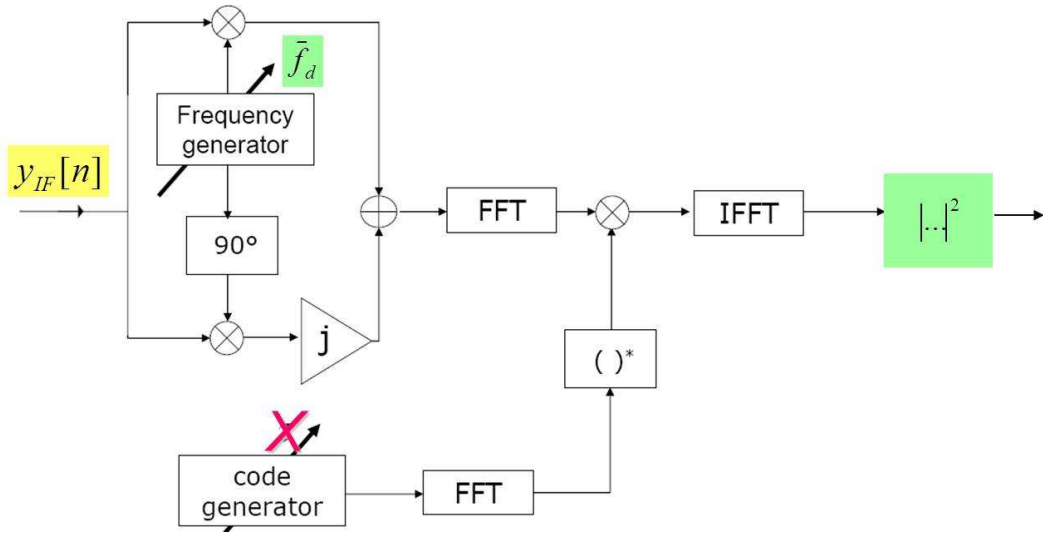


Figure 7.1: Time parallel acquisition scheme: the CAF is determined by using a circular convolution employing efficient FFTs

- C is the receiver GNSS signal power;
- c is the spreading sequence received with a delay τ ;
- d is the navigation data bit stream;
- f_{IF} is the intermediate frequency;
- f_D is the Doppler frequency affecting the GNSS signal;

In such acquisition scheme, the single digitized GNSS received signal $y_{IF}[n]$ is multiplied by the factor $\exp \{-j2\pi (f_{IF} + \bar{f}_D) n\}$ obtaining the sequence

$$q_l[n] = y_{IF}[n] \exp \{-j2\pi (f_{IF} + \bar{f}_D) n\} \quad (7.2)$$

Then, the correlation output for each bin of the search space is obtained by means of a circular correlation function defined as

$$Y(\bar{\tau}, \bar{f}_D) = \frac{1}{N} IDFT \{ DFT \{ q_l[n] \} \cdot DFT \{ c[n] \}^* \} \quad (7.3)$$

It is easy to show that the Cross Correlation Function (CCF) and the circular CCF coincide only in presence of periodic sequences. This is the case

when locally generated complex exponential perfectly matches the expected Doppler frequency f_D , except for the noise contribution and a residual term due to a double frequency $2f_D$ component contained in the term $q_l[n]$. In the other frequency bins, the presence of a sinusoidal component could alter the periodicity of the sequence [103]. Finally the evaluated CAF $S(\bar{\tau}, \bar{f}_D)$ can be evaluated as the squared modulus of the correlation output $Y(\bar{\tau}, \bar{f}_D)$, and written as

$$S(\bar{\tau}, \bar{f}_D) = [Y_I(\bar{\tau}, \bar{f}_D)]^2 + [Y_Q(\bar{\tau}, \bar{f}_D)]^2 \quad (7.4)$$

highlighting the in-phase and quadrature components.

7.4.1 Acquisition threshold determination

The basic metrics of the performance evaluation of an acquisition scheme are the detection and the false alarm probabilities of a single cell of the search space, hereinafter indicated, respectively as P_d and P_{fa} ; they are also referred as single trial probabilities. In general, the acquisition threshold determination is performed according to a required P_{fa} and to an assumption of the statistical distribution of the CAF in each cell of the search space in the null hypothesis H_0 , representing the case when the signal is not present. Whilst, once the acquisition threshold is set, the single cell detection probability can be evaluated under the statistical assumption of the distribution of the CAF in each cell in the so called alternative hypothesis H_1 when the signal is present and correctly aligned. Thus, given a determined acquisition threshold β_{th} , and naming X the generic random variable related to the single cell of the search space, the false alarm and detection probabilities can be defined as

$$\begin{aligned} P_{fa}(\beta_{th}) &= P(X > \beta_{th} | H_0) = P(X > \beta_{th} | \bar{\tau} \neq \tau \cup \bar{f}_D \neq f_D) \\ P_d(\beta_{th}) &= P(X > \beta_{th} | H_1) = P(X > \beta_{th} | \bar{\tau} = \tau \cap \bar{f}_D = f_D) \end{aligned} \quad (7.5)$$

In our case the decision variable X is the value of $S(\tau, f_D)$ in a bin of the search space. In the following the statistical characterization of the random variable X is obtained.

7.4.1.1 Coherent Acquisition

When only coherent integration time is used, each cell of the search space is obtained as the squared absolute value of a complex Gaussian random variable with independent real and imaginary part. Under the H_0 hypothesis $Y_I(\bar{\tau}, \bar{f}_D)$ and $Y_Q(\bar{\tau}, \bar{f}_D)$ are both Gaussian distributed with zero mean and variance σ_n^2 expressed as

$$\sigma_n^2 = \frac{\sigma_{IF}^2}{N_c} = \frac{N_0 B}{N_c} \quad (7.6)$$

with N_0 and B respectively the power spectral noise density and the pre correlation filter bandwidth, whilst N_c is the number of samples in one coherent integration time. Thus, being $S(\bar{\tau}, \bar{f}_D)|H_0$ the sum of the squares of two independent zero mean Gaussian random variable, the resultant probability density function is a central χ^2 distribution with two degrees of freedom

$$f_{S(\bar{\tau}, \bar{f}_D)|H_0}(x) = \frac{1}{2\sigma_n^2} \exp\left\{-\frac{x}{2\sigma_n^2}\right\}, x \geq 0; \quad (7.7)$$

Consequently the probability of false alarm is derived as

$$P_{fa} = \int_{\beta_{th}}^{\infty} f_{S(\bar{\tau}, \bar{f}_D)|H_0}(x) dx = \exp\left\{-\frac{\beta_{th}}{2\sigma_n^2}\right\} \quad (7.8)$$

Such relation can be easily inverted in order to retrieve the single cell acquisition threshold β_{th} according to a required false alarm probability.

Under the H_1 hypothesis $Y_I(\tau, f_D)$ and $Y_Q(\tau, f_D)$ are no longer zero mean, as it is shown in [103]. Thus the sum of the square of two non-zero mean independent Gaussian random variables leads to a non-central χ^2 random variable with two degrees of freedom and non-centrality parameter λ defined as

$$\lambda = E^2 [Y_I(\bar{\tau}, \bar{f}_D)] + E^2 [Y_Q(\bar{\tau}, \bar{f}_D)] = \frac{A^2}{4} = \frac{C}{2} \quad (7.9)$$

Then, the resultant probability density function is

$$f_{S(\bar{\tau}, \bar{f}_D)|H_1}(x) = \frac{1}{2\sigma_n^2} \exp\left\{-\frac{x+\lambda}{2\sigma_n^2}\right\} I_0\left(\frac{\sqrt{x\lambda}}{\sigma_n^2}\right), \quad x \geq 0; \quad (7.10)$$

Under this hypothesis the single cell detection probability can be evaluated as

$$P_d(\beta_{th}) \int_{\beta_{th}}^{\infty} f_{S(\bar{\tau}, \bar{f}_D)|H_1}(x) dx = Q_1\left(\sqrt{\frac{\lambda}{\sigma_n^2}}, \sqrt{\frac{\beta_{th}}{\sigma_n^2}}\right) \quad (7.11)$$

where $Q_k(a, b)$ is the generalized Marcum Q-function of order k^{th} .

7.4.1.2 Non-coherent Acquisition

Acquisition performance can be improved exploiting non-coherent summations, which simply consists in summing a certain number K instances of the output of the acquisition block, as shown in Figure 7.2.

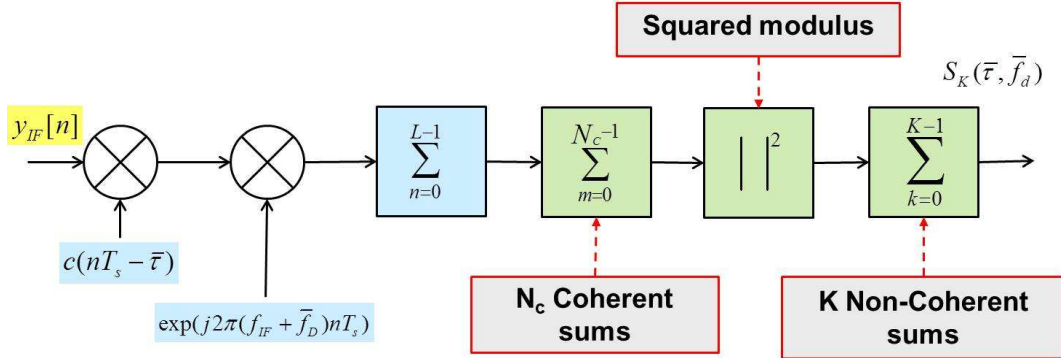


Figure 7.2: Non-coherent accumulations in acquisition scheme

The squaring blocks remove the phase dependence and the CAFs are non-coherently summed. The final decision variable becomes

$$S_K(\bar{\tau}, \bar{f}_D) = \sum_{k=0}^{K-1} S_k(\bar{\tau}, \bar{f}_D) \quad (7.12)$$

Under the H_0 hypothesis, the final CAF is the sum of K central χ^2 random variables with two degrees of freedom. Thus the final distribution is a central χ^2 with $2K$ degrees of freedom [104] which can be expressed as

$$f_{S_K(\bar{\tau}, \bar{f}_D)|H_0}(x) = \frac{1}{2\sigma_n^2} \frac{1}{\Gamma(K)} \left(\frac{x}{2\sigma_n^2}\right)^{K-1} \exp\left\{-\frac{x}{2\sigma_n^2}\right\}, \quad x \geq 0; \quad (7.13)$$

The probability of false alarm is then given by

$$P_{fa} = \int_{\beta_{th}}^{\infty} f_{S_K(\bar{\tau}, \bar{f}_D)|H_0}(x) dx = \frac{\Gamma_K\left(\frac{\beta_{th}}{2\sigma_n^2}\right)}{\Gamma(K)} \quad (7.14)$$

where $\Gamma_K(x)$ is the complementary incomplete Gamma function of order K . Under the H_1 hypothesis, the final random variable $S_K(\tau, f_D)|H_1$ is the sum of K non-central χ^2 random variables with non-centrality parameter equal to

$$\lambda = \sum_{k=0}^{K-1} \lambda_k \quad (7.15)$$

Thus, the probability density function is given by

$$f_{S_K(\bar{\tau}, \bar{f}_D)|H_1}(x) = \frac{1}{2\sigma_n^2} \left(\frac{x}{\lambda}\right)^{(K-1)/2} \exp\left\{-\frac{x+\lambda}{2\sigma_n^2}\right\} I_{K-1}\left(\frac{\sqrt{x\lambda}}{\sigma_n^2}\right), \quad x \geq 0; \quad (7.16)$$

where I_K is the modified Bessel function of the first kind of order K . Thus the probability of detection can be then derived as

$$P_d(\beta_{th}) = \int_{\beta_{th}}^{\infty} f_{S_K(\bar{\tau}, \bar{f}_D)|H_1}(x) dx = Q_K\left(\sqrt{\frac{\lambda}{\sigma_n^2}}, \sqrt{\frac{\beta_{th}}{\sigma_n^2}}\right) \quad (7.17)$$

7.4.2 Searching Strategies

So far the probabilities definitions, are related to the single cell domain. Such probabilities denoted as P_{fa} and P_d play an important role in determining the overall performance, but the acquisition decision is taken observing the whole search space, i.e. considering the statistical event generated by the combination of the random variables at the single-bin level. Thus the acquisition performances are also strongly dependent on the decision statistic and on the overall detection and overall false alarm probabilities, denoted as P_D and P_{FA} respectively. Before going to through the description and derivation of such overall probabilities, few assumptions have to be mentioned [105]

- The alternative hypothesis H_1 is verified only in one single cell of the search space. This means that, if code delay and Doppler shift are

rightly compensated on the n^{th} , only the n^{th} cell is distributed as $f_A(x)$, according to the assumption made under the hypothesis H_1 . The random cell verifying this condition is denoted with X_A .

- Only one random variable X_A is present over the whole search space.
- The variable X_A can be in any cell with a uniform probability $1/N$, being N the dimension of the whole search space
- All the random cells of the search space are supposed to be statistically independent.

Expressions of the overall false alarm and detection probabilities are strongly dependent on the chosen searching strategies. The main acquisition strategies employed in order to explore the search space are:

- *Maximum*: The correlation function is evaluated all over the search space, for each value of Doppler shift and code delay. Then only the maximum value of the CAF is compared with the acquisition threshold β_{th} .
- *Serial*: Here the ambiguity function is serially evaluated cell by cell. Each value is compared to the acquisition threshold, and the acquisition process stops at the first threshold crossing.
- *Hybrid*: The ambiguity function is evaluated row-by-row, exploiting for example FFT-based algorithms and the decision is taken on the maximum of each row-by-row. The acquisition process terminates as soon as the maximum in the current row exceeds the threshold.

The acquisition performance study will be carried on taking into account the Maximum strategy search.

7.4.2.1 MAXIMUM Strategies: detection probability P_D

Using this strategy, a right decision is obtained when X_A assumes the maximum value within the search space and it passes the threshold β_{th} . Thus the overall detection probabilities can be rewritten as

$$P_D(\beta_{th}) = P\left(X_A = \max_n \{X_n\}, X_A > \beta_{th}\right) \quad (7.18)$$

Denoting with γ the value assumed by the random variable X_A , using the theorem of the total probability, the overall detection probability can be rewritten as

$$P_D(\beta_{th}) = \int_{\beta_{th}}^{\infty} \prod_{n=1}^N P(X_A \geq X_n | X_A = \gamma) f_A(x) dx \quad (7.19)$$

In the last product all the terms are equal except to the one corresponding to the case $X_A \equiv X_n$. So there are $N - 1$ terms equal of the type

$$P(X_A \geq X_n | X_A = \gamma) = P(X_n < \gamma | H_0) = 1 - P(X_n > \gamma | H_0) = 1 - P_{fa}(\gamma) \quad (7.20)$$

and only one term equal to

$$P(X_A \geq X_n | X_A = \gamma) = P(\gamma \geq \gamma | X_A = \gamma) = 1 \quad (7.21)$$

Thus the overall detection probability expression becomes

$$P_D = \int_{\beta_{th}}^{\infty} [1 - P_{fa}(\gamma)]^{N-1} f_A(x) dx \quad (7.22)$$

If $P_{fa}(\gamma)$ is small enough, then the overall detection probability reduces to

$$P_D \approx \int_{\beta_{th}}^{\infty} f_A(x) dx \quad (7.23)$$

7.4.2.2 MAXIMUM Strategies: false alarm probabilities P_{FA}

Differently from the false alarm probability P_{fa} at cell level, which is by definition in absence of signal, the overall false alarm probability P_{FA} changes depending if the signal is present or not. In order to avoid confusion the false alarm probabilities in absence or presence of signal will be named respectively

P_{FA}^a and P_{FA}^p . The case of signal absence is analysed first.

In this scenario a wrong detection happen when the maximum of the ambiguity function crosses the acquisition threshold β_{th} . Then the P_{FA}^a becomes

$$\begin{aligned}
 P_{FA}^a &= P\left(\max_n \{X_n\} > \beta_{th}\right) = \\
 &= 1 - P\left(\max_n \{X_n\} < \beta_{th}\right) = \\
 &= 1 - \prod_{n=1}^N (1 - P(X_n > \beta_{th})) = \\
 &= 1 - (1 - P_{fa}(\beta_{th}))^N
 \end{aligned} \tag{7.24}$$

Figure 7.3 shows the increasing trend of the P_{FA}^a with respect the increasing number of bins in the search space, for a given $P_{fa} = 10^{-8}$ at cell level.

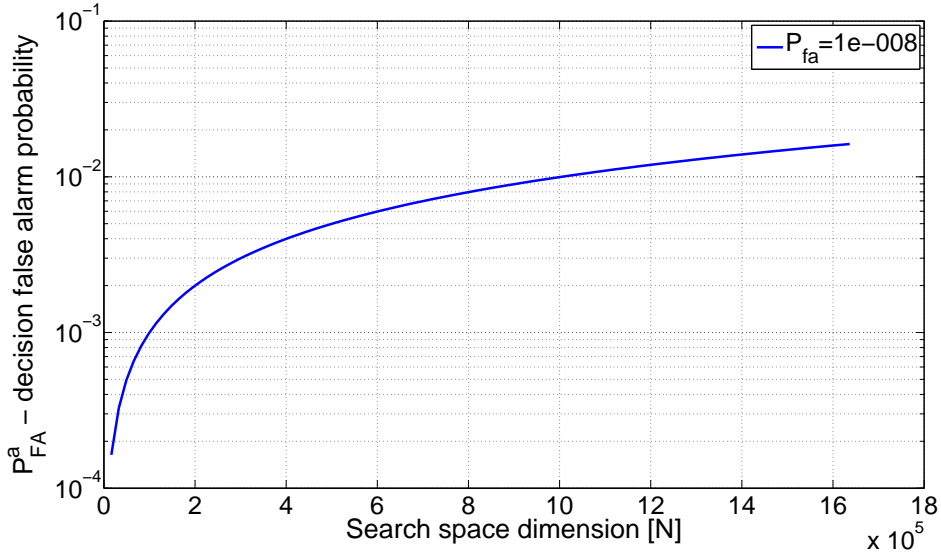


Figure 7.3: False alarm probability at search space level versus the number of bins in the search space for a fixed false alarm probability at cell level

Figure 7.4 shows the P_{FA}^a trend versus the P_{fa} at cell level. The four curves are related to four different value of N . In both Figure 7.3 and Figure 7.4 it can be observed that the false alarm probability P_{FA}^a at search space level improves together with the reduction of the number of bins in the search space. However it has to be noticed that P_{FA}^a assumes higher values with respect the false alarm probability at cell level P_{fa} .

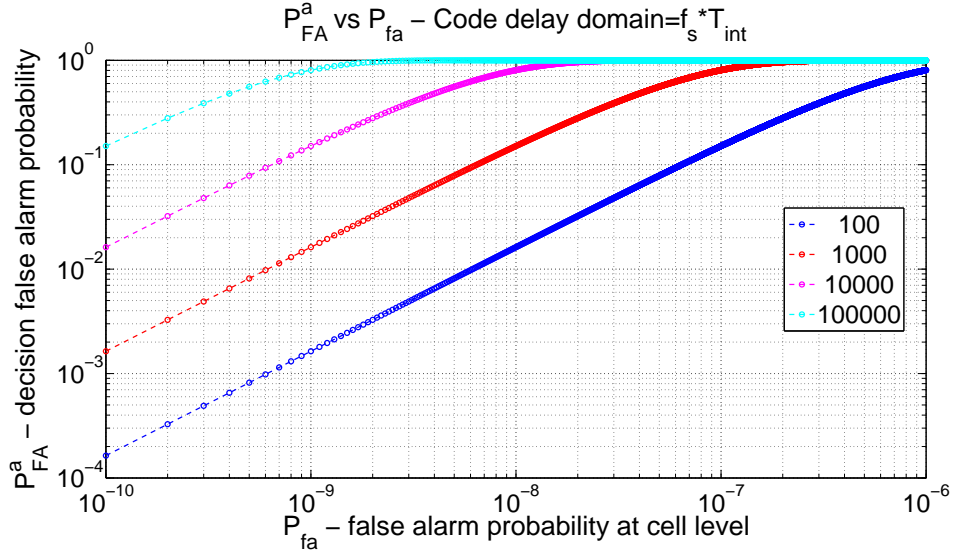


Figure 7.4: False alarm probability at search space level versus false alarm probability at cell level for a fixed number of bins in the search space

When the signal is present, the expression of the P_{FA}^p can be easily obtained by difference, as

$$P_{FA}^p(\beta_{th}) = 1 - P_D(\beta_{th}) - P_{MD}(\beta_{th}) \quad (7.25)$$

where $P_{MD}(\beta_{th})$ is the overall missed-detection probability. A missed-detection occurs when the satellite is present but it is not detected. This happens when no cell value exceeds the acquisition threshold. Thus, the overall missed-detection probability can be defined as

$$P_{MD}(\beta_{th}) = \sum_{n=1}^N P(X_n < \beta_{th}) \quad (7.26)$$

where

$$P(X_n < \beta_{th}) = \begin{cases} 1 - P_d(\beta_{th}), & \text{when } X_A \equiv X_n \\ 1 - P_{fa}(\beta_{th}), & \text{when } X_A \neq X_n \end{cases} \quad (7.27)$$

Therefore the overall missed-detection probability becomes

$$P_{MD}(\beta_{th}) = [1 - P_{fa}(\beta_{th})]^{N-1} \cdot \int_0^{\beta_{th}} f_A(x) dx \quad (7.28)$$

7.5 Theoretical Acquisition Sensitivity Analysis

A method for assessing the acquisition performance is based on the evaluation of the **SNR** defined along the receiver processing chain. Hereafter, the definitions of coherent **SNR** and **SNR** after non coherent accumulation will be provided.

7.5.1 Coherent SNR

As proved in [102], the coherent **SNR** is defined as the ratio of the post-correlation signal power and the noise power

$$SNR = \left(\frac{S}{\sigma_N} \right)^2 \quad (7.29)$$

where S is the amplitude of the correlation peak, while σ_N , is the standard deviation of the noise after correlation. Denoting with N_c , the number of samples accumulated within a coherent integration time, considering an idealized coherent integration (infinite bandwidth and uncorrelated noise), the signal magnitude grows by N_c , and the noise standard deviation by $\sqrt{N_c}$. Thus, the coherent **SNR** ρ_c will grow as

$$\rho_c = SNR_{pre} \cdot \left(\frac{N_c^2}{\sqrt{N_c}} \right) = SNR_{pre} \cdot N_c \quad (7.30)$$

where N_c represent the ideal coherent gain. Thus, in ideal condition, use of higher sampling frequency would lead to an increased coherent gain. However, the increase of the sampling frequency may not be a solution for achieving higher coherent **SNR**. As it is shown in [102], use of a higher sampling frequency with respect the Nyquist sampling frequency can lead to a decrease of ρ_c caused by the correlated noise samples.

Figure 7.5 shows the coherent **SNR** for GPS L1 C/A code ($R_c = 1.023$ Mchips/s), signal at 5 dB-Hz, according to the ideal front-end parameter

showed in Table 7.1. The blue curve represents the coherent SNR ρ_c plotted versus the coherent integration time. The three coloured straight lines refer to three different values of the squared ratio between the acquisition threshold β_{th} and the correlation noise standard deviation (i.e.in dBs $20 \cdot \log_{10}(\beta_{th}/\sigma_N)$), obtained for three different false alarm probabilities P_{fa} at single cell level. Such level represents the SNR threshold corresponding to the chosen threshold β_{th} .

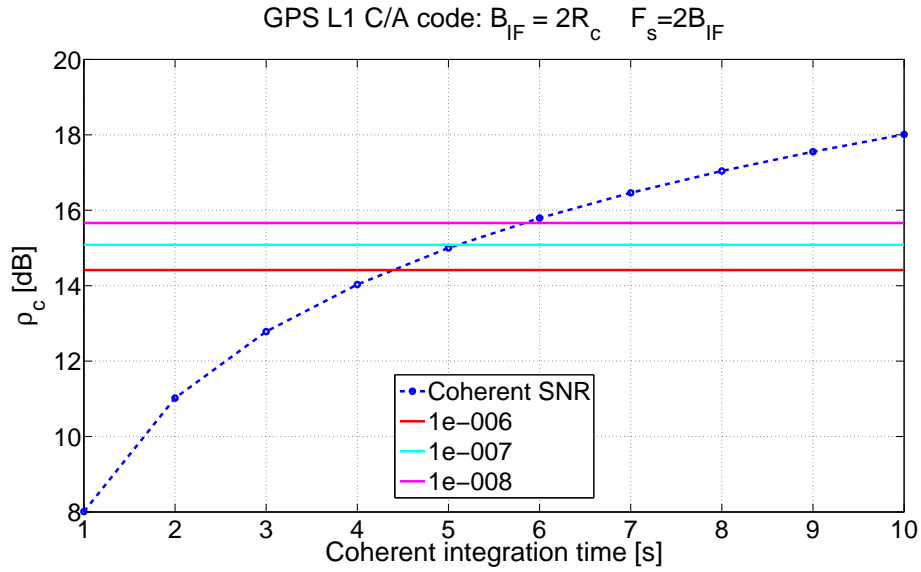


Figure 7.5: Coherent SNR

Table 7.1: Ideal Front-end parameter for GPS L1 C/A code

Front-end parameters	Value
B_{IF}	$2R_c$ (GPS L1 C/A code)
F_s	$2B_{IF}$

Figure 7.6 shows different Receiver Operating Characteristic (ROC) curves obtained for different values of coherent integration time. It can be noted that, for a $P_{fa}10^{-8}$, which will guarantee a false alarm probability at search space level P_{FA}^a of 10^{-2} , as it will be shown later during the theoretical investigation, a P_d more than approximately of 90% can be achieved if a coherent integration time larger than 16 seconds is used, in the ideal case. Results shown in Figure

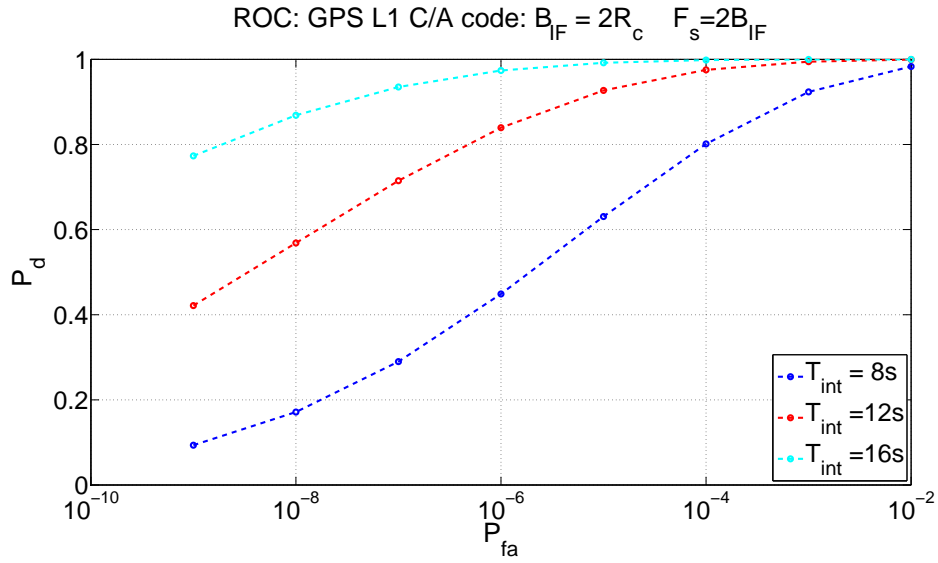


Figure 7.6: ROC curve - Coherent integration

7.5 and Figure 7.6 are obtained in an idealized case, where losses related to the IF filtering of the GNSS signal, quantization, frequency mismatch, code alignment and correlated noise are neglected. Such losses are described in details in [102].

7.5.2 Non-Coherent signal accumulation

When non-coherent signal accumulation is present, the Sum-of-Squares (SS) operation changes the correlation peak magnitude as well as the standard deviation of the correlation noise floor. Such an effect is limited by the so called squaring loss, which can be defined as

$$L = \frac{\text{post SS SNR}}{\rho_c} \quad (7.31)$$

A generalized expression for the squaring loss is presented in [104] as

$$L = 10 \cdot \log_{10} \left(\frac{4 - \pi}{\pi} \right) + \rho_c|_{dB} - 20 \cdot \log_{10} \left\{ \exp \left(-\frac{\rho_c}{4} \right) \left[\left(1 + \frac{\rho_c}{2} \right) I_0 \left(\frac{\rho_c}{4} \right) + \left(\frac{\rho_c}{2} \right) I_1 \left(\frac{\rho_c}{4} \right) \right] - 1 \right\} \quad (7.32)$$

where I_n is the modified Bessel function of the first kind of order n . Thus after the non-coherent accumulation of K instances of $S(\tau, f_D)$, the final SNR ρ_{nc} becomes

$$\rho_{nc}|_{dB} = \rho_c|_{dB} - L + 10 \cdot \log_{10} K \quad (7.33)$$

Figure 7.7 shows the non-coherent SNR ρ_{nc} with respect three different values of the squared ratio between the acquisition threshold β_{th} and the correlation noise standard deviation, obtained at three different false alarm probabilities P_{fa} at single cell level and for different values of non-coherent summations K .

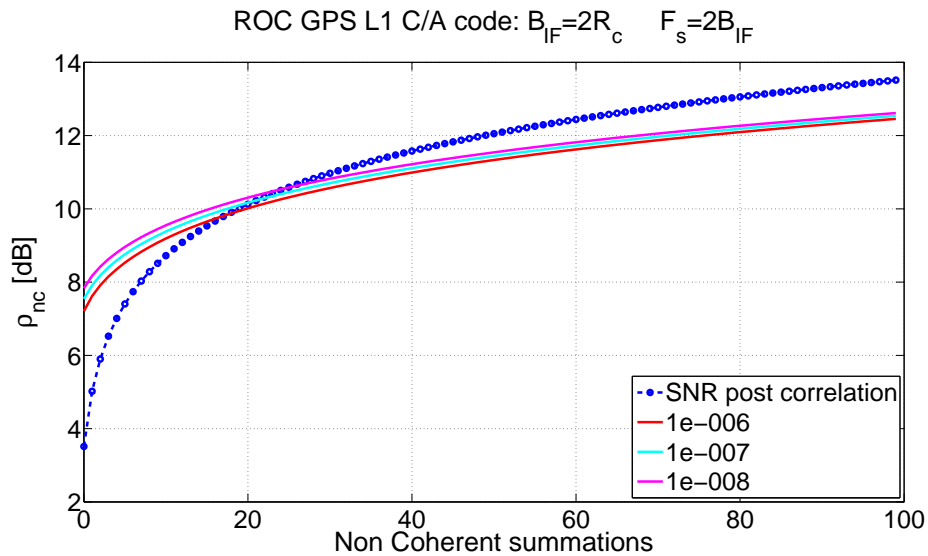


Figure 7.7: Non coherent acquisition performance

Such theoretical results have been obtained for GPS signal and for a coherent integration time of 1s. This example shows how it is then possible to reduce the coherent integration time but a large number of non-coherent accumulations are needed. Figure 7.8 shows the different ROC curves in the case of different values of non-coherent accumulations. Each ROC curve is obtained fixing a coherent integration time equal to 1 s.

Good detection performances at cell level can be achieved with a number of non-coherent summations above larger than 35, as confirmed in the results in Figure 7.7. A great portion of signal needs to be processed in order to achieve

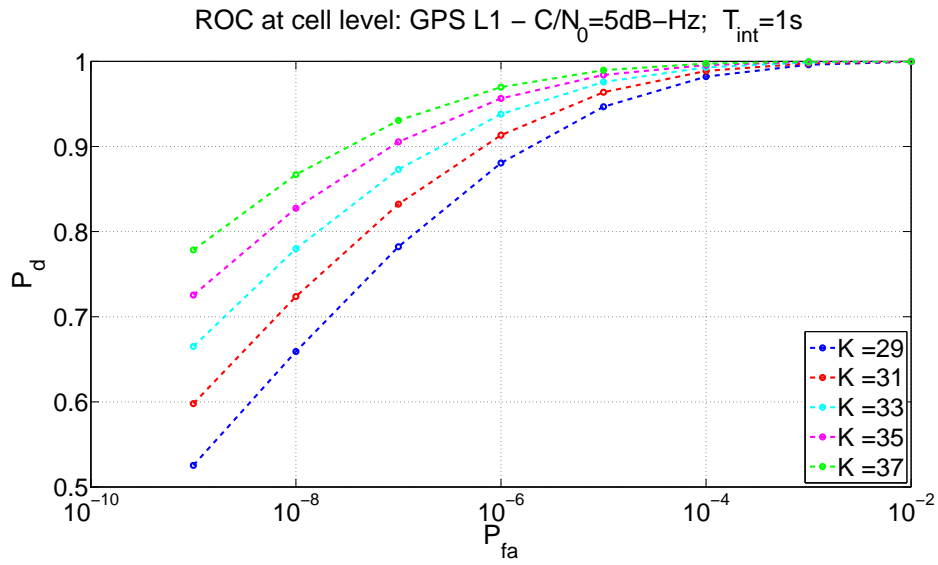


Figure 7.8: ROC curve- Non coherent integration

correct signal acquisition. This is due to the fact that, at 5 dB-Hz a coherent integration time equal to 1s leads to a low coherent SNR resulting in a not negligible squaring loss of 1 dB, as seen in Figure 7.9, where (7.32) is plotted with respect the coherent integration time.

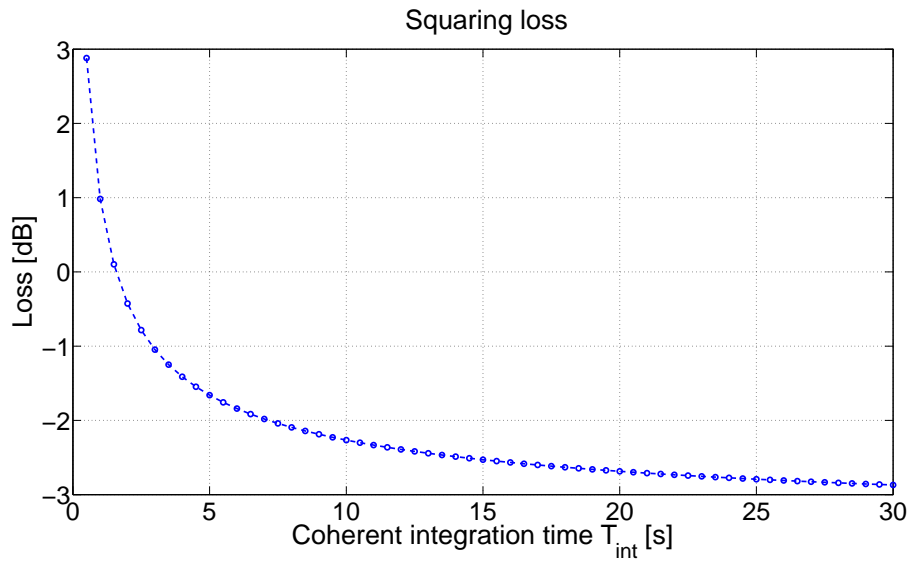


Figure 7.9: Squaring loss

However, such an analytical formula expressed in (7.32) has to be considered valid for coherent SNR lower than 10 dB, thus for coherent integration time lower than 2 second.

The results previously presented represent a theoretical bound of the acquisition performance according to the parameter in 7.1. In a more realistic scenario where GNSS receiver exploits wider bandwidth and greater sampling frequency, GNSS signal acquisition at 5 dB-Hz can be achieved employing shorter coherent integration time and a smaller number of non-coherent accumulations. Use of proper higher sampling frequency, which will minimize the digital noise samples correlation, will increase the number of samples coherently integrated which in turns means higher coherent SNR. The actual performance of the acquisition scheme depends on several others factor that might increase the required total processing time.

However, the bounds obtained demonstrates how the availability of assistance data is mandatory in order to achieve the acquisition of the signals. The role of the assistance data will be to allow for coherent integration times longer than the bit duration, and reduction of the size of the search space thanks to the availability of Doppler estimates. In case of Galileo signals the availability of the assistance for the data wipe-off can be avoided thanks to the presence of the pilot channel. Nevertheless, assistance for the reduction of the search space to investigate is always needed.

7.6 Assisted GNSS: theoretical performance and requirements definition

Due to the harsh environments addressed in the framework of the lunar GNSS project, an A-GNSS system is required. Generally speaking, assistance data could be able to increase the acquisition and tracking sensitivity of the receiver thus allowing to process extremely low GNSS signals. It has been shown in Section 7.5 that the acquisition of low GPS L1 signal (down to 5 dB-Hz) can be achieved exploiting long coherent integration time or a combination of

shorter coherent integration time and a large number of non-coherent accumulations. Nevertheless, extension of coherent integration time beyond the data duration would require assistance information (i.e. the delivery of binary message content) in order to perform a data wipe-off operation. Such an assistance may be avoided when dealing with acquisition of GNSS signal featuring pilot channel. However, such a choice, raises a further problem concerning the processing of a signal with 3dB loss, and proper techniques for the secondary code synchronization have to be implemented. Other significant assistance options foresee the delivery of ephemeris of the GNSS satellites, which would increase the receiver sensitivity, avoiding ephemeris data demodulation, as well as the delivery of reference time and location information that integrated in an orbital filter that would allow estimation of Doppler frequency thus reducing the size of the search space domain and the MAT. In the following sections a methodology for the design of a HS acquisition scheme is presented. The analysis is carried out assuming the presence of an external or receiver embedded Doppler aiding capable of providing accurate Doppler and Doppler rate information to the receiver acquisition block.

7.6.1 Search space reduction: Doppler domain

As shown in Section 7.4, the acquisition metrics defined at search space level strongly depends on the search space dimension. Use of advanced signal processing technique, such as a kalman filter based orbital filter capable of integrating assistance data as reference time and location of the receiver together with satellite position and velocity, and providing Doppler frequency and Doppler rate within few Hz, will reduce the acquisition search space in the Doppler domain thus improving false alarm probability at cell level, as expected from (7.24). Acquisition search space dimension is of course determined by the chosen code delay step and Doppler step. Concerning the parallel acquisition scheme under investigation, the code delay step is mainly

determined by the number of points used in the FFT computation. The employed MATLAB® version of N-Gen software receiver, performs FFT over a number of points equal to the number of samples within one code period T_{code} . Indeed, for a given sampling frequency f_s

$$N_{FFT} = T_{code} \cdot f_s \quad (7.34)$$

Therefore the code delay domain size will be equal to N_{FFT} .

Concerning the Doppler frequency domain, the Doppler step is mainly determined by the coherent integration time T_{int} through the following empirical rule [7]

$$\Delta_f = \frac{2}{3T_{int}} \quad (7.35)$$

which allows to minimize the losses at the boundary of the bin. Thus, knowing the maximum and minimum Doppler frequency ($f_{D,max}$ and $f_{D,min}$), the search space dimension N can be determined by

$$N = \left(\frac{f_{D,max} - f_{D,min}}{\Delta_f} + 1 \right) \cdot N_{FFT} \quad (7.36)$$

Defining T_P as the portion of signal processed in order to obtain the whole search space, for a fast acquisition scheme parallel in the time domain, it becomes

$$T_P = K \cdot T_{int} \cdot \left(\frac{f_{D,max} - f_{D,min}}{\Delta_f} + 1 \right) \quad (7.37)$$

where K is the number of CAF non-coherently accumulated.

7.6.2 Assisted GNSS definition requirements: methodology

In order to provide requirements on the assistance system which in turns coincides with the definition of the accuracy required by an internal/external Doppler aiding source, the following approach has been adopted:

1. Choice of a false alarm probability at search space level in absence of signal P_{FA}^a and evaluation of the related false alarm probability at cell

level P_{fa} through (7.24), considering different aiding scenarios. Each aiding scenario is identified according to the errors computed by an internal Doppler aiding system or uncertainty of the external Doppler assistance data, as well as the drift of the on board clock in generating the frequency. Defining ϵ_{f_D} such a total uncertainty, in case of Doppler aiding, the number of bins in the Doppler domain reduces to

$$N_{bins,D} = \frac{\epsilon_{f_D}}{\Delta_f} + 1 \quad (7.38)$$

which will also impact on the processing time T_P .

2. Assessment of the detection probability at cell level P_d by means of theoretical ROC curves.
3. Assessment of detection probability at search space level P_D .
4. Assessment of missed-detection probability at search space level P_{MD} .
5. Assessment of false alarm probability at search space level in presence of signal P_{FA}^P
6. Assessment of processing time T_P needed for whole search space computation.

It has to be mentioned that, even if in presence of high accurate Doppler aiding, residual Doppler may be still present due to the finite accuracy of the local oscillator frequency, which usually differs from the nominal value of an amount related to the adopted oscillator technology. Typical figures of (relative) frequency accuracy are 10^{-6} for Temperature Compensated Crystal Oscillators (TCXOs) and 10^{-8} for Oven Controlled Crystal Oscillators (OCXOs). A first consideration is that the OCXOs technology is suggested in order to preserve the accuracy achievable with Doppler estimation algorithms and limit the frequency search range for HS acquisition stages, which can thus afford for the required complexity due to the extension of the integration time. For the scope of the analysis ϵ_{f_D} is the total uncertainty, including the clock drift effect.

7.6.3 Case study: Acquisition on the lunar orbit

The theoretical investigation on the optimal acquisition system parameters and the definition of the Doppler aiding requirements for feeble GNSS signals detection on the lunar orbit have been carried out considering the following frequency band:

- Galileo E1;
- GPS L1;
- Galileo E5a;

For the GNSS signals acquisition in the Galileo E1/E5a frequency bands, only pilot channels processing has been considered assuming full secondary code synchronization. Furthermore, concerning the Galileo E1c channel, reception of the full Composite Binary Offset Carrier (CBOC) modulation has been assumed. Analysis on the GPS L1 C/A code acquisition has been performed assuming perfect data wipe-off. The results achieved by the theoretical design of the overall systems are then validated by means of software simulations exploiting the N-Genie fully software receiver [77]. For this purpose, the fully software GNSS signal generator at Intermediate Frequency, N-Fuels [98] has been adopted for the generation of the expected GNSS environment on the Low Lunar Orbit (LLO). Such a signal generator has been modified in order to exclude the presence of secondary code for those signals featuring the pilot channel (e.g. Galileo E1/E5a in this Section).

7.6.3.1 Galileo E1c channel acquisition

When acquiring the pilot channel only, the acquisition scheme has to deal with 3dB of loss which then will require higher coherent integration time. However, taking into account the GNSS space environment presented in [6],

a 5 dB-Hz of acquisition threshold on the Galileo E1c pilot channel only allows for an acceptable number of satellites in view.

Galileo E1c pilot channel features a primary code of a duration equal to 4 ms and a secondary code tiered to the primary code composed of 25 chips for a final length of 100 ms. The analysis is based on the assumption that synchronization with secondary code is already achieved, thus only the synchronization within one primary code period duration is required. As a consequence, the dimension of the search space along the code delay domain will be

$$N_{FFT} = T_{code} \cdot f_s = 0.004 \cdot f_s \quad (7.39)$$

four times larger with respect the code delay domain in case of GPS L1 signal acquisition.

Table 7.2 summarizes the scenario parameters considered during the theoretical investigation. Since the full CBOC modulation is considered for the Galileo E1c pilot channel, the theoretical investigation on the Doppler aiding requirements is carried out assuming a wider front-end bandwidth (e.g. 20.46 MHz), and thus higher sampling frequency with respect those needed for the reception of the BOC modulation only.

Table 7.2: E1c Galileo signal: scenario parameters

Signal and RX front-end parameters	Values
Signal	E1c
C/N_0	5 dB-Hz
Front-end bandwidth	20.46 MHz
T_{int}	2
K	10
f_s	50 MHz

The coherent integration time T_{int} and the number of non coherent accumulations K reported in 7.2 leads to optimal detection probability P_d at single cell level even for extremely small false alarm probability P_{fa} , as it can be observed in Figure 7.10 where the ROC curves are shown.

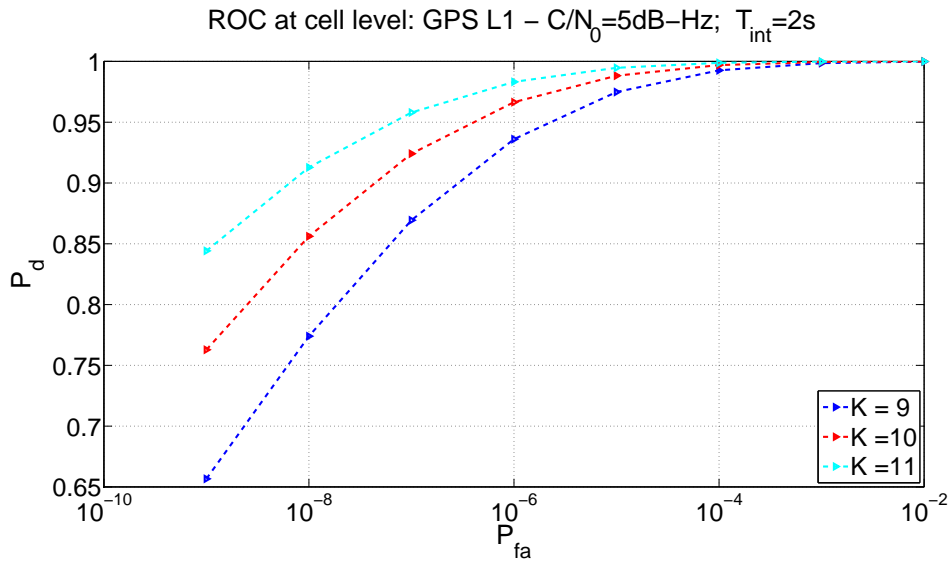


Figure 7.10: Galileo E1c non coherent acquisition: Theoretical ROC curves at cell level

Targeting an overall false alarm probability P_{FA}^a of 10^{-2} , and exploiting 2s of coherent integration time T_{int} combined with 10 non coherent accumulations, a Doppler aiding accuracy of 0.5 Hz is required, as reported in Figure 7.11

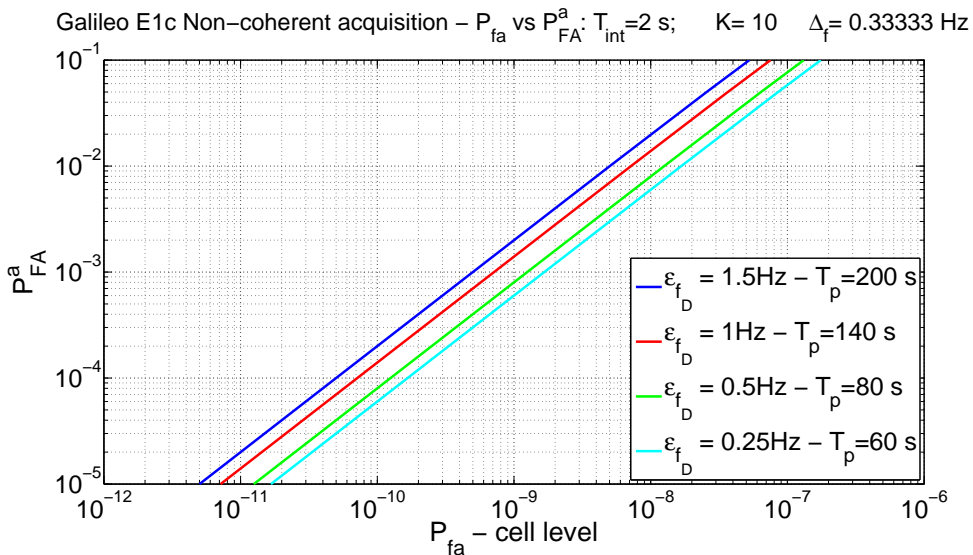


Figure 7.11: Galileo E1c non coherent acquisition: Acquisition metrics P_{FA}^a vs P_{fa} for different aiding scenario

Figure 7.12, Figure 7.13 and Figure 7.14 provide respectively the detection probability P_D , the missed detection probability P_{MD} and the false alarm

probability in presence of signal P_{FA}^p which can be achieved at whole search space level.

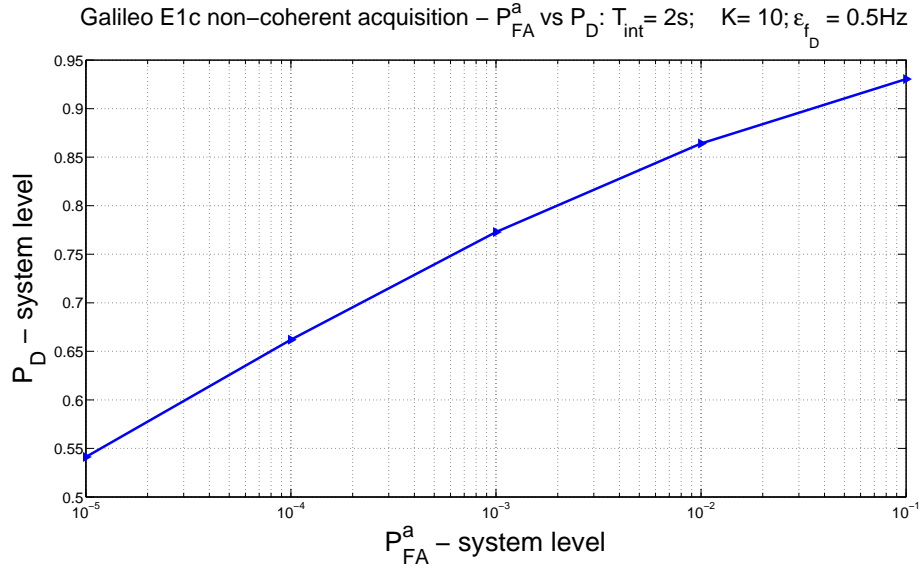


Figure 7.12: Galileo E1c non coherent acquisition: Theoretical ROC curve at search space level (P_D)

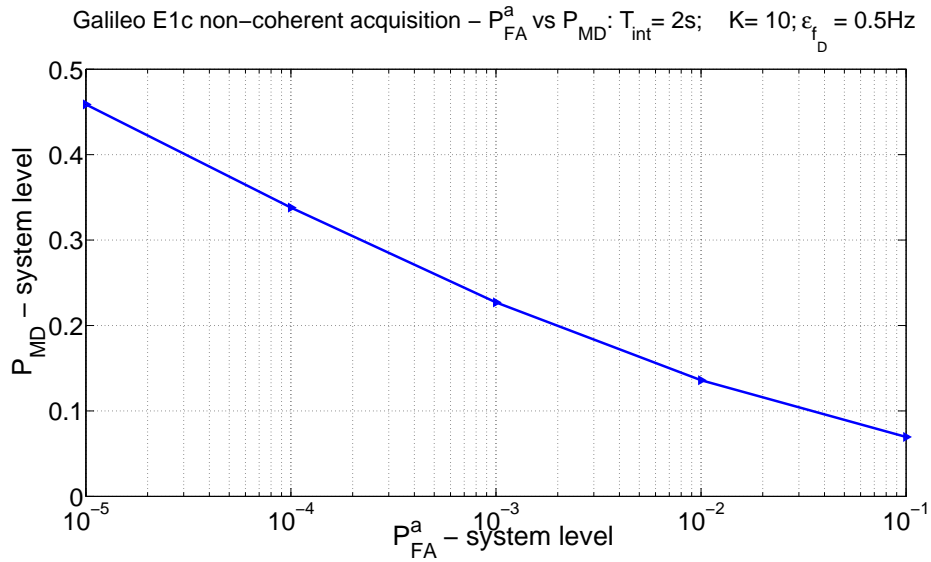


Figure 7.13: Galileo E1c non-coherent acquisition: Theoretical ROC curve at search space level (P_{MD})

A summary of the acquisition system design for weak Galileo E1c signal detection is proposed in Tables 7.3 and 7.4. where pure coherent acquisition strategy and non coherent acquisition strategy are respectively considered.

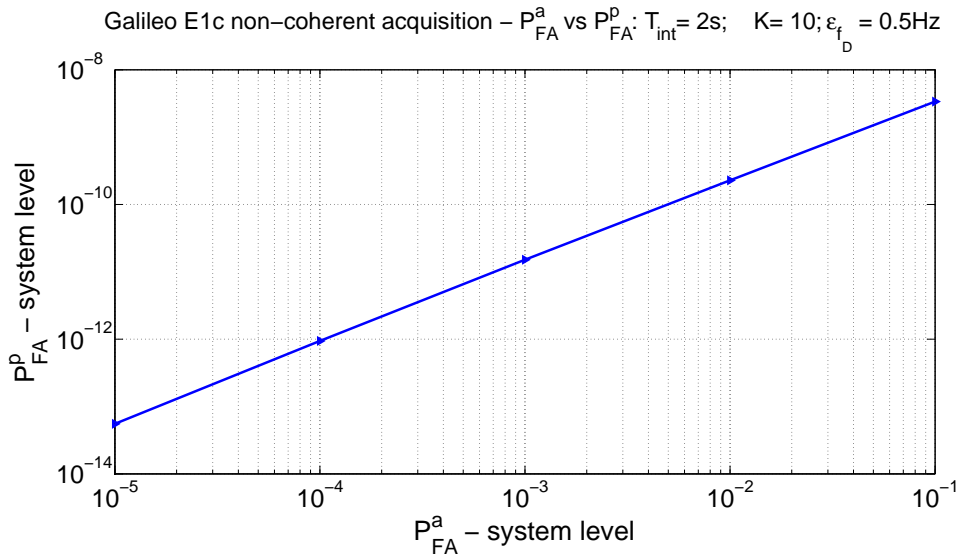


Figure 7.14: Galileo E1c non coherent acquisition: Theoretical ROC curve at search space level (P_{FA}^p)

Table 7.3: Assisted GNSS: Theoretical results for pure coherent Galileo E1c signal acquisition

C/N_0	5 dB-Hz	10 dB-Hz
Acquisition parameters	$T_{int} = 13s$	$T_{int} = 5s$
P_{FA}^a	$\approx 10^{-2}$	10^{-2}
P_{fa}	10^{-8}	10^{-8}
ϵ_{f_D}	0.25 Hz	0.5 Hz
P_d	86.3%	96.5%
P_D	83.2%	96.5%
P_{MD}	16.5%	0.03
P_{FA}^p	$2 \cdot 10^{-3}$ Hz	$5 \cdot 10^{-4}$
T_P	143 s	45.6 s

The results in Tables 7.3 and 7.4 show how the acquisition of the E1c channel is a challenging operation. Coherent integration time needs to be increased due to a wider IF filter bandwidth which increases the noise power at the input of the acquisition block. Such an increased coherent integration time causes also the increasing of the search space dimension according to (7.35) and (7.36). However the use of non-coherent accumulations strategy should be preferred with respect the pure coherent acquisition scheme, since it allows

Table 7.4: Assisted GNSS: Theoretical results for non coherent Galileo E1c signal acquisition

C/N_0	5 dB-Hz	10 dB-Hz
Acquisition parameters	$T_{int} = 2\text{s}; K = 10$	$T_{int} = 0.7\text{s}; K = 9$
P_{FA}^a	$\approx 10^{-2}$	10^{-2}
P_{fa}	10^{-8}	10^{-8}
ϵ_{fD}	0.5 Hz	1.5 Hz
P_d	85.6%	87.7%
P_D	85.4%	87.7%
P_{MD}	13.6%	12.26%
P_{FA}^p	$2.2 \cdot 10^{-10}$ Hz	$6.8 \cdot 10^{-10}$
T_P	80 s	31.5 s

for the reduction of the coherent integration time leading to less stringent requirements on the Doppler aiding. Substantial gain is also achieved in terms of processing time T_p needed for the whole search space computation when comparing the pure coherent acquisition performance with the acquisition performance achieved exploiting non coherent accumulations. In order to achieve the targeted false alarm probability at search space level of 10^{-2} , pure coherent acquisition schemes require extremely high accurate Doppler aiding (within 0.25 and 0.5 Hz respectively at 5 and 10 dB-Hz as shown in Table 7.3). Exploiting a proper number of non-coherent accumulations, such a targeted decision probability can be achieved with a less stringent requirement on the accuracy provided by the Doppler aiding.

On the basis of the theoretical analysis presented in Sections 7.6, where the overall design of the acquisition system together with the definition of the Doppler aiding accuracy requirements have been investigated, a simulation test campaign for assessing acquisition performance in case of Galileo E1c pilot channel reception in a LLO scenario, defined in Table 7.5, has been performed.

In such a scenario the on-board GNSS receiver operates in an environment

Table 7.5: Lunar Low Orbit scenario: Galileo E1bc CBOC

Number of SVN	5
PRN	from 1 to 5
Doppler Frequency f_D	[15; 20; -5; -10; 15] kHz
Code delay τ	[2; 0.5; 1.6; 0.8; 1] ms
C/N_0	[8; 9; 11; 15; 28] dB-Hz

characterized by GNSS signals with Doppler between +20 kHz and -20 kHz and Doppler rates reaching 5 Hz/s. Concerning the Galileo constellation coverage, only 5 satellites have been assumed visible to the on-board GNSS antenna on the LLO. Concerning the level power, values between 5 and 15 dB-Hz have been assumed for the C/N_0 . Furthermore, the considered scenario foresee the presence of only one Galileo E1c signal coming from the main lobe of a satellite for small portion of the time, thus leading to a C/N_0 of 25 dB-Hz, 20 dB over the weakest Galileo E1c received signal.

In order to assess the presence of near far effect impact on the Galileo E1c PRN1 acquisition, Doppler frequency of the weakest and strongest Galileo E1c, respectively (PRN 1 and PRN 5) has been set to the same value of 15 KHz.

N-Fuels signal generator have been set in order to generate for each PRN the full Galileo E1bc CBOC modulation according to the values reported in Table 7.5.

Figure 7.15 shows the acquisition search space of the Galileo E1c channel (PRN 1) achieved by the software received exploiting 9 non coherent accumulations with a coherent integration time of 2s. Correct acquisition of Doppler frequency and code delay is achieved, as it can be observed from the main acquisition peak crossing the threshold (black floor).

The achieved correct acquisition is also confirmed looking at the CAF in the code delay and Doppler domain respectively in Figure 7.16(a) and Figure 7.16(b), where the highest correlation peak is detecting in correspondence of

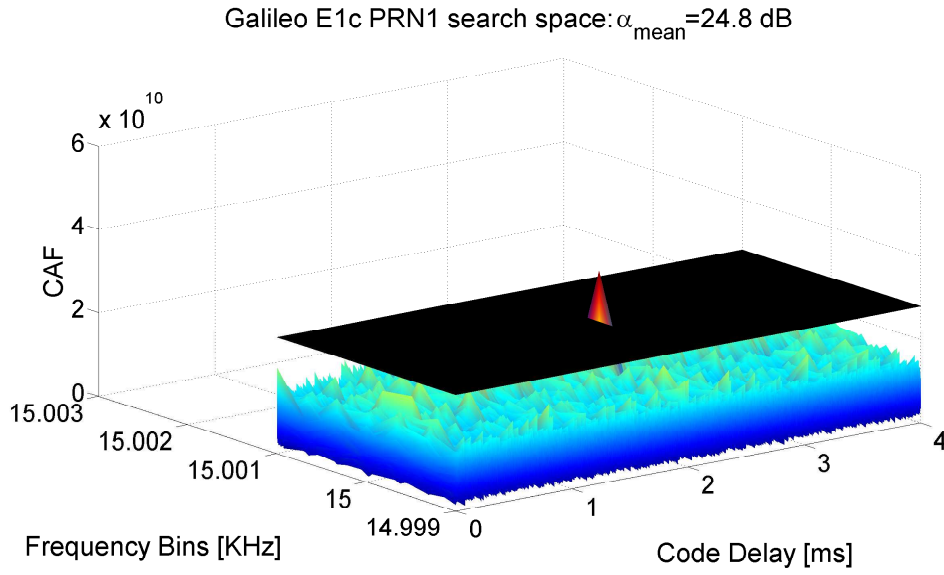


Figure 7.15: Galileo E1c non coherent acquisition: Search Space

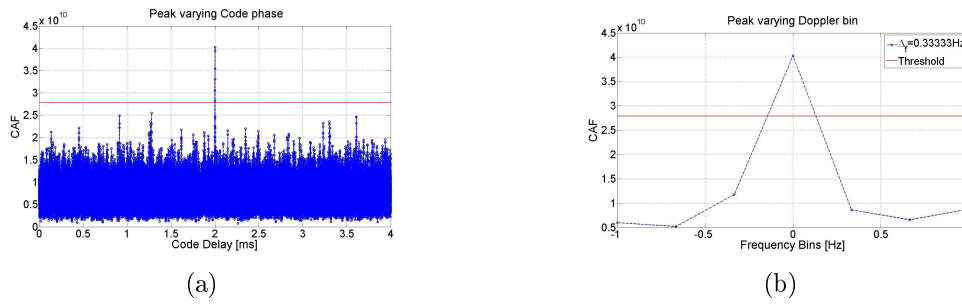


Figure 7.16: Galileo E1c acquisition at 5 dB-Hz: CAF in the code delay 7.16(a) and Doppler 7.16(b) domain

$\tau = 2$ ms and $f_D = 15$ kHz.

Furthermore cross correlations with the received strong PRN5 are mitigated due to the use of a smaller coherent integration time and a sufficient numbers of non-coherent accumulations which leads to an averaging of the noise floor.

7.6.3.2 GPS L1 C/A code acquisition

Following the same methodology presented in Section 7.6.2, investigation and Doppler aiding requirements definition for weak GPS L1 C/A code acquisition on the LLO has been performed and results are summarised in Table 7.6 and Table 7.7.

Table 7.6: Assisted GNSS: Theoretical results for pure coherent GPS L1 C/A signal acquisition

C/N_0	5 dB-Hz	10 dB-Hz
Acquisition parameters	$T_{int} = 7\text{s}$	$T_{int} = 3\text{s}$
P_{FA}^a	10^{-2}	10^{-2}
P_{fa}	10^{-7}	10^{-7}
ϵ_{fD}	0.25 Hz	0.5 Hz
P_d	85.5%	95.6%
P_D	85.3%	95.4%
P_{MD}	14.4%	0.01
P_{FA}^p	$\approx 10^{-3}$ Hz	$2.5 \cdot 10^{-4}$
T_P	43.75 s	18 s

Table 7.7: Assisted GNSS: Theoretical results for non coherent GPS L1 C/A signal acquisition

C/N_0	5 dB-Hz	10 dB-Hz
Acquisition parameters	$T_{int} = 1\text{s}; K = 12$	$T_{int} = 0.5\text{s}; K = 8$
P_{FA}^a	10^{-2}	10^{-2}
P_{fa}	10^{-7}	10^{-7}
ϵ_{fD}	2 Hz	3 Hz
P_d	87.5%	92.6%
P_D	87.1%	91.5%
P_{MD}	12.8%	3.4%
P_{FA}^p	$4.6 \cdot 10^{-11}$ Hz	$1.8 \cdot 10^{-9}$
T_P	84 s	24 s

As expected, lower coherent integration time for GPS L1 C/A acquisition at 5 and 10 dB-Hz are needed with respect the values reported in Table 7.3 and 7.4, due to the smaller front-end bandwidth and consequent reduction of the noise power leaking through the correlators. Both Tables confirm that the use of non-coherent accumulations allows for a reduction of the coherent integration time and thus to a less stringent requirements on the Doppler aiding accuracy.

Near-Far effect on the weakest received GPS L1 C/A signal (PRN1) acquisition has been investigated and the result is presented in Figure 7.17. N-Fuels signals generator has been tuned in order to generate synthetic data at IF in the GPS L1 representative of the multiple satellites scenario defined in Table 7.8. In this case, for all the selected PRNs, generation of the data navigation message has been excluded.

Table 7.8: Lunar Low Orbit scenario: GPS L1 C/A

Number of SVN	8
PRN	from 1 to 8
Doppler Frequency f_D	[15; 20; 10; 5; -5; -10; -15; 15] kHz
Code delay τ	[0.5; 0.1; 0.2; 0.3; 0.4; 0.5; 0.6; 0.7] ms
C/N_0	[5; 6; 6.5; 7; 7.5; 15; 22; 27] dB-Hz

Figure 7.17 shows the acquisition search space when acquiring the PRN1 at 5 dB-Hz, exploiting 1 second of coherent integration time and 12 non-coherent accumulations. From the search space it is possible to notice that, in correspondence of the Doppler bin representing the true Doppler affecting the weakest and the strongest received PRNs, several peaks crosses the acquisition threshold. These peaks, which are the effect of the cross correlations between the locally generated PRN 1 and the received PRN 5, threat the acquisition process. However, the considered GNSS scenario is quite pessimistic since same dynamic has been considered for both the weakest and the strongest received PRNs. It is most likely that signals characterized by a very large difference of power are also characterized by different dynamics.

7.6.3.3 Galileo E5a-Q and GPS L5-Q channel acquisition

Table 7.9 and Table 7.10 provides the optimal acquisition parameters and Doppler aiding requirements for the detection of the Galileo E5a-Q pilot channel in lunar orbit environment.

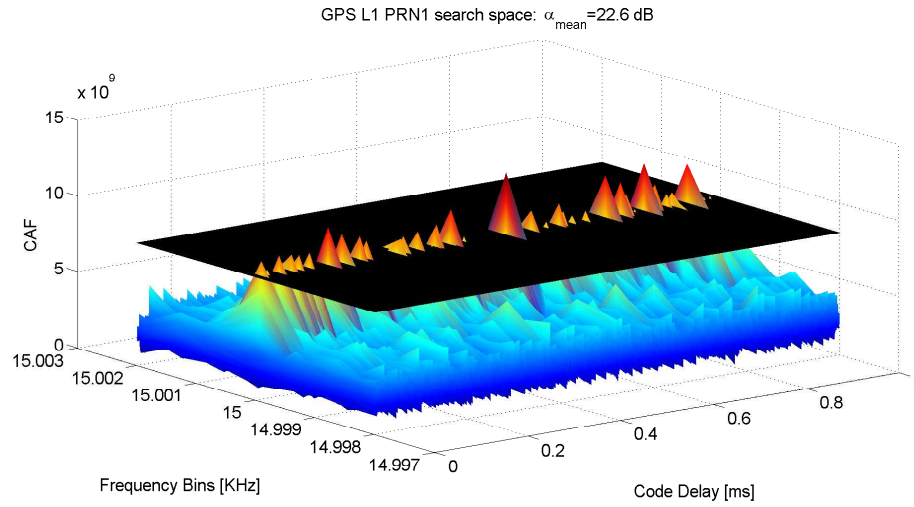


Figure 7.17: GPS L1 C/A non coherent acquisition: Search Space

Table 7.9: Assisted GNSS: Theoretical results for pure coherent E5a-Q channel acquisition

C/N_0	5 dB-Hz	10 dB-Hz
Acquisition parameters	$T_{int} = 12\text{s}$	$T_{int} = 4\text{s}$
P_{FA}^a	$\approx 10^{-2}$	10^{-2}
P_{fa}	10^{-8}	10^{-8}
ϵ_{fD}	0.5 Hz	3 Hz
P_d	87.5%	90.9%
P_D	87%	90.8%
P_{MD}	12.5%	0.09
P_{FA}^p	10^{-3} Hz	$7 \cdot 10^{-10}$
T_P	228 s	76 s

Although the same front-end filter bandwidth has been considered in the theoretical analysis for the acquisition system design in the Galileo E1/E5a frequency bands, less stringent requirements on the Doppler aiding accuracy can be observed in Table 7.9 and 7.10. This is mainly due to the fact that, Galileo E1c primary code period is four times longer than the primary code in the Galileo E5a-Q pilot channel (1 ms), thus leading to a bigger number of bins in the code delay domain of the search space. The increase of the number of bins in the search space leads to a worsening of the P_{FA}^a according

Table 7.10: Assisted GNSS: Theoretical results for non coherent Galileo E5a-Q channel acquisition

C/N_0	5 dB-Hz	10 dB-Hz
Acquisition parameters	$T_{int} = 2\text{s}; K = 9$	$T_{int} = 0.8\text{s}; K = 7$
P_{FA}^a	$\approx 10^{-2}$	10^{-2}
P_{fa}	10^{-8}	10^{-8}
ϵ_{fD}	3 Hz	7 Hz
P_d	87.1%	90.9%
P_D	87%	90.8%
P_{MD}	12.9%	0.09%
P_{FA}^p	$7 \cdot 10^{-10}$ Hz	$7.7 \cdot 10^{-10}$
T_P	342 s	50.4 s

to (7.24).

Table 7.11: Lunar Low Orbit scenario: Galileo E5a-Q

Number of SVN	5
PRN	from 1 to 5
Doppler Frequency f_D	[15; 20; -10; 5; 15] kHz
Code delay τ	[0.5; 0.1; 0.2; 0.3; 0.4] ms
C/N_0	[5; 6; 8; 12; 25] dB-Hz

Finally, acquisition of the Galileo E5a-Q pilot channel in a multiple satellites scenario has been performed. The GNSS lunar low orbit scenario is defined in Table 7.11. The same pessimistic scenario where the strongest and the weakest received PRN are affected by the same Doppler frequency has been considered, the acquisition performance achieved by the employed software receiver are shown in Figure 7.18.

The correct acquisition of Doppler and code delay characterizing the weakest PRN1 is achieved and no impact of the near-far effect is detected, as in the case of Galileo E1c channel acquisition.

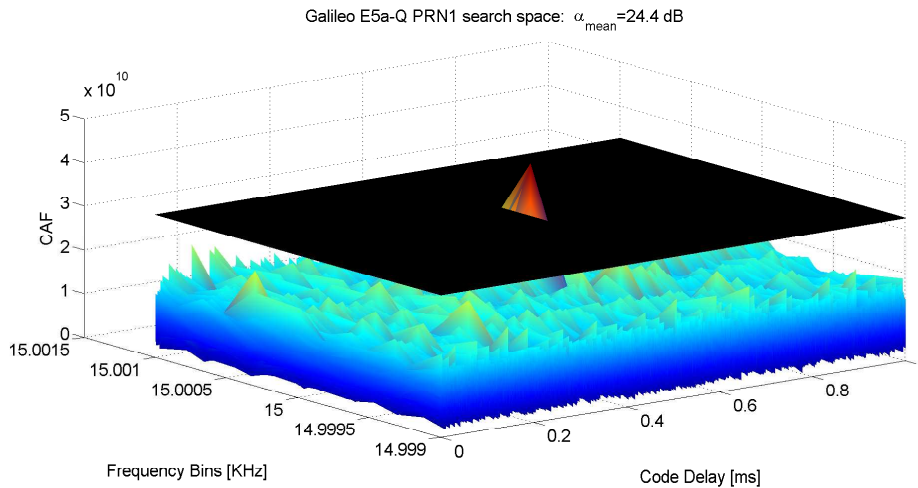


Figure 7.18: Galileo E5a-Q channel non coherent acquisition: Search Space

7.7 Conclusions

Weakest GNSS signal acquisition on the moon, can be achieved exploiting higher coherent integration time and optimal non-coherent accumulations. However, extension of coherent integration time requires the integration with assisted GNSS techniques. In fact, in case of signal featuring only data channel, as the GPS L1 C/A, delivery of the navigation data bit transition information is needed. When considering GNSS signal featuring also the pilot channel, self assistance techniques allowing the receiver to achieve full synchronization with secondary code, are required. However, when dealing with pilot channel 3 dB of loss need to be accounted for. Finally, due to high dynamics characterizing the considered GNSS environment and due to the considered long coherent integration time adopted for the acquisition process, an accurate Doppler aiding to the receiver is also needed. The presented signal processing analysis has been mainly focused on the definition of the Doppler aiding requirements for GNSS signals acquisition at low signal to noise ratio.

In this context, it has been shown that use of non-coherent accumulations has to be preferred with respect coherent acquisition scheme only since requirements on the Doppler aiding accuracy can be relaxed. This is mainly due to

the fact that, use of non-coherent accumulations allows for a reduction of the coherent integration time, which in turn means an increase of the Doppler step in the Doppler domain. Since the targeted false alarm probability at search space level P_{FA}^a determines the number of cells of the whole search space, the increase of the Doppler step will lead to a wider Doppler range to scan and thus to a less stringent requirements on the Doppler aiding. The high Doppler aiding accuracy, required when acquiring the Galileo E1c channel, is justified by the presence of a longer primary code (4 ms) which thus results in an increased code delay dimension in the search space. Nevertheless, it is worth to mention that, even in presence of an extremely accurate Doppler aiding, residual Doppler error may be generated by receiver clock anomalies.

The acquisition simulations with fully software receiver have been performed in order to assess acquisition performance in realistic LLO scenarios, where the receiver has to deal with very weak signals. In this scenario, the focus was to assess the presence of near far effect, which may mask the correct acquisition peak in the search space, as in the case of GPS L1 C/A acquisition. Such a problem has not been detected in the case of Galileo E1c and E5a-Q channel acquisition. These results can be justified by the fact that, Galileo E1c and E5a-Q feature longer primary codes with respect the GPS L1 C/A code. The presence of long codes increases the un-correlation properties of the PRNs transmitted by the satellites. However, use of non-coherent accumulations strongly help in mitigating the near far effect, since the cross correlations peaks are averaged together with noise.

Bibliography

- [1] Luciano Musumeci, Jaron Samson, and Fabio Dovis. Experimental Assessment of Distance Measuring Equipment and Tactical Air Navigation Interference on GPS L5 and Galileo E5a Frequency Bands. In *Satellite Navigation Technologies and European Workshop on GNSS Signals and Signal Processing, (NAVITEC), 2012 6th ESA Workshop on*, pages 1–8, Noordwijk, The Netherlands, 5-7 December 2012.
- [2] Fabio Dovis and Luciano Musumeci. Use of Wavelet Transforms for Interference Mitigation. In *International Conference on Localization and GNSS (ICL-GNSS)*, pages 116–121, Tampere, Finland, 29-30 June 2011.
- [3] Luciano Musumeci and Fabio Dovis. A Comparison of Transformed-Domain Techniques for Pulsed Interference Removal on GNSS Signals. In *International Conference on Localization and GNSS (ICL-GNSS)*, pages 1–6, Starnberg, Germany, 25-27 June 2012.
- [4] L. Musumeci and F. Dovis. Performance Assessment of Wavelet Based Technique in Mitigating Narrow-Band Interference. In *International Conference on Localization and GNSS (ICL-GNSS)*, pages 1,6, Turin, Italy, 25-27 June 2013.
- [5] Fabio Dovis, Luciano Musumeci, and Jaron Samson. Performance Comparison of Transformed-Domain Techniques for Pulsed Interference Mitigation. In *Proceedings of the 25th International Technical Meeting of The Satellite Division of the Institute of Navigation (ION GNSS 2012)*, Nashville, TN, pages 3530–3541, Nashville, TN, September 2012.

- [6] P. F. Silva, H. D. Lopes, T. R. Peres, J. S. Silva, J. Ospina, F. Cichocki, F. Dervis, L. Musumeci, D. Serant, T. Calmettes, I. Pessina, and J. V. Perello. Weak GNSS Signal Navigation to the Moon. In *Proceedings of the 26th International Technical Meeting of The Satellite Division of the Institute of Navigation (ION GNSS+ 2013)*, Nashville, TN, September,16-20 2013.
- [7] E. D. Kaplan and C. Hegarty. *Understanding GPS: Principles and Applications*. Artech House, 2005.
- [8] J. Bao and Y. Tsui. *Fundamentals of Global Positioning System Receivers, a software approach*. John Wiley and Sons, Inc, 2nd edition, 2005.
- [9] <http://www.gps.gov/systems/gps/space/>
- [10] P. Misra and P. Enge. *Global Positioning System: Signals, Measurements and Performance*. Ganga Jumuna Press, 2006.
- [11] Navstar GPS Space Segment/Navigation User Interfaces, IS-GPS-200 Rev.D, IRN-200D-001, March 2007.
- [12] Navstar GPS Space Segment/User Segment L5 Interfaces, IS-GPS-705, January 2005.
- [13] Navstar GPS Space Segment/User Segment L1C Interfaces, Draft IS-GPS-800 Rev.D, April 2006.
- [14] RTCA DO-229D. Minimum Operational Performance Standards for Global Positioning System/Wide Area Augmentation System Airborne Equipment. Technical report, 2006.
- [15] Galileo (European GNSS) Open Service Signal in Space Interface Control Document (OS SIS ICD), Issue 1, Revision 1, September 2010.
- [16] <http://www.gsc-europa.eu/galileo-overview/what-is-galileo>
- [17] Davide Margaria, Mario Nicola, Fabio Dervis, Nicola Linty, and Luciano Musumeci. Galileo In-Orbit Validation E1 and E5 Signals: Experimental Results and Assessment. In *Satellite Navigation Technologies and European Workshop on GNSS Signals and Signal Processing*,

- (NAVITEC), 2012 6th ESA Workshop on, pages 1–8, Noordwijk, The Netherlands, 5-7 December 2012.
- [18] D. Margaria, M. Fantino, and L. Musumeci. Acquisition and Tracking of Galileo IOV E5 Signals: Experimental Results and Performance Evaluation. In *European Navigation Conference on GNSS*, Gdansk, Poland, April 24-27 2012.
- [19] E. Rebeyrol, C. Macabiau, L. Lestarquit, L. Ries, J-L. Issler, M.L. Boucheret, and M. Bousquet. BOC Power Spectrum Densities. In *Proceedings of the National Technical Meeting of the Institute of Navigation, ION-NTM 2005*, ong Beach, CA, 24-26 January 2005.
- [20] G. W. Hein, J.-A. Avila-Rodriguez, S. Wallner, A.R. Pratt, J.I.R. Owen, J.-L. Issler, J.W. Betz, C.J. Hegarty, S. Lenahan, J.J. Rushanan, A.L. Kraay, and T.A. Stansell. MBOC: The New Optimized Spreading Modulation Recommended for Galileo L1 OS and GPS L1C. In *Proceedings of the International Technical Meeting of the Institute of Navigation, IEEE/ION PLANS 2006*, Loews Coronado Bay Resort, San Diego, CA, 24-27 April 2006.
- [21] J.W. Betz. Binary Offset Carrier Modulations for Radionavigation. *NAVIGATION: Journal of The Institute of Navigation*, 48(4), Winter 2001/02.
- [22] J.-A. Avila-Rodriguez, G. W. Hein, S. Wallner, A.R. Pratt, J.I.R. Owen, J.-L. Issler, J.W. Betz, C.J. Hegarty, S. Lenahan, J.J. Rushanan, A.L. Kraay, and T.A. Stansell. Mboc: The new optimized spreading modulation recommended for galileo e1 os and gps l1c. In *ESA Navitec 2006*, Noordwijk, The Netherlands, 11-13 December 2006.
- [23] Parkinson and Spilker. *Global Positioning System: Theory and Applications*. American Institute of Aeronautics and Astronautics, Inc., Washington DC, 1996.
- [24] M S Braasch and A J Van Dierendonck. Gps receiver architectures and measurements. in *Proceedings of the IEEE*, 87(1), January 1999.

- [25] L. Scott, A. Jovancevic, and S. Ganguly. Rapid Signal Acquisition Techniques for Civilian and Military User Equipment Using DSP Based FFT Processing. In *in Proceedings of 14th International Technical Meeting of the Satellite Division of the Institute of Navigation*, September 2001.
- [26] J. A. Volpe. Vulnerability assessment of the transportation infrastructure relying on the global position system. In *National Transportation Systems*, January 2000.
- [27] B. Motella, S. Savasta, D. Margaria, and F. Dovis. Assessing gps robustness in presence of communication signals. In *International Workshop on Synergies in Communications and Localization, International Conference on Communications*, Dresden, Germany, June 2009.
- [28] E. Backer, D. Van Willigen, and R. Rawlings. Technical and operational assessment of the suitability of gps to meet the brnav requirements. Delft University of Technology, Telecommunications and Traffic Control Systems Group, August 1997.
- [29] Beatrice Motella, Marco Pini, and Fabio Dovis. Investigation on the Effect of Strong Out-of-Band Signals on Global Navigation Satellite Systems Receivers. *GPS Solution*, 12:77–86, 2008.
- [30] P. De Bakker, J. Samson, P. Joosten, M. Spelat, M. Hoolreiser, and B. Ambrosius. Effect of radio frequency interference on gnss receiver output. In *in the Proc. of 3rd ESA Workshop on Satellite Navigation User Equipment Technologies (NAVITEC 2006)*, ESA/ESTEC, Noordwijk, The Netherlands, Dec 2006.
- [31] A. T. Balaei, B. Motella, and A. G. Dempster. Gps interference detected in sydney-australia. In *IGNSS conference*, Sydney, Australia, December 2007.
- [32] D. Borio. GNSS Acquisition in the Presence of Continuous Wave Interference. *Aerospace and Electronic Systems, IEEE Transactions on*, 46(1):46,70, January 2010.
- [33] Fabio Dovis, Luciano Musumeci, Nicola Linty, and Marco Pini. Recent

- Trends in Interference Mitigation and Spoofing Detection. *International Journal of Embedded and Real-Time Communication Systems*, 3:1–17, 2012.
- [34] R. J. Landry and A. Renard. Analysis of potential interference sources and assessment of present solutions for GPS/GNSS receivers. *4th Saint-Petersburg on INS*, May 1997.
- [35] ETSI. *Digital Video Broadcasting (DVB); Framing structure, channel coding and modulation for digital terrestrial television*, 2004-2006.
- [36] G. Dimos, T. Upadhyay, and T. Jenkins. Low cost solution to narrowband gps interference problem. In *in Proc. of NAECON*, 1995.
- [37] G. Kuriger, H. Grant, A. Cartwright, and D. Heirmann. Investigation of spurious emission from cellular phones and the possible effect on aircraft navigation equipment. *IEEE TRANSACTION ON ELECTROMAGNETIC COMPATIBILITY*, 45(2), May 2003.
- [38] F. Bastide, E. Chatre, C. Macabiau, and B. Roturier. GPS L5 and GALILEO E5a/E5b Signal-to-Noise Density Ratio Degradation due to DME/TACAN Signals: Simulations and Theoretical Derivations. In *Proceedings of the 2004 National Technical Meeting of The Institute of Navigation*, pages 1049–1062, San Diego, CA, 26-28 January 2004. 2004.
- [39] H. Denks, A. Steingass, and A. Hornbostel. GNSS Receiver Testing by Hardware Simulation with Measured Interference Data from Flight Trials. In *Proceedings of the 22nd International Technical Meeting of the Satellite Division of The Institute of Navigation*, Savannah, GA, September, 22-25 2009.
- [40] G. R. Opshaug and P. Enge. Integrated gps and uwb navigation system (motivates the necessity of non-interference). In *in Proc. of ieee conference*, 2002.
- [41] M. Hamalainen, V. Hovinen, R. Tesi, J. H. J. Iinatti, and M. Lavta-aho. On the uwb system coexistence with gsm900, umts/wcdma, and gps.

IEEE JOURNAL ON SELECTED AREAS IN COMMUNICATIONS,
20(9), Dec 2002.

- [42] D. A. Cummings. Aggregate ultra wideband impact on global positioning system receivers. *IEEE RAW-CON*, Aug 2001.
- [43] D. S. Andenon, E. F. Drocella, S. K. Jones, and M. A. Settle. Assessment of compatibility between ultrawideband systems and global positioning system (gps) receivers. *NT1A Special Publication*, Feb 2001.
- [44] Y. T. Morton, M. P. French, and Tsui Q. Zhou. A software approach to access ultra-wide band interference on gps receivers. In *in Proc. of PLANS*, Apr 2004.
- [45] R. Giuliano and F. Mazzenga. On the coexistence of power-controlled ultrawide-band systems with umts, gps, dcs1800, and fixed wireless systems. *ieee transaction ON VEHICULAR TECHNOLOGY*, 54(1), Jan 2005.
- [46] <http://www.gps.gov/spectrum/lightsquared>
- [47] LightSquared Technical Working Group. Final Report . Technical report, 2011.
- [48] C. O' Driscoll, M. Rao, D. Borio, E. Cano, J. Fortuny, F. Bastide, and D. Hayes. Compatibility analysis between LighthSquared signals and L1/E1 GNSS reception. In IEEE/ION, editor, *Position Location and Navigation Symposium (PLANS)*, pages 447–454, April 23-26 2012.
- [49] S. Savasta. *GNSS Localization Techniques in Interfered Environment*. PhD thesis, Politecnico di Torino, 2010.
- [50] Frederic Bastide, D Akos, C Macabiau, and B Roturier. Automatic Gain Control (AGC) as an Interference Assessment Tool. In *Proceedings of the 16th International Technical Meeting of the Satellite Division of The Institute of Navigation (ION GPS/GNSS 2003)*, pages 2042–2053, Portland, OR, September 2003.
- [51] C. Hegarty, A.J. Van Dierendonck, D. Bobyn, M. Tran, and J. Grabowski. Suppression of Pulsed Interference through Blanking.

- In *Proceedings of the IAIN World Congress and the 56th Annual Meeting of The Institute of Navigation*, pages 399,408, San Diego, CA, June 2000.
- [52] Simone Savasta, Beatrice Motella, Fabio Dovis, R Lesca, and Davide Margaria. On the Interference Mitigation Based on ADC Parameters Tuning. In *Position, Location and Navigation Symposium, 2008 IEEE/ION*, pages 689–695, 5-8 May, 2008.
- [53] B. Motella, M. Pini, and L. Lo Presti. GNSS Interference Detector Based on Chi-Square Goodness- of-Fit Test. In *Satellite Navigation Technologies and European Workshop on GNSS Signals and Signal Processing, (NAVITEC), 2012 6th ESA Workshop on*, pages 1,6, Noordwijk, The Netherlands, December, 5-7 2012.
- [54] D. S. Moore and G. P. McCabe. *Introduction to the practice of Statistics*. 1993.
- [55] Frederic Bastide, Eric Chatre, and Christophe Macabiau. GPS Interference Detection and Identification Using Multicorrelator Receivers. In *Proceedings of the 14th International Technical Meeting of the Satellite Division of The Institute of Navigation (ION GPS 2001)*, pages 872–881, Salt Lake City, UT, September 2001.
- [56] Christophe Macabiau, Olivier Julien, and Eric Chatre. Use of Multicorrelator Techniques for Interference Detection. In *Proceedings of the 2001 National Technical Meeting of The Institute of Navigation*, pages 353 – 363, Long Beach, CA, January 22 - 24, 2001.
- [57] M. Pini, B. Motella, and M. Troglia Gamba. Detection of Correlation Distortions Through Application of Statistical Methods. In *Proceedings of the 26th International Technical Meeting of The Satellite Division of the Institute of Navigation (ION GNSS 2013)*, pages 3279 – 3289, Nashville, TN, September 16 - 20 2013.
- [58] M. Raimondi, O. Julien, C. Macabiau, and F. Bastide. Mitigating Pulsed Interference Using Frequency Domain Adaptive Filtering. In

- Proceedings of the 19th International Technical Meeting of the Satellite Division of The Institute of Navigation (ION GNSS 2006)*, pages 2251–2260, Fort Worth, TX, September 2006.
- [59] D. Borio, L. Camoriano, L. Lo Presti, and P. Mulassano. Analysis of the One-Pole Notch Filter for Interference Mitigation: Wiener Solution and Loss Estimations. In *Proceedings of the 19th International Technical Meeting of the Satellite Division of The Institute of Navigation (ION GNSS 2006)*, pages 1849–1860, Fort Worth, TX, September, 26 - 29 2006.
- [60] D. Borio, L. Camoriano, and L. Lo Presti. Two Pole and Multi Pole Notch Filters: A Computationally Effective Solution for GNSS Interference Detection and Mitigation. *Systems Journal, IEEE*, 2(1):38,47, March 2008.
- [61] Daniele Borio, Cillian O'Driscoll, and Joaquim Fortuny. GNSS Jammers: Effects and Countermeasures. In *Satellite Navigation Technologies and European Workshop on GNSS Signals and Signal Processing, (NAVITEC), 2012 6th ESA Workshop on*, pages 1,7, Noordwijk, The Netherlands, 5-7 Dec. 2012 2012.
- [62] M. Troglia Gamba, E. Falletti, D. Rovelli, and A. Tuozi. FPGA Implementation Issues of a Two-pole Adaptive Notch Filter for GPS/Galileo Receivers. In *Proceedings of the 25th International Technical Meeting of The Satellite Division of the Institute of Navigation (ION GNSS 2012)*, pages 3549–3557, Nashville, TN, September 2012.
- [63] Grace Xingxin Gao. DME/TACAN Interference and its Mitigation in L5/E5 Bands. In *Proceedings of the 20th International Technical Meeting of the Satellite Division of The Institute of Navigation (ION GNSS 2007)*, pages 1191–1200, Fort Worth, TX, September 2007.
- [64] M. De Angelis, R. Fantacci, S. Menci, and C. Rinaldi. An Analysis of Air Traffic Control Systems Interference Impact on Galileo Aeronautics Receiver. In *Radar Conference, 2005 IEEE International*, pages

- 585,595, 9-12 May 2005.
- [65] J. Grabowski and C. Hegarty. Characterization of L5 Receiver Performance Using Digital Pulse Blanking. In *ION GPS*, pages 1630,1635, Portland, OR, September 2002.
- [66] A. Konovaltsev, D. S. De Lorenzo, A. Hornbostel, and P. Enge. Mitigation of Continuous and Pulsed Radio Interference with GNSS Antenna Arrays. In *Proceedings of the 21st International Technical Meeting of the Satellite Division of The Institute of Navigation (ION GNSS 2008)*, pages 2786,2795, Savannah, GA, September, 16-19 2008.
- [67] L. Kurz, E. Tasdemir, D. Bornkessel, T. G. Noll, G. Kappen, F. Antreich, M. Sgammini, and M. Meurer. An architecture for an embedded antenna-array digital GNSS receiver using subspace-based methods for spatial filtering. In *Satellite Navigation Technologies and European Workshop on GNSS Signals and Signal Processing, (NAVITEC), 2012 6th ESA Workshop on*, pages 1,8, Noordwijk, The Netherlands, December, 5-7 2012.
- [68] International Civil Aviation Organization (ICAO). *Aeronautical Telecommunications - Radio Navigation Aids*, volume I of *Annex 10*. 6th edition, 2006.
- [69] A. Simsky, W. De Wilde, T. Willems, D. Mertens, E. Koitsalu, and J. Sleewaegen. First Field Experience with L5 Signals: DME Interference Reality Check. In *Proceedings of the 22nd International Technical Meeting of the Satellite Division of The Institute of Navigation*, Savannah, GA, September, 22-25 2009.
- [70] RTCA DO-292. Assessment of Radio Frequency Interference Relevant to the GNSS L5/E5a Frequency Band. Technical report, 2004.
- [71] R. J. Erlandson, T. Kim, C. Hegarty, and A.J. Van Dierendonck. Pulsed RFI Effects on Aviation Operation Using GPS L5. In *Proceedings of the 2004 National Technical Meeting of The Institute of Navigation*,, pages 1063–1076, San Diego, CA, 28-26 January 2004.

- [72] D. Borio, L. Lo Presti, and P. Mulassano. Spectral Separation Coefficients for Digital GNSS Receiver. In *14th European Signal Processing Conference (EUSIPCO 2006)*, Florence, Italy, September, 4-8 2006.
- [73] J. W. Betz. Effect of Narrowband Interference on GPS Code Tracking Accuracy. In *Proceedings of ION 2000 National Technical Meeting, Institute of Navigation*, Anaheim, CA, January, 26-28 2000.
- [74] J. Soubielle, W. Vigneau, J. Samson, Banos, D.J., and L. Musumeci. Description of an Interference Test Facility (ITF) to Assess GNSS Receivers Performance in presence of Interference. In *Proceedings of the 5th ESA Workshop on Satellite Navigation Technologies and European Workshop on GNSS Signal and Signal Processing (NAVITEC)*, 8-10 December, 2010.
- [75] K. Borre, D.M. Akos, N. Bertelsen, P. Rinder, and S. H. Jensen. *A Software-Defined GPS and Galileo Receiver A Single-Frequency Approach*. Birkhäuser Boston.
- [76] M. Pini. *Constraints Analysis of Radio Frequency Front-End Components: Impact on the GNSS Signal Processing*. PhD thesis, Politecnico di Torino, 2007.
- [77] M. Fantino, M. Nicola, and A. Molino. N-Genie GNSS Receiver: Benefits of Software Radio in Navigation. In *ENC-GNSS*, Naples, Italy, May 3-6 2009.
- [78] D. Borio, S. Savasta, L. Camoriano, and L. Lo Presti. Time-Frequency Excision for GNSS Applications. *Systems Journal, IEEE*, 2(1):27–37, March 2008.
- [79] J. B. Allen and L. Rabiner. A unified approach to short-time Fourier analysis and synthesis. In *Proceedings of the IEEE*, volume 65, pages 1558,1564, November 1977.
- [80] B. Boashash and P. Black. An efficient real-time implementation of the Wigner-Ville distribution. *Acoustics, Speech and Signal Processing, IEEE Transactions on*, 35(11):1611,1618, November 1987.

- [81] C-C. Sun and S-S. Jan. GNSS Interference Detection and Excision Using Time-Frequency Representation. In *Proceedings of the 2011 International Technical Meeting of The Institute of Navigation*, pages 365–373, San Diego, CA, January, 24-26 2011.
- [82] S. Savasta, L. Lo Presti, and M. Rao. Interference Mitigation in GNSS Receivers by a Time-Frequency Approach. *Aerospace and Electronic Systems, IEEE Transactions on*, 49(1):415–438, January 2013.
- [83] D. Gabor. Theory of communication. *Journal of the IEE*, 93(3):429–457, November 1946.
- [84] E. Anyaegbu, G. Brodin, J. Cooper, E. Aguado, and S. Boussakta. An Integrated Pulsed Interference Mitigation for GNSS Receivers. *Journal of Navigation*, 61:239–255, 2008.
- [85] M. Paonni, J. G. Jang, B. Eissfeller, S. Wallner, J. A. Avila Rodriguez, J. Samson, and F. Amarillo Fernandez. Innovative Interference Mitigation Approaches, Analytical Analysis, Implementation and Validation. In *Satellite Navigation Technologies and European Workshop on GNSS Signals and Signal Processing, (NAVITEC), 2010 5th ESA Workshop on*, Noordwijk, The Netherlands, December 2010.
- [86] M. Elhabiby, A. El-Ghazouly, and N. El-Sheimy. A New Wavelet Based Multipath Mitigation Technique. In *ION GNSS*, Savannah, GA, September 16-19 2008.
- [87] Y. L. Xiong, X. L. Ding, W. J. Dai, W. Chen, and D. F. Huang. Mitigation of Multipath Effects Based on GPS Phase Frequency Feature Analysis for Deformation Monitoring Applications. In *ION GNSS*, Long Beach, CA, September 21-24 2004.
- [88] X. Linyuan and L. Jingnan. Approach for Multipath Reduction Using Wavelet Algorithm. In *ION GPS*, Salt Lake City, UT, September 11-14 2001.
- [89] A. El-Ghazouly. The Aid of Wavelet Correlator in Carrier Phase Multipath Reduction and Motion Detection. In *ION GNSS*, Savannah, GA,

- September 22-25 2009.
- [90] E. M. de Souza. Multipath Reduction from GPS Double Differences using Wavelet: How far we can go? In *ION GNSS*, Long Beach, CA, September 21-24 2009.
- [91] M. Elhabiby, A. El-Ghazouly, and N. El-Sheimy. Singularity Detection Technique for GPS Cycle Slip in Wavelets Domain. In *ION GNSS*, Savannah, GA, September 22-25 2009.
- [92] W. Jian and W. Jinling. Reducing Carrier Phase Errors with EMD-Wavelet for Precise GPS Positioning. In *National Technical Meeting of The Institute of Navigation*, San Diego, CA, January 22-24 2007.
- [93] W. E. Travis S. M. Martin, J. J. Dawkins and D. Bevly. Terrain Characterization and Feature Extraction for Automated Convoys. In *ION GNSS*, Portland, OR, September 21-24 2010.
- [94] C. Maccone. The KLT (Karhunen-Loève Transform) to extend SETI Searches to Broad-band and Extremely Feeble Signals. *Acta Astronautica*, 67(11-12):1427 – 1439, 2010.
- [95] A. Szumski. Finding the Interference, Karhunen-Loève Transform as an Instrument to Detect Weak RF Signals. *InsideGNSS*, (3):56–64, 2010.
- [96] P.P. Vaydianathan. *Multirate Systems and Filter Banks*. Signal Processing Series. Prentice-Hall, 1993.
- [97] Y. Meyer, editor. *Wavelets Algorithms and Applications*. Society for Industrial and Applied Mathematics, 1993.
- [98] D. Margaria, E. Falletti, B. Motella, M. Pini, and G. Povero. N-FUELS, a GNSS Educational Tool for Simulation and Analysis of a Variety of Signal in Space. In *ENC-GNSS*, Braunschweig, Germany,, October 19-21 2010.
- [99] F. Dovis. *Wavelet Based Designed of Digital Multichannel Communications Systems*. PhD thesis, Politecnico di Torino, 1999.
- [100] F. Dovis, M. Mondin, and F. Daneshgaran. The modified Gaussian:

- a novel wavelet with low sidelobes with applications to digital communications. *Communications Letters, IEEE*, 2(8):208,210, August 1998.
- [101] Marvin. K. Simon, Jim K. Omura, Robert A. Scholtz, and Barry K. Levitt. *Spread Spectrum Communications Handbook*. McGraw-Hill, Inc., revised edition, 1994.
- [102] F. S. Van Diggelen. *A-GPS: Assisted GPS, GNSS, and SBAS*. Artech House, 2009.
- [103] D. Borio. *A Statistical Theory for GNSS Signal Acquisition*. PhD thesis, Politecnico di Torino, 2008.
- [104] Cillian O ' Driscoll. *Performance Analysis of the Parallel Acquisition of Weak GPS Signals*. PhD thesis, National University of Ireland, 2007.
- [105] D. Borio, L. Camoriano, and L. Lo Presti. Impact of GPS acquisition strategy on decision probabilities. *Aerospace and Electronic Systems, IEEE Transactions on*, 44(3):996,1011, July 2008.